Universidade Federal de Minas Gerais
Instituto de Ciências Exatas
Departamento de Química

DIANA QUINTÃO LIMA DE OLIVEIRA

DEGRADAÇÃO OXIDATIVA DE COMPOSTOS ORGÂNICOS EM MEIO AQUOSO POR VIA CATALÍTICA HETEROGÊNEA COM MAGNETITA E GOETHITA DOPADAS COM NIÓBIO

Belo Horizonte
2011

UFMG – ICEx/DQ-872ª
T. 373ª

DIANA QUINTÃO LIMA DE OLIVEIRA

DEGRADAÇÃO OXIDATIVA DE COMPOSTOS ORGÂNICOS EM MEIO AQUOSO POR VIA CATALÍTICA HETEROGÊNEA COM MAGNETITA E GOETHITA DOPADAS COM NIÓBIO

Tese apresentada ao Departamento de Química do Instituto de Ciências Exatas da Universidade Federal de Minas Gerais, como requisito parcial para a obtenção do grau de Doutor em Ciências - Química.

Belo Horizonte
2011

Oliveira, Diana Quintão Lima de

Degradação oxidativa de compostos orgânicos em meio aquoso por via catalítica heterogênea com magnetita e goethita dopadas com nióbio./Diana Quintão Lima de Oliveira. 2011.

xv: 77 f. : il

Orientador: José Domingos Fabris

Co-Orientador: Luiz Carlos Alves de Oliveira

Tese (Doutorado) – Universidade Federal de Minas Gerais. Departamento de Química.
Bibliografia p. 67-73

1.Físico-Química - Teses 2.Óxidos de ferro – Teses

UFMG

PROGRAMA DE PÓS-GRADUAÇÃO EM QUÍMICA
DEPARTAMENTO DE QUÍMICA - ICEx
31270-901 - BELO HORIZONTE - MG
TEL.: 031 - 3409-5732
FAX: 031 - 3409-5711
E-MAIL: pgquimic@qui.ufmg.br

"Degradação Oxidativa de Compostos Orgânicos em Meio Aquoso por Via Catalítica Heterogênea com Magnetita e Goethita Dopadas com Nióbio"

Diana Quintão Lima de Oliveira

Tese aprovada pela banca examinadora constituída pelos Professores:

Prof. José Domingos Fabris - Orientador
UFMG

Prof. Luiz Carlos Alves de Oliveira - Co-Orientador
UFMG

Profa. Sibele Berenice Castellã Pergher
UFRN

Prof. Márcio César Pereira
UFVJM

Prof. Rodrigo Lassarote Lavall
UFMG

Prof. Rochel Montero Lago
UFMG

Belo Horizonte, 25 de agosto de 2011.

A presente tese foi realizada sobre a orientação do Prof. José Domingos Fabris (DQ/UFMG) e co-orientação do Prof. Luiz Carlos Alves de Oliveira (DQ/UFMG).

Dedico este trabalho aos meus pais, Dilson e Anália; aos meus irmãos, Patrícia e Marcos Janer; e ao meu marido, Luiz; por todo apoio e amor.

.

AGRADECIMENTOS

A Deus, por ter me dado saúde e forças para enfrentar todas as dificuldades no decorrer deste trabalho.

À minha família, em especial aos meus pais, Dilson e Anália, e aos meus irmãos, Patrícia e Marcos Janer, por todo apoio, amor e incentivo. Ao meu marido, Luiz, pelo amor, carinho, paciência, apoio, além das ajudas nos momentos difíceis em que não me deixou desistir de lutar para finalizar esse trabalho.

Ao professor José Domingos Fabris, pelos ensinamentos e, sobretudo, pela confiança e paciência depositada em mim.

Ao professor Luiz Carlos Alves de Oliveira, pela dedicação demonstrada durante a realização deste trabalho e pelas ótimas idéias sempre, além da grande ajuda para que esse trabalho fosse concluído.

Ao professor Yadong Yin, pela hospitalidade, disponibilidade em discutir os resultados obtidos e tantos ensinamentos no período em que estive trabalhando em seu laboratório, na Universidade da Califórnia, em Riverside.

Ao professor Igor Frota de Vasconcelos, do Departamento de Engenharia Metalúrgica e de Materiais da Universidade Federal do Ceará, pela ajuda na interpretação dos dados XAFS obtidos no LNLS, que contribuíram bastante para a tese.

Ao professor Karim Sapag, do Laboratorio de Ciencias de Superficies y Medios Porosos, Universidade Nacional de San Luis, Argentina, pela amizade e colaboração com as análises de áreas superficiais dos materiais.

Ao prof. Rochel Montero Lago pelas discussões, sugestões e por nos conceder gentilmente o seu laboratório sempre que necessário.

À profa. Maria Irene Yoshida pela amizade e pela realização das análises termogravimétricas no Laboratório de Análise Térmica.

Ao prof. Wagner da Nova Mussel e Juliana Oliveira do Departamento de Química da Universidade Federal de Minas Gerais, pelas medidas de difração de raios X.

Ao Laboratório Nacional de Luz Síncrotron (LNLS), por possibilitar a realização das medidas de absorção e difração de raios X.

Ao prof. Paulo Couceiro (UFAM), por me acompanhar em uma das visitas ao LNLS.

Aos colegas de laboratório, Luis Carlos (Piripiri), Cássius, Adilson (Zé), Jake, Vitor,

Flavinha, Fernanda, Almerindo, Lucas, Poly, Mariana, Amanda, Sarah, Camila, Nath, Jéssica e Josi, pelos bons momentos no lab e nos “cafés”. Em especial ao Marcinho (agora professor Márcio!!!), pela amizade e por toda ajuda no lab, desde o começo e à Ana Rosa (agora pelo mundo afora, né Aninha?, pela grande amizade, cumplicidade e grande ajuda nesses anos.

Aos colegas de laboratório dos EUA, que convivi durante o doutorado sanduíche, por toda a ajuda, em especial aos chineses tão queridos Qiao Zhang, Yongxing Hu e Miaomiao Ye, pela amizade e momentos tão divertidos que passamos juntos.

A todos os professores e colegas de laboratório de Lavras, em especial a Malu, Guerreiro, Téo, Matheus, Jonas, Kátia, Paulize, Maraísa, Sarah e Guilherme, pela amizade e ajuda durante esse período. A todos os amigos do DQ/UFMG, em especial, Juan, Roberta, Virgínia, Arlete, Juliana, Patrícia, Marcelo e Raquel.

Aos professores e amigos, Patterson Patrício e Patrícia Santiago, pela amizade, carinho e apoio; Flávia Moura e Maria Helena Araújo, pela ajuda, paciência e incentivo durante esse final de doutorado, quando eram muitas as aulas a serem dadas no DQ.

À minha irmã Patty, e demais colegas da república Pagu, por me acolherem na república enquanto eu fazia a ponte rodoviária Lavras-BH.

Às amigas Ana Paula, Dri e Aline, por toda amizade e bons conselhos durante esses anos, por sempre torcerem por mim. Aos amigos Smurfs, que torceram, mesmo longe, por mais essa etapa alcançada na minha vida.

À amiga Ana Rosa R. Bastos, que mesmo em Lavras, sempre esteve junto de mim nessa jornada, pelo carinho e ajuda.

Aos professores, técnicos, secretárias e demais funcionários do Departamento de Química da UFMG que de alguma forma contribuíram para o desenvolvimento deste trabalho. Em especial às funcionárias da pós-graduação Paulete, Kátia, Lílian e Fabiana, por todo trabalho, dedicação e amizade. Aos funcionários da oficina eletrônica e mecânica, Jacaré, Rúbio, Rogério e Anderson pelo empenho em solucionar os problemas para o bom funcionamento do laboratório. Às funcionarias do xerox, Rebeka e Laura, pela ajuda e paciência na hora de montar a tese.

Ao CNPq pelo auxílio financeiro e bolsa de doutorado sanduíche no exterior.

À CAPES e à FAPEMIG.

RESUMO

Este trabalho foi dividido em duas partes essenciais: (i) síntese, caracterização e avaliação das propriedades catalíticas de goethitas dopadas com nióbio e (ii) transformação *via* redução química com hidrogênio gasoso, das goethitas dopadas ($\alpha Fe_{1-x}Nb_xOOH$), para a obtenção das magnetitas dopadas com nióbio ($\left(Fe^{2+}, Fe^{3+}\right)_{3-x}Nb_xO_4$) correspondentes. Os óxidos de ferro magnéticos isoestruturais ao espinélio, como a magnetita, apresentam algumas propriedades interessantes, tal como a ocorrência estrutural simultânea de Fe^{2+} e Fe^{3+}, que são primordialmente consideradas promotoras da eficiência catalítica, em processos redoxes.

As amostras dos catalisadores sólidos preparados neste trabalho foram testadas na oxidação de compostos orgânicos em meio aquoso, empregando-se, como substratos, os corantes orgânicos azul de metileno e rodamina B, para servirem de modelos moleculares de substâncias poluentes. As amostras de Nb-magnetita, e das Nb-goethita precursoras, foram caracterizadas e testadas em reações oxidativas de substratos orgânicos, em meio aquoso.

As caracterizações físico-químicas e das propriedades estruturais dos materiais permitiram a identificação dos principais compostos de ferro formados. Verificou-se a formação de óxidos com promissoras propriedades catalíticas. Os resultados revelaram comportamentos diferenciados: para a reação de oxidação do substrato constituído de azul de metileno na presença de peróxido de hidrogênio, em meio aquoso, as goethitas contendo nióbio foram quimicamente mais efetivas, comparativamente às magnetitas correspondentes e levaram a, aproximadamente, 90% de descoloração da solução inicial.

A busca experimental de elucidação dos mecanismos químicos, fundamentada na identificação da natureza dos intermediários, formados durante a oxidação do corante orgânico, por espectrometria de massas, com injeção por electrospray, levou a importantes evidências sobre etapas catalíticas envolvidas no processo oxidativo. A presença de Nb na estrutura aumenta a eficiência catalítica da goethita, na oxidação de compostos orgânicos, por um mecanismo que envolve a formação de espécies *peroxo* com o nióbio, de forte caráter oxidante, na superfície dos grãos. Essas espécies oxidantes geradas *in situ* podem ainda ser regeneradas, por ação do peróxido de hidrogênio, adicionado ao meio reacional.

ABSTRACT

This work was divided into two main parts: (i) Synthesis, characterization and study of catalytic properties of niobium-doped goethites and (ii) Transformation of the goethites described in part (i) via chemical reduction with H_2 to obtain magnetite. The catalysts were tested in the oxidation reaction of organic compounds in aqueous medium, employing the organic dyes methylene blue and rhodamine B as model organic molecules to simulate the pollutant substrate. The magnetic iron oxides, isostructurals to the spinel, have some interesting properties, such as the presence of Fe^{2+} and Fe^{3+} simultaneously in the structure to be applied as catalysts in this redox processes. The magnetites were also characterized and tested in the same reactions as the goethite precursors.

The physicochemical characterizations and textural properties of the materials allowed the identification of the iron compounds formed, as well as their key characteristics that reveal iron oxides with promising catalytic properties. For the oxidation reaction tested using hydrogen peroxide and organic dyes in aqueous medium, the goethites containing niobium were the most active comparatively to magnetites, with approximately 90% of solution discoloration. It was carried out an identification study of the intermediates formed during the methylene blue dye oxidation, using the mass spectrometry technique with electrospray injection, allowing it to elucidate, at least partially the catalytic mechanism involved.

The experimental search for elucidation of chemical mechanisms, based on the identification of the intermediates nature formed during the oxidation of organic dye, by mass spectrometry with electrospray injection, led to important evidences about the steps involved in the catalytic oxidation process. The presence of Nb in the structure increases the catalytic efficiency of goethite in the oxidation of organic compounds by a mechanism involving the formation of *peroxo* species with niobium, with strong oxidizing character, on the surface of the grains. These oxidizing species generated *in situ* can also be regenerated by the action of hydrogen peroxide, added to the reactionary medium.

LISTA DE FIGURAS

LISTA DE TABELAS

LISTA DE ABREVIATURAS

Gt – Goethita

Mt – Magnetita

Wt – Wüstita

RhB – Rodamina B

AM – Azul de metileno

EM – Espectroscopia Mössbauer

Δ – Desdobramento quadrupolar

δ – Deslocamento isomérico

ε – Deslocamento quadrupolar

Γ – Largura de linha à meia altura do (sub)espectro Mössbauer

Bhf – Campo hiperfino magnético

XAS – X-ray Absorption Spectroscopy

XANES – X-ray Absorption Near Edge Structure

EXAFS – Extended X-ray Absorption Fine Structure

LNLS – Laboratório Nacional de Luz Síncrotron

DSC – Calorimetria Exploratória Diferencial

DRX – Difratometria de raios X

RTP – Redução à Temperatura Programada

SUMÁRIO

1. INTRODUÇÃO

1.1. ÓXIDOS DE FERRO

Os óxidos de ferro, devido à sua ampla disponibilidade e propriedades químicas e físicas, são catalisadores ou promotores em vários processos químico-industriais, tais como, síntese de amônia, reação de desidrogenação de etilbenzeno a estireno e síntese de Fischer-Tropsch [1-4]. Além disso, o grande interesse pelo tratamento de efluentes industriais envolvendo materiais de ampla disponibilidade natural e relativamente baixo custo, tem atraído a atenção tanto da indústria como da comunidade científica no uso de compostos de ferro para a remoção de compostos orgânicos em água [5-6]. A habilidade que os compostos de ferro possuem de ativar peróxido de hidrogênio para gerar radicais $^{\bullet}OH$, *in situ*, faz com que os óxidos de ferro apresentem grande potencial como catalisador na oxidação de compostos orgânicos em meio aquoso. O processo de geração de $^{\bullet}OH$ é bastante conhecido e largamente empregado em sistemas homogêneos, onde o H_2O_2 é decomposto pelo $Fe^{2+}_{(aq)}$, proveniente da dissolução de sulfato ferroso em água. Esse processo apresenta alguns inconvenientes, como sua difícil reutilização [7-8]. Um processo similar, conhecido como Fenton heterogêneo, que emprega compostos de ferro como óxidos, tem apresentado resultados promissores no tratamento de efluentes. É importante ressaltar que os óxidos de ferro, por apresentarem propriedades semicondutoras, têm sido amplamente utilizados como catalisadores em reações de fotodegradação em meio aquoso, que ocorrem via geração de radicais hidroxilas [9-11]. Os processos envolvendo radiação e H_2O_2, comumente conhecidos como processos avançados de oxidação, serão discutidos com mais detalhes na seção 1.3.

Dentre os óxidos de ferro comumente empregados em processos de descontaminação ambiental destaca-se a hematita (αFe_2O_3), maghemita (γFe_2O_3), magnetita (Fe_3O_4) e goethita ($\alpha FeOOH$). A seguir, serão descritas com mais detalhes as propriedades dos óxidos empregados nesse trabalho: goethita e magnetita.

1.1.1 Goethita

A goethita, $\alpha FeOOH$, é um dos minerais mais facilmente formados em condições naturais e portanto, encontrado em abundância no geoambiente. Tem estrutura química de coordenação com poliedros de duplas camadas de octaedros $FeO_3(OH)_3$ compartilhados pela aresta (Figura1). As duplas camadas são ligadas

pelos vértices formando “túneis” octaedrais do tipo 2 x 1, mantidos por ligações de hidrogênio [1]. O pó tem coloração marrom-amarelada, ocorre em quase todos os solos e outras formações superficiais contendo ferro e possui estrutura menos compacta do que outros óxidos de ferro (Por isso, a substituição isomórfica do Fe por outros cátions na estrutura da goethita [12] é mais favorável), como a magnetita (Fe_3O_4) ou hematita (αFe_2O_3), que são óxidos mais comumente empregados em reações catalíticas heterogêneas. Com o objetivo de aumentar a atividade catalítica da goethita em um determinado processo, sua rede cristalina pode ser modificada pela introdução de cátions via substituição isomórfica dos íons ferro. Além disso, nanopartículas de goethita podem ser depositadas em um material suporte, visando à obtenção de fases cristalográficas com pequeno tamanho de partícula e elevada área específica. No que se refere às substituições isomórficas, cátions dopantes são adicionados, por exemplo, para modificar a eficiência de processos redoxes, como na reação de Fenton heterogêneo. Aliadas à facilidade com que se consegue alterar sua estrutura visando maximizar suas propriedades catalíticas, as goethitas podem ser facilmente obtidas sinteticamente por diferentes rotas, com pureza arbitrariamente controlada.

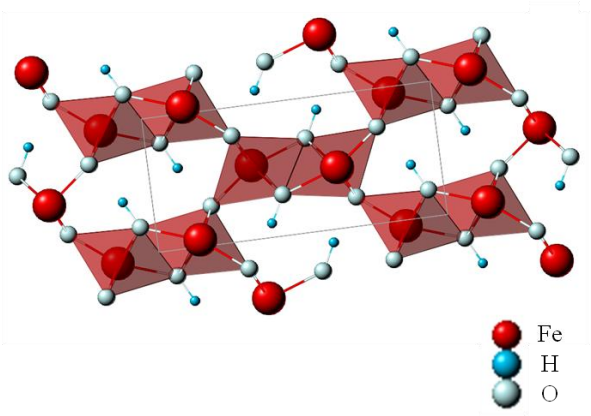

Figura 1. Representação cristalográfico-estrutural da goethita em que as esferas vermelhas representam os íons Fe^{3+} coordenados por átomos de oxigênio (em azul claro); as esferas menores (azul claro) referem-se aos átomos de hidrogênio.

Com relação às propriedades catalíticas, as goethitas têm sido empregadas em trabalhos recentes nos processos de geração de espécies altamente oxidantes, em meio aquoso, por exemplo, para o tratamento de efluentes contendo pesticidas, como

relatado por Gajovic et al. 2011 [13]. Dentre os diversos trabalhos citados na literatura científica, pode-se destacar o artigo publicado por Han et al., 2011, que relata a combinação entre H_2O_2 e luz visível, na degradação de corantes orgânicos em água [14].

1.1.2 Magnetita

A estrutura de espinélio invertido da magnetita confere ao óxido de ferro importantes propriedades elétricas e magnéticas [15]. Uma característica química marcante da magnetita, que determina seu uso na catálise, é a presença simultânea de Fe^{2+} e Fe^{3+} na estrutura, o que permite oxidação e redução sequenciais em processos envolvendo a transferência de elétrons. A magnetita cristaliza-se no sistema cúbico, em estrutura do tipo espinélio invertido, em que o Fe^{3+} está coordenado a oxigênios em simetria tetraédrica e o Fe^{2+} e Fe^{3+} em simetria octaédrica (Figura 2). A fórmula da magnetita pode ser escrita como $[Fe^{3+}]\{Fe^{3+}Fe^{2+}\}O_4$, em que [ ] representa o sítio tetraédrico [sítio A] e { } representa o sítio octaédrico {sítio B} [16]. Outro aspecto importante da magnetita é a possibilidade de introdução por dopagem química e substituição isomórfica de diversos cátions metálicos em sua estrutura (em diferentes estados de oxidação), acarretando mudanças significativas das propriedades redoxes e, consequentemente, da atividade catalítica desses materiais [16].

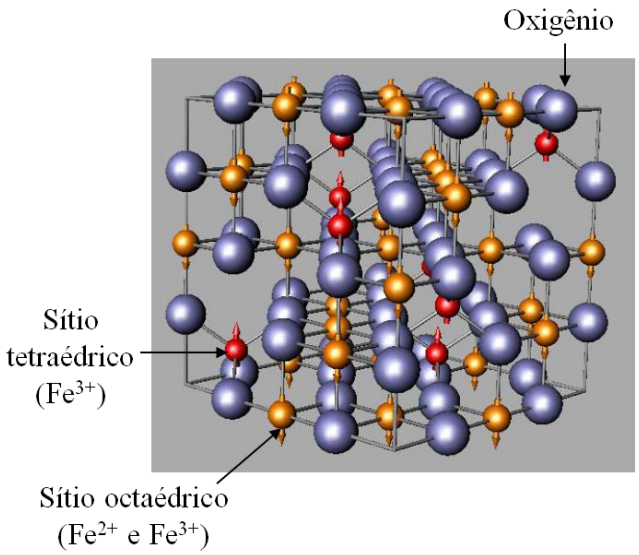

Figura 2. Representação estrutural dos arranjos octaédricos e tetraédricos da magnetita. As esferas vermelhas representam os íons Fe^{3+} tetraédricos (sítio A), as esferas amarelas representam os íons Fe^{3+} e Fe^{2+} octaédricos (sítio B) coordenados por átomos de oxigênio (em azul).

Assim como descrito para a goethita, a magnetita tem sido modificada, seja pela introdução de cátions em sua estrutura ou pela redução química dos íons Fe^{3+}, com o objetivo de melhorar suas propriedades catalíticas. As modificações estruturais por redução química, com gás, principalmente com H_2, têm transformado a magnetita em um catalisador com elevada capacidade de geração de radicais hidroxilas, em meio aquoso, quando na presença de peróxido de hidrogênio [17]. Já a dopagem com diferentes cátions, como por exemplo a incorporação de Mn, Ni, Co ou Mg, promove interessantes mudanças nas propriedades texturais da magnetita, aumentado sua área específica e, ainda, facilitando o processo transferência de elétrons [16].

No presente trabalho, foi empregado o Nb^{5+} como íon dopante da goethita e da magnetita. As razões pelas quais se decidiu pelo uso do nióbio como dopante estão relacionadas com as propriedades químicas conferidas por esse elemento aos óxidos. As principais características químico-cristalográficas e ocorrência mineralógica dos compostos de nióbio são descritas com mais detalhes na seção seguinte.

1.2 NIÓBIO

O Brasil é o maior produtor mundial de nióbio. Dados de 2008 apontam uma produção de aproximadamente 86 mil toneladas, o que representa cerca de 96% do total mundial. A produção brasileira vem crescendo, devido, sobretudo, ao aquecimento na demanda de ferroligas, provocada principalmente pela elevada expansão do PIB dos países asiáticos, que estimulou o aumento da produção mundial de aço bruto. As principais empresas produtoras no Brasil são: Companhia Brasileira de Metalurgia e Mineração (CBMM), 60,7%; Anglo American Brasil (Mineração Catalão), 21%; Mineração Taboca, 12,8% e outros (5,5%). No Brasil, os principais estados produtores são: MG (61%), GO (21%) e AM (12%) [18]. Das reservas mundiais, que correspondem a 5,7 milhões de toneladas de óxido de nióbio, 5,2 milhões de toneladas, estão em território brasileiro. O Brasil tem mais de 90% da reserva total do minério do mundo. No Brasil, as reservas de nióbio estão localizadas nos estados de MG (principalmente em Araxá com 73%), AM (25%) e GO (1,4%) [18].

O elemento nióbio foi descoberto em 1801 por Charles Hatchett a partir do mineral ferrocolumbita (fórmula química ideal, $FeNb_2O_6$), extraído de um minério da região de Massachusetts (EUA) e enviado para a Inglaterra. Denominado, então,

colúmbio, foi posteriormente nomeado nióbio, em homenagem à deusa mitológica Níobe, filha do rei Tântalo. A denominação nióbio foi oficialmente adotada pela IUPAC em 1950. Sua ocorrência natural na crosta terrestre é de aproximadamente 20 mg kg^{-1}. Não ocorre no estado livre, sendo usualmente encontrado associado ao tântalo, presente no mineral $(Fe,Mn)M_2O_6$ (se M = Nb, o mineral é ferrocolumbita; se M = Ta, ferrotantalita) [19]. O nióbio, um metal do grupo VA, tem número atômico 41 e massa molar (M) igual a 92,9064 g mol^{-1}. Quando puro, é macio e dúctil, mas impurezas o tornam mais duro. Embora apresente estados de oxidação formais variando de +5 até -1, o seu estado de oxidação mais estável no geoambiente é o +5. O estado de oxidação +4 pode ocorrer em haletos, enquanto os estados +2 e +3 aparecem em *clusters* estruturados em octaedros do tipo M_6X_{12} [19].

As informações mais antigas sobre o uso de nióbio datam de 1925, na substituição do tungstênio usado em ferramentas de aço. No início da década de 1930, o nióbio passou a ser utilizado como material de ligas, na prevenção de corrosão intergranular em aços inoxidáveis [20]. Devido às suas propriedades catalíticas, compostos de nióbio têm se tornado importantes para várias reações químicas, sendo o interesse nos mesmos cada vez maior. A função dos compostos de nióbio em catálise pode ser de promotor ou fase ativa, suporte, catalisador ácido ou material redox.

Algumas reações nas quais catalisadores à base de nióbio (principalmente seu óxido, Nb_2O_5) já foram estudados são as seguintes: desidratação de alcoóis, desidrogenação, esterificação, alquilação, isomerização, hidrodessulfurização e fotocatálise [19]. De fato, compostos de nióbio são catalisadores interessantes e importantes para várias reações. Embora existam poucas diferenças de eletronegatividade e raio iônico entre Nb e seus vizinhos na tabela periódica (V, Zr, Mo), é intrigante que os comportamentos catalíticos dos compostos de nióbio sejam bastante diferentes daqueles de compostos dos elementos circundantes.

Por isso, a pesquisa e desenvolvimento tecnológico envolvendo compostos de nióbio têm sido muito considerados nos últimos 20 anos. Como mencionado anteriormente, os compostos de nióbio têm características que os permitem atuar como fase ativa ou como suporte catalítico. Óxidos de nióbio melhoram notavelmente a atividade catalítica e prolongam a vida de catalisadores conhecidos, quando

pequenas quantidades são adicionados a eles. Óxidos mistos contendo nióbio também mostram o efeito acima [21].

Existem poucos trabalhos relatados na literatura voltados para o uso de nióbio como elemento dopante em óxidos metálicos. Recentemente, nosso grupo de pesquisa sintetizou e testou os efeitos da presença de Nb na estrutura da hematita em reações do tipo Fenton e para a degradação de corante orgânico em água na presença de radiação UV (fotocatálise) [22]. Os resultados desse trabalho mostraram que o Nb causa uma alteração favorável, do ponto de vista fotocatalítico, das propriedades eletrônicas da hematita, levando à diminuição do *band gap*, o que melhora as propriedades do material. Para o caso das reações na presença de H_2O_2 (Fenton modificado), foi observado que a geração de espécies reativas na superfície da hematita (identificadas como grupos peroxos, gerados pela presença do Nb (Figura 3)) maximizou a atividade catalítica do material, melhorando significativamente a remoção de um corante.

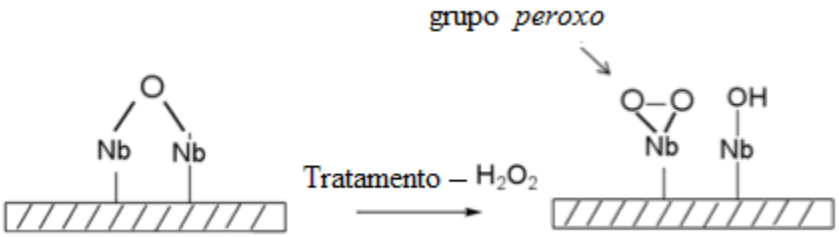

Figura 3. Esquema com a representação do grupo *peroxo* formado na presença de nióbio.

No presente trabalho, o nióbio foi empregado na dopagem de goethita e magnetita visando a obtenção de materiais do tipo $Fe_{1-x}Nb_xOOH$ e $Fe_{3-x}Nb_xO_4$, respectivamente. Esses materiais foram utilizados na oxidação de compostos orgânicos em água através dos processos avançados de oxidação (PAO). Foram empregados na presença de peróxido de hidrogênio (processo Fenton heterogêneo) ou sob radiação ultravioleta visando à geração de radical hidroxila para oxidação de corantes orgânicos.

1.3 TECNOLOGIAS DE OXIDAÇÃO DE COMPOSTOS ORGÂNICOS

Existem diferentes classes de poluentes orgânicos oriundos de diversas atividades industriais, tais como têxtil, plástica, farmacêutica, metalúrgica, refinarias de óleo, produção de pesticidas, resinas, papéis e explosivos [23]. A toxicidade desses compostos em ambientes aquáticos tem sido estudada e verificou-se que a sua presença em doses subletais afeta os sistemas nervoso e circulatório, com redução do crescimento de células sanguíneas [24,25]. Mesmo em concentrações extremamente baixas, poluentes, como por exemplo os do tipo fenólico, produzem um sabor identificável na água o que acarreta sérios problemas operacionais para a saúde da população, bem como para os diversos ramos da indústria, tais como, alimentos, cervejarias, destilarias e unidades de engarrafamento de água mineral. De acordo com o relatório 2004 do Instituto Mineiro de Gestão das Águas (IGAM) [26] sobre a qualidade das águas, os elevados índices de substâncias orgânicas representam as maiores ocorrências de desconformidade com a legislação em todo o Estado de Minas Gerais (Figura 4). Cerca de 70% dos resultados das análises não atendem aos limites das classes de enquadramento dos cursos d'água monitorados [26]. Grande parte da carga orgânica encontrada tem origem em processos industriais, onde os efluentes não foram adequadamente tratados. Consciente de que o tratamento remediador de efluentes industriais deve considerar fatores econômicos e de eficiência química do processo empregado, o objetivo é alcançar completa mineralização do poluente, por conversão completa a dióxido de carbono, água e sais minerais, ou, pelo menos, reduzir a toxicidade dos compostos intermediários. As principais tecnologias usualmente empregadas na remoção de compostos orgânicos em efluentes industriais são: tratamento biológico, tratamento com carvão ativado, processos térmicos, arraste com ar ou osmose reversa [27,28]. No entanto, processos onde radicais livre hidroxila são gerados *in situ*, conhecidos como processos avançados de oxidação (PAO), têm despontado como uma tecnologia alternativa promissora.

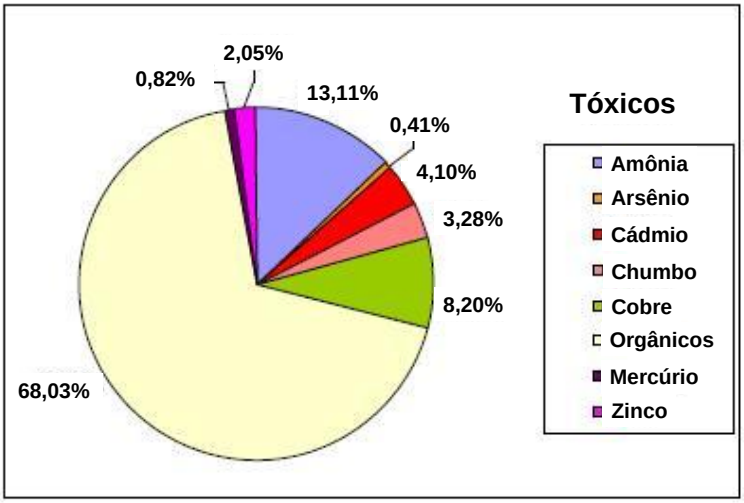

Figura 4. Participação de fontes químicas de contaminação em cursos d'água no estado de Minas Gerais [26].

Os processos avançados de oxidação (PAO) constituem uma classe especial de métodos de oxidação apontadas como promissoras na remediação ambiental. Geralmente, requerem baixas temperaturas e baixas pressões, visando à geração de radicais hidroxilas ($^{\bullet}$OH), que são espécies reativas com as moléculas orgânicas rápida e indiscriminadamente, seja por adição à insaturação ou por abstração do átomo de hidrogênio, em moléculas orgânicas alifáticas [29]. O resultado é a formação de radicais orgânicos que reagem com oxigênio, dando início a uma série de reações de degradação, que podem culminar em espécies ambientalmente menos nocivas, tipicamente dióxido de carbono e água [30].

Os PAOs têm tido importância crescente, em razão das aplicabilidades em casos mais específicos, como contaminantes xenobióticos (exemplo, pesticidas e fenóis) e compostos refratários e não-biodegradáveis (exemplo, corantes têxteis e organoclorados), que são contaminantes de difícil degradação. Uma característica única e muito importante dos PAOs é serem eficientes para a degradação de contaminantes orgânicos mesmo em concentrações muito baixas [16]. As equações (1-3) apresentam possíveis reações envolvendo a geração de radicais hidroxila pela decomposição de peróxido de hidrogênio por íons ferrosos.

1.3.1 Sistema Fenton

O sistema proposto por Fenton (1894) [31] tem sido extensivamente usado nos últimos anos para a decomposição de diferentes tipos de contaminantes orgânicos em água [32, 33].

No sistema Fenton, o agente ativador é o Fe^{2+} solúvel, que funciona como redutor da molécula de H_2O_2, para produzir o radical $HO^{\bullet}$ e o íon HO^{-}, como descrito

$$Fe^{2+} + H_2O_2 \rightarrow Fe^{3+} + HO^{\bullet} + HO^{-} \quad \text{Eq. 1}$$

$$H_2O_2 + HO^{\bullet} \rightarrow H_2O + {}^{\bullet}O_2^{-} + H^{+} \quad \text{Eq. 2}$$

$$H_2O_2 + {}^{\bullet}O_2^{-} + H^{+} \rightarrow O_2 + HO^{\bullet} + H_2O \quad \text{Eq. 3}$$

na Eq. 1 e que pode levar a reações como descritas nas Eq. 2-3, através de um mecanismo conhecido como Haber-Weiss [34].

Apesar de muito eficiente, o processo Fenton clássico, ou seja, o sistema homogêneo (Fe^{2+} dissolvido em água), apresenta desvantagens para a aplicação em grande escala. Por exemplo, a necessidade de pH abaixo de 3 ocasiona um gasto de grandes volumes de ácido. Assim, antes do descarte do efluente, deve-se realizar a neutralização com grandes quantidades de base, tal como NaOH, que leva à formação de um resíduo (lodo) de hidróxido de ferro (III) [34, 35]. Outra desvantagem do sistema Fenton clássico homogêneo é a necessidade de quantidade estequiométrica de Fe^{2+} e peróxido de hidrogênio em solução.

Há, pois, interesse maior no desenvolvimento de novos sistemas ativos, do tipo heterogêneo, que operem em pH próximo da neutralidade para que possam ser recuperados e reciclados sem geração de resíduos [36].

1.3.1.1 Sistema Fenton heterogêneo

O sistema Fenton heterogêneo apresenta várias vantagens em relação ao sistema Fenton clássico (homogêneo) [37]:

- As operações de carga/descarga, limpeza e reciclagem dos tanques/reatores são mais fáceis.
- É realizado em pH neutro, não necessitando as etapas de acidificação (para pH 3) e posterior neutralização, evitando-se assim, a geração de lodo.

- O sistema pode ser reciclado ou, até, plenamente regenerado.

Diversos trabalhos de pesquisa científica têm sido dedicados ao uso de diferentes sólidos contendo ferro em sistemas do tipo Fenton heterogêneo, tais como Fe_2O_3, $Fe_2Si_4O_{10}(OH)_2$ [37-40], goethita [41-43], Fe(II) suportado em zeólita, Al_2O_3 ou SiO_2 [44,45] e Fe^0/Al_2O_3 [46]. Foi observado que, dependendo das condições utilizadas, esses materiais, na presença de peróxido de hidrogênio, são capazes de promover a oxidação avançada de diferentes contaminantes orgânicos, como por exemplo, compostos aromáticos, ácidos alifáticos, fenol [47], compostos clorados [48] e corantes orgânicos. Entretanto, alguns desses sistemas mostraram baixa atividade ou levam à lixiviação de grande quantidade de ferro, devido ao baixo pH.

Recentemente, nosso grupo de pesquisa desenvolveu um novo sistema Fenton heterogêneo baseado em óxidos de ferro do tipo $Fe_{3-x}M_xO_4$ (onde M = Ni, Co, Mn, Nb) e compósitos envolvendo as espécies Fe^o/Fe_3O_4, que se mostraram altamente eficientes para a oxidação de contaminantes orgânicos em efluentes aquosos, utilizando H_2O_2 [16,49,50].

1.3.2 Fotocatálise

A fotocatálise é um processo alternativo para tratamento de água visando à remoção do poluente através da sua mineralização pelo emprego de um semicondutor sólido e radiação UV. O princípio da aplicação da fotocatálise envolve a ativação por luz solar ou artificial de um semicondutor (geralmente, TiO_2 na forma de "anatásio", pois este apresenta características de elevada estabilidade, bom desempenho catalítico e baixo custo) [51]. Um semicondutor sólido é caracterizado por apresentar bandas de valência (BV) e bandas de condução (BC) com uma região intermediária de energia entre essas duas bandas, denominada *bandgap*. A absorção de fótons com energia superior à energia de *bandgap* resulta na promoção de um elétron da banda de valência para a banda de condução com geração concomitante de uma lacuna (h^+) na banda de valência, como representado no esquema mostrado na Figura 5. Essas lacunas mostram potenciais bastante positivos, na faixa de +2,0 a +3,5 eV, dependendo do semicondutor e do pH do meio. Esse potencial é suficientemente positivo para gerar radicais $HO^{\bullet}$, a partir de moléculas de água ou íons hidroxila ($^-$OH) adsorvidos na superfície do semicondutor, os quais podem subseqüentemente

oxidar o contaminante orgânico [51]. O processo de geração do radical hidroxila via processo fotocatalítico pode ser descrito pelas seguintes equações:

Catalisador + radiação → catalisador ativado (h^+ + e^-) Eq. 4

H_2O + h^+ → $^{\bullet}OH$ + H^+ Eq. 5

$2H^+$ + $2e^-$ → H_2 Eq. 6

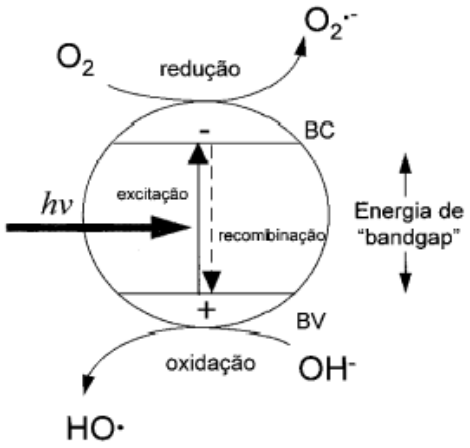

Figura 5. Esquema representativo da estrutura de banda de uma partícula de um semicondutor em processo de geração de radical hidroxila via fotocatálise. BV: banda de valência; BC: banda de condução [51].

2. OBJETIVOS

O objetivo geral do presente trabalho foi o preparo de catalisadores baseados em óxidos de ferro, estruturalmente dopados com Nb^{5+}. Os óxidos de ferro escolhidos foram goethita (αFeOOH) e magnetita (Fe_3O_4), sendo que a escolha dos mesmos foi baseada nas propriedades anteriormente descritas. Além disso, foi estudada a influência da dopagem desses óxidos com diferentes proporções de nióbio na eficiência dos materiais testados como catalisadores, na reação de oxidação de moléculas orgânicas em água. As propriedades catalíticas dos catalisadores modificados com Nb foram testadas frente aos processos avançados de oxidação do tipo Fenton heterogêneo e fotocatálise.

Os objetivos específicos são:

1) Sintetizar e caracterizar óxidos de ferro puros e dopados com nióbio:

a) αFeOOH (goethita) e Fe_3O_4 (magnetita);

b) $\alpha Fe_{1-x}Nb_xOOH$ e $Fe_{3-x}Nb_xO_4$.

2) Caracterizar os materiais quanto às propriedades químicas, texturais e morfológicas:

(i) Identificar os compostos de ferro formados empregando a difratometria de raios X, espectroscopia Mössbauer e espectroscopia no infravermelho;

(ii) Analisar a morfologia por microscopia eletrônica de varredura e transmissão.

3) Testar a capacidade desses materiais para a produção de radical hidroxila através dos processos de fotocatálise e oxidação com H_2O_2 (sistema Fenton heterogêneo), para a oxidação dos corantes rodamina B e azul de metileno (AM), usados como moléculas modelo de substratos orgânicos(simulação de substratos orgânicos poluentes em água).

4) Estabelecer o mecanismo químico de decomposição do AM, para o catalisador quimicamente mais eficiente, através da identificação dos intermediários de reação formados por electrospray-LC/MS Trap.

3. MATERIAIS E MÉTODOS

3.1 SÍNTESE DOS MATERIAIS

3.1.1. Goethitas

A amostra de goethita foi sintetizada através do método descrito por Cornell e Schwertmann (2000) [1], gotejando-se, lentamente, 180 mL de KOH (5 mol L^{-1}) em um frasco de polietileno contendo 100 mL de $Fe(NO_3)_3$ (1 mol L^{-1}), sob agitação constante (100 rpm). Em seguida, a suspensão foi diluída com água destilada para 2 L e mantida a 60 °C por 72 horas. O precipitado foi então lavado até pH = 7, para a remoção de todo os íons ^{-}OH e NO_3^- em solução.

Para a síntese das goethitas substituídas, foi adicionado o sal de nióbio, ($NH_4[NbO(C_2O_4)_2(H_2O)](H_2O)_n$) ao sal de ferro, antes de se gotejar a base, nas quantidades desejadas de dopagem (3, 10, 15 e 20% em mol de nióbio com relação à fórmula teórica da goethita). O sal de nióbio foi fornecido pela CBMM (Companhia Brasileira de Metalurgia e Mineração).

3.1.2. Magnetitas

As magnetitas foram obtidas através das goethitas preparadas no item anterior, por um processo de redução química das mesmas. Para isso, as amostras foram colocadas em um tubo de vidro, com um fluxo de hidrogênio (80 mL min^{-1}), que foi aquecido em um forno tubular, com uma taxa de aquecimento de 10 °C min^{-1}, até 430 °C, temperatura em que permaneceu por 30 min. A temperatura de redução da goethita para magnetita foi determinada por uma análise via Redução à Temperatura Programada (RTP). O perfil de redução da goethita sintética e sem dopagem é mostrado na Figura 20. Ressaltamos que todos os materiais, mesmo aqueles modificados pela dopagem com Nb, sofreram o mesmo tipo de tratamento térmico para formação da magnetita.

3.2. CARACTERIZAÇÃO DOS MATERIAIS

3.2.1. Análises Químicas

Inicialmente, foi determinado o teor de ferro presente nos materiais. A determinação de Fe total foi realizada por volumetria de oxirredução, utilizando o método de dicromatometria [52]. O método se baseia na redução do Fe(III) para Fe(II)

e consequente titulação do ferro (II) com uma solução de dicromato de potássio (Equação 7):

$$Cr_2O_7^{2-} + 6Fe^{2+} + 14\ H^+ \rightarrow 2Cr^{3+} + 6Fe^{3+} + 7H_2O \qquad \text{Eq. 7}$$

Para a análise do teor total de ferro nas amostras, pesou-se aproximadamente 0,05 g de cada amostra, em triplicata, tanto para as goethitas quanto para as magnetitas, e transferiu-se para um erlenmeyer de 250 mL. Adicionou-se cerca de 10 mL de HCl concentrado e aqueceu-se até a completa solubilização da amostra. Ao final, adicionou-se mais 5 mL de HCl concentrado e transferiu-se para um balão de 100,00 mL, completando-se o volume com água e efetuando uma homogeneização da solução.

Uma alíquota de 25,00 mL da solução da amostra foi retirada, em triplicata, e colocada em um erlenmeyer de 250 mL. Aqueceu-se a solução até próximo a ebulição. Adicionou-se algumas gotas de $SnCl_2$ (6% em massa) até a descoloração da solução. O $SnCl_2$ foi utilizado para reduzir o Fe^{3+} a Fe^{2+} em HCl quente. Resfriou-se a solução até a temperatura do ambiente. Adicionou-se, sob agitação, 5 mL de H_2SO_4(1:5), 2,5 mL de H_3PO_4 concentrado, 30 mL de água destilada e 5mL de $HgCl_2$ 5%. O excesso de redutor ($SnCl_2$) é eliminado pela adição de $HgCl_2$ (Eq. 8).

$$Sn^{2+} + 2HgCl_2 \rightarrow Sn^{4+} + Hg_2Cl_2 + 2Cl^- \qquad \text{Eq. 8}$$

Uma coloração branca perolada (Hg_2Cl_2) indica o ponto em que o excesso de Sn^{2+} foi removido, evitando-se, assim, consumo de dicromato de potássio pelo estanho divalente. Nessa etapa deve-se evitar a formação de uma coloração cinza, pois indica excesso de íons estanho e contínua redução do mercúrio a mercúrio metálico. Adicionou-se 8 gotas de indicador difenilaminossulfonato de bário e titulou-se com $K_2Cr_2O_7$ 0,0016 mol/L. A mudança de cor foi observada do verde-azulado para púrpura.

Em seguida, para as amostras de magnetita, determinou-se o teor de Fe^{3+} presente pela diferença entre o valor dosado de ferro total e o valor dosado de Fe^{2+}, segundo o procedimento descrito a seguir [52,37].

Para a determinação do teor de Fe^{2+} presente nas amostras de magnetitas (Figura 6), a dissolução da amostra (cerca de 0,1 g) foi feita, a quente, com 30 mL de HCl concentrado em atmosfera de CO_2 (cerca de 0,3 g de $NaHCO_3$ foram colocados juntamente com a amostra antes da adição do HCl).

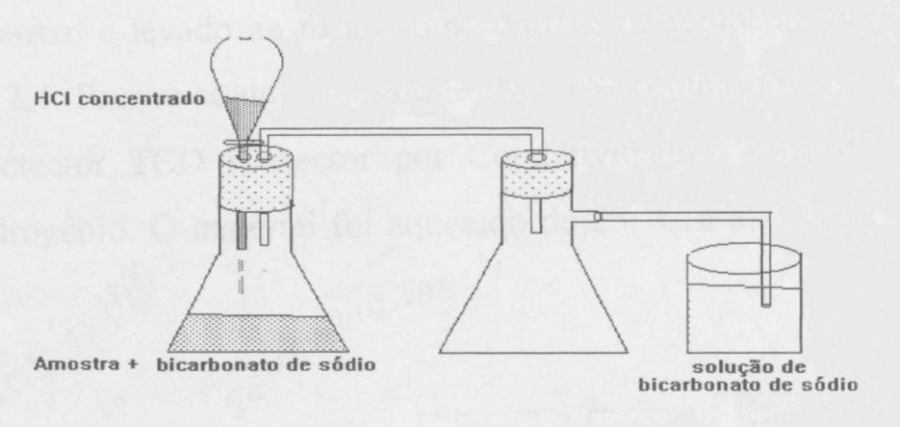

Figura 6. Montagem utilizada na determinação de Fe^{2+}.

Ao final da abertura da amostra (dissolução do sólido), adicionou-se 15,00 mL de solução HNO_3:H_2SO_4 2:1 para garantir a complexação de todo o Fe^{2+} presente e a titulação foi feita em seguida com a solução de dicromato de potássio de maneira semelhante a descrita anteriormente para o teor de ferro total.

Devido à dificuldade de se determinar o teor de nióbio com precisão, utilizou-se a técnica de espectroscopia de energia dispersiva (EDS, Energy Dispersive Spectroscopy) para a obtenção de valores aproximados. O teor de nióbio foi estimado por análises pontuais na amostra no Laboratório de Microanálise do Departamento de Física-UFMG. Foi utilizado o equipamento Jeol, modelo JXA-8900RL, com energia de 15,0 keV, potencial de aceleração de 15,0 kV e corrente de feixe de 12 nA.

3.2.2. Microscopia eletrônica de varredura

A morfologia dos materiais foi estudada utilizando-se um microscópio eletrônico de varredura (Jeol, modelo JSM-840A), operando com tensão de 15 kV e corrente de 10^{-10} A. Para isso, as amostras foram fixadas em fitas de carbono e, posteriormente, cobertas com ouro, para análise.

3.2.3. Espectroscopia no infravermelho

As amostras foram analisadas por espectroscopia na região do infravermelho (FTIR) (Digilab Excalibur, série FTS 3000), para identificação de grupos químico-funcionais característicos da fase mineralógica formada. Os espectros foram obtidos utilizando-se pastilhas de KBr (aproximadamente 3,0 mg de amostra para 97,0 mg de KBr).

3.2.4. Microscopia eletrônica de transmissão

Um microscópio eletrônico de transmissão (Tecnai, modelo T12) foi usado para complementar a caracterização já feita da morfologia dos materiais por microscopia eletrônica de varredura. As amostras foram dispersas em etanol e em seguida, uma gota dessa dispersão foi depositada sobre uma grade de cobre coberta com carbono, e depois levada à evaporação sobre vácuo a temperatura ambiente. As medidas foram feitas no laboratório central de microscopia e microanálise da Universidade da Califórnia, em Riverside, em colaboração com o Professor Yadong Yin, durante o período de estágio de doutorado-sanduíche (de Abril a Dezembro de 2009).

3.2.5. Difratometria de Raios X

Para, identificar as fases cristalinas presentes, os materiais foram caracterizados por difratometria de raios X (DRX), método do pó, utilizando-se um difratômetro Rigaku, modelo Geigerflex, radiação de CoKα (λ= 1.78897 Å), tensão de 32,5 kV e corrente de 25,0 mA. A varredura foi feita no intervalo de 20-80° (2θ) e as velocidades de varreduras foram de 1° (2θ) min^{-1} para as goethitas e 4° (2θ) min^{-1} para as magnetitas. Para a análise mineral qualitativa dos difratogramas, foi utilizada a biblioteca do banco de dados PCPDFWIN® versão 1.30* [53].

A análise quantitativa do difratograma foi realizada pelo método de Rietveld (Rietveld, 1969) usando-se o programa de computador Fullprof_Suíte disponível em *http://www.ill.eu/sites/fullprof/,* (*a*cesso em Janeiro 2011). Foram coletados dados de difração de raios X, com fonte de radiação síncrotron, da linha XPD 1 (método do pó), no Laboratório Nacional de Luz Síncrotron (LNLS), em Campinas (SP). Os dados foram coletados à temperatura do ambiente (298 K), com radiação de comprimento de onda λ = 1,23844 Å, com varredura entre os ângulos $10º < 2\theta < 100º$

* JCPDS-ICDD (1997) Mineral Powder Diffaction.

na velocidade de varredura de 0,05º 2θ/min, com 2 segundos de contagem por incremento.

3.2.6. Espectroscopia Mössbauer

A espectroscopia Mössbauer (EM) é uma técnica que envolve emissão e absorção ressonante de raios gama pelos núcleos de alguns elementos químicos. O efeito da absorção ressonante da radiação gama nuclear foi observado pela primeira vez pelo cientista Rudolph L. Mössbauer, razão essa o nome dado à técnica. A espectroscopia Mössbauer é uma poderosa ferramenta de pesquisa experimental para o estudo estrutural, químico e magnético da matéria condensada [54].

Essencialmente, o processo ressonante consiste na emissão de radiação γ por um núcleo excitado e na absorção dessa radiação por outro núcleo idêntico, sem perda de energia pelo recuo dos núcleos, se o emissor ou o absorvedor estiverem incorporados a uma matriz sólida. O núcleo emissor é colocado em movimento oscilatório longitudinal para que a radiação γ seja emitida com um intervalo de energia modulado, através do efeito Doppler [54], para compensar os desdobramentos dos níveis nucleares devido às interações hiperfinas.

A partir de um espectro Mössbauer, pode-se obter os seguintes parâmetros:

- Deslocamento isomérico: parâmetro relacionado com o estado de oxidação ou valência dos átomos que compõem a amostra;
- Desdobramento quadrupolar: parâmetro relacionado com o gradiente de campo elétrico que acopla com os momentos elétricos nucleares;
- Campo hiperfino: parâmetro relacionado com a interação do campo magnético com os momentos magnéticos dos núcleos dos átomos envolvidos na ressonância.

Os espectros Mössbauer foram coletados com as amostras a 298 e a 110 K (criostato de banho, com nitrogênio líquido), por um espectrômetro convencional de transmissão com aceleração constante, CMTE modelo MA250 e uma fonte de ~50 mCi de ^{57}Co em matriz de ródio. A massa da amostra para a medida foi estimada para conter ferro na proporção de ~10 mg cm^{-2}. Os deslocamentos isoméricos são expressos em relação ao αFe, padrão também usado para a calibração da escala de

velocidade Doppler. Os dados coletados foram ajustados por um algoritmo dos mínimos quadrados, com uso do programa de computador NORMOS® 90† [55].

3.2.7. Espectroscopia de absorção de raios X

O espectro XAS das amostras de goethita e magnetita contendo nióbio foram coletados nas bordas K do ferro (7112 eV) e do nióbio (18700 eV). As medidas de absorção de raios X foram feitas na linha de feixe de luz XAFS1 do Laboratório Nacional de Luz Síncrotron (LNLS), localizado em Campinas, SP. O anel de armazenamento do LNLS opera em 1,37 GeV com corrente nominal de 130 mA. Os dados de absorção de raios X foram coletados no modo transmissão utilizando câmaras de ionização preenchidas com ar. O feixe incidente foi monocromatizado com um monocromador de Si (111) do tipo *channel-cut*. A energia foi calibrada no primeiro ponto de inflexão do salto da borda no espectro XANES da folha metálica (7112 eV para a borda do ferro, 18986 eV na borda do nióbio). Espectros EXAFS na borda-K do ferro foram coletados na faixa 6900-8100 eV, enquanto que os espectros XANES na borda-K do nióbio foram coletados na faixa de 18700-19200 eV. Todos os espectros foram normalizados pelo salto na borda. Os espectros EXAFS foram analisados utilizando-se o procedimento padrão de redução de dados [56] dentro do pacote de programação ifeffit [57]. Para a interpretação dos dados, teve-se a ajuda primordial do professor Igor Frota de Vasconcelos, do Departamento de Engenharia Metalúrgica e de Materiais, da Universidade Federal do Ceará.

3.2.8. Redução à temperatura programada (RTP)

A análise de RTP foi realizada utilizando-se cerca de 50 mg de cada amostra, que foram colocadas num tubo de quartzo e levadas ao forno com controle de temperatura (Eurotherm). Passou-se um fluxo de H_2/N_2, a uma taxa de 50 mL min^{-1}, sendo utilizado um detector TCD (Detector por Condutividade Térmica), para monitorar o consumo de hidrogênio. As amostras foram aquecidas de 25 ºC a 1000 ºC a uma taxa de 10 ºC min^{-1}.

† Programa de computação desenvolvido por R. A. Brand, Laboratórium för Argewandte Physik, Universität Duisburg, D-47048, Duisburg-Germany.

3.2.9. Área BET

A textura dos materiais foi caracterizada por adsorção/dessorção de nitrogênio a -196 ºC, usando-se o equipamento AUTOSORB-1 da Quantachrome. Para isso, a amostra foi previamente tratada a 300 °C sob fluxo de nitrogênio por três horas. A distribuição de tamanho de poros foi calculada a partir da isoterma usando o modo BJH. A área específica foi calculada utilizando a equação BET na região de baixa pressão relativa ($p/p_o = 0,200$).

3.2.10 Calorimetria exploratória diferencial (DSC)

As análises de DSC foram realizadas em um aparelho da marca Rigaku MOD 8065 D1, utilizando termistor de Pt e αAl_2O_3 como material de referência. Utilizou-se cerca de 5 mg das amostras, que foram aquecidas continuamente com temperatura variando de 25 a 400 °C, em atmosfera de ar com uma taxa de aquecimento de 10 °C min^{-1}.

3.3 OXIDAÇÃO DO CORANTE AZUL DE METILENO E DECOMPOSIÇÃO DE H_2O_2

3.3.1. Decomposição de H_2O_2

O potencial catalítico dos materiais foi analisado inicialmente através da decomposição de peróxido de hidrogênio (H_2O_2), monitorando-se o volume de O_2 liberado, utilizando-se um equipamento fechado e pressão atmosférica (Figura 7). O volume de O_2 formado foi medido pelo deslocamento da coluna de água em uma bureta. Para tal, foram utilizados 30 mg do material, 5 mL de água destilada e 2 mL de H_2O_2.

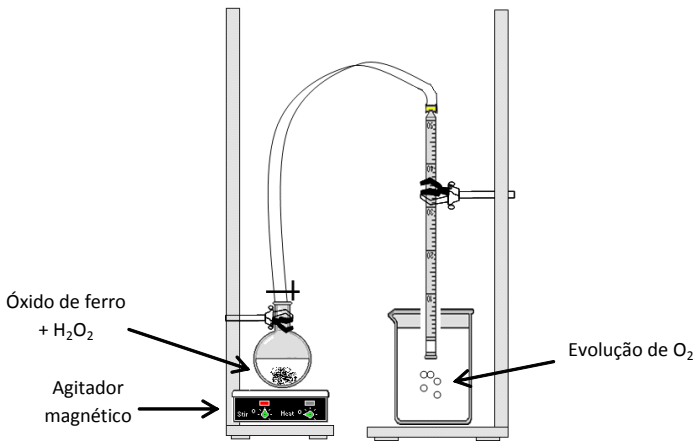

Figura 7. Sistema para medida da decomposição fotocatalítica de peróxido de hidrogênio.

3.3.2 Degradação de azul de metileno via Fenton heterogêneo

Os testes de degradação do composto orgânico modelo azul de metileno (AM) foram realizados utilizando-se 9,90 mL da solução na concentração de 25 mg L^{-1}, 0,10 mL de H_2O_2 30% e 10 mg do material, sob agitação constante de 100 rpm, nos tempos 0, 15, 30, 60, 120 e 180 min. A temperatura usada no teste foi 25 ± 1 ºC.

A degradação foi monitorada por espectroscopia de UV-Visível (Shimadzu-UV-1601 PC), no comprimento de onda de absorção máxima do AM: 665 nm.

3.3.3 Espectrometria de massas com ionização via electrospray (ESI-MS)

Devido à possibilidade de formação de intermediários durante a oxidação do corante azul de metileno, os produtos de degradação foram analisados por ESI-MS (espectrometria de massas com ionização por electrospray), modo positivo, em um espectrômetro de massas com ionização por eletrospray Trap (Agilent-1100).

As alíquotas da reação foram inseridas no aparelho por infusão a um fluxo de 5 μL min^{-1}. Os espectros foram obtidos como uma média de 5 scans de 0,2 s. As condições da análise foram: temperatura do gás de secagem (N_2): 325 ºC e fluxo de 4 L min^{-1}, controle de carga no quadrupolo (ICC) ajustado para 30000, potencial de extração de íons de -3500 V.

3.4 FOTOCATÁLISE UTILIZANDO O CORANTE RODAMINA B

Os testes de degradação fotocatalítica foram feitos utilizando-se o corante rodamina B (RhB), por possuir uma degradação mais difícil que o corante azul de metileno. Utilizou-se um béquer de 100 mL contendo 50 mL de solução de RhB 1,0 x 10^{-5} mol/L, sob agitação constante de 650 rpm e 30,0 mg dos diferentes catalisadores. A solução foi agitada no escuro por 30 min para se garantir que o corante RhB tivesse sido adsorvido até a saturação pelos catalisadores. Para a fonte de irradiação UV, uma lâmpada de 15 W (254 nm, XX-15G, USA) foi mantida a 6 cm sobre o meio reacional. A intensidade média da luz que atinge a superfície da solução foi de aproximadamente 1,55 mW cm^{-2}.

A atividade fotocatalítica foi avaliada por meio do monitoramento da banda de absorção característica em 553 nm para medir a taxa de degradação da rodamina B (RhB), utilizando-se um espectrômetro de UV-Visível (Ocean Optics HR2000CG-

UV-NIR). A Figura 8 apresenta uma foto do sistema experimental para a realização da fotocatálise.

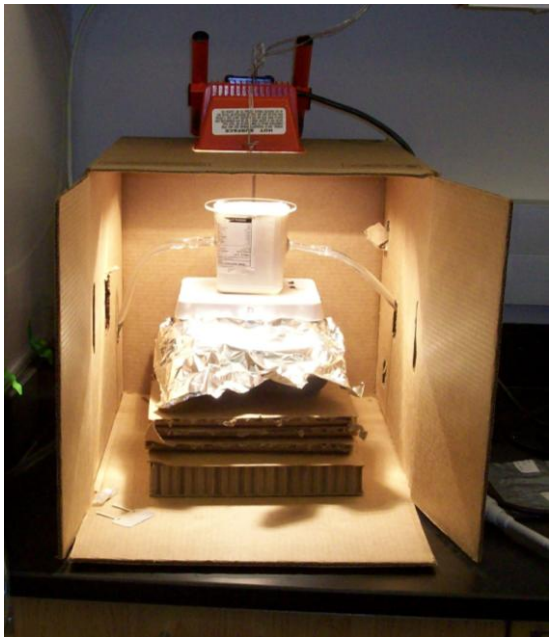

Figura 8. Sistema experimental utilizado para os estudos via fotocatálise.

4. RESULTADOS E DISCUSSÕES

4.1. GOETHITAS

As amostras de goethitas estudadas nesse trabalho foram sintetizadas pelo método de co-precipitação descrito por Cornell e Schwertmann (2000) [1]. Dentre as caracterizações físico-químicas realizadas para os materiais resultantes da síntese estão a difratometria de raios X, espectroscopia Mössbauer, espectroscopia de absorção de raios X e medidas de área específica. Para avaliar o comportamento catalítico dos materiais, foram realizados testes de oxidação utilizando-se os corantes azul de metileno e rodamina B como moléculas modelo e os resultados encontram-se a seguir.

4.1.1. Análises Químicas

Os resultados das análises de composição química em ferro total (determinados por dicromatometria) e de nióbio (estimados por EDS - espectroscopia de energia dispersiva) para as goethitas são apresentados na Tabela 1.

Os resultados obtidos pelas análises de EDS (Figura 9) indicaram a presença de nióbio nas amostras dopadas e algum potássio como impureza.

Tabela 1. Composição química das goethitas contendo Nb, expressa em (% em massa) para o ferro total, e (% atômica) para o nióbio. As incertezas indicadas para os valores para ferro são estimativas a partir do desvio padrão sobre a média, calculada de três aberturas de amostras.

Amostra	Teor de Ferro /%	Teor de Nióbio/%
01	57 ± 1	0
02	56 ± 1	1
03	52 ± 1	4
04	49 ± 1	8
05	46 ± 1	11

As análises químicas confirmaram um decréscimo na quantidade de ferro com o aumento da incorporação de nióbio pelas goethitas. As amostras foram então rotuladas de acordo com o teor aproximado de nióbio em sua estrutura, como sendo **Gtpura, Gt-Nb1, Gt-Nb4, Gt-Nb8 e Gt-Nb11**. As análises de EDS para as diferentes goethitas estão mostradas na Figura 9.

Para confirmar a incorporação de Nb^{5+} na estrutura, outras caracterizações dos materiais foram feitas, tais como espectroscopia Mössbauer, difratometria de raios X e análise térmica (DSC).

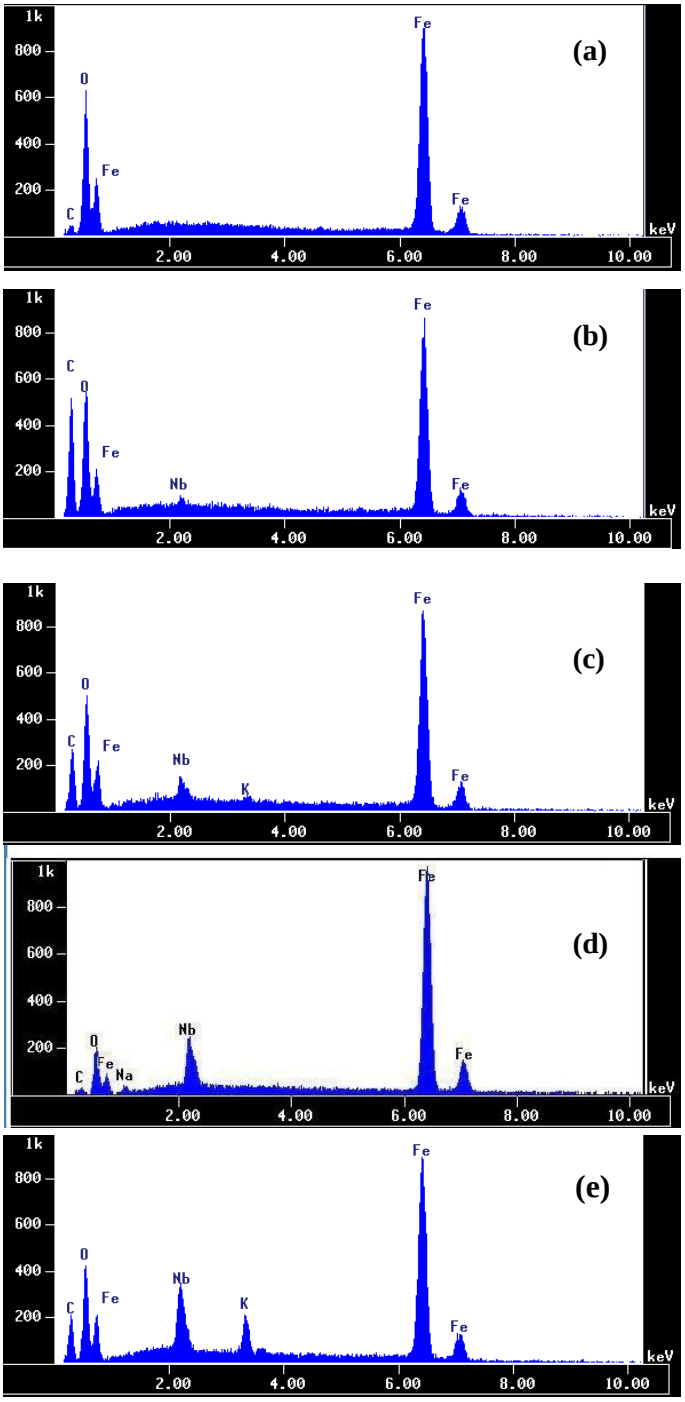

Figura 9. Espectros EDS para a série de goethitas: Gtpura (a), Gt-Nb1 (b), Gt-Nb4 (c), Gt-Nb8 (d) e Gt-Nb11(e).

4.1.2. Espectroscopia no infravermelho

As goethitas foram caracterizadas pela espectroscopia na região do Infravermelho. Essa é uma técnica importante na identificação desse material, pois

existem modos vibracionais característicos. O espectro de infravermelho da goethita pura (Figura 10) mostra uma banda intensa em 3125 cm^{-1}, devido ao estiramento da hidroxila interna estrutural (O–H bulk). Pode-se perceber que à medida que se tem um aumento do teor de nióbio no material, há uma diminuição na intensidade dessa banda, indicando perda de OH interno. Um diagnóstico importante para se verificar a formação da goethita são as bandas de deformação angular O–H em aproximadamente 889 (Fe–OH) e 794 (Fe–OH) cm^{-1}, que são vibrações dentro e fora do plano, respectivamente [1], e em 644 cm^{-1} (estiramento Fe–O). O espectro FTIR da goethita com menor teor de Nb, Gt-Nb1, mostrou um perfil parecido com o espectro da amostra Gtpura. Porém, com o aumento do teor de nióbio na estrutura da goethita, verificou-se diminuição na intensidade e deslocamento das bandas, principalmente na amostra Gt-Nb11. Dentre as diferenças asseguradas, a banda relativa ao estiramento Fe–O é alargada e deslocada para 593 cm^{-1}. Além disso, a banda de desdobramento O–H em 889 cm^{-1} fica deslocada para 875 cm^{-1}, o que é evidência de Nb incorporado na estrutura da goethita [58]. Stiers e Schwertmann [59] também reportaram deslocamentos na banda de deformação O–H em 888 cm^{-1}, com o aumento da substituição por Mn^{3+} ou Al^{3+} em goethita. A Figura 11 apresenta um esquema simplificado das espécies responsáveis pelas vibrações observadas nos espectros na região do infravermelho.

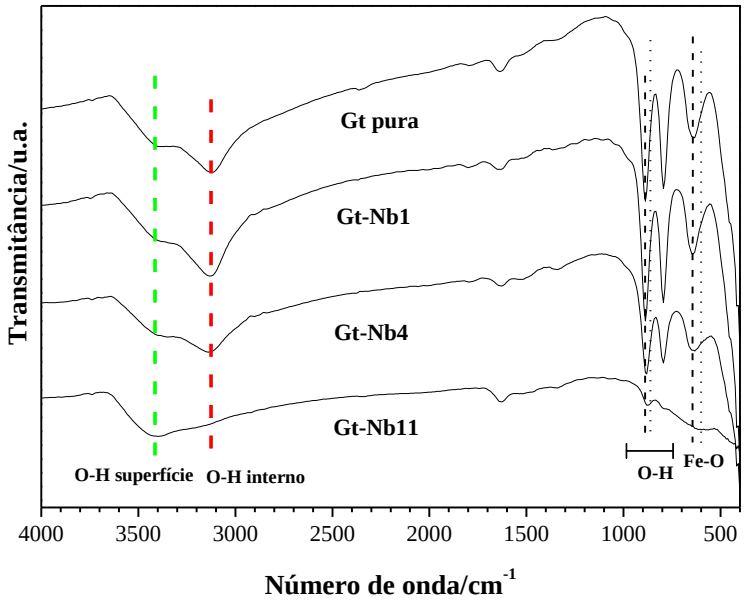

Figura 10. Espectros na região do infravermelho (FTIR) para a goethita pura e para as modificadas com Nióbio.

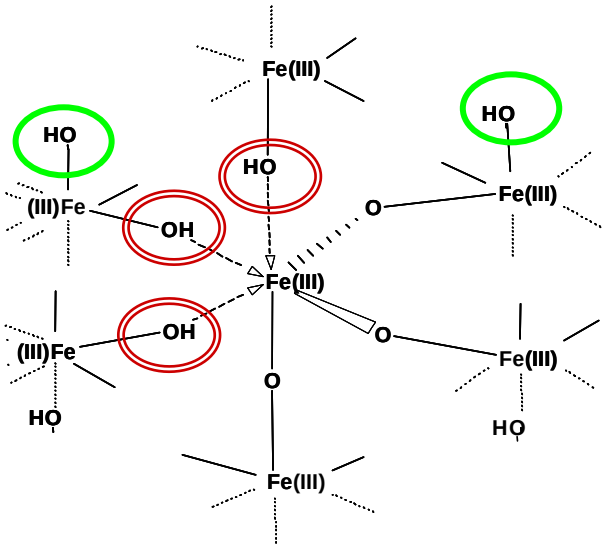

Figura 11. Representação esquemática da estrutura da goethita contendo as hidroxilas internas (círculos vermelho) e as de superfície (círculos verdes).

4.1.3. Espectroscopia de absorção de raiosX

A espectroscopia de absorção de raios X na região do XANES para as goethitas permitiu confirmar que o estado de oxidação do nióbio presente nas amostras é o +5, uma vez que a posição da borda-K para cada uma das amostras se sobrepõe com a do padrão de nióbio, Nb_2O_5, e difere bem da posição da borda do padrão de nióbio metálico (Figura 12).

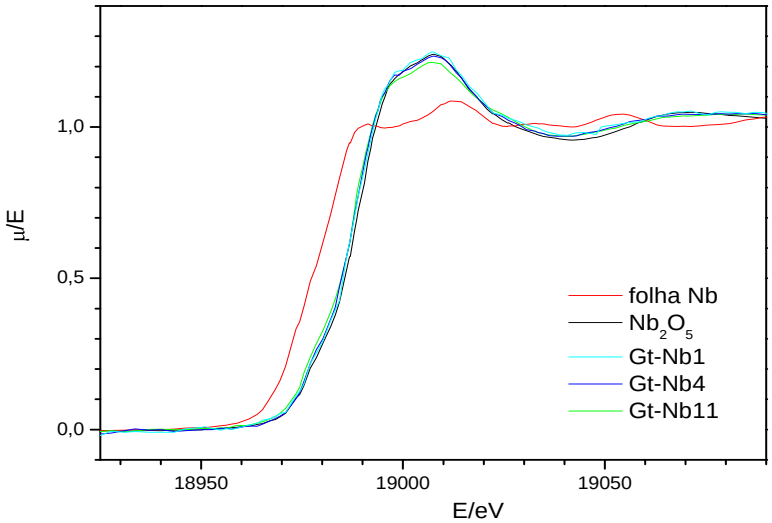

Figura 12. Espectro XANES para a goethita pura e para as amostras contendo nióbio.

Não foi possível obter informações sobre as ligações do Nb na estrutura da goethita, uma vez que os dados EXAFS não permitiram separar a contribuição espectral das ligações Nb-O. Seria necessário coletar os dados no modo de fluorescência para então poder fazer os ajustes necessários para obtenção dos dados quantitativos na região do EXAFS.

4.1.4. Microscopia eletrônica de varredura e transmissão

A morfologia dos grãos das goethitas foi observada com o auxílio da microscopia eletrônica de varredura (MEV) e as micrografias são mostradas na Figura 13. A goethita pura (Gtpura) apresenta uma morfologia essencialmente acicular com variedade de formas e tamanhos, o que está de acordo com o encontrado por outros autores [1]. O mesmo foi observado para a amostra com menor teor de nióbio, Gt-Nb1 (Figura 13 (b)). Com o aumento do teor de nióbio na estrutura, como para a amostra Gt-Nb4, as formas aciculares típicas começam a se alterar com a formação de um material mais irregular. As amostras Gt-Nb8 e Gt-Nb11 praticamente não apresentaram cristais aciculares, mas sim partículas irregulares, em aglomerados. Teores mais elevados de nióbio tendem a modificar a estrutura da goethita, gerando um material estruturalmente diferente das amostras com teores mais baixos.

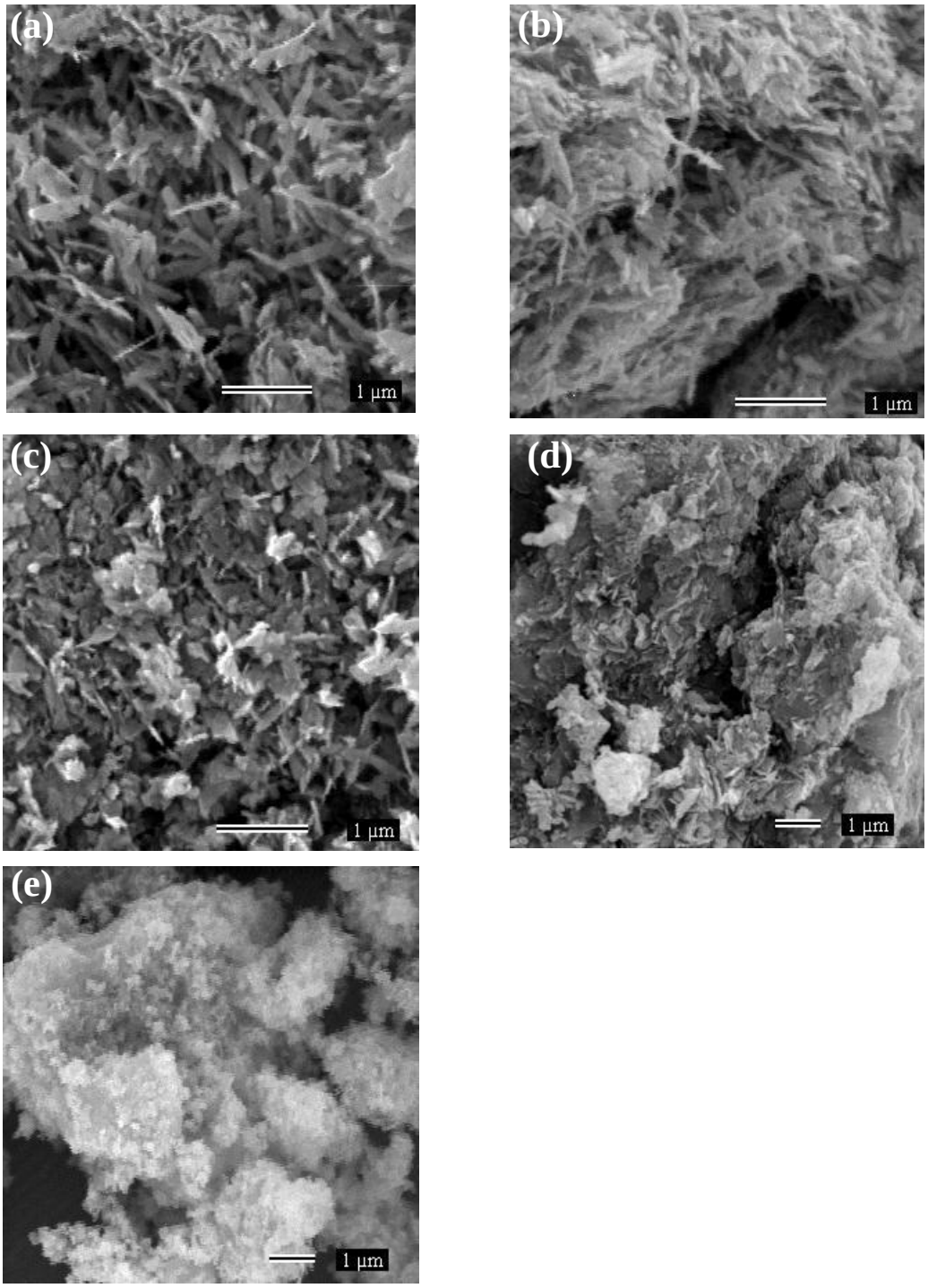

Figura 13. Micrografias eletrônicas de varredura das amostras de (a) goethita pura e das goethitas dopadas com nióbio (b) Gt-Nb1, (c) Gt-Nb4, (d) Gt-Nb8 e (e) Gt-Nb11

As imagens obtidas por microscopia eletrônica por transmissão são mostradas na Figura 14.

.

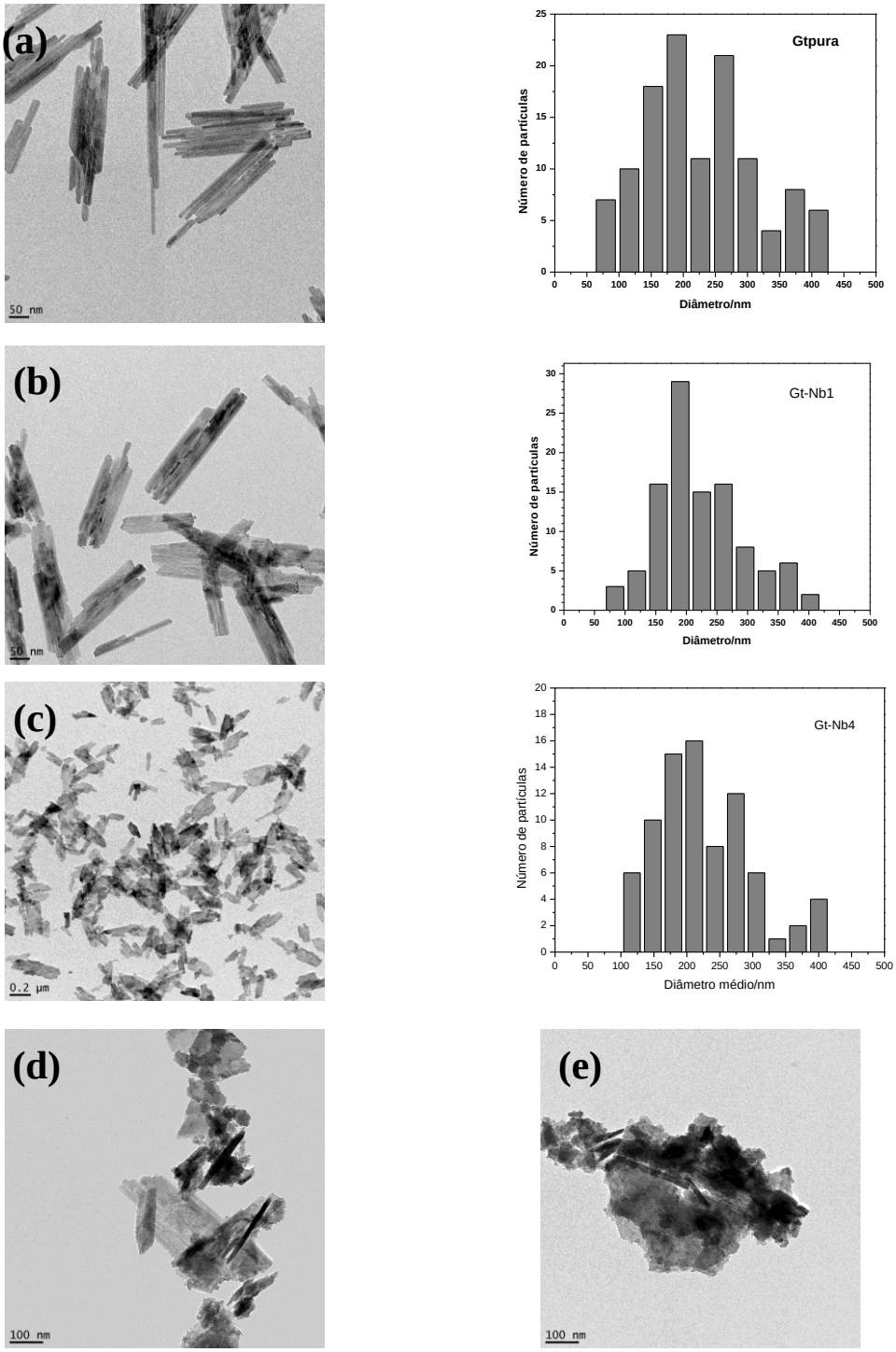

Figura 14. Imagens dos catalisadores de nióbio obtidas por microscopia eletrônica de transmissão para. (Gtpura (a), Gt-Nb1 (b), Gt-Nb4 (c), Gt-Nb8 (d) e Gt-Nb11(e)).

Na escala nanométrica, fornecida pela microscopia eletrônica de transmissão, pode-se observar com maior nitidez a forma acicular tão característica dessa fase mineralógica de ferro. Novamente, corroborando os dados obtidos por MEV, observa-se claramente a alteração na forma das partículas com o aumento do teor de nióbio. Além disso, para o material puro e com os dois menores teores de nióbio, pôde-se estimar a distribuição de diâmetro de partículas (Figura 14). Porém, ainda que evidente pelas imagens, a determinação da relação entre o teor de nióbio e o tamanho de partícula foi inconclusiva, podendo estar compreendido entre 100-400 nm.

Para as amostras Gt-Nb8 e Gt-Nb11, a alteração brusca no formato das partículas, possivelmente devido à formação de outra fase cristalina causado pela quantidade elevada de nióbio na estrutura, não permitiu a obtenção dos diâmetros médios de partículas. Essa outra fase mineralógica formada, de aspecto esférico, apresenta TEM semelhante ao de ferridrita formada por hidrólise rápida, como reportado por Schwertmann [1].

4.1.5. Difratometria de Raios X (DRX) e espectroscopia Mössbauer

As técnicas DRX e espectroscopia Mössbauer fornecem informações decisivas sobre a estrutura cristalina das fases cristalográficas presentes nos materiais. Os difratogramas das goethitas pura e contendo nióbio são mostrados na Figura 15. Ressalta-se, aqui, que os difratogramas foram refeitos empregando luz síncrotron, para se obter melhores resultados acerca das fases cristalográficas presentes. De fato, as reflexões obtidas apresentaram-se com baixo valor sinal/ruído, comparativamente aos difratogramas obtidos a partir do difratômetro convencional. O DRX da amostra sem nióbio, Gtpura, e aquelas com menores teores de nióbio (Gt-Nb1 e Gt-Nb4) apresentaram apenas reflexões referentes à goethita com relativamente alta cristalinidade. Já a amostra Gt-Nb8, apesar de apresentar reflexões características da amostra pura, possui uma menor cristalinidade, devido ao alargamento de alguns picos [1]. O difratograma de raios X da amostra contendo maior teor de nióbio, Gt-Nb11, praticamente não apresentou reflexões características referentes à goethita; essa amostra apresentou picos largos, sugerindo a ocorrência de fases cristalográficas com baixa cristalinidade. Estes resultados indicam uma diminuição da cristalinidade, na medida em que se aumenta o teor de Nb na amostra, com possível formação de uma

fase mineralógica diferente da goethita, nos materiais com maiores teores de Nb. Estes dados corroboram os obtidos por microscopias eletrônicas de varredura e transmissão. As duas reflexões alargadas do difratograma da amostra com maior teor de nióbio (Gt-Nb11) e, que também se mostra presente na amostra Gt-Nb8, porém em menor grau, coincidem com os dados apresentados por Cornell & Schwertmann (2003) para ferridrita, sugerindo a formação da mesma [1].

A partir dos dados obtidos para os parâmetros de rede (Tabela 2), observa-se ligeiro aumento da célula unitária da goethita com a introdução do nióbio. Apesar do Nb^{5+} (64 pm) ter praticamente o mesmo valor de raio iônico do Fe^{3+} (65 pm), a diferença de carga é muito grande. Isso pode gerar distorções da simetria da célula unitária da goethita, com a substituição isomórfica de parte dos íons Fe^{3+} por Nb^{5+}. O plano b da célula unitária da goethita é o mais afetado de acordo com os parâmetros de rede obtidos.

Tabela 2. Parâmetros de rede obtidos através do refinamento Rietveld

Amostra	**Parâmetros de rede/Å**			**Volume/ A^3**
Gtpura	a = 4,6155	b = 9,9456	c = 3.0223	138,717
Gt-Nb1	a = 4,6160	b = 9,9548	c = 3.0228	138,901
Gt-Nb4	a = 4,6221	b = 9,9615	c = 3.0258	139,318

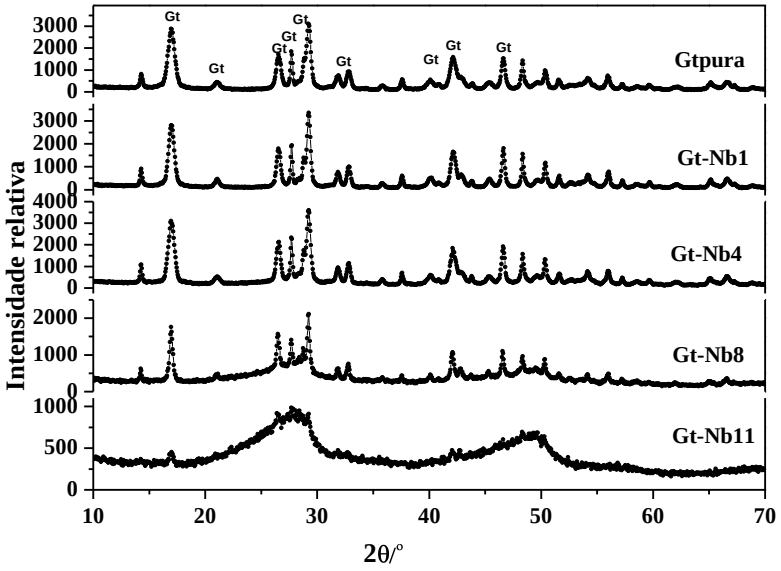

Figura 15. Padrão de difração de raios X das goethitas pura e dopadas com nióbio (Gt = goethita).

Isolando-se o sinal referente à reflexão hkl 110 dos materiais (Figura 16) não foi possível observar deslocamento que pudesse confirmar a substituição isomórfica do Fe pelo Nb [37]. Outra observação foi o fato de a reflexão ter uma ligeira diminuição de sua largura a meia altura, sugerindo que o material apresenta aumento no tamanho do cristalito, com a dopagem. Espera-se que a substituição isomórfica possa causar distorção de simetria da rede cristalina, formando materiais com menor cristalinidade.

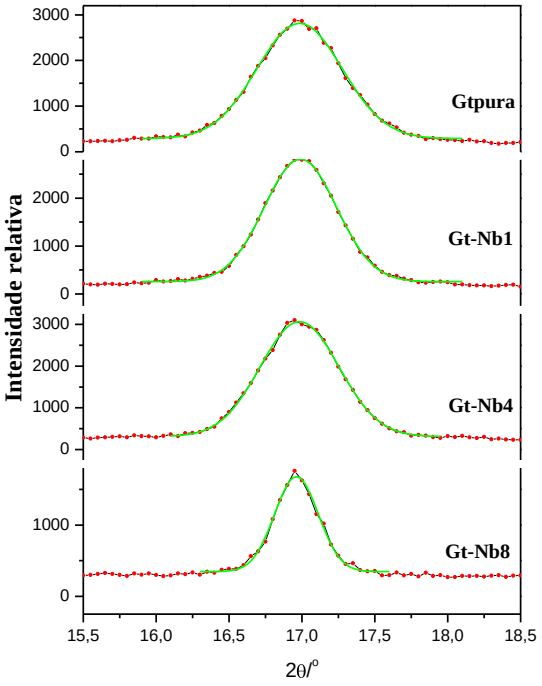

Figura 16. Detalhe do padrão de difração de raios X apresentando a reflexão referente ao plano 110 da goethita.

A espectroscopia Mössbauer (espectros apresentados na Figura 17) foi empregada na busca de se identificar com clareza as fases cristalográficas presentes. A Figura 17a mostra a caracterização por espectroscopia Mössbauer obtida à temperatura do ambiente (298 K). Os espectros foram ajustados com um modelo independente de distribuição de campo hiperfino (Figura 17b). Uma goethita pura, com certa cristalinidade, fornece um espectro Mössbauer ordenado (sexteto) à temperatura do ambiente, bastante semelhante ao apresentado para a amostra Gtpura.

Na medida em que os íons Fe^{3+} são substituídos na estrutura da goethita por cátions diamagnéticos (ex. Nb^{5+}), o tamanho do domínio magnético diminui e o ordenamento magnético desaparece, causando um colapso do sexteto, com aparecimento de um dupleto [38]. Esse resultado é observado nos materiais com maior teor nióbio, onde o sexteto dá lugar a um dupleto.

Além disso, o espectro Mössbauer da goethita pura apresenta um perfil típico para uma amostra com cristalinidade menor do que a esperada para uma goethita sintética [1], devido às linhas alargadas e desvio da linha de base, sugerindo que a goethita obtida apresenta pequeno tamanho de partícula, porém de forma heterogênea, como verificado por TEM . Corroborando as informações obtidas por DRX, a amostra Gtpura apresentou parâmetros Mössbauer (Tabela 3), tais como, campo hiperfino máximo (B_{hf}), 36,0 T e deslocamento isomérico (δ) 0,38(3) mm s^{-1}, em relação ao αFe, típicos da goethita pura e cristalina [1]. Estes resultados mostram que foi obtida apenas goethita (αFeOOH), sem a presença de outras espécies químicas de oxi-hidróxido de ferro, como comumente surgem, particularmente lepidocrocita (γFeOOH) ou akaganeíta (βFeOOH).

A distribuição de campo hiperfino (Figura 17b) para as amostras Gtpura, Gt-Nb1 e Gt-Nb4 confirma a presença de goethitas (pelos valores de campo hiperfino apresentados), uma vez também que não foi possível identificar outras fases cristalográficas pelo DRX. Para as amostras com 8 e 11% de nióbio, a proporção de sexteto é muito pequena, o que indicaria a formação de outra fase ferruginosa, evidenciada pela presença do dupleto central, mas que não alteraria os valores de campo hiperfino, para espécies magneticamente ordenadas. Esse dupleto é característico para pequenos tamanhos de partícula, e também para a fase mineralógica ferridrita presente, como mostrado por DRX.

A distribuição para os valores de campo hiperfino nessas amostras pode ser devida também ao tamanho de partícula da goethita e aos diferentes graus de substituição isomórfica do Fe por Nb.

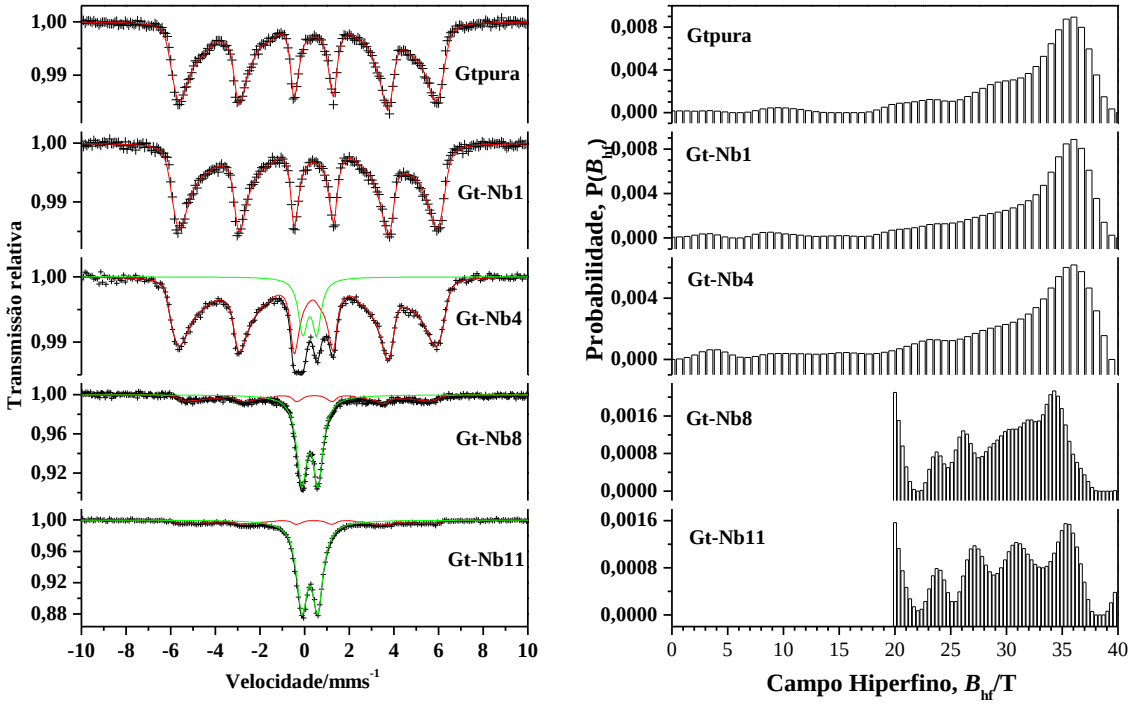

(a) **(b)**

Figura 17. Espectroscopia Mössbauer das goethitas pura e dopadas com nióbio (Gt = goethita) a T = 298 K.

Fica assim, evidente, pelos dados de espectroscopia Mössbauer, que a amostra contendo o menor teor de nióbio, Gt-Nb1, não apresentou diferenças significativas com relação à Gt pura. Por outro lado, as amostras Gt-Nb4, Gt-Nb8 e Gt-Nb11, apresentaram um dupleto acentuado, principalmente Gt-Nb8 e Gt-Nb11, possivelmente devido ao teor de nióbio substituindo isomorficamente o ferro na estrutura da goethita e também pela formação de ferridrita, corroborando os dados de DRX e TEM, principalmente na amostra Gt-Nb11, além de um decréscimo de cristalinidade.

A substituição do ferro na estrutura da goethita causa relaxação superparamagnética e reduz ou suprime o acoplamento magnético hiperfino. Nas amostras Gt-Nb8 e Gt-Nb11, o tamanho do domínio magnético é tão pequeno que a estrutura hiperfina magnética praticamente não aparece no espectro.

Tabela 3. Parâmetros Mössbauer obtidos à temperatura de 298 K para as amostras em estudo.

Amostra	**Sítio ^{57}Fe**	δ**/mm s^{-1}**	ε, Δ**/mm s^{-1}**	B_{hf}**/T**	Γ**/mm s^{-1}**	***AR*/%**
Gtpura	Gt	0,38(3)	-0,272(5)	36,0*	0,31**	100
Gt-Nb1	Gt	0,39(3)	-0,260(5)	36,0*	0,31**	100
Gt-Nb4	Gt	0,369(4)	-0,281(7)	36,0*	0,31**	87
	$^{VI}Fe^{3+}$	0,331(7)	0,62(2)		0,48(3)	13
GT-Nb8	Gt	0,40(2)	-0,272(5)	34,3*	0,31**	28
	$^{VI}Fe^{3+}$	0,351(3)	0,726(2)		0,583(4)	72
Gt-Nb11	Gt	0,38(1)	-0,29(2)	35,6*	0,31**	19
	$^{VI}Fe^{3+}$	0,334(1)	0,706(2)		0,567(3)	81

*Campo hiperfino máximo da distribuição.
**Parâmetros fixados.
δ = deslocamento isomérico relativo ao αFe; ε = deslocamento quadrupolar; Δ = desdobramento quadrupolar; B_{hf} = campo magnético hiperfino; Γ = largura de linha a meia altura; *AR* = área subespectral relativa.

Além das informações obtidas acerca das espécies ferruginosas presentes, a espectroscopia Mössbauer pode fornecer dados qualitativos a respeito de defeitos estruturais nos óxidos de ferro, o que pode explicar determinados aspectos dos efeitos catalíticos desses materiais. Assim, alguns autores [60] relatam que o desaparecimento do sexteto com formação de um dupleto no espectro Mössbauer é favorecido em goethitas contendo vacância de oxigênio, sendo que os sítios de vacância tendem a aumentar com a diminuição do tamanho de partícula. Desse modo, a presença de elevados teores de nióbio pode aumentar o número de sítios vacantes evidenciados pelo dupleto nas amostras Gt-Nb4, Gt-Nb8 e, principalmente, Gt-Nb11, além da presença do dupleto pela formação da espécie ferridrita.

Observa-se, ainda, uma variação do valor absoluto do deslocamento quadrupolar, muito provavelmente devido a distorções da simetria na rede cristalina da goethita, causada pela substituição isomórfica do ferro por nióbio.

Com o objetivo de um melhor entendimento das fases cristalográficas formadas, foram realizadas análises Mössbauer a 110 K. Os espectros Mössbauer obtidos a 110 K (Figura 18) foram ajustados com um modelo de distribuição de campo hiperfino

para a goethita (Figura 18), mantendo-se os subespectros (dupletos) como sítios cristalinos.

É interessante observar que, com as medidas a baixa temperatura, ocorre o ordenamento magnético de parte dos spins dos átomos de Fe ainda não ordenados, comportamento esse visto através das linhas espectrais mais estreitas e com menor relaxação. Este resultado confirma que os materiais são de pequeno tamanho de partícula, como discutido para os espectros Mössbauer a 298 K. Ainda assim, nas amostras Gt-Nb4 e Gt-Nb11, persistem o dupleto central, sugerindo que materiais com partículas pequenas foram obtidos e também a fase mineralógica ferridrita, que apresenta um dupleto nessa temperatura, necessitando medidas a uma temperatura ainda menor para que os spins possam ser ordenados.

Assim, os dados Mössbauer obtidos a 298 e a 110 K mostram que os materiais obtidos apresentam elevado potencial como catalisadores, uma vez que foram obtidas partículas muito pequenas.

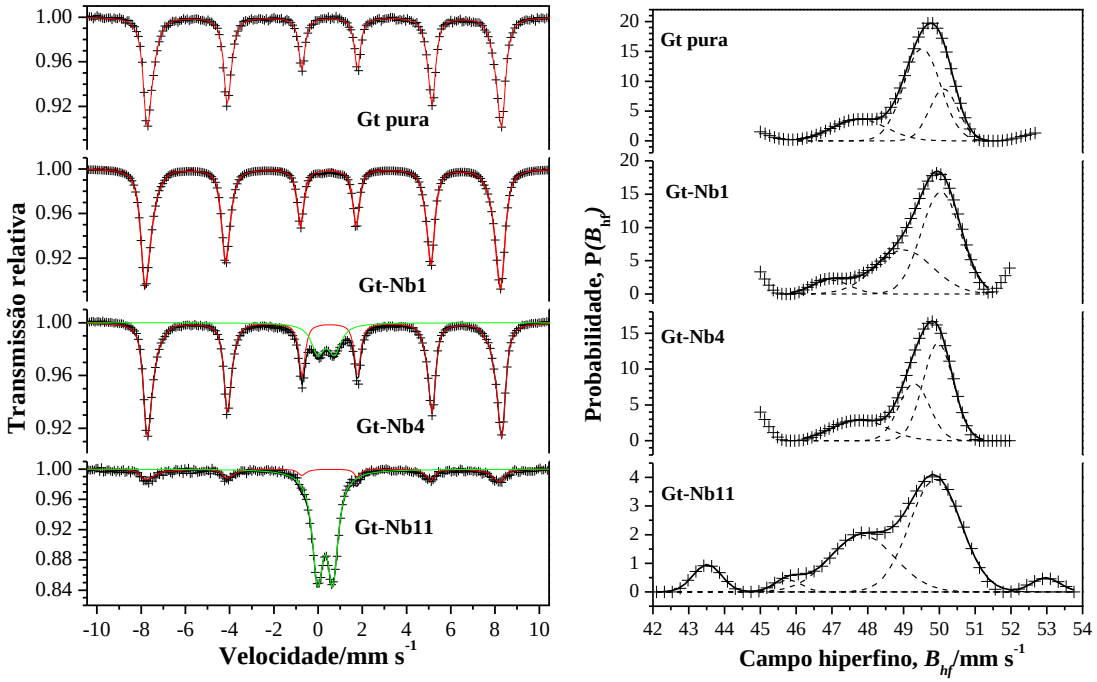

Figura 18. Espectroscopia Mössbauer das goethitas pura e dopadas com nióbio à T = 110 K.

Tabela 4. Parâmetros Mössbauer obtidos à temperatura de 110 K, para as amostras em estudo.

Amostra	**Sítio ^{57}Fe**	δ**/mm s^{-1}**	ε, Δ**/mm s^{-1}**	B_{hf}**/T**	Γ**/mm s^{-1}**	***AR*/%**
Gtpura	Gt	0,4771(7)	-0,240(1)	49,8*	0,31**	100
Gt-Nb1	Gt	0,485(6)	-0,240(2)	49,9*	0,31**	100
Gt-Nb4	Gt	0,4821(3)	-0,2376(7)	49,8*	0,31**	84
	$^{VI}Fe^{3+}$	0,439(3)	0,757(5)		0,70**	16
Gt-Nb11	Gt	0,49(5)	-0,27(2)	49,8*	0,31**	20
	$^{VI}Fe^{3+}$	0,457(2)	0,680(2)		0,569(4)	80

*Campo hiperfino máximo da distribuição;
**Parâmetros fixados;
δ = deslocamento isomérico relativo ao αFe; ε = deslocamento quadrupolar; Δ = desdobramento quadrupolar; B_{hf} = campo magnético hiperfino; Γ = largura de linha a meia altura; *AR* = área subespectral relativa.

4.1.4. DSC (Calorimetria exploratória diferencial) e Redução a temperatura programada (RTP)

Os resultados discutidos até aqui sugerem fortemente que o Nb foi incorporado isomorficamente na estrutura da goethita e também da ferridrita. Os dados de DSC podem, no entanto, apresentar informações conclusivas a esse respeito. Schwertmann (2003) [1] relata que a transformação de goethita em hematita deve ser dificultada com o aumento da cristalinidade da goethita precursora e que a presença de alumínio estrutural em óxidos naturais causa diminuição da cristalinidade e consequente diminuição da temperatura de formação da hematita.

No presente trabalho, as análises DSC revelaram que o aumento do teor de Nb na amostra aumentou a temperatura na qual a transição de fase mineralógica de goethita para hematita ocorre (Figura 19), deslocando a temperatura característica de aproximadamente 248 °C para a goethita pura, em ar, para 269 °C, para a amostra Gt-Nb11, respectivamente. Para goethitas naturais e sintéticas, como discutido anteriormente, a temperatura desse evento endotérmico é conhecida por aumentar com o aumento do tamanho de partícula. Porém, como mostrado por espectroscopia Mössbauer, aumentando o teor de Nb, há o decréscimo da cristalinidade da amostra. Assim, o aumento da temperatura de transição dá-se devido à estabilização estrutura

da goethita e da ferridrita, causado pela incorporação do nióbio na rede cristalina. Essa observação foi relatada também por Silva et al., [22].

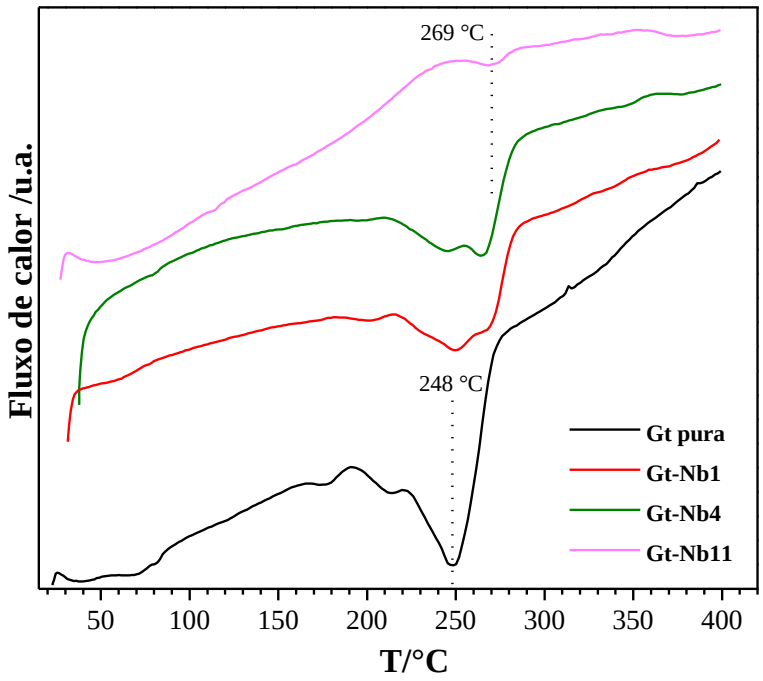

Figura 19. Análises DSC das goethitas pura e dopadas com nióbio.

Análises por redução a temperatura programada (RTP) corrobora, em alguma extensão, as informações obtidas por DSC. O estudo do perfil de redução de catalisadores pode fornecer importantes informações sobre a extensão da incorporação do íon dopante, bem como sobre sua estabilidade térmica. Desse modo, foram realizadas análises por redução a temperatura programada dos materiais (Figura 20). O perfil de redução obtido para a goethita pura (Gtpura) apresenta 3 picos típicos para a redução de óxidos de Fe^{3+}. A goethita sofre desidratação para formar a hematita que, então, é reduzida para magnetita. Podemos expressar as etapas de redução iniciando da goethita, como mostrado nas Equações 4-6. Os picos identificados na Figura 20 são atribuídos à redução até o ferro metálico de acordo com as equações [37]:

(I) $3FeOOH + ½H_2 \rightarrow Fe_3O_4 + 2H_2O$ Eq. 4

(II) $Fe_3O_4 + H_2 \rightarrow 3FeO + H_2O$ Eq. 5

(III) $FeO + H_2 \rightarrow Fe^0 + H_2O$ Eq. 6

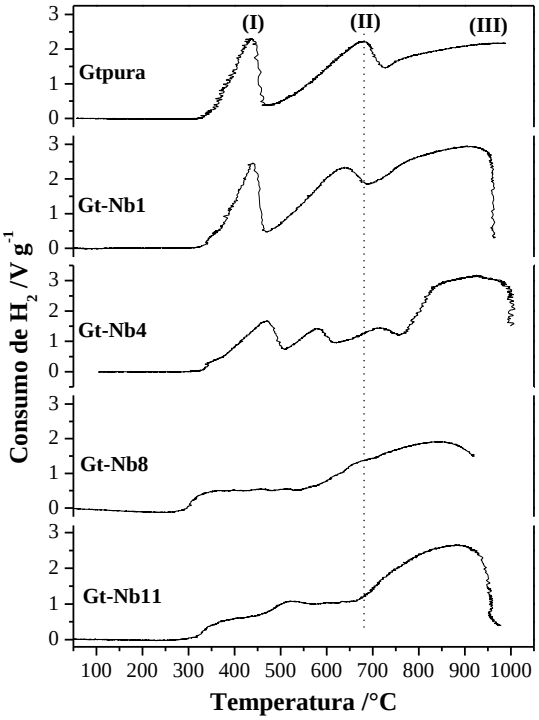

Figura 20. Redução a temperatura programada das goethitas pura e dopadas com nióbio.

A amostra contendo 1% de Nb (Gt-Nb1) apresenta um perfil semelhante àquele da amostra pura. A temperatura de transição Fe_3O_4 → FeO (pico II; Figura 20) é, no entanto, mais baixa do que para a amostra Gtpura. Por outro lado, as amostras com maiores teores de nióbio apresentaram perfis complexos de redução, sinalizando que houve a formação de uma fase mineralógica distinta da goethita, como observado na espectroscopia Mössbauer.

Além disso, o perfil RTP mostra claramente que a transformação para magnetita (pico (II)) ocorre de maneira distinta na medida em que o teor de Nb é aumentado. Esse fato, não apenas indica a existência do Nb na estrutura como a sua permanência após a transformação da goethita para magnetita. O fato de o Nb permanecer na estrutura da magnetita é importante, pois a sua presença pode alterar as propriedades

catalíticas também dessa fase mineralógica de ferro, o que, será estudado na sequência desse trabalho.

4.1.5. Área específica (BET)

O estudo da área superficial disponível ao catalisador pode auxiliar de maneira decisiva o entendimento da atividade catalítica apresentada pelos materiais. As propriedades texturais dos materiais foram estudadas por adsorção/dessorção de N_2 e os resultados estão mostrados na Figura 21. Obtiveram-se os seguintes valores de área específica: 119, 120, 122 e 174 $m^2\ g^{-1}$, para Gtpura, Gt-Nb1, Gt-Nb4 e Gt-Nb11, respectivamente.

Observa-se que o nióbio estruturalmente adicionado à goethita não causou aumento perceptível de área específica. Apenas o material Gt-Nb11 teve sua área superficial aumentada. Porém, como mostraram as técnicas discutidas anteriormente, outra fase mineralógica distinta da goethita foi formada nesse material. De fato, observa-se nas isotermas de adsorção da Figura 21 que a amostra pura (Gtpura) e aquelas com menor teor de Nb apresentaram perfis bastante semelhantes, com a mesma capacidade de adsorção de N_2 para todo o intervalo de pressão relativa. As alterações estruturais causadas pela elevada quantidade de Nb na amostra Gt-Nb11 fez com que esse material apresentasse maior capacidade de adsorção em menores valores de pressão relativa.

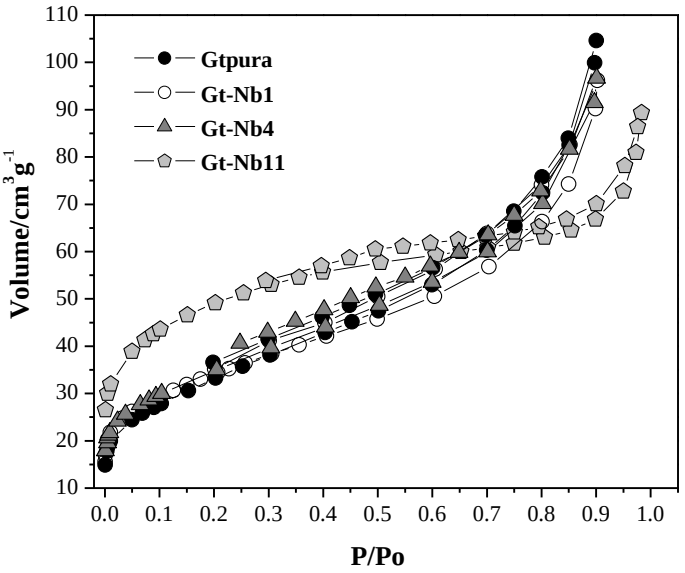

Figura 21. Isotermas de adsorção de nitrogênio para as goethitas pura e contendo nióbio.

A influência do Nb no diâmetro de poros dos materiais é apresentada na Figura 22. O aumento observado na área superficial BET é acompanhado de uma maior adsorção em poros com diâmetros ligeiramente acima de 20 Å. As distribuições dos tamanhos de poros foram determinadas com o método Barrett–Joyner–Halenda e claramente mostram que a presença de Nb produz materiais com diâmetros de poros maiores que 20 Å, mas com predominância de mesoporos (20<x<500 Å). Esse fato pode ser interessante, uma vez que a presença de mesoporos pode favorecer reações catalíticas envolvendo moléculas volumosas que não reagiriam em materiais microporosos [63].

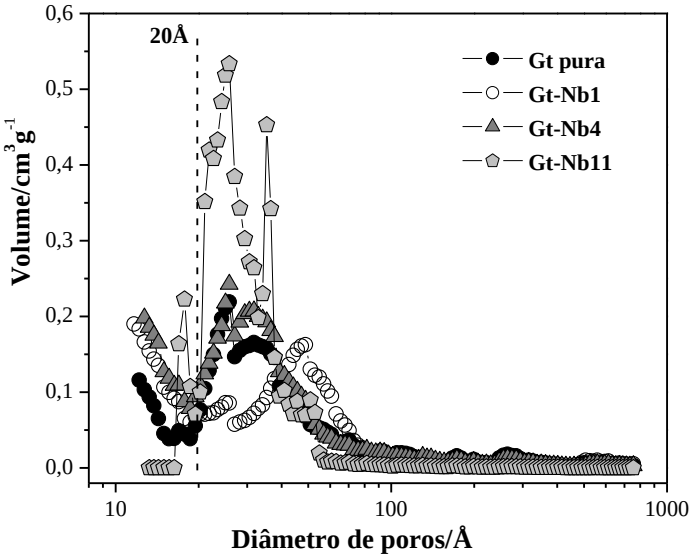

Figura 22. Distribuição de poros das goethitas dopadas com nióbio.

4.2. TESTES CATALÍTICOS EMPREGANDO AS GOETHITAS

4.2.1. Decomposição de H_2O_2

A atividade catalítica das goethitas foi estudada para duas reações: decomposição de peróxido de hidrogênio (H_2O_2) e oxidação do corante orgânico azul de metileno na presença de peróxido de hidrogênio. A capacidade de decomposição de H_2O_2 é medida indiretamente pelo O_2 formado (Eq. 7).

$H_2O_2 \rightarrow H_2O + ½O_2$ Eq. 7

Observa-se que a decomposição de H_2O_2 é acelerada na medida em que se aumenta o teor de nióbio na estrutura da goethita (Figura 23). Estes resultados indicam claramente que a presença do nióbio na estrutura da goethita possui um papel importante na decomposição do peróxido de hidrogênio.

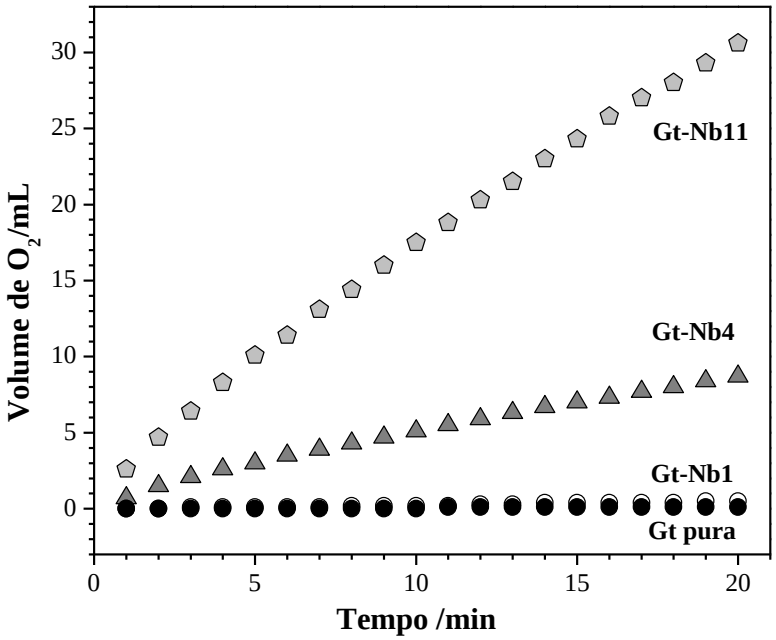

Figura 23. Perfil da liberação de O_2 da decomposição de H_2O_2 para as diferentes goethitas.

Para tentar elucidar o mecanismo de decomposição de H_2O_2, a reação de decomposição foi realizada na presença de diferentes compostos orgânicos, tais como fenol, quinolina e ácido ascórbico. Esses compostos, que apresentam afinidade por radicais $^{\bullet}OH$, podem fornecer informações preliminares sobre a possibilidade de o catalisador decompor o H_2O_2 via intermediários radicalares. Foi testada a decomposição de H_2O_2 na presença dos compostos orgânicos para o catalisador com quantidades intermediárias de Nb. Os resultados para a amostra Gt-Nb4 estão mostrados na Figura 24.

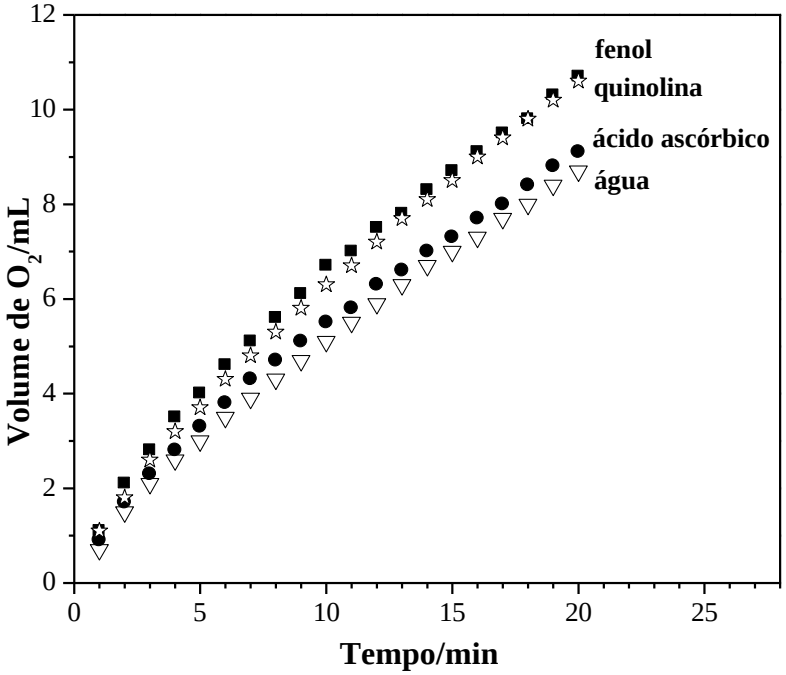

Figura 24. Perfil da liberação de O_2 da decomposição de H_2O_2 para a Gt-Nb4 em presença dos orgânicos: fenol, quinolina e ácido ascórbico.

Os resultados na Figura 24 indicam que a adição de compostos com afinidade por radicais hidroxilas, que seriam formados na decomposição de H_2O_2 em um sistema do tipo Fenton, não afeta significativamente a reação. Alguns autores sugerem que o mecanismo da decomposição de H_2O_2, nesses casos, não envolve o processo radicalar típico do sistema Fenton, indicando que goethitas sintéticas podem agir em um mecanismo envolvendo sítios de vacância de oxigênio [64]. Nesse tipo de mecanismo, o H_2O_2 sofre redução ao interagir com vacâncias de oxigênio, [ ], seguido por dessorção de O_2, conforme esquematizado nas Eq. 8 e Eq. 9. No entanto, resultados recentes do nosso grupo, onde hematitas sintéticas foram dopadas com diferentes proporções de Nb, apontam a formação de grupos oxidantes superficiais, conhecidos como grupos *peroxos* [65], pela reação de Nb com H_2O_2. A formação desses grupos, altamente oxidantes, poderia explicar o comportamento observado para as reações de decomposição do peróxido de hidrogênio.

$$[\ ] + H_2O_2 \rightarrow H_2O + [O_{ads}] \qquad \text{Eq. 8}$$

$$2[O_{ads}] \rightarrow O_2 \qquad \text{Eq. 9}$$

4.2.2. Degradação de azul de metileno

Para estudar a capacidade de oxidação das goethitas contendo diferentes quantidades de nióbio, foi utilizado como modelo o corante orgânico azul de metileno. Esse composto foi escolhido porque pode ser facilmente monitorado por técnicas simples, como a espectroscopia UV-Visível no comprimento de onda de 665 nm. Além disso, apresenta baixa adsorção pelas goethitas, conforme verificado em experimentos preliminares [17].

A Figura 25 apresenta o perfil de descoloração de uma solução contendo o corante azul de metileno pela reação de alguns materiais na presença de H_2O_2.

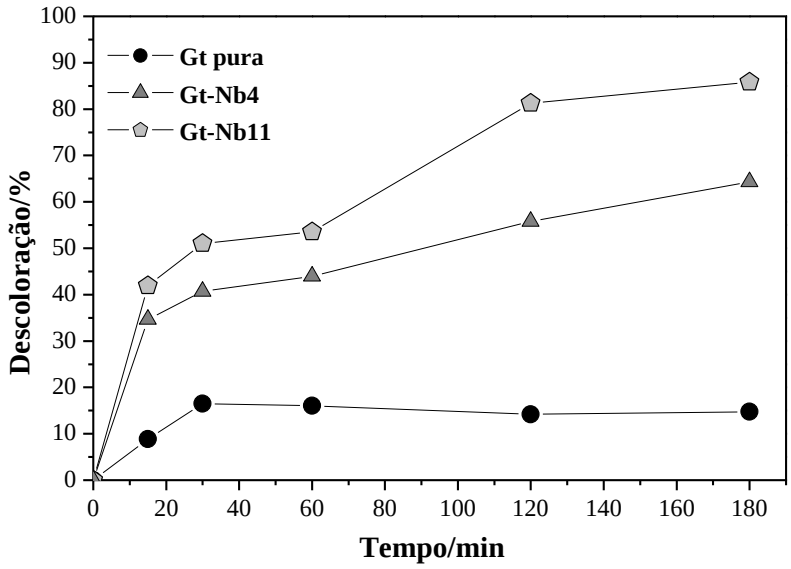

Figura 25. Degradação do azul de metileno, utilizando diferentes goethitas em presença de H_2O_2.

Os resultados da Figura 25 mostram claramente a dependência da presença do nióbio no aumento da capacidade de descoloração da solução de azul de metileno. O aumento do número de sítios de vacância, como sugerido pela espectroscopia Mössbauer, pode estar relacionado com o aumento na capacidade de oxidação do corante. No entanto, deve-se considerar ainda que a maior atividade possa estar relacionada principalmente aos grupos *peroxos* gerados *in situ* pela reação do peróxido de hidrogênio e o Nb na estrutura da goethita e/ou ferridrita.

A literatura relata a ocorrência de mecanismos químicos envolvendo *peroxo* metalatos e *oxo* metalatos para transferência de oxigênio ao reagente [66]. "Caminhos" por *peroxo* metalatos, comumente envolvem elementos de transição com configuração d^0. A existência de mecanismos por *oxo* metalatos ou *peroxo* metalatos também depende da natureza do substrato. Wachs et al., 2001 [67] estudaram a oxidação do metanol com nióbia suportada em sílica e peneiras moleculares Nb_2O_5/MCM-41 e verificaram que a presença de ligações Nb-O-Si na estrutura do material determina sua atividade oxidativa. Tais ligações influenciam não apenas a reducibilidade do nióbio, mas também a atividade do oxigênio, que pode ser armazenado no nióbio. Resultados obtidos por outros grupos de pesquisa [68] sustentam a hipótese sobre a formação de espécies reativas de oxigênio em peneiras moleculares do tipo MCM-41 com nióbio incorporado a sua rede. Esse oxigênio exibe também alta atividade catalítica em reações de sulfoxidação e epoxidação.

Desse modo, a presença de Nb na estrutura da goethita e/ou ferridrita pode maximizar a atividade catalítica desses óxidos na oxidação de compostos orgânicos gerando espécies oxidantes na superfície. Essas espécies oxidantes geradas *in situ* podem ainda ser regeneradas pelo peróxido de hidrogênio adicionado ao meio reacional, de acordo com o esquema mostrado na Figura 26.

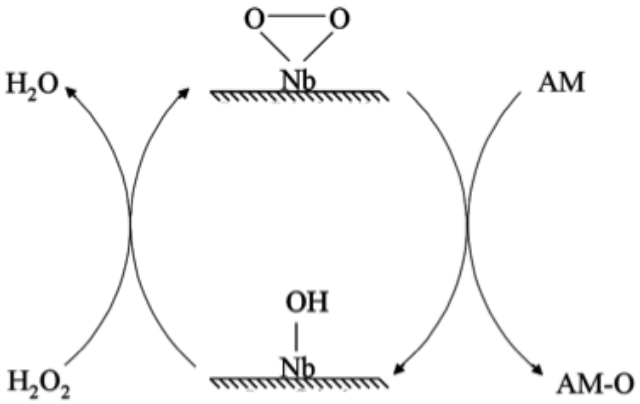

Figura 26. Esquema da oxidação do corante azul de metileno (AM) sendo oxidado pelos grupos *peroxos* e sua regeneração *in situ* pela reação com H_2O_2.

O mecanismo de remoção do corante azul de metileno pode ser mais bem entendido conhecendo-se os compostos que foram formados durante sua oxidação. Estudos empregando espectrometria de massas com ionização *via* electrospray (ESI-

MS) podem auxiliar nessa parte do trabalho. Para a amostra com maior teor de nióbio (Gt-Nb11), e que apresentou melhor atividade, foram realizados estudos de degradação do azul de metileno monitorados por ESI-MS. A Figura 27 mostra os espectros de massa da solução padrão de azul de metileno (50 mg L^{-1}) e após a reação com o catalisador Gt-Nb11 na presença de H_2O_2.

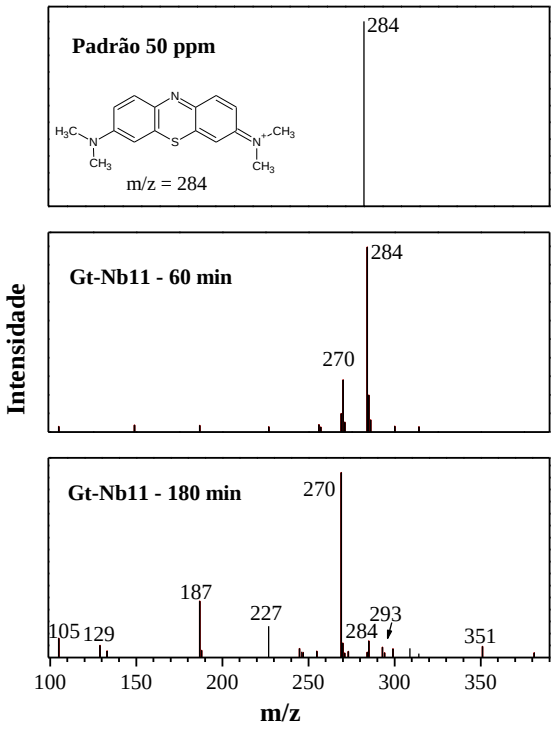

Figura 27. Espectros de massas (m/z) da solução padrão de azul de metileno 50 mg L^{-1} e após reação com o catalisador Gt-Nb11.

Análises por electrospray, operando em modo positivo, mostram que após 60 min de reação aparece um sinal *m/z* = 270 devido à degradação do corante, sendo que nesse tempo de reação o sinal referente ao corante (*m/z* = 284) ainda é intenso. Apesar da elevada intensidade do sinal m/z = 284, a análise por espectroscopia UV-Visível havia mostrado uma descoloração acima de 50%. No entanto, após 180 min de reação o sinal do corante desaparece quase completamente, corroborando os dados desse tempo de reação, mostrados no monitoramento por espectroscopia UV-Vis (Figura 25), onde a descoloração da solução foi de aproximadamente 90%. É interessante observar, no entanto, que embora a Figura 25 apresente um desaparecimento quase completo do corante pela descoloração da solução, análises por electrospray mostram

que ocorre a formação de intermediários orgânicos com sinais *m/z* = 270, 227, 186, 129 e 105. Este resultado reforça a necessidade de se estudar os intermediários formados e a importância de que ocorra a total oxidação dos poluentes, uma vez que compostos intermediários podem ser formados e algumas vezes serem mais tóxicos que o composto alvo.

Em um trabalho correlato anterior [69] sobre a oxidação do azul de metileno, foram observados sinais *m/z* = 300, 316 e 332, típicos de hidroxilações do anel do corante que ocorrem em sistemas radicalares do tipo Fenton. A ausência desses sinais nas análises por electrospray é outro indício de que o mecanismo não ocorre via processo radicalar. Baseado na detecção desses sinais nas análises ESI-MS, um esquema simplificado da formação dos compostos é apresentado na Figura 28 [70]. Nessas propostas de estruturas formadas não se observa incorporação de espécies de oxigênio na estrutura do corante, como é típico para reações com radicais. Porém, o mecanismo de reação desses materiais dopados com Nb deverá ser estudado com mais detalhes, empregando-se outras moléculas substrato em trabalhos futuros do nosso grupo de pesquisa.

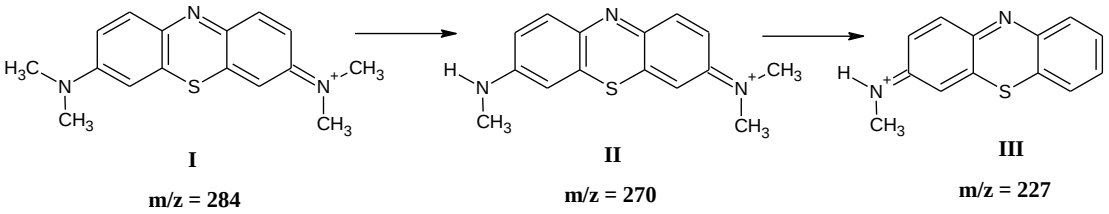

Figura 28. Esquema com os intermediários propostos para a oxidação do corante azul de metileno (m/z = 284) pelas goethitas em presença de H_2O_2 [70].

4.2.3. Degradação de Rodamina B

Os resultados encontrados para a oxidação fotocatalítica do corante Rodamina B (Figura 29) estão apresentados na Figura 30. Observou-se que a capacidade fotocatalítica do material aumenta com o aumento do teor de nióbio presente na amostra. A amostra Gt-Nb11, que além de ter nióbio dopando a estrutura da goethita, apresentou a maior quantidade de uma segunda espécie química, ferridrita, como visto por espectroscopia Mössbauer e DRX, foi a responsável por uma remoção em torno de 40% com 150 min de reação. Segundo Silva et al., 2009 [22], a incorporação de

nióbio na estrutura da hematita também favoreceu sua capacidade catalítica em reações de fotocatálise, porém menos eficiente do que em reações do tipo Fenton, conforme também visto nesse trabalho.

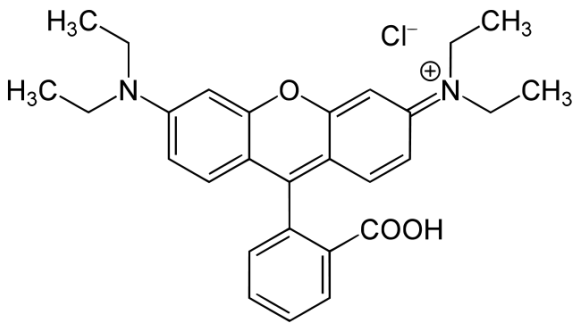

Figura 29. Estrutura molecular do corante rodamina B

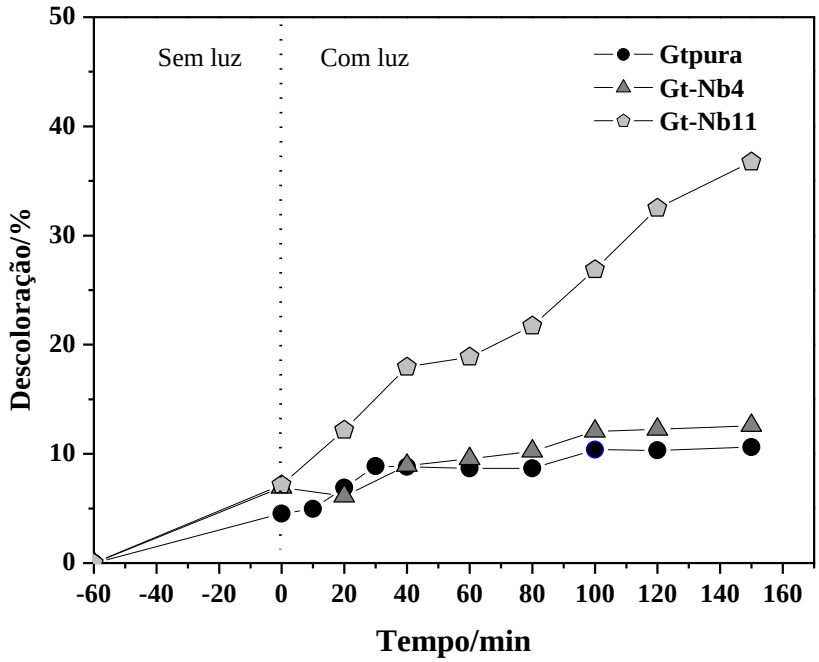

Figura 30. Degradação de rodamina B utilizando diferentes goethitas em presença de luz ultravioleta.

4.3. CONCLUSÕES - PARTE GOETHITAS

A parte inovadora deste trabalho consiste na síntese de goethitas e/ou ferridritas dopadas com nióbio, pois não há relato na literatura do uso do nióbio como cátion estrutural dopante nesses oxidróxidos de ferro. Os novos materiais, assim preparados, foram testados na oxidação dos corantes azul de metileno e rodamina B, usados como modelos moleculares de substância orgânica contaminante em água.

A caracterização dos materiais mostrou que ocorreu a formação de goethita ($\alpha Fe_{1-x}Nb_xOOH$), com a substituição isomórfica de parte dos íons Fe por Nb. As amostras com maiores teores contêm, também, outro composto de ferro formado.

Além disso, a presença de nióbio causa aumento da área específica, que favorece o aumento da atividade catalítica das amostras nas reações de decomposição de H_2O_2 e de oxidação do substrato corante.

A hipótese de que a substituição de Nb cria vacâncias de oxigênio na camada superficial da goethita é suportada tanto por dados Mössbauer quanto pelo comportamento cinético, na reação de decomposição de peróxido de hidrogênio na presença de capturadores de radicais livres, e na oxidação catalítica do corante orgânico, como evidenciado por dados ESI-MS. A formação, na superfície, de espécies do tipo *peroxo* é reportada na literatura científica de vários trabalhos com compostos de Nb na presença de peróxido de hidrogênio, e pode ser considerada como envolvida no mecanismo químico dos processos estudados neste trabalho.

Em etapa posterior deste estudo, as amostras de goethita foram termicamente tratadas sob atmosfera de hidrogênio, visando à obtenção de magnetitas. Materiais similares são classicamente estudados, em reações de degradação oxidativa de poluentes orgânicos, em meio contendo H_2O_2. A razão primordial do interesse é o fato de óxidos de ferro isoestruturais ao espinélio terem Fe^{2+} e Fe^{3+} na estrutura cristalina, favorecendo a transferência de elétrons na reação química. Por serem magnéticos, a extração da fase sólida do meio reativo, após uso, tem maior viabilidade prática. Essa circunstância permite a reutilização da fase sólida em outros ciclos catalíticos.

5. RESULTADOS E DISCUSSÕES

5.1. MAGNETITAS

As amostras de magnetitas foram preparadas a partir das goethitas (conforme discutido no capítulo anterior), na temperatura encontrada para a transformação Gt → Mt, a partir do perfil de redução da goethita pura por redução a temperatura programada (Figura 20). As amostras de goethitas foram submetidas a regime de aquecimento contínuo (10 ^{o}C/min), até 430 °C, com um fluxo de hidrogênio (80 mL min^{-1}) durante 30 min.

Os materiais obtidos foram preliminarmente caracterizados. Serão apresentados os resultados das análises por espectroscopia Mössbauer, difratometria de raios X e de medidas de área específica, além de testes em reações de oxidação do corante azul de metileno.

5.1.1. Análises Químicas, MEV/EDS e microscopia eletrônica de transmissão

Os resultados do teor de ferro total, determinados por dicromatometria, e de nióbio, por EDS (espectroscopia de energia dispersiva), para as magnetitas encontram-se na Tabela 5.

Tabela 5. Composição química das magnetitas contendo Nb, expressa em (% em massa) para o ferro total, e (% atômica) para o nióbio. As incertezas indicadas para os valores de ferro são estimativas a partir do desvio padrão sobre a média, calculada de três aberturas de amostras.

Amostra	Teor de Ferro /%	Teor de Nióbio /%
01	70 ± 3	0
02	67 ± 1	1
03	61 ± 1	4
04	59 ± 1	8
05	58 ± 1	11

Assim como para as goethitas, as análises químicas para as magnetitas (Mt) confirmaram decréscimo correspondente na proporção de ferro, com o aumento do teor de nióbio. As amostras foram então rotuladas de acordo com o teor aproximado de nióbio em sua estrutura: **Mtpura, Mt-Nb1, Mt-Nb4, Mt-Nb8 e Mt-Nb11**.

Os resultados por EDS, para as diferentes magnetitas estão mostradas na Figura 31 e apresentados na Tabela 5. Observa-se que o teor aproximado de nióbio foi o mesmo para as goethitas e para as magnetitas. As análises por EDS das magnetitas indicaram a presença de ferro e nióbio.

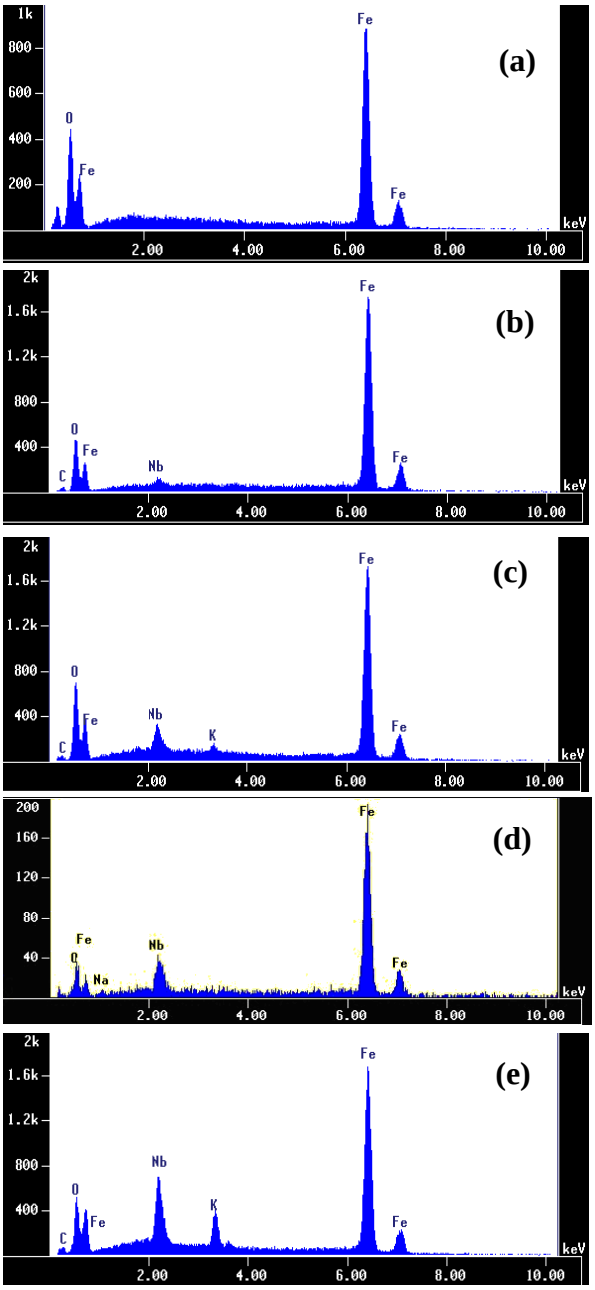

Figura 31. Análises EDS para a série de magnetitas: Mtpura (a), Mt-Nb1(b), Mt-Nb4 (c), Mt-Nb8(d) e Mt-Nb11(e).

Nas micrografias eletrônicas apresentadas na Figura 32 verificam-se aglomerados regulares de grãos. Na medida em que houve um aumento da quantidade de nióbio no material, observou-se uma distinção em relação ao material puro, com gradativo achatamento e formação de placas. A morfologia apresentada para o material com maior teor de nióbio, apresentou-se distinta das demais, com formas completamente

irregulares. A análise mais detalhada da morfologia dos materiais foi realizada por microscopia eletrônica de transmissão.

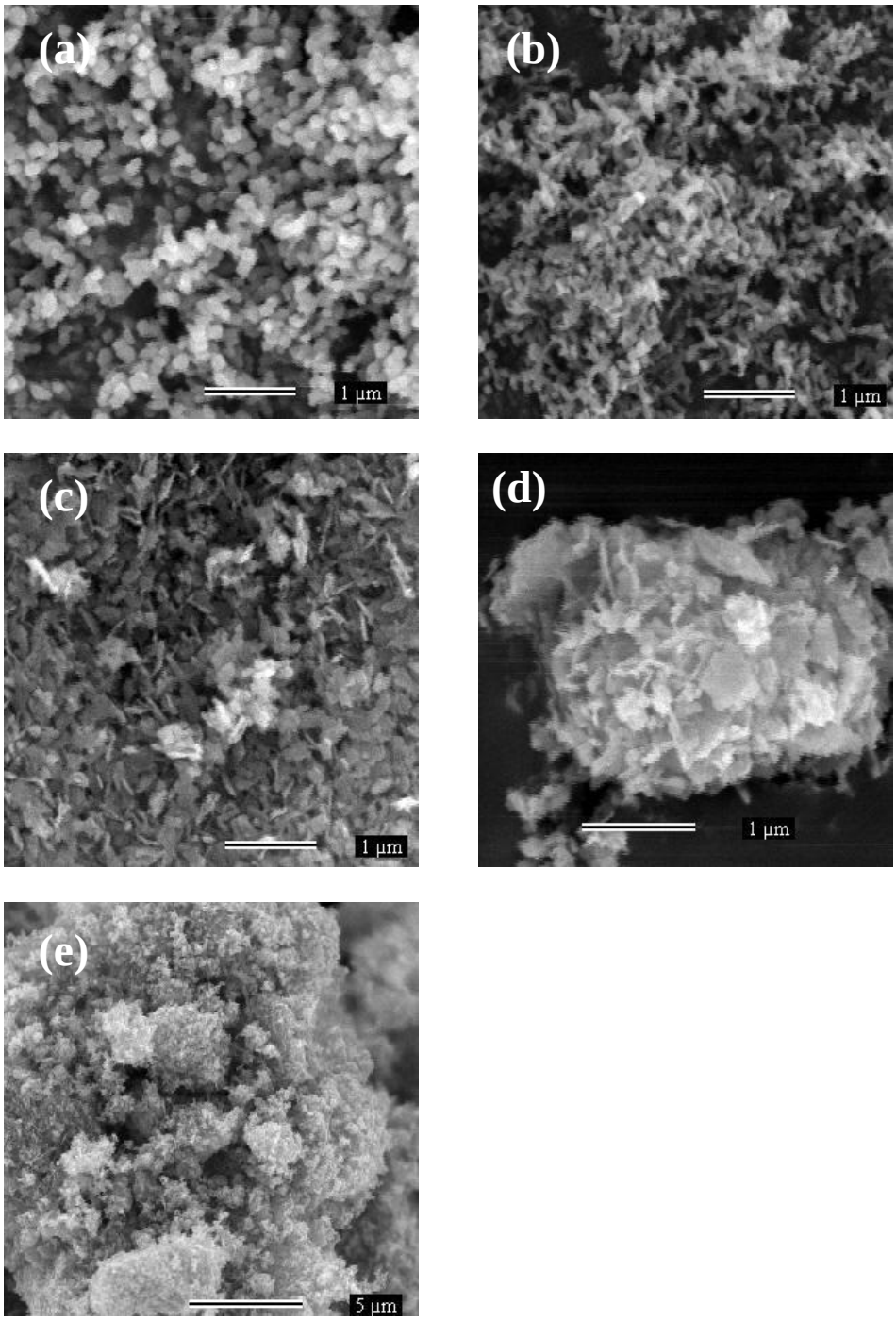

Figura 32. Micrografias da magnetita pura (a) e das amostras contendo nióbio (Mt-Nb1(b), Mt-Nb4(c), Mt-Nb8(d) e Mt-Nb11(e).

As imagens obtidas por microscopia eletrônica de transmissão (Figura 33) corroboram os dados obtidos por MEV. A magnetita obtida a partir da goethita sem a presença de Nb apresentou morfologia típica da fase cristalográfica magnetita, como descrito por Schuwertman [1]. Os materiais contendo mais nióbio: Mt-Mb4 e Mt-Nb11 apresentam micrografias distintas. Estes resultados mostram que o nióbio permanece na estrutura do óxido após o tratamento térmico de redução da goethita para magnetita.

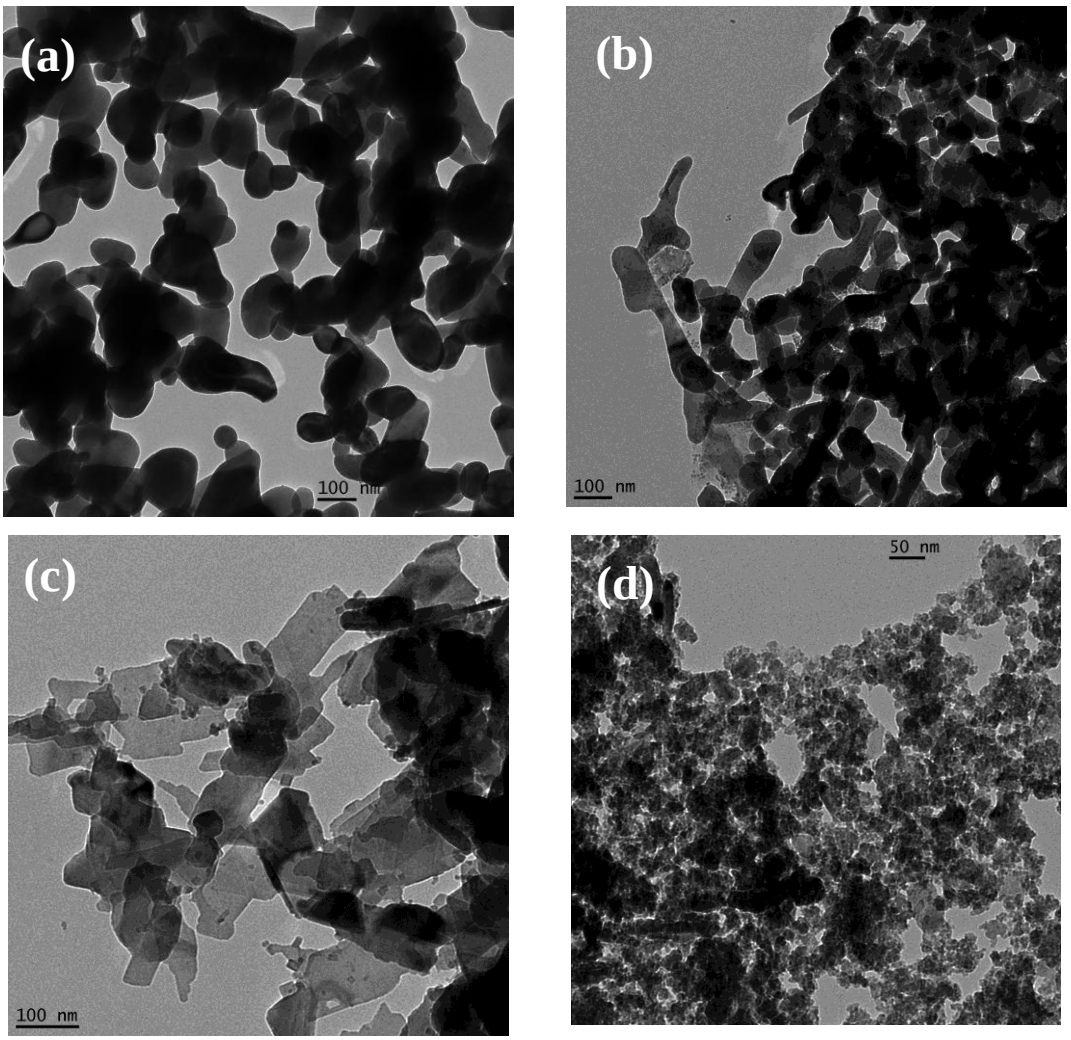

Figura 33. Imagens obtidas por microscopia eletrônica de transmissão para os catalisadores. (Mtpura (a), Mt-Nb1 (b), Mt-Nb4 (c), Mt-Nb11(d)).

5.1.2 Espectroscopia Mössbauer e Difratometria de Raios X

Os espectros Mössbauer obtidos à temperatura do ambiente, para as amostras de magnetita pura e contendo nióbio, são mostrados na Figura 34. Enquanto os espectros da magnetita pura, Mt-Nb1 e Mt-Nb4 mostram dois sextetos característicos que podem ser atribuídos ao Fe^{3+} no sítios A e Fe^{2+}/Fe^{3+} nos sítios B da estrutura de espinélio, a amostra Mt-Nb11 mostra apenas indicação de proporção secundária de magnetita.

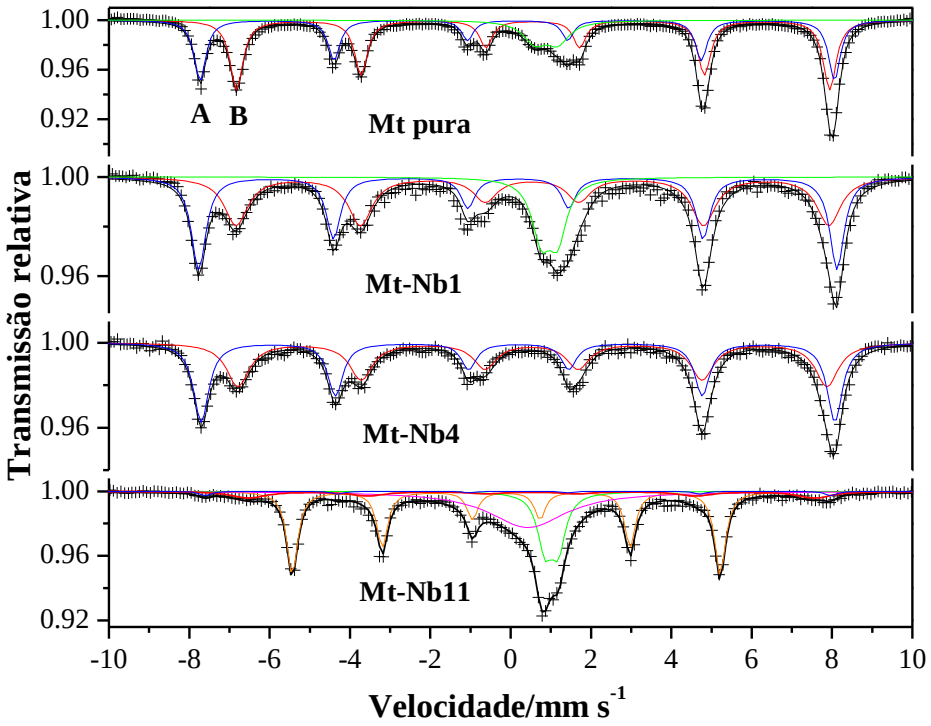

Figura 34. Espectros Mössbauer das magnetitas contendo nióbio à T = 298 K.

Análises dos espectros Mössbauer (Tabela 6) mostram o sítio de coordenação tetraédrico (A) da amostra Mtpura com campo hiperfino (B_{hf}) de 48,960(6) T e o sítio octaédrico (B) com campo hiperfino de 45,786(5) T. Enquanto os parâmetros hiperfinos correspondem aos da magnetita estequiométrica [71], a razão entre as áreas de ressonância dos sítios B em relação ao sítio A (1,39) indica que a amostra Mtpura tem composição correspondente à fórmula $Fe_{2,94}\otimes_{0,06}O_4$, sugerindo oxidação $Fe^{2+} \rightarrow Fe^{3+}$ em alguma extensão. Foi observada também diminuição gradativa da área relativa do sítio octaédrico (sítio B) em relação ao sítio tetraédrico (sítio A)

(1,07 para Mt-Nb1, e 1,00 para Mt-Nb4) com a inserção do Nb, sugerindo que o nióbio permanece incorporado à estrutura do novo óxido formado a partir das goethitas.

As larguras de linhas de ressonância nos espectros para as magnetitas contendo nióbio, particularmente as larguras correspondentes aos sítios B, são significantemente maiores que as da magnetita pura. O alargamento aumenta com o aumento da proporção de nióbio na estrutura, sugerindo incorporação do mesmo.

Para a amostra contendo o maior teor de nióbio (Mt-Nb11), a formação de magnetita é inibida, com a presença de ferro metálico ordenado magneticamente e FeO paramagnético. Este resultado mostra que uma elevada incorporação de Nb torna a estrutura menos estável, podendo sofrer uma redução mais acentuada. Esse comportamento pode influenciar significativamente as propriedades catalíticas desse material.

Tabela 6. Parâmetros Mössbauer a temperatura ambiente (~298 K) para a magnetita pura e as magnetitas contendo nióbio.

Amostra	**Sítio ^{57}Fe**	δ**/mm s^{-1}**	ε,Δ**/mm s^{-1}**	B_{hf}**/T**	Γ**/mm s^{-1}**	***AR*/%**
Mtpura	A	0,2831(8)	-0,010(1)	48,960(6)	0,349(2)	36,6(2)
	B	0,6680(7)	0,010(1)	45,786(5)	0,388(2)	50,8(2)
	FeO	1,000(4)	0,571(7)		0,70**	12,6(1)
Mt-Nb1	A	0,295(2)	-0,013(3)	49,27(1)	0,433(5)	40,6(4)
	B	0,649(3)	0,012(6)	45,75(2)	0,72(1)	43,5(1)
	FeO	1,076(3)	0,408(6)		0,55**	15,9(1)
Mt-Nb4	A	0,304(3)	-0,020(5)	48,90(2)	0,458(9)	50(1)
	B	0,642(5)	0,020(9)	45,46(4)	0,69(2)	50(1)
Mt-Nb11	A	0,30**	-0,02**	48,2(1)	0,42(6)	3,0(4)
	B	0,63**	0**	43,7(1)	0,71**	7,2(3)
	Fe^0	-0,0020(8)	0**	33,034(6)	0,323(3)	41,0(3)
	FeO	1,124(3)	0,326(4)		0,42(1)	16,6(5)
	dupleto	0,59(2)	0**		2,29(4)	32,2(6)

**Parâmetros fixados;

δ = deslocamento isomérico relativo ao αFe; ε = deslocamento quadrupolar; Δ = desdobramento quadrupolar; B_{hf} = campo magnético hiperfino; Γ = largura de linha a meia altura; *AR* = área subespectral relativa.

Para o melhor entendimento das fases formadas foram realizadas análises Mössbauer a 110 K (Figura 35). O principal aspecto dos espectros Mössbauer das magnetitas obtidos a 110 K está relacionado à transição de Verwey (temperatura, T_V ~120 K) : (i) as magnetitas sofrem alterações presumivelmente devidas à transição de Verwey, que inclui alterações nas estruturas cristalográficas e magnéticas [72] ; (ii) os espectros são muito complexos (não há modelo definitivo para a estrutura hiperfina em temperaturas abaixo de $T_{V;}$ somente os padrões espectrais experimentais são apresentados (Figura 35).

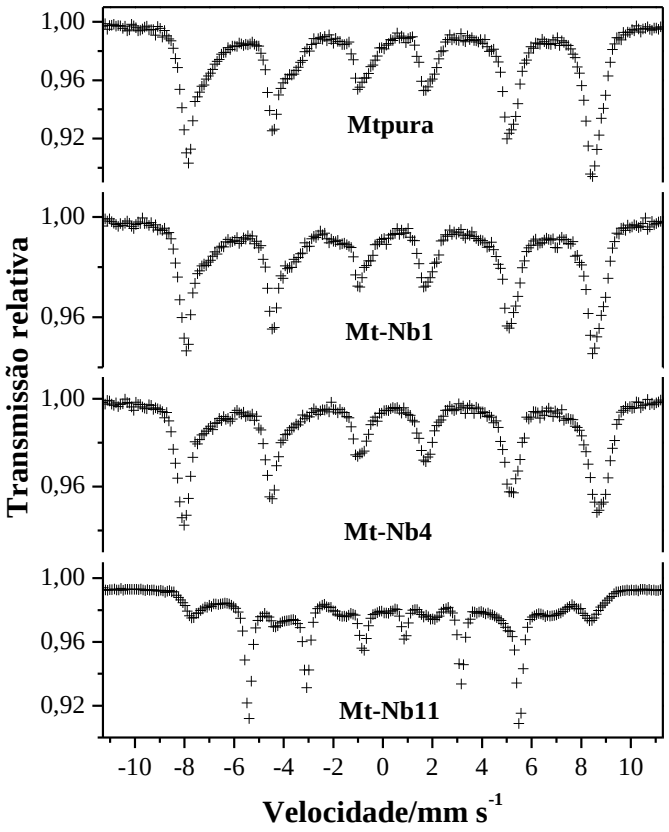

Figura 35. Espectros Mössbauer à T = 110 K das magnetitas contendo nióbio.

Os padrões de difração de raios X para as amostras obtidas após a redução das goethitas estão apresentados na Figura 36. Os difratogramas também mostram que as amostras têm proporções variadas de magnetita, confirmando os resultados Mössbauer. A amostra Mt-Nb11 mostrou a menor proporção de magnetita. As

amostras Mt-pura, Mt-Nb1 e Mt-Nb11 mostraram presença de wüstita (forma oxídica não-estequiométrica, $Fe_{1-x}O$, em que x pode variar de 0,83 a 0,95).

Os padrões resultantes não mostram uma variação sistemática da posição do pico de maior intensidade (311) como uma função da concentração do nióbio. Dessa forma, o DRX não fornece uma evidência conclusiva da incorporação do nióbio na estrutura da magnetita. Isso pode ser devido ao fato dos raios iônicos serem parecidos (64 pm para o nióbio, na coordenação octaédrica, e 65 pm para o Fe^{3+} alto spin octaédrico) [72]. Entretanto, os difratogramas mostram um significante alargamento dos picos da magnetita, com o aumento de nióbio na amostra. O tamanho dos cristalitos foi calculado usando a equação de Scherrer [1] para a reflexão (311) da magnetita e os valores encontrados (62, 44, 24 e 8 nm para as amostras Mtpura, Mt-Nb1, Mt-Nb4 e Mt-Nb11, respectivamente) confirmam essas observações.

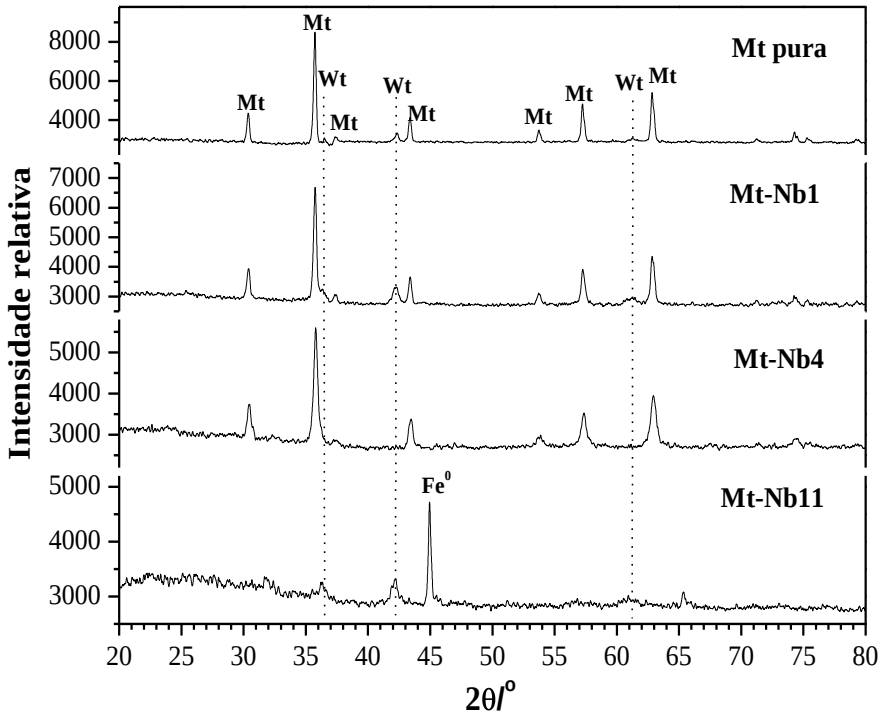

Figura 36. Padrão de difração de raios X das amostras de magnetita pura e de magnetitas contendo nióbio (Mt = Magnetita e Wt = Wüstita).

5.1.3. Área específica (BET)

As propriedades texturais dos materiais foram estudadas por adsorção/dessorção de N_2 e os resultados estão mostrados na Figura 37. Os perfis das isotermas sugerem

materiais não-porosos com isotermas do tipo II segundo a IUPAC [74]. Obtiveram-se os seguintes valores de área específica: 9, 19, 32 e 25 m^2 g^{-1} para Mtpura, Mt-Nb1, Mt-Nb4 e Mt-Nb11, respectivamente. Observa-se que, na medida em que se aumenta o teor de nióbio na estrutura da magnetita (Mtpura, Mt-Nb1 e Mt-Nb4), tem-se um ligeiro aumento de área específica, exceto para amostra contendo o maior teor de nióbio, Mt-Nb11, que apresentou área BET menor do que a amostra contendo 4% de Nb (Gt-Nb4). Porém, esse material, como mostrado por DRX e Mössbauer, apresentou fases cristalográficas de ferro diferentes das demais amostras, o que poderia explicar esse resultado.

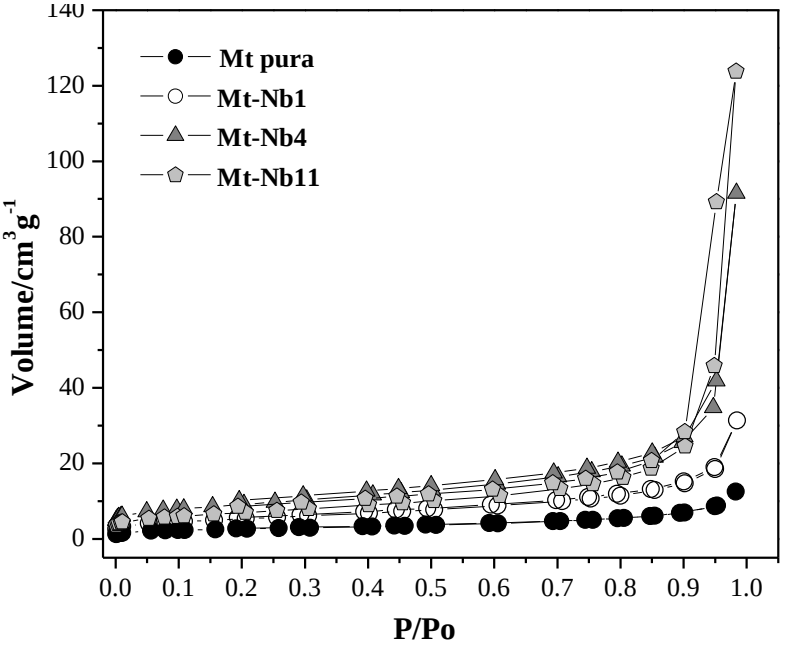

Figura 37. Isotermas de adsorção de nitrogênio para as magnetitas.

A distribuição de tamanho dos poros obtida pelo método BJH (Barrett–Joyner–Halenda) para as magnetitas é apresentada na Figura 38.

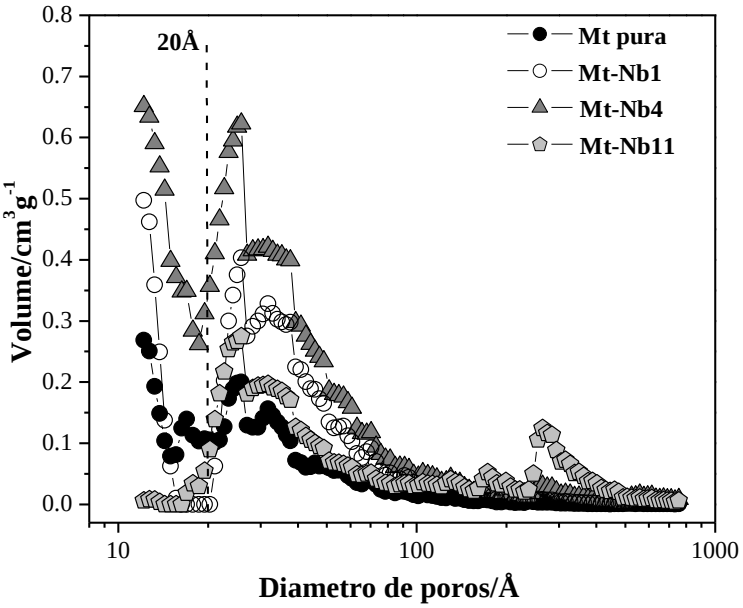

Figura 38. Distribuição de poros das magnetitas

As magnetitas obtidas da transformação térmica das goethitas apresentam um perfil de distribuição de poros distinto das goethitas precursoras, apresentando alguns poros na região tanto de micro quanto de mesoporos. Deve-se ressaltar que o volume de poros é bem menor que aqueles obtidos para as goethitas e que o tratamento térmico com H_2 modifica drasticamente as propriedades texturais dos óxidos de ferro.

5.1.4. Espectroscopia de absorção de raios X

A espectroscopia de absorção de raios X na região do XANES (Figura 39) para as magnetitas mostrou que, mesmo após o tratamento térmico sofrido durante a redução química das goethitas contendo nióbio para a síntese das magnetitas, o estado de oxidação do nióbio não se alterou. Isso pode ser percebido através da posição da borda-K para todas as amostras coincidindo com a borda do padrão de nióbio, Nb_2O_5, indicando a presença de apenas Nb^{5+}. Esse fato foi confirmado pela posição diferente da borda-K para o estado de oxidação zero, visto no espectro atribuído a folha metálica de nióbio.

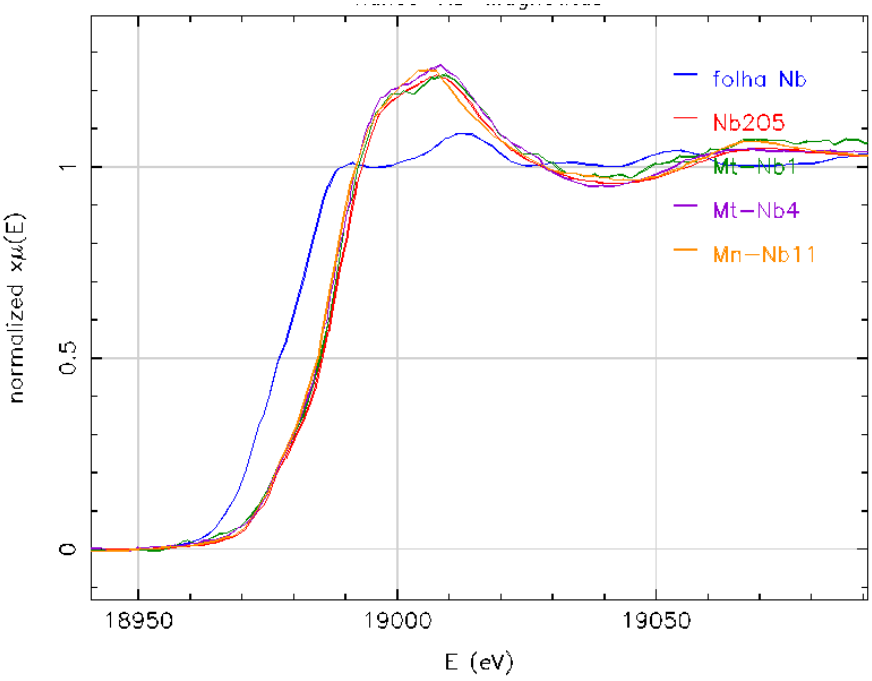

Figura 39. Espectro XANES para as magnetitas contendo nióbio e para o padrão Nb_2O_5 na borda do nióbio.

Através da análise dos resultados de absorção de raios-X na região do EXAFS para a borda do Nb, verificou-se que os dados não estavam suficientemente resolvidos para um ajuste quantitativo. Dados de melhor qualidade seriam necessários, mas estes só poderão ser obtidos por fluorescência. Com isso não foi possível obter informações a respeito das ligações químicas do nióbio no material.

Já o EXAFS das magnetitas na borda do Fe corroborou muito bem os resultados obtidos para as porcentagens de fases cristalográficas presentes nas amostras encontradas pela espectroscopia Mössbauer (Tabela 7). O ajuste foi feito com duas componentes, uma para o sítio tetra (4 O + 12 Fe + 12 O) e outro para o octa (6 O + 6 Fe + 6 Fe). O que varia é a amplitude relativa de cada componente. Através das amplitudes das contribuições de cada sítio para o sinal total, pode-se calcular a porcentagem de cada sítio.

A porcentagem de oxigênios em coordenação tetraédrica se encontra muito próxima do valor encontrado para o sitio tetraédrico da magnetita. Somando-se o valor das porcentagens encontradas para o sitio octaédrico da magnetita e para a fase mineralógica Wüstita presente na amostra, constatou-se que o resultado encontrado por EXAFS para a quantidade de oxigênios em coordenação octaédrica também foi

confirmado, mostrando assim uma maior certeza ainda sobre as espécies químicas formadas nas amostras após a redução com hidrogênio.

Tabela 7. Porcentagem de espécies de ferro encontradas por Mössbauer e por EXAFS

Amostra	**EXAFS**		**MÖSSBAUER**	
		Proporção/%	**Espécies**	***AR*/%**
Mtpura	sítios tetra (4 O + 12 Fe + 12 O)	36	[ ] Mt	36,6(2)
	sítios octa (6 O + 6 Fe + 6 Fe)	64	{ } Mt	50,8(2)
			Wt	12,6(1)
Mt-Nb1	sítios tetra (4 O + 12 Fe + 12 O)	39	[ ] Mt	40,6(4)
	sítios octa (6 O + 6 Fe + 6 Fe)	61	{ } Mt	43,5(1)
			Wt	15,9(1)
Mt-Nb4	sítios tetra (4 O + 12 Fe + 12 O)	47	[ ] Mt	50(1)
	sítios octa (6 O + 6 Fe + 6 Fe)	53	{ } Mt	50(1)

Mt = Magnetita, Wt = Wustita, *AR* = área subespectral relativa, { } = sitio octaédrico, [ ] = sítio tetraédrico de coordenação Fe-O, na estrutura da magnetita.

5.2 TESTES CATALÍTICOS

5.2.1. Azul de metileno via Fenton heterogêneo

A atividade catalítica das magnetitas contendo nióbio foi inicialmente avaliada na oxidação de um contaminante modelo (corante azul de metileno) na presença de H_2O_2 em meio aquoso. Para isso, a descoloração da solução do corante foi medida por espectroscopia UV-Visível (Figura 40).

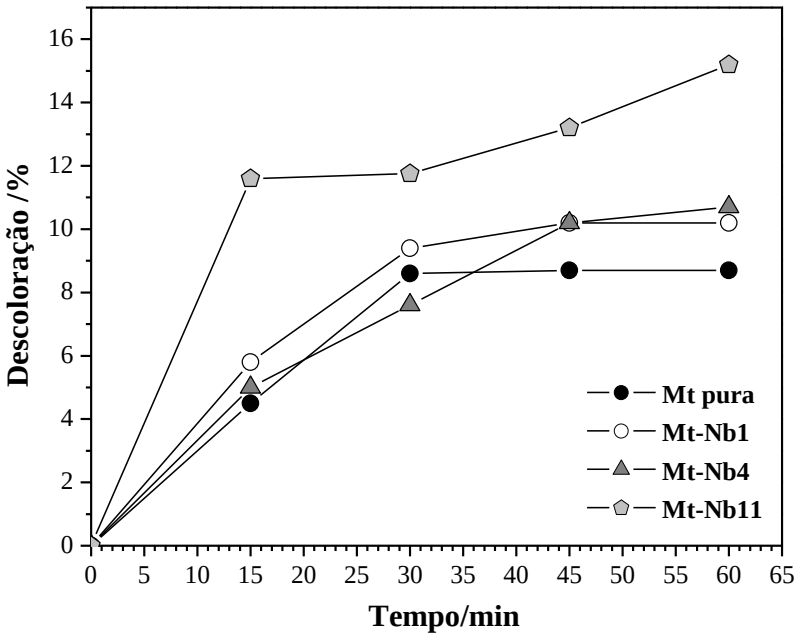

Figura 40. Descoloração do azul de metileno na presença das magnetitas com nióbio.

O experimento controle (apenas azul de metileno e H_2O_2, mas sem catalisador) não mostrou descoloração significativa, mesmo após 60 min de reação. Por outro lado, na presença das magnetitas contendo nióbio e H_2O_2 como oxidante, a descoloração pode ser observada em alguma extensão. A descoloração é moderada na presença da magnetita pura e das que possuem os menores teores de nióbio. A amostra contendo o maior teor de nióbio (Mt-Nb11) produz uma descoloração de aproximadamente 15%, após 60 min de reação. A descoloração observada para as magnetitas foi bem inferior àquelas obtidas para as goethitas precursoras sugerindo que as modificações texturais pelo tratamento térmico têm papel importante no efeito catalítico.

Como discutido anteriormente, a medida da descoloração por espectroscopia de UV-Vis não fornece nenhuma informação sobre os intermediários formados na reação de oxidação do azul de metileno. Tal identificação pode ser feita usando-se a espectrometria de massas com ionização por electrospray.

A identificação dos intermediários foi estudada obtendo-se espectros depois de 60 min de reação na presença de H_2O_2 para cada material (Figura 41). O espectro da solução de azul de metileno (sem catalisadores) mostrou apenas um pico em m/z = 284 devido à estrutura catiônica do AM. Após uma hora de reação, foram observados

intermediários de reação nos espectros para as magnetitas, confirmando que a mineralização não foi total. Entretanto, a intensidade do pico em m/z = 284 diminuiu como visto anteriormente na espectroscopia de UV-Visível. Além disso, um pico observado em m/z = 270 sugere o começo da degradação da estrutura do corante [74].

Os sinais em m/z = 300, 316 e 332 são provavelmente devidos à hidroxilação sucessiva do anel aromático [74]. O perfil dos intermediários de reação obtido para as magnetitas foi diferente daquele observado para as goethitas e sugere a formação de radicais durante a decomposição de H_2O_2. Alguns autores têm relatado que isso se deve à ação de um mecanismo do tipo Fenton, ocorrendo em condição heterogênea [76]. O pico em m/z = 149 é indicativo da ruptura do anel, o que indica a possibilidade de subseqüente mineralização [69].

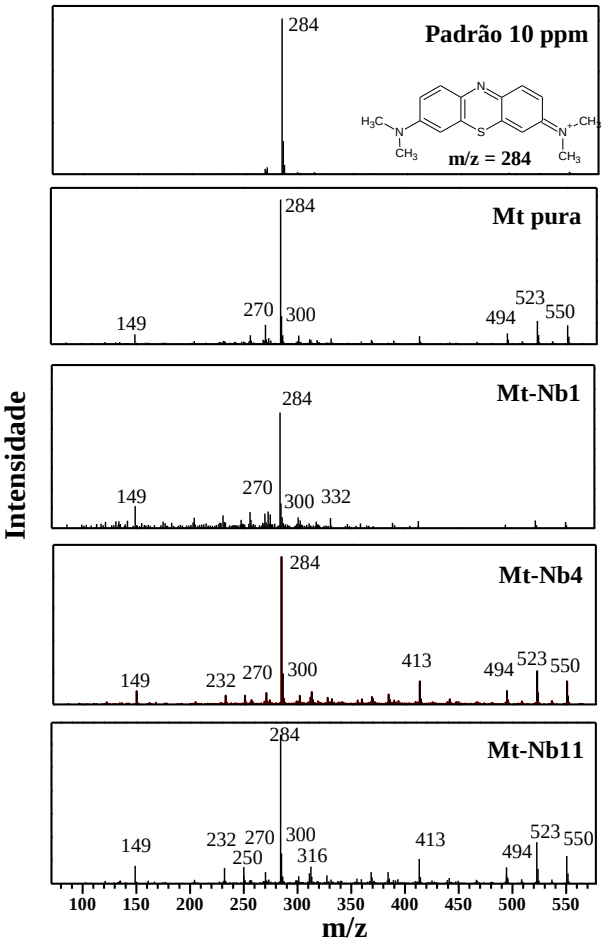

Figura 41. Espectros de massa (m/z) dos produtos de reação da oxidação do azul de metileno com ionização por electrospray em função da concentração de nióbio nas amostras.

5.3 CONCLUSÕES - PARTE MAGNETITAS

A presença de nióbio associado à magnetita e também possivelmente à wüstita teve um efeito significativo na cristalinidade e na atividade catalítica do óxido. Quanto maior o teor de nióbio, menor foi a cristanilidade e maior a eficiência catalítica apresentadas. Pôde-se perceber que a oxidação de compostos orgânicos com H_2O_2 mostrou ser provavelmente via radical, como sugerido pelos dados de ESI-MS.

Um mecanismo de oxidação pelo ataque do radical livre $^{\bullet}OH$ sobre o azul de metileno foi evidenciado pelo aumento dos produtos de hidroxilação como principais subprodutos, embora compostos resultantes da ruptura do anel também sejam detectados. A presença de nióbio na estrutura do material aumenta a atividade catalítica do óxido para a degradação do corante azul de metileno e a superfície dos materiais contendo nióbio parece agir diretamente nas propriedades catalíticas dos mesmos. No entanto, as magnetitas obtidas da transformação térmica das goethitas apresentam menor atividade na remoção do corante do meio aquoso, provavelmente devido às diferenças nas propriedades texturais dos diferentes óxidos.

6 CONCLUSÕES FINAIS

Através do estudo realizado nesse trabalho, foram obtidos novos catalisadores baseados em óxidos de ferro modificados pela incorporação estrutural de nióbio. Os materiais apresentaram propriedades catalíticas promissoras no que diz respeito à oxidação de poluentes orgânicos na presença de H_2O_2. Pôde-se perceber ainda, que a introdução do nióbio na estrutura dos catalisadores influenciou significativamente suas propriedades físico-químicas e texturais, com um aumento da área específica e grande mudança na morfologia dos mesmos. Esses aspectos foram fundamentais para os resultados catalíticos encontrados.

Os resultados catalíticos obtidos revelaram comportamentos diferenciados para a reação de oxidação do corante orgânico azul de metileno na presença de peróxido de hidrogênio. As goethitas contendo nióbio foram cataliticamente mais efetivas, em comparação às magnetitas correspondentes e levaram à, aproximadamente, 90% de descoloração da solução inicial. A descoloração observada para as magnetitas foi de apenas 15%, sugerindo que as modificações texturais pelo tratamento térmico têm papel importante no efeito catalítico. Os valores de área superficial obtidos corroboram essa informação, uma vez que foram obtidos valores de áreas superficiais muito pequenos para as magnetitas (9, 19, 32 e 25 m^2g^{-1} para Mtpura, Mt-Nb1, Mt-Nb4 e Mt-Nb11, respectivamente) e conforme indicou os estudos por microscopia, uma sinterização também pode ter ocorrido.

Além da diferença na área específica dos materiais, com valores de 119, 120, 122 e 174 m^2g^{-1}, para Gtpura, Gt-Nb1, Gt-Nb4 e Gt-Nb11, outro fator que contribui para a melhor atividade das goethitas nas reações de degradação do corante azul de metileno, é a presença de mecanismos diferentes envolvidos na reação, com a formação de espécies peroxo com o nióbio no caso das reações com as goethitas, como indicaram as análises por espectrometria de massas com ionização via electrospray.

7 REFERÊNCIAS BIBLIOGRÁFICAS

1. Cornell, R.M., Schwertmann, U. The Iron Oxides, 3th ed., Weinheim-VHC: New York, **2003**.
2. Sciré, S. et al., Catalytic combustion of volatile organic compounds over group IB metal catalysts on Fe_2O_3. *Catalysis Communications* 2, **2001**, 229-232.
3. Lin, S.S.; Gurol, M.D. Catalytic Decomposition of Hydrogen Peroxide on Iron Oxide: Kinetics, Mechanism, and Implications. *Environmental Science & Technology* 32, **1998**, 1417-1423.
4. Watts, R.J. et al., Oxidative and Reductive Pathways in Manganese-Catalyzed Fenton's Reactions. *Journal of Environmental Engineering*, 131, **2005**, 158-164.
5. Melero, J.A.; Martínez, F.; Botas, J.A.; Molina, R.; Pariente, M.I. Heterogeneous catalytic wet peroxide oxidation systems for the treatment of an industrial pharmaceutical wastewater *Water research* 43, **2009**, 4010-4018.
6. Dantas, T.L.P.; Mendonça, V.P.; Jos, H.J.; Rodrigues, A.E.; Moreira, R.F.P.M.; Treatment of textile wastewater by heterogeneous Fenton process using a new composite Fe_2O_3/carbon *Chemical Engineering Journal* 118, **2006**, 77-82.
7. Wang, S. A Comparative study of Fenton and Fenton-like reaction kinetics in decolourisation of wastewater *Dyes and Pigments*, 76, **2008**, 714-720.
8. Cao, G.; Sheng, M.; Niu, W.; Fei, Y.; Li, D. Regeneration and reuse of iron catalyst for Fenton-like reactions *Journal of Hazardous Materials*, 172, **2009**, 1446-1449.
9. Rongcheng, W.; Jiuhui, Q. Removal of Azo Dye from Water by Magnetite Adsorption-Fenton Oxidation. *Water Environment Research* 76, **2004**, 2637-2642.
10. He, J. et al., Heterogeneous Photo-Fenton Degradation of an Azo Dye in Aqueous H_2O_2/Iron Oxide Dispersions at Neutral pHs. *Chemistry Letters* 1, **2002**, 86-87.

11. Feng, J.Y. et al., Degradation of Azo-Dye Orange Ii by a Photoassisted Fenton Reaction Using a Novel Composite of Iron Oxide & Silicate Nan. *Industrial & Engineering Chemistry Research* 42, **2003**, 2058-2066.

12. Santos, C. A.; Horbe, A.M.C.; Barcellos, C.M.O.; Marimon da Cunha, J.B.; Some structure and magnetic effects of Ga incorporation on α-FeOOH *Solid State Commun.* 31, **2001**, 449-452.

13. Gajović, A.; Silva, A.M.T.; Segundo, R.A.; Šturm, S.; Jančar, B.; Čeh, M. Tailoring the phase composition and morphology of Bi-doped goethite–hematite nanostructures and their catalytic activity in the degradation of an actual pesticide using a photo-Fenton-like process *Applied Catalysis B: Environmental*, 103, **2011**, 351-361.

14. Han, Z.; Dong, Y.; Dong, S. Copper–iron bimetal modified PAN fiber complexes as novel heterogeneous Fenton catalysts for degradation of organic dye under visible light irradiation *Journal of Hazardous Materials*, 189, **2011**, 241-248.

15. Ashiq, M.N.; Bibi, N.; Malana, M.A. Effect of Sn–Ni substitution on the structural, electrical and magnetic properties of mixed spinel ferrites *Journal Alloys and Compounds*, 490, **2010**, 594-597.

16. Carvalho Costa, R.C. Novos processos avançados de oxidação a base de óxido de ferro. Belo Horizonte: Tese UFMG/ICEx/Química, **2005**. 165f.

17. Guimarães, I.R.; Oliveira, L.C.A.; Queiroz, P.F.; Ramalho, T.C.; Pereira, M.; Fabris, J.D.; Ardisson, J.D. Modified goethites as catalyst for oxidation of quinoline: Evidence of heterogeneous Fenton process. *Applied catalysis A: Genera*l 347, **2008**, 89–93.

18. http://www.dnpm.gov.br, acessada em 09/02/2009.

19. Nowak, I.; Ziolek, M. Niobium compounds: preparation, characterization, and application in heterogeneous catalysis. *Chemical Reviews*, 99, **1999**, 3603-3624.

20. http://www.cbmm.com.br, acessada em 09/02/2009.

21. Tanabe, K. Catalytic application of niobium compounds *Catalysis Today*, 78, **2003**, 65-77.

22. Silva, A.C.; Oliveira, D.Q.L.; Oliveira, L.C.A.; Anastácio, A.S.; Ramalho, T.C.; Lopes, J.H.; Carvalho, H.W.P.; Rodriguez Torres, C.E. Nb-containing hematites $Fe_{2-x}Nb_xO_3$: The role of Nb^{5+} on the reactivity in presence of the H_2O_2 or ultraviolet light *Applied Catalysis A: General*, 357, **2009**, 79-84.

23. Assalin, M.R.; Silva, P.L.; Durán, N. Comparação da eficiência do processo de ozonização e ozonização catalítica (Mn II e Cu II) na degradação de fenol. *Química Nova*, 29, **2006**, 24-27.

24. Zhou, G.M.; Fang, H.P.; Co-degradation of phenol and m-cresol in a UASB reactor. *Bioresource Technology*, 61, **1997**, 47-52.

25. Guerra, R.; Ecotoxicological and chemical evaluation of phenolic compounds in industrial effluents. *Chemosphere*, 44, **2001**, 1737-1747.

26. IGAM (Instituto Mineiro de Gestão das Águas) Relatório de monitoramento das águas superficiais na Bacia do Rio Grande em 2004 - Belo Horizonte, 2005 - 250p. Disponível em: http://www.igam.mg.gov.br

27. Pera Titus, M. et al.; Degradation of chlorophenols by means of advanced oxidation processes: a general review. *Applied Catalysis B: Environmental* 47, **2004**, 219-256.

28. Kojima, T.; Nishijima, K.; Matsukata, M.; Removal and recovery of phenol from FCC effluent. *Journal of Membrane Science*, 102, **1995**, 43-47.

29. Bird, C. Química Ambiental. Porto Alegre: Bookman, **2002**, 2.ed.

30. Tiburtius, E.R.L.; Peralta-Zamora,P.; Contaminação de águas por BTXs e processos utilizados na remediação de sítios contaminados. *Química Nova*, 27, **2004**, 441- 446.

31. Fenton H.J.H. Oxidation of tartaric acid in presence of iron. Journal of the Chemical Society, Transactions, 65, **1894**, 899-910.

32. Chan K.H.; Chu, W. The dose and ratio effects of Fe(II) and H_2O_2 in Fenton's process on the removal of atrazine. *Environ. Technol* 24, **2003**, 703-710.

33. Vitolins A.R. et al.; Fenton's Reagent-Based In Situ Chemical Oxidation Treatment of Saturated and Unsaturated Soils at a Historic Railroad Site *Soil & Sediment Contam.*, 12, **2003**, 139-150.

34. Neyens, E.; Baeyens, J. A review of classic Fenton's peroxidation as an advanced oxidation technique. *Journal of Hazardous Materials* 98, **2003**, 33-50.

35. Dunford, H.B. Oxidations of iron(II)/(III) by hydrogen peroxide: from aquo to enzyme. *Coordination Chemistry Reviews* 233, **2002**, 311-318.

36. Guedes, A.M.F.M. et al., Fenton oxidation of cork cooking wastewater—overall kinetic analysis. *Water Research* 37, **2003**, 3061-3069.

37. Oliveira, L.C.A. Síntese, caracterização e propriedades catalíticas da magnetita dopada com manganês ou magnésio. **2000**. 75 p. Dissertação de Mestrado. Belo Horizonte: UFMG/ICEx/Química.

38. Bhargava, S.C.; Knudsen, J.E.; Mørup, S. Mössbauer study of spin-spin relaxation of Fe^{3+} ions in the presence of other paramagnetic ions J*ournal of Physics and Chemistry of Solids* 40, **1979**, 45-53.

39. Valentine, R.L.; Ann Wang, H.C. Iron Oxide Surface Catalyzed Oxidation of Quinoline by Hydrogen Peroxide *J. Environ. Eng.* 124, **1998**, 31–38.

40. He, J.; Tão, X.; Ma, W.; Jincai, W. Heterogeneus photo-Fenton degradation of azo dye in aqueous H_2O_2/iron oxide dispersions at neutral pHs *Chem. Lett.* 1, **2002**, 66–87.

41. Andreozzi, R.; D'Apuzzo, A.; Marotta, R. Oxidation of aromatic substrates in water/goethite slurry by means of hydrogen peroxide. *Water Research* 36, **2002**, 4691-4698.

42. Lu, M.; Chen, J.; Huang, H.; Role of goethite dissolution in the oxidation of 2-chlorophenol with hydrogen peroxide. *Chemosphere*, 46, **2002**, 131-136.

43. Kunel, S.R.; Neppolian, B.; Choi, H.; Yang, J.W. Heterogeneous Catalytic Oxidation of Phenanthrene by Hydrogen Peroxide in Soil Slurry: Kinetics, Mechanism, and Implication *Soil Sediment Contam.* 12, **2003**, 101–117.

44. Ceti, G.; Perathoner, P.; Torre, T.; Verduna, M.G. Catalytic wet oxidation with H2O2 of carboxylic acids on homogeneous and heterogeneous Fenton-type catalysts *Catal. Today* 55, **2000**, 61–69.

45. N. Al-Hayek, M. Dore, Oxidation of phenols in water by hydrogen peroxide on alumine supported iron *Water Res.* 24, **1990**, 973–982.

46. R.J. Watts, M.D. Udell, S.H. Kong, Fenton-Like Soil Remediation Catalyzed by Naturally Occurring Iron Minerals *Environ. Eng. Sci.* 16, **1999**, 93–103.

47. Lee, S.; Oh, J.; Park, Y.; Degradation of phenol with Fenton-like treatment by using heterogeneous catalyst (modified iron oxide) and hydrogen peroxide. *Bull. Korean Chem. Soc.*, 27, **2006**, 489-494.

48. Huang, H.; Lu, M.; Chen, J. Catalytic Decomposition of Hydrogen Peroxide and 2-chlorophenol with iron oxides. *Water Research* 35, **2001**, 2291-2299.

49. Costa, R. C. C.; Lelis, F.; Oliveira, L. C. A.; Fabris, J. D.; Ardisson, J. D.; Rios, R. R. A.; Silva, C. N.; Lago, R. M.; Remarkable effect of Co and Mn on the activity of $Fe_{3-x}M_xO_4$ promoted oxidation of organic contaminants in aqueous medium with H_2O_2 *Catal. Commun.* 4, **2003**, 525-529.

50. Oliveira, L. C.; Rios, R. V. A.; Sapag, K.; Fabris, J. D.; Garg, V. K. Lago, R. M.; Clay–iron oxide magnetic composites for the adsorption of contaminants in water *Appl. Clay Sci.* 22, **2003**, 169-177.

51. Nogueira, R.F.P.; Jardim, W.F. A fotocatálise heterogênea e sua aplicação ambiental. *Química Nova*, 21, **1998**, 69-72.

52. Ohlweiler, O.A. Química Analítica Quantitativa. 3a ed. Rio de Janeiro: Livros Tecnicos e Cientificos Ed., vol.2, **1981**. 223p.

53. Joint Committee on Powder Diffraction Standards-JCPDS; Mineral powder diffraction files data book, Swarthmore, Pennsylvania, 1980.

54. http://www.fmt.if.usp.br/~goya/mosseffectp.htm, acessado em janeiro de 2009.

55. http://www.uni-uisburg.de/FB10/LAPH/Keune/englisch/brand/r.a.brand.homepage.htm#Normos, acessada em março de 2009.

56. Koningsberger, D.C.; Prins, R.; X-Ray Absorption 1998, Wiley, New York.

57. Ravel, B.; Newville, M.; ATHENA, ARTEMIS, HEPHAESTUS: data analysis for X-ray absorption spectroscopy using IFEFFIT. *J. Synchrotron Radiat.* **2005**, 12, 537.

58. Krehula, S.; Music, S.; Popovic, S. Influence of Ni-dopant on the properties of synthetic goethite *J. Alloys Compd.* 403, **2005**, 368–375.

59. Stiers, W.; Schwertmann, U. Evidence for manganese substitution in synthetic goethite *Geochim. Cosmochim. Acta* 49, **1985**, 1909–1911.

60. Bocquet, S.; Pollard, R. J.; Cashion, J. D.; Dynamic magnetic phenomena in fine-particle goethite *Phys. Rev. B: Condens. Matter Mater. Phys.* 46, **1992**, 11657-11664.

61. Morales, A.L.; Barrero, C.A.; Jaramillo, F.; Arroyave, C.; Greneche, J.M. Properties of Goethite Grown under the Presence of Cr^{3+}, Cu^{2+} and Mn^{2+} Ions *Hyp. Interact.* 148, **2003**, 135–144.

62. Schwertmann, U.; Gasser, U.; Sticher, H. Chromium-for-iron substitution in synthetic goethites *Geochim. Cosmochim. Acta* 53, **1989**, 1293–1297.

63. Martins, L.; Cardoso, D. Aplicação catalítica de peneiras moleculares básicas micro e mesoporosas *Quim. Nova*, 29, **2006**, 358-364.

64. Teel, A. L.; Warberg, C. R.; Atkinson, D. A.; Watts, R. J.; Comparison of mineral and soluble iron Fenton's catalysts for the treatment of trichloroethylene *Water Res*. 35, **2001**, 977-984.

65. Silva, A.C.; Cepera, R.; Pereira, M.C.; Lima, D.Q.; Fabris, J.D. ; Oliveira, L.C.A. Heterogeneous catalyst based on peroxo-niobium complexes immobilized over iron oxide for organic oxidation in water (APCATB-D-11-00401R1)-Aceito. *Appl. Catal. B, Environmental* (Print), **2011**.

66. Arends, I.W.C.E.; Sheldon, R.A. Activities and stabilities of heterogeneous catalysts in selective liquid phase oxidations: recent developments. *Appl. Catal. A* 212, **2001**, 175-187.

67. Gao, X.; Wachs, I.E.; Wong, M.S.; Ying, J.Y. Structural and Reactivity Properties of Nb---MCM-41: Comparison with That of Highly Dispersed Nb_2O_5/SiO_2. *J. Catal.* 203, **2001**, 18-24.

68. Ziolek, M.; Sobczak, I.; Lewandowska, A.; Nowak, I.; Decyk, P.; Renn, M.; Jankowska, B. Oxidative properties of niobium-containing mesoporous silica catalysts *Catal. Today* 70, **2001**, 169-181.

69. Oliveira, L.C.A.; Fabris, J.D.; Guerreiro, M.C.; Gonçalves, M.; Sapag, K.; Ramalho, T.C. A new catalyst material based on niobia/iron oxide composite on

the oxidation of organic contaminants in water via heterogeneous Fenton mechanisms. *Appl. Catal. A, General,* 316, **2007**, 117-124.

70. Oliveira, L.C.A.; Ramalho, T.C.; Souza, E.F.; Gonçalves, M.; Oliveira, D.Q.L.; Pereira, M.C.; Fabris, J.D.; Catalytic properties of goethite prepared in the presence of Nb on oxidation reactions in water: Computational and experimental studies. *Applied Catalysis B, Environmental,* 83, **2008**, 169-176.

71. Murad, E.; Cashion, J. Mössbauer spectroscopy of Environmental Materials and their Industrial Utilization. Kluwer Academic Publishers, Norwell, **2004**.

72. Honig, J.M. Analysis of the Verwey transition in magnetite. *Journal of Alloys and Compounds*, 229, **1995**, 24-39.

73. Kaye and Laby Tables of Physical and Chemical Constants and some Mathematical Functions p. 386, **1975**.

74. IUPAC – International Union of Pure and Applies Chemistry. Reporting physisorption data for gas / solid systems. *Pure & Appl. Chem*., 57, **1985**, 603-619.

75. Oliveira, L.C.A.; Ramalho, T.C.; Gonçalves, M.; Cereda, F.; Carvalho, K.T.; Nazzarro, M.S.; Sapag, K. Pure niobia as catalyst for the oxidation of organic contaminants: Mechanism study via ESI-MS and theoretical calculations. *Chem. Phys. Letters* 446, **2007**, 133-137.

76. Moura, F.C.C.; Oliveira, G.C.; Araujo, M.H.; Ardisson, J.D.; Macedo, W.A.A.; Lago, R.M. Highly reactive species formed by interface reaction between Fe^0–iron oxides particles: An efficient electron transfer system for environmental applications. *Appl. Cat. A: Gen.* 307, **2006**,195-204.

ANEXO I

RESULTADOS OBTIDOS EM TRABALHOS DURANTE O DOUTORADO-SANDUÍCHE

Durante o período de 04/2009 a 12/2009, foi realizado um estágio de doutorado no Departamento de Química da Universidade da Califórnia, em Riverside, CA, EUA, sob supervisão do professor Yadong Yin, dedicado à preparação de fotocatalisadores baseados em TiO_2, como estudo complementar aos sistemas Fenton, foco maior desta tese.

Em resumo, foram feitos dois trabalhos:

(i) Síntese de *clusters* de nanocristais mesoporosos de TiO_2 anatásio, com alta área superfícial e alta atividade fotocatalítica. A síntese envolve a auto-montagem de nanocristais TiO_2 hidrofóbicos em *clusters,* revestindo estes *clusters* com uma camada de sílica, e tratando termicamante para remover ligantes orgânicos e melhorar a cristalinidade dos *clusters,* e, finalmente, a remoção de sílica para expor os catalisadores mesoporosos. Com a ajuda do revestimento de sílica, os *clusters* não só mantém seu tamanho pequeno de grão, mas também mantém a sua estrutura mesoporosa, após calcinação a altas temperaturas (com área superficial BET de 277 m^2/g). A retirada de SiO_2 também resulta em *clusters* com alta dispersibilidade em água. Foi possível identificar a temperatura de calcinação ideal para produzir os nanocristais de TiO_2, grupos que possuem tanto alta cristalinidade quanto alta superfície e, portanto, mostrando assim, excelente eficiência catalítica na decomposição de moléculas orgânicas sob luz UV. O uso de dopagem com nitrogênio converte esses *clusters* de nanocristais em fotocatalisadores ativos na luz visível e luz solar natural. A estratégia de formação bem definida *clusters* mesoporosos usando nanocristais promete um método versátil e útil para a concepção de fotocatalisadores com maior atividade e estabilidade.

(ii) Síntese de fotocatalisador do tipo $SiO_2/Au/TiO_2$ com alta eficiência na decomposição de compostos orgânicos sob iluminação de luz UV, visível e luz solar natural. O projeto estrutural do fotocatalisador aproveita a interação sinérgica entre o ouro adsorvido e nitrogênio implantado, e produz nanopartículas de anatásio dopadas com não-metal e com decoração precisamente controlada com nanopartículas de Au.

A excelente eficiência fotocatalítica pode ser atribuída à dopagem com não-metal na interface, o que melhora a atividade sob a luz visível, frente ao efeito plasmônico pela decoração com metal, o qual contribui para o aumento da captura de luz e da separação de carga, e para o pequeno tamanho de grão dos nanocristais de anatásio, o que reduz a taxa de recombinação do par elétron-buraco em um semicondutor.

Os artigos correspondentes foram publicados nas revistas Nano Research 2011, 4(1): 103-114 e Angewandte Chemie 2011, 123(31): 7226–7230 e cópias dos artigos se encontram a seguir.

ANEXO II

REFERÊNCIAS DE PUBLICAÇÕES OBTIDAS DURANTE ESTE TRABALHO

São relacionadas nesta seção, as referências dos trabalhos publicados que reportam resultados experimentais desta tese e também durante o período de doutorado em colaboração com outros grupos de pesquisa.

1) **Artigo publicado na Applied Catalysis B: Environmental, 2008**

Oliveira, L.C.A.; Ramalho, T.C.; Souza, E.F.; Goncalves, M.; Oliveira, D.Q.L.; Pereira, M.C.; Fabris, J.D. **Catalytic properties of goethite prepared in Nb presence on oxidation reactions in water: computational and experimental studies** *Appl. Catal.B, Environmental*, 83, 2008, 169-176.

2) **Artigo publicado na Hyperfine Interactions, 2009**

Oliveira, Diana Q.L.; Oliveira, Luiz C.A.; Murad, Enver; Fabris, José D.; Silva, Adilson C.; Menezes, Lucas M. **Niobian iron oxides as heterogeneous Fenton catalysts for environmental remediation.** *Hyperfine Interactions* 195, 2009, 27-34.

3) **Artigo publicado na Applied Catalysis A, 2009**

Silva, A.C.; Oliveira, D.Q.L.; Oliveira, L.C.A.; Anastacio, A.S.; Ramalho, T.C.; Lopes, J.H.; Carvalho, H.W.P.; Torres, C.E.R. **Nb-containing hematites $Fe_{2-x}Nb_xO_3$: The role of Nb^{5+} on the reactivity in presence of the H_2O_2 or ultraviolet light** *Appl. Catal. A, General*, 357, 2009, 79-84.

4) **Artigo publicado na Applied Catalysis A, 2009**

Oliveira, Luiz C.A.; Zaera, Francisco; Lee, Ilkeun; Lima, Diana Q.; Ramalho, Teodorico C.; Silva, Adilson C.; Fonseca, Emanuella M.B. **Nb-doped hematites for decomposition of isopropanol: Evidence of surface reactivity by in situ CO adsorption** *Appl. Catal. A, General*, 368, 2009, 17-21.

5) **Artigo aceito Applied Catalysis B, 2011**

Silva, A.C.; Cepera, R.; Pereira, M.C.; Lima, D.Q.; Fabris, J.D.; Oliveira, L.C.A. **Heterogeneous catalyst based on peroxo-niobium complexes immobilized over iron oxide for organic oxidation in water** (APCATB-D-11-00401R1)-Aceito. *Appl. Catal. B, Environmental* (Print), 2011.

6) **Artigo publicado Jornal de Magnetism and Magnetic Materials, 2010**

Braga, Tiago P.; Vasconcelos, Igor F.; Sasaki, José M.; Fabris, J.D.; Oliveira, Diana Q.L.; Valentini, Antoninho **Magnetic composites based on hybrid spheres of aluminum oxide and superparamagnetic nanoparticles of iron oxides** *Journal of Magnetism and Magnetic Materials*, 322, 2010, 633-637.

7) **Artigo aceito Hyperfine Interactions, 2011**

Ribeiro, Andreza A.; Lima, Diana Q.; Duarte, Hélio A.; Murad, Ever; Pereira, Márcio C.; Suita, Marcos T.D.F.; Ardisson, José D.; Fabris, José D.; "Structural characteristics of chalcopyrite from a Cu(Au) ore deposit in the Carajás Mineral Province, Brazil", *Hyperfine Interactions*, aceito.

Nano Res. 2011, 4(1): 103–114
DOI 10.1007/s12274-010-0058-9
Research Article

ISSN 1998-0124
CN 11-5974/O4

Self-Assembly and Photocatalysis of Mesoporous TiO_2 Nanocrystal Clusters

Qiao Zhang, Ji-Bong Joo, Zhenda Lu, Michael Dahl, Diana Q. L. Oliveira, Miaomiao Ye, and Yadong Yin (✉)

Department of Chemistry, University of California, Riverside, California 92521, USA

Received: 31 July 2010 / Revised: 24 August 2010 / Accepted: 12 October 2010

ABSTRACT

Mesoporous nanocrystal clusters of anatase TiO_2 with large surface area and enhanced photocatalytic activity have been successfully synthesized. The synthesis involves the self-assembly of hydrophobic TiO_2 nanocrystals into submicron clusters, coating of these clusters with a silica layer, thermal treatment to remove organic ligands and improve the crystallinity of the clusters, and finally removing silica to expose the mesoporous catalysts. With the help of the silica coating, the clusters not only maintain their small grain size but also keep their mesoporous structure after calcination at high temperatures (with BET surface area as high as 277 m^2/g). The etching of SiO_2 also results in the clusters having high dispersity in water. We have been able to identify the optimal calcination temperature to produce TiO_2 nanocrystal clusters that possess both high crystallinity and large surface area, and therefore show excellent catalytic efficiency in the decomposition of organic molecules under illumination by UV light. Convenient doping with nitrogen converts these nanocrystal clusters into active photocatalysts in both visible light and natural sunlight. The strategy of forming well-defined mesoporous clusters using nanocrystals promises a versatile and useful method for designing photocatalysts with enhanced activity and stability.

KEYWORDS

Mesoporous, titanium dioxide, photocatalysis, self-assembly, nitrogen doping, nanocrystals

1. Introduction

Clean and sustainable solar energy has been extensively explored in order to overcome the increasingly serious energy and environmental challenges. Among numerous approaches, chemical utilization of solar energy through photocatalysis has been recognized as one of the most promising methods [1–5]. Since the discovery of water splitting on the surface of titanium dioxide (TiO_2) electrodes under UV light irradiation [6], TiO_2 has been the most widely used photocatalyst in practical applications, including water splitting, water purification, and carbon dioxide conversion, due to its favorable features such as low cost, good chemical and mechanical stability, high photocatalytic activity, and non-toxic nature [7–16]. Three polymorphs of crystalline TiO_2—rutile, anatase, and brookite—occur in nature, of which anatase and rutile are usually employed as photocatalysts, while the photocatalytic activity of brookite has been little investigated. In photocatalysis, anatase TiO_2 is more active than the rutile crystalline form which has been

Address correspondence to yadong.yin@ucr.edu

attributed to its lower charge recombination rate and higher surface adsorption affinity for organic compounds [17–19]. Anatase TiO_2 is thermodynamically metastable and transforms to the rutile phase at high temperature (~600 ˚C).

The harvesting of solar energy by a TiO_2 photocatalyst can be roughly described in three sequential steps: (1) generation of electron–hole (e^-–h^+) pairs upon absorption of photons; (2) charge separation and migration to the catalyst surface; and (3) surface redox reactions. Much effort has been devoted to developing highly active TiO_2-based photocatalysts, with the aim of trying to improve the performance in some of these three steps [20–22]. For example, the main drawback of a pristine anatase TiO_2 photocatalyst is its large band gap energy (~3.2 eV) which allows it to absorb only UV light. As a result, many researchers have focused on developing visible-light-active TiO_2 photocatalysts that can make use of both UV (290–400 nm) and visible (400–700 nm) radiation to enhance process efficiencies. Dye-sensitization has been employed to extend the absorption from the UV range to the visible range. Organic dyes are usually transition metal complexes with low lying excited states, including polypyridine complexes, phthalocyanines, and metalloporphyrins [23–26]. However, the promise of such dye-sensitized TiO_2 materials and devices for practical applications is still under debate because of the instability of organic dyes on light irradiation [27]. Metal-ion doping is another popular method to make visible-light-active TiO_2-based photocatalysts. In many cases, however, these suffer from a serious deterioration in their photocatalytic performance because the metal ions themselves can act as the recombination centers of e^- and h^+ [28–30]. It has been demonstrated recently that doping with non-metals, including N, C, P, and S, can be useful in preparing visible-light-active TiO_2-based photocatalysts, even though an understanding of the origin of the enhanced activity is still controversial [27, 31–34]. On the other hand, the improved absorption of photons may not necessarily guarantee better photocatalytic performance because the efficiency of a photocatalyst is also determined by the charge separation and transportation step during the photoexcitation process. Due to the fast recombination of e^-–h^+ pairs, most excited charges recombine and are quenched before they can reach the surface. From this point of view, small crystal size and high crystallinity are desirable in order to enhance charge separation efficiency. Small crystal size can reduce the migration distance of charges, leading to a lower recombination rate. Another favorable consequence of small crystal size is the large surface area, which may improve the performance in the last step because it can provide more reactive sites. High crystallinity can also reduce the number of defects, which normally act as recombination centers. Since the rise of nanotechnology in the 1990s, great efforts have been made to synthesize semiconductor nanoparticles in order to enhance their specific surface area and, consequently, their catalytic activity. Many methods have been developed to synthesize TiO_2 nanoparticles [35], but further thermal treatment of the TiO_2 nanocrystals is usually needed to improve their crystallinity and photocatalytic activity. Owing to the large surface area and high surface energy of nanocrystals, thermal treatment at high temperatures usually causes ripening or fusion of small nanoparticles and finally leads to larger particles with a reduced surface area, which leads to a deterioration in the overall photocatalytic performance. It is thus of great importance to prepare highly efficient photocatalysts with high crystallinity and large surface area.

Mesoporous structures of TiO_2 represent another type of photocatalyst which promises high efficiency due to their large surface area. However, there are great challenges in preparing mesoporous anatase TiO_2 which possesses both large surface area and high crystallinity. Although it has been possible to produce TiO_2 mesoporous materials with large surface area by carrying out the sol–gel process with surfactant templates, a heat treatment step is usually required to convert the products into a crystalline anatase phase, which causes collapse of mesopores and a marked decrease in the surface area. Typically reported values [36, 37] of Brunauer–Emmett–Teller (BET) surface area for mesoporous TiO_2 materials are around 100 m^2/g, which is much smaller than that of their amorphous counterparts. Additionally, due to the uncontrollable pore collapse during the heat treatment process, it is also difficult to control the pore size distribution, which is important in some catalysis applications.

Recently, we and other groups reported a general strategy for the fabrication of novel porous nanostructured materials based on the self-assembly of nanocrystals [38–40]. We have demonstrated that the as-prepared mesoporous nanocrystal clusters can be used for selective enrichment of peptides and proteins from complex biological samples [40–42]. From the perspective of photocatalysis, there are also several attractive features of these materials, including clean surfaces, high crystallinity, small grain size, and large surface area even after high temperature treatment, good water dispersity, and a pore size distribution which is controllable by simply tuning the initial nanocrystal size and shape. Herein, we report their use as highly efficient and stable photocatalysts by taking advantage of this unique combination of features. Hydrophobic anatase TiO_2 nanocrystals were synthesized through a nonhydrolytic solution-based reaction. An emulsion-based bottom-up assembly approach was then used to self-assemble the colloidal nanocrystals into densely packed clusters by evaporating the low-boiling-point oil phase. After coating with a shell of silica, the as-obtained clusters were calcined at high temperature to improve their crystallinity and remove the organic ligands. Subsequent etching of the SiO_2 shell by an alkaline solution can remove the outer silica layer and give the TiO_2 cluster a hydrophilic surface, which allows better water accessibility to the pores. As a result of the calcination process, the mesoporous TiO_2 cluster retains its porous structure after the etching step. By optimizing the synthesis conditions, principally the calcination temperature, TiO_2 clusters with good photocatalytic activity have been obtained. It is believed that the enhanced photocatalytic performance comes from the unique cluster structure and the post-treatment steps of silica coating and etching, which results in small grains of TiO_2 clusters (~5 nm), large surface area, and hydrophilic surfaces. An N-doping process was also carried out in order to make the clusters catalytically active under irradiation by visible light. The catalytic activities of the mesoporous photocatalysts for the degradation of organic pollutants under UV, visible light, and direct sunlight were investigated using rhodamine B (RhB) as a model compound.

2. Experimental

2.1 Chemicals

Trioctylphosphine oxide (TOPO), sodium dodecyl sulfate (SDS), ammonium hydroxide solution (NH_4OH, ~28% NH_3 in water), tetraethylorthosilicate (TEOS, 98%), and rhodamine B (RhB, 99%) were purchased from Aldrich Chemical Co. Tetrabutylorthotitanate (TBOT) and titanium tetrachloride ($TiCl_4$) were obtained from Fluka. Ethanol (denatured), toluene, sodium hydroxide, cyclohexane, and acetone were obtained from Fisher Scientific.

2.2 Synthesis of TiO_2 nanocrystals

TiO_2 nanocrystals were prepared by a nonhydrolytic solution-based reaction [43]. Typically, TOPO (5 g) was heated at 150 ℃ for 5 min in vacuum to remove any low boiling point materials. After increasing the temperature to 200 ℃ under N_2 atmosphere, TBOT (1.4 mL) was injected into the hot liquid. The resulting mixture was then heated to 320 ℃, followed by a rapid addition of 0.55 mL of $TiCl_4$. The solution was kept at 320 ℃ for 20 min to ensure complete reaction. After cooling to 80 ℃, 10 mL of acetone was added to yield a white precipitate, which was isolated by centrifugation and subsequently washed with a toluene/acetone mixture to remove excess TOPO. The resulting powder was re-dispersed in 10 mL of cyclohexane.

2.3 Self-assembly of nanocrystals into clusters

The clusters were formed by assembling the nanocrystals in emulsion oil droplets and subsequent evaporation of the low-boiling-point solvent (the oil phase). In a typical process, 1 mL of a cyclohexane solution of nanocrystals was mixed with an aqueous solution of sodium dodecyl sulfate (SDS) (56 mg in 10 mL H_2O) under sonication for 5 min. The mixture was then heated at 70–72 ℃ in a water bath for 4 h. A clear nanoparticle solution was obtained by evaporating the cyclohexane. The reaction solution was cooled to room temperature and the final product was washed three times with water and re-dispersed in 3 mL of distilled water.

2.4 Surface modification of the clusters

TiO_2 nanocrystal clusters were coated with a layer of SiO_2 by using a modified Stöber process [44]. Typically, the above aqueous solution of TiO_2 clusters (3 mL) was first mixed with ethanol (20 mL) and ammonium hydroxide (1 mL, 28% aqueous solution). Then TEOS (0.1 mL) was injected into the solution and reacted for 20 min under vigorous stirring. The core/shell colloids were collected by centrifugation and washed three times with ethanol. After drying under vacuum overnight, the precipitate was heated to the desired temperature at a rate of 1 ˚C /min and heated for 1 h in air to remove the organic species. In the cases where N-doping was needed, the TiO_2@SiO_2 core–shell particles were heated under a NH_3/Ar flow in a Lindberg/Blue M tube furnace to the desired temperature at a rate of 1 ˚C/min and heated for another hour to ensure the successful nitrogen doping and removal of organic species. The calcined particles were then dispersed in aqueous NaOH solution (5 mL, 0.5 mol/L) for 3–4 h with stirring, in order to dissolve the silica shell. The particles were collected by centrifugation and washed three times with distilled water.

2.5 Characterization

A Tecnai T12 transmission electron microscope (TEM) was used to characterize the morphology of the colloids in each step. Samples dispersed in ethanol at an appropriate concentration were cast onto a carbon-coated copper grid, followed by evaporation under vacuum at room temperature. The crystal structures of the samples were evaluated by X–ray diffraction (XRD), carried out on a Bruker D8 Advance diffractometer with Cu $K\alpha$ radiation (λ = 1.5418 Å). The surface area and porosity of the products were estimated by measuring the nitrogen adsorption–desorption isotherms on a Micromeritics ASAP 2020M Accelerated Surface Area and Porosimetry System. UV/Vis diffuse reflectance spectra were measured on a Shimadzu UV 3101PC double-beam, double-monochromator spectrophotometer. $BaSO_4$ powder was used as a reference (100% reflectance). A probe-type Ocean Optics HR2000CG-UV-NIR spectrometer was used to measure the UV–Vis absorption spectra of solutions in order to monitor the concentration of RhB at different time intervals. A three-electrode system (VersaSTAT 4, Princeton Applied Research) was utilized to characterize the electrochemical properties of the photocatalysts by using Ag/AgCl as the reference electrode, Pt wire as the counter electrode, and TiO_2 catalysts deposited on a 1-cm^2 ITO glass as the working electrode. An aqueous solution of RhB and Na_2SO_4 was used as the electrolyte.

2.6 Photocatalytic activity measurements

Photocatalytic degradation of RhB was carried out in a 100-mL beaker, containing 50 mL of reaction slurry agitated by magnetic stirring (650 r/min). The as-obtained TiO_2 clusters were first irradiated by UV light for 1 h to completely remove any residual organic ligands, followed by drying in an oven at 60 ˚C for 2 h. The aqueous slurry, prepared with different catalysts and 1.0×10^{-5} mol/L RhB was stirred in the dark for 30 min to ensure that the RhB was adsorbed to saturation on the catalysts. For the UV irradiation experiment, a 15 W UV lamp (254 nm, XX-15G, USA), 6 cm above the reaction slurry, was used as UV radiation source. The average light intensity striking the surface of the reaction solution was ~1.55 $mW \cdot cm^{-2}$. The concentration of titania was 200 mg/L for all the runs. For the visible light irradiation experiment, a 150 W tungsten lamp was used as the light source, and a cutoff filter was used to block the UV light (< 400 nm). The reaction flask was placed in a cooling water system to keep the reaction system at room temperature. To explore the photocatalytic performance in sunlight, the reaction flask was exposed directly to natural sunshine.

3. Results and discussion

The synthesis of TiO_2 nanocrystals involves a solution phase nonhydrolytic reaction between the two precursors TBOT and $TiCl_4$, with TOPO as both the solvent and surfactant [43]. The particle size as well as the morphology of the as-prepared TiO_2 nanocrystals can be simply tuned by varying the concentration of reactants and surfactants. Figure 1(a) shows a TEM image of a typical sample of TiO_2 nanocrystals

with an average diameter of 5 nm. The hydrophobic nanocrystals were dissolved in cyclohexane and then dispersed in water to form an oil-in-water emulsion with SDS acting as the surfactant. Upon evaporation of the low-boiling-point solvent (cyclohexane in this case), the nanocrystals confined in the oil droplets self-assembled into microspheres, with the size being controllable by adjusting the nanocrystal concentration or the extent of ultrasonication during emulsification (Fig. 1(b)). Generally, the lower the concentration of TiO_2 nanocrystals and the longer the sonication time, the smaller the size of the as-obtained TiO_2 clusters. The inset in Fig. 1(b) shows an enlarged TEM image of a single cluster, from which one can clearly appreciate the porous nature of the structure. The clusters were then successfully coated with a silica layer by a modified sol–gel process, as confirmed by the TEM image shown in Fig. 1(c). The thickness of the coated silica layer can be easily controlled by adjusting the amount of TEOS. Calcination of the resulting TiO_2/SiO_2 core–shell structure in air removes the organic ligands and improves the crystallinity as well as the mechanical stability. Finally, the silica layer was etched away to re-expose TiO_2 clusters by using a dilute solution of NaOH. The clusters retained their spherical shape and porous nature after the calcination and etching treatments (Fig. 1(d)), suggesting they have the good mechanical stability required for photocatalytic applications.

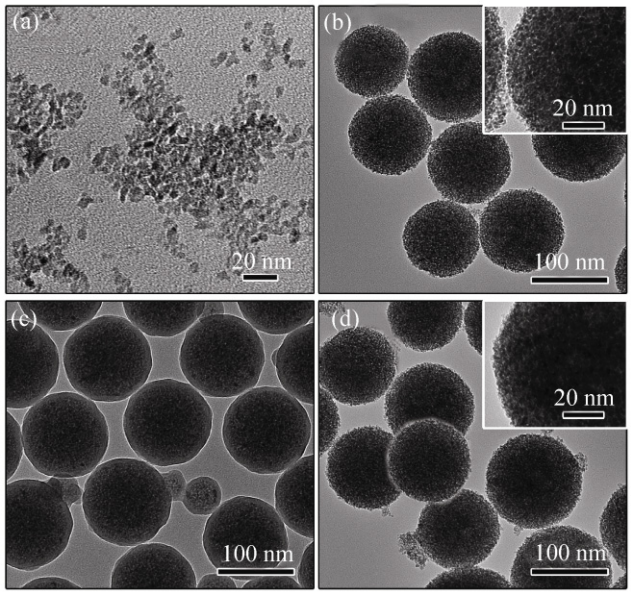

Figure 1 TEM images showing the preparation process of TiO_2 nanocrystal clusters: (a) TiO_2 nanocrystals; (b) self-assembled TiO_2 nanocrystal clusters; (c) SiO_2-coated TiO_2 clusters; (d) TiO_2 clusters after calcination of (c) at 400 ˚C for 1 h and subsequent removal of the SiO_2 shell by etching in NaOH. The insets in (b) and (d) are higher magnification images of the nanocrystal clusters

The crystallographic phases of the as-prepared catalysts were studied by recording their XRD patterns. As shown in Fig. 2, all the reflection peaks of the TiO_2 clusters can be indexed as a pure anatase structure with cell parameters $a = b = 3.78$ Å, $c = 9.51$ Å, in good agreement with the literature value (JCPDS card No. 21-1272). The peaks are all broad, indicating that the clusters are composed of small nanocrystals, which is consistent with the TEM observations. For all the samples, calcination at higher temperatures did not change the crystallographic phase of the as-prepared clusters, while the grain size of the clusters increased slightly during the calcination process. The Scherrer formula was used to estimate the average grain sizes of the TiO_2 clusters

$$D = \frac{0.89\lambda}{\beta \cos\theta} \quad (1)$$

where D is the diameter of the grains, λ the X-ray wavelength in nanometers ($\lambda = 0.15418$ nm in this case), β the width of the XRD peak at the half-peak height in radians, and θ the angle between the incident and diffracted beams in degrees. Figure 2(a) shows the XRD patterns of TiO_2 clusters after silica coating, calcination at different temperatures, and then silica etching. The grain size of the TiO_2 nanocrystals gradually increased from the initial value of 4.8 nm to about 5.5 nm for the sample calcined at 500 ˚C for 1 h. In contrast, as shown in Fig. 2(b), the TiO_2 nanocrystal clusters without silica protection underwent an increase in grain size to 6.9 nm at 400 ˚C and 8.4 nm at 500 ˚C, clearly suggesting that the silica shell has a protecting effect. The limited size increase of the nanocrystals in silica-protected clusters during calcination favors the retention of the anatase phase even after high-temperature treatment, as the grain size is still well below the critical value of 14 nm at which the anatase phase transforms to the rutile phase [45, 46].

As the surface-to-volume ratio of catalysts has a critical effect on their overall catalytic efficiency, the

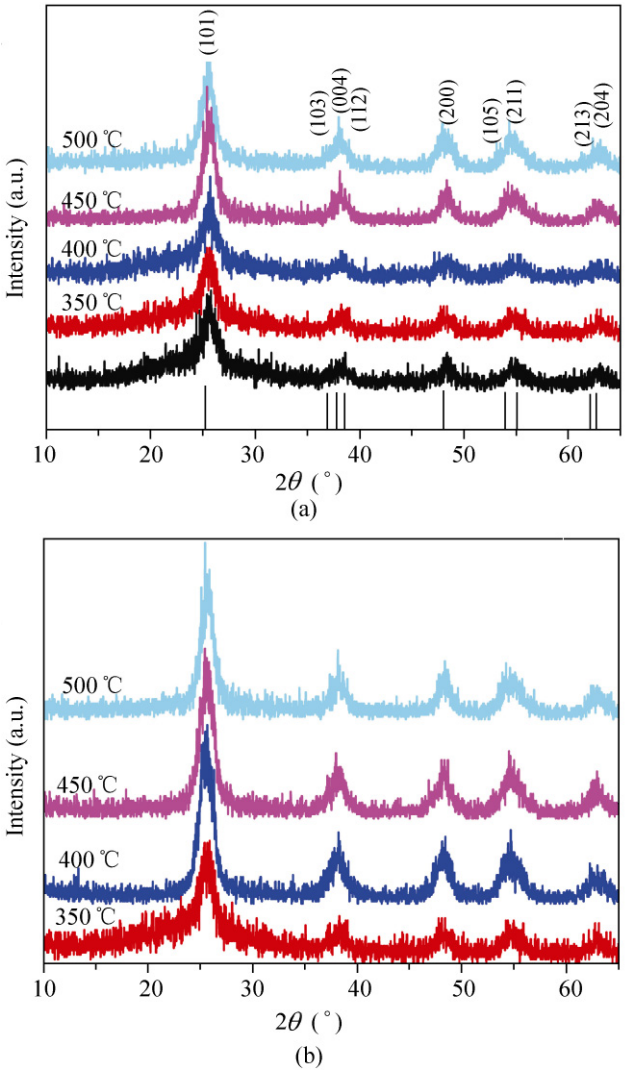

Figure 2 (a) XRD patterns of self-assembled TiO_2 clusters after calcination at different temperatures: 350 ˚C (TC350), 400 ˚C (TC400), 450 ˚C (TC450), and 500 ˚C (TC500). The black curve is for a sample prepared without calcination. All samples were prepared by sequential steps of self-assembly in emulsion droplets, silica coating, calcination, and silica etching. (b) XRD patterns of self-assembled TiO_2 clusters without silica protection after calcination at different temperatures

surface area, and porosity of the TiO_2 clusters after calcination at different temperatures were investigated by measuring their nitrogen adsorption–desorption isotherms. Figure 3(a) shows the nitrogen adsorption–desorption isotherms and the corresponding pore size distribution of the TiO_2 clusters calcined at 400 ˚C (TC400). The average pore diameter, as determined by using the Barrett–Joyner–Halenda (BJH) method on the desorption branch of the isotherm (inset of Fig. 3), increases slightly from 2.1 nm to 2.3 nm, and 2.4 nm after calcination at 350, 400, and 500 ˚C. The BET surface areas also decreased slightly with increasing calcination temperature, from 277 m^2/g for the sample treated at 350 ˚C to 268 m^2/g at 400 ˚C, and 253 m^2/g at 500 ˚C. Both changes can be ascribed to the gradual increase in grain size during calcination. We note that silica coating can help to maintain the mesoporous structure and therefore the large surface area of the clusters. As shown in Fig. 3(b), although the clusters without the silica coating still retained their mesoporous structure after calcination at 400 ˚C for 1 h, their surface area decreased markedly to 137 m^2/g, which is consistent with the significant grain growth of the unprotected samples during calcination.

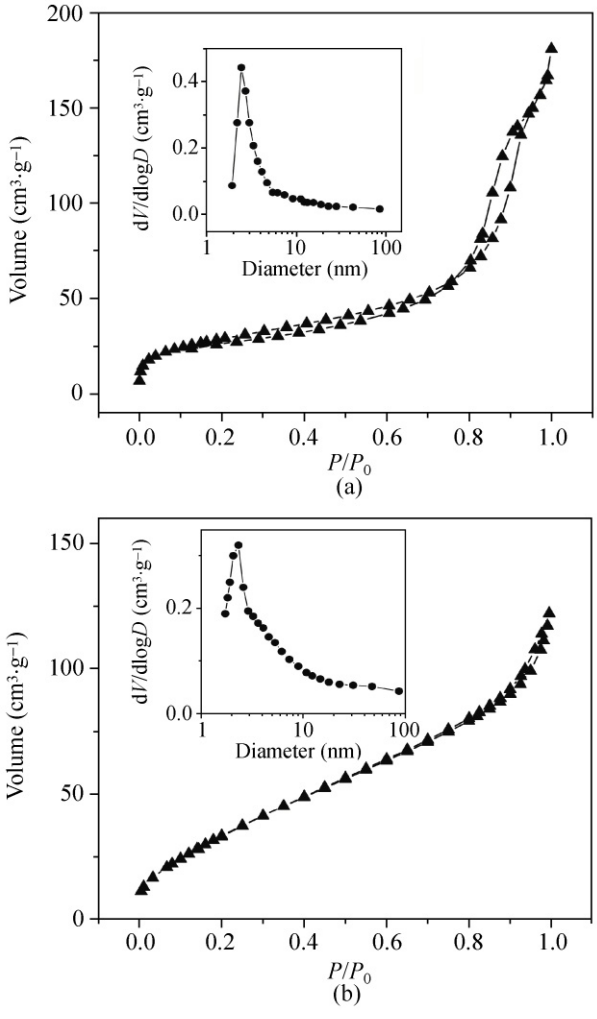

Figure 3 Nitrogen adsorption–desorption isotherms of TiO_2 clusters after calcination at 400 ˚C: (a) a layer of silica was coated on the clusters before calcination, and removed afterwards; (b) clusters were calcined without the silica treatment. The insets show the BJH pore size distribution of the corresponding samples

Electrochemical characterization was carried out to investigate the potential for use of the TiO_2 nanocrystal clusters in photocatalysis. Electrochemical impedance spectroscopy (EIS) was performed to characterize electrochemical interfacial reactions, in which the photocatalytic decomposition of RhB was used as the model reaction. A three-electrode system was utilized to measure the EIS spectrum by using Ag/AgCl as the reference electrode, Pt wire as the counter electrode, and TiO_2 catalyst deposited on ITO glass as the working electrode. An aqueous solution of RhB and Na_2SO_4 was used as the electrolyte. Figure 4(a) shows the EIS Nyquist plots under UV irradiation for AEROXIDE® P25 TiO_2 and the TiO_2 clusters calcined at different temperatures. It is well accepted that a smaller arc radius of an EIS Nyquist plot implies a higher efficiency of charge separation. Of the five samples, P25 TiO_2, and TC400 show the smallest arc radii, suggesting they have the highest charge separation efficiency. The relative charge separation efficiency increases in the order TC350 < TC500 < TC450 < TC400 ≈ P25.

Chronoamperometry (CA) experiments were used to characterize the photogenerated current density under a potential of 0.8 V and a periodic illumination of UV light. The photogenerated current density is usually regarded as equivalent to photocatalytic activity. As shown in Fig. 4(b), each of the five samples shows a photogenerated current, indicating their active response to UV irradiation. The shape of the CA curves was maintained after many cycles of light illumination, implying good photocatalytic stability. The current densities are consistent with the EIS measurements, with TC400 showing the highest value (~1.5 μA/cm^2).

The catalytic activity of the photocatalysts was evaluated by measuring degradation rates of RhB under irradiation by different light sources. Figure 5(a) shows typical absorption spectra of an aqueous solution of RhB exposed to UV light for various time periods using TC400 as the catalyst. The strong absorption peak at 553 nm gradually diminished in intensity as the UV irradiation was prolonged, and completely disappeared after 30 min, suggesting the complete photodegradation of the organic dye. The changes in RhB concentration (C) over the course of

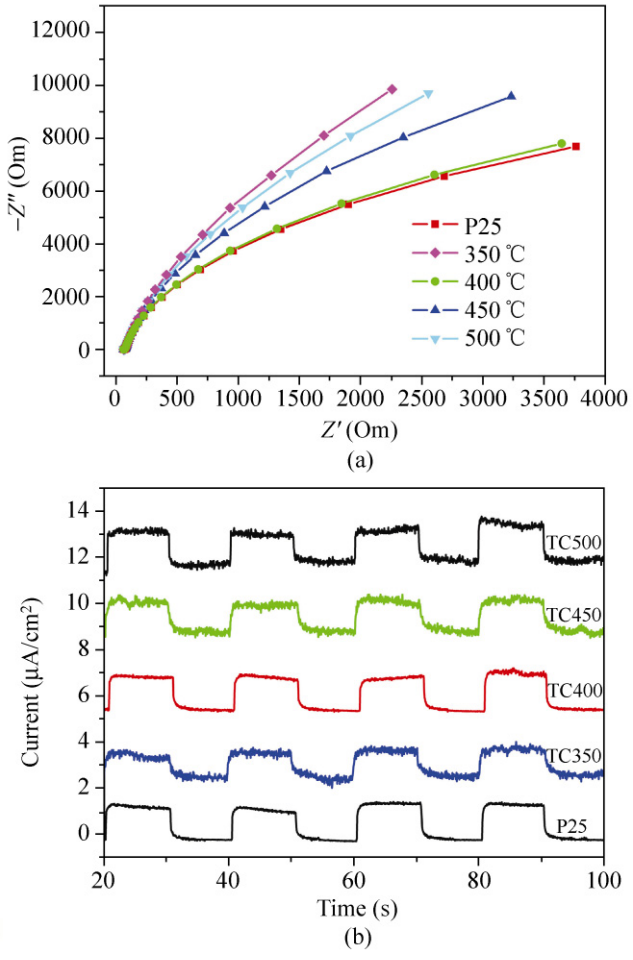

Figure 4 (a) Nyquist plots for P25 and TiO_2 clusters calcined at different temperatures in an aqueous solution of RhB under UV light illumination. Symbols and lines indicate the experimental data and fitted curves, respectively. (b) Chronoamperometry study of P25 and TiO_2 clusters calcined at different temperatures

photocatalytic degradation reactions using different photocatalysts subjected to the silica coating/removal process are summarized in Fig. 5(b). The photocatalysts were first illuminated by UV light for 1 h to rule out the influence of any organic residues in the cluster. To compare the photocatalytic activities, the total amount of TiO_2 was kept the same. Before illuminating the mixture it was stirred in the dark for 30 min to ensure that the RhB was adsorbed to saturation on the catalysts. The adsorption of RhB decreased for TiO_2 clusters treated at higher temperatures, while P25 showed the lowest adsorption due to its smallest surface area (~50 m^2/g). This is consistent with the BET measurements, which showed the surface area decreasing with increasing calcination temperatures.

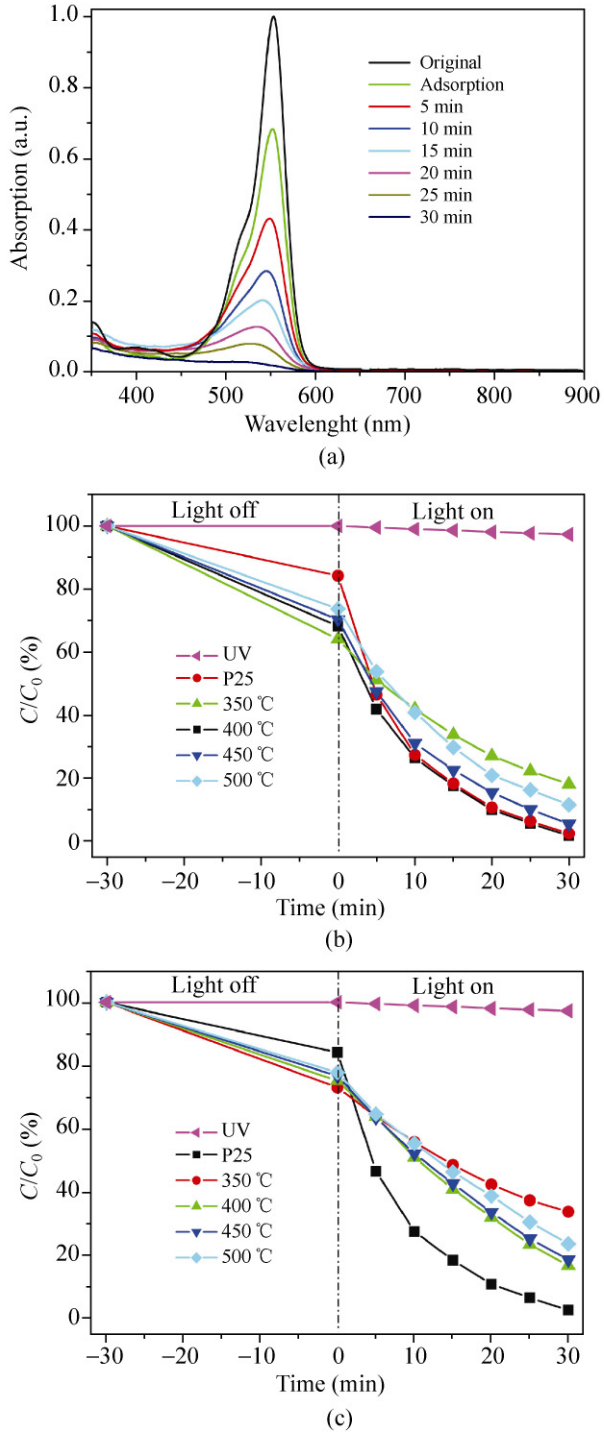

Figure 5 (a) UV absorption spectra showing the gradual decomposition of RhB under 254-nm UV irradiation in the presence of TiO_2 porous catalysts (calcined at 400 ℃). Photocatalytic conversion of RhB under UV irradiation by using TiO_2 clusters calcined at different temperatures and P25 as the photocatalysts: (b) the TiO_2 clusters were coated with a layer of silica before calcination, which was removed afterwards; (c) the clusters were calcined without silica treatment

However, the photocatalytic activity did not follow this simple trend. Although it showed the highest adsorption, the photocatalytic activity of TC350 was the lowest, probably due to its relatively low crystallinity. TC400 gave the highest photocatalytic activity, equivalent to that of P25, while TC450 showed similar activity to TC400 under UV irradiation in spite of its lower adsorption ability. Calcination at higher temperature resulted in reduced efficiency, as evidenced by the performance of TC500. Generally, higher photocatalytic activity is favored by larger surface area and the higher crystallinity of a catalyst. As pointed out above, higher calcination temperature leads to an improvement in the crystallinity by removing defects in the nanocrystals, but it also leads to a smaller surface area. It is apparent that calcination at an intermediate temperature of 400 ℃ is optimal for preparing mesoporous TiO_2 clusters with large surface area and relatively high crystallinity. The overall photocatalytic performance of the TiO_2 clusters is consistent with the results of electrochemical measurements.

We also studied the effect of the silica coating/removal process on the catalytic performance of the TiO_2 nanocrystal clusters. Compared to the samples treated with silica, clusters without silica protection during calcination showed much lower adsorption of RhB, as shown in Fig. 5(c). During the initial adsorption process, ~30% of RhB was adsorbed by the silica-treated clusters, while only 20% of RhB could be adsorbed by the untreated clusters. We have pointed out previously that the silica coating and etching processes enhances the surface charge and water dispersity of such clusters [40], which is confirmed by these experiments. Without the silica coating/removing treatment, the calcined TiO_2 clusters are in the form of large aggregates and cannot be well dispersed in water even after 10 min of sonication, while the silica-treated clusters can be well dispersed in water. Furthermore, as discussed above, the silica coating can help to maintain the mesoporous structure and therefore the large surface area of the clusters, which also favors a higher photocatalytic activity.

The porous structure of the TiO_2 nanocrystal clusters allows convenient nitrogen doping under NH_3/Ar gas flow. After reaction at the desired temperature, the

white powder became yellowish, suggesting successful nitrogen doping, which was further confirmed by measuring the diffuse reflectance UV–Vis spectra. Figure 6 shows the UV–Vis spectra of three samples: P25, and TiO_2 clusters before and after N-doping (NTC400). Compared with P25 and the undoped TiO_2 clusters that absorb only UV light, a noticeable shift of the absorption edge to the visible region was observed for the N-doped sample. To quantitatively study the influence of the N-doping process, the band gap energy change was calculated. As TiO_2 is a crystalline indirect transition semiconductor, the band gap energy of undoped and N-doped TiO_2 clusters can be estimated from the following equation

$$\alpha h\nu = A(h\nu - Eg)^{\gamma} \quad (2)$$

where α is the absorption coefficient, $h\nu$ is the energy of the incident photon, A is a constant, Eg is the optical energy gap of the material, and γ is a characteristic of the optical transition process which depends on whether the transition is symmetry allowed or not [47, 48]. The calculations show that the N-doping process does only red-shift the absorption edge, as evidenced by the second gap at 2.85 eV, but also reduces the main band edge from 3.2 eV to about 3.05 eV.

The successful N-doping process was also confirmed by the active response of the material under visible light irradiation. The degradation of RhB under visible light illumination was used as a model system to study the catalytic performance of the catalysts, as shown in Fig. 7(a). Upon illumination by visible light ($\lambda > 400$ nm) for 5 h, there was almost no change in the concentration of RhB if no catalyst was present, ruling out any possible sensitization process of RhB under visible light irradiation. The calcination temperature showed a significant influence on the photocatalytic activity, which is in good agreement with the results of irradiation by UV light. Due to the presence of rutile titania that can absorb visible light, the conversion of RhB using P25 as the catalyst was about 40% with an irradiation period of 5 h. Consistent with the data for the undoped samples, NTC400 showed the highest efficiency of all the calcined samples under the same conditions due to its optimal crystallinity and surface area: ~50% of the RhB was removed in the same period.

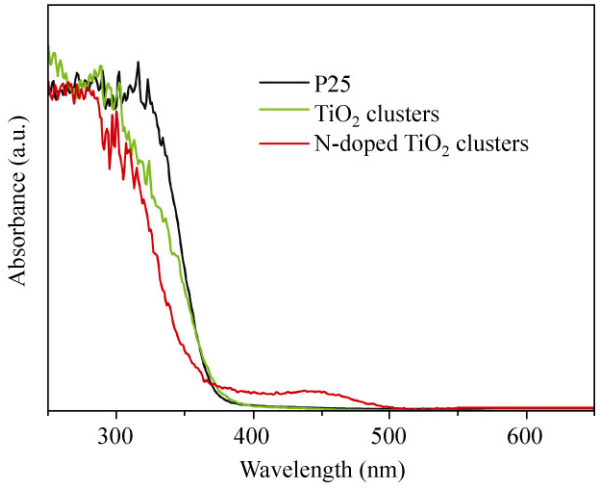

Figure 6 UV–Vis diffuse reflectance absorption spectra of P25, TiO_2 clusters (TC400), and N-doped TiO_2 clusters (calcined at 400 ˚C, denoted NTC400)

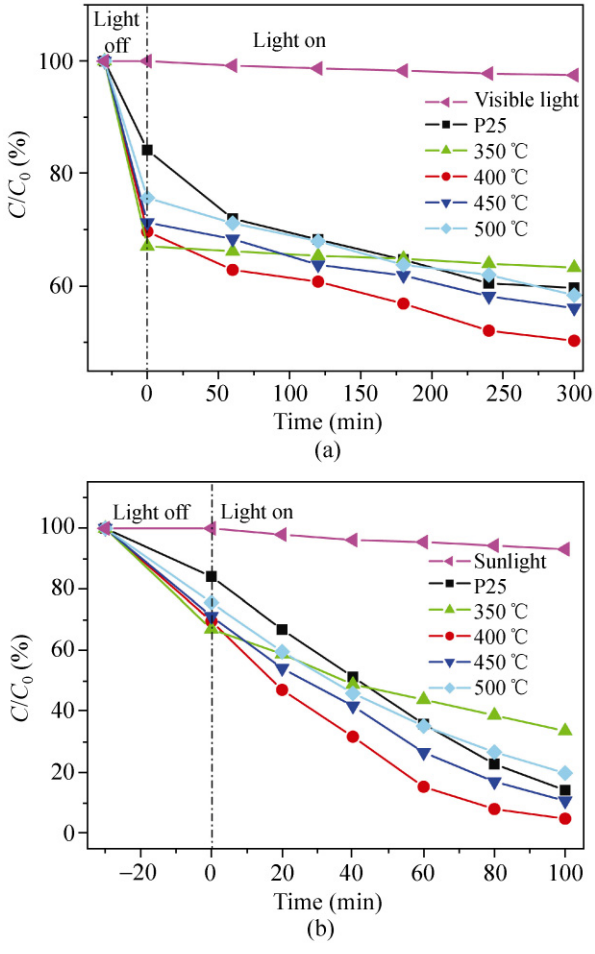

Figure 7 Photocatalytic conversion of RhB under (a) visible light irradiation ($\lambda > 400$ nm) and (b) illumination by direct sunlight using no catalyst, P25, and N-doped TiO_2 clusters calcined at different temperatures as the photocatalysts

To explore the photocatalytic activity of the as-prepared products for real applications in the photodegradation of organic pollutants, the photodegradation of RhB was also investigated under natural sunlight. As shown in Fig. 7(b), no sensitization of RhB was observed on illumination by sunlight. Commercial P25 showed higher activity compared to that under irradiation by pure visible light due to the contribution of the UV component in sunlight. With the aid of the cluster-structured photocatalysts, the sunlight can efficiently decompose RhB. As shown in Fig. 7(b), when using NTC400 as the photocatalyst, decomposition of RhB was complete within 100 min—much shorter than the time required under illumination by visible light. Consistent with the previous results for both UV and visible irradiation, NTC350 showed the lowest activity, while NTC450 and NTC500 showed lower activities than NTC400, which had the maximum activity.

As recyclability is very important for a catalyst, we also demonstrated that the cluster-structured photocatalysts can be recovered and reused to catalyze degradation under direct sunlight. Photocatalysis was performed in an aqueous solution over many cycles by repeatedly adding RhB and irradiating with natural sunlight. To ensure that RhB was completely removed and had no influence on the next cycle, further direct sunlight irradiation for 1 h was conducted after each cycle was complete. Centrifugation was used to recover the photocatalyst from the aqueous solution. As shown in Fig. 8, the catalyst did not exhibit any significant loss of photocatalytic activity after seven cycles. The slight differences in the extent of decomposition of RhB in different cycles might be caused by variations in the intensity of the sunlight.

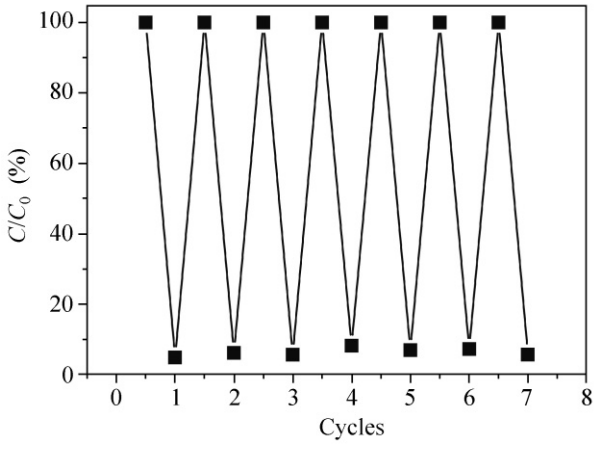

Figure 8 Seven cycles of photocatalytic degradation of RhB in the presence of NTC400 clusters under direct irradiation by sunlight

4. Conclusion

We have demonstrated the preparation of mesoporous anatase TiO_2 nanocrystal clusters with large surface area and enhanced photocatalytic activity. The synthesis involves the self-assembly of hydrophobic TiO_2 nanocrystals into submicron clusters in emulsion droplets, coating of these clusters with a silica layer, thermal treatment at high temperatures to remove the organic ligands and improve the crystallinity of clusters, and finally etching of the silica to reveal the mesoporous catalyst. The initial silica coating helps the clusters maintain their small grain size and high surface area after calcination at high temperatures, while the eventual removal of the silica gives the clusters high dispersibility in water. TiO_2 nanocrystal clusters with an optimal balance of high crystallinity and large surface area can be produced at a calcination temperature of 400 °C, which ensures an enhanced photocatalytic activity as demonstrated by the high charge separation efficiency in electrochemical measurements, and the efficient decomposition of an organic dye under illumination by UV light. The porous structure of the TiO_2 nanocrystal clusters also allows convenient nitrogen doping, which promotes the photocatalytic performance in visible light and natural sunlight. We believe that organizing nanocrystals into mesoporous clusters represents a versatile and useful strategy for designing photocatalysts with enhanced activity and stability.

Acknowledgements

Y. Y. thanks the University of California, Riverside, 3M Company, and the Donors of the Petroleum Research Fund, administered by the American Chemical Society, for support of this research. Financial support of this work was also provided by Basic Energy Sciences–U.S. Department of Energy and the National Science Foundation. Y. Y. is a Cottrell Scholar of the Research Corporation for Science Advancement. We thank Dr. Jimin Shen in Harbin

Institute of Technology (China) for BET measurements. J. B. J. was partially supported by a National Research Foundation of Korea Grant funded by the Korean Government (No. NRF-2009-352-D00056).

References

[1] Fox, M. A.; Dulay, M. T. Heterogeneous photocatalysis. *Chem. Rev.* **1993**, *93*, 341–357.

[2] Kamat, P. V. Photochemistry on nonreactive and reactive (semiconductor) surfaces. *Chem. Rev.* **1993**, *93*, 267–300.

[3] Legrini, O.; Oliveros, E.; Braun, A. M. Photochemical processes for water-treatment. *Chem. Rev.* **1993**, *93*, 671–698.

[4] Kudo, A.; Miseki, Y. Heterogeneous photocatalyst materials for water splitting. *Chem. Soc. Rev.* **2009**, *38*, 253–278.

[5] An, C. H.; Peng, S. N.; Sun, Y. G. Facile synthesis of sunlight-driven AgCl:Ag plasmonic nanophotocatalyst. *Adv. Mater.* **2010**, *22*, 2570–2574.

[6] Fujishima, A.; Honda, K. Electrochemical photolysis of water at a semiconductor electrode. *Nature* **1972**, *238*, 37–38.

[7] Kormann, C.; Bahnemann, D. W.; Hoffmann, M. R. Photolysis of chloroform and other organic-molecules in aqueous TiO_2 suspensions. *Environ. Sci. Tech.* **1991**, *25*, 494–500.

[8] Prairie, M. R.; Evans, L. R.; Stange, B. M.; Martinez, S. L. An investigation of TiO_2 photocatalysis for the treatment of water contaminated with metals and organic-chemicals. *Environ. Sci. Tech.* **1993**, *27*, 1776–1782.

[9] Linsebigler, A. L.; Lu, G. Q.; Yates, J. T. Photocatalysis on TiO_2 surfaces—principles, mechanisms, and selected results. *Chem. Rev.* **1995**, *95*, 735–758.

[10] Hoffmann, M. R.; Martin, S. T.; Choi, W. Y.; Bahnemann, D. W. Environmental applications of semiconductor photocatalysis. *Chem. Rev.* **1995**, *95*, 69–96.

[11] Herrmann, J. M. Heterogeneous photocatalysis: Fundamentals and applications to the removal of various types of aqueous pollutants. *Catal. Today* **1999**, *53*, 115–129.

[12] Tan, S. S.; Zou, L.; Hu, E. Photocatalytic reduction of carbon dioxide into gaseous hydrocarbon using TiO_2 pellets. *Catal. Today* **2006**, *115*, 269–273.

[13] Li, H. X.; Bian, Z. F.; Zhu, J.; Zhang, D. Q.; Li, G. S.; Huo, Y. N.; Li, H.; Lu, Y. F. Mesoporous titania spheres with tunable chamber structure and enhanced photocatalytic activity. *J. Am. Chem. Soc.* **2007**, *129*, 8406–8407.

[14] Chen, X. B. Titanium dioxide nanomaterials and their energy applications. *Chin. J. Catal.* **2009**, *30*, 839–851.

[15] Chen, S. F.; Li, J. P.; Qian, K.; Xu, W. P.; Lu, Y.; Huang, W. X.; Yu, S. H. Large scale photochemical synthesis of M@TiO_2 nanocomposites (M = Ag, Pd, Au, Pt) and their optical properties, CO oxidation performance, and antibacterial effect. *Nano Res.* **2010**, *3*, 244–255.

[16] Ye, M.; Zhang, Q.; Hu, Y.; Ge, J.; Lu, Z.; He, L.; Chen, Z.; Yin, Y. Magnetically recoverable core–shell nanocomposites with enhanced photocatalytic activity. *Chem. Eur. J.* **2010**, *16*, 6243–6250.

[17] Stafford, U.; Gray, K. A.; Kamat, P. V.; Varma, A. An *in situ* diffuse reflectance FTIR investigation of photocatalytic degradation of 4-chlorophenol on a TiO_2 powder surface. *Chem. Phys. Lett.* **1993**, *205*, 55–61.

[18] Riegel, G.; Bolton, J. R. Photocatalytic efficiency variability in TiO_2 particles. *J. Phys. Chem.* **1995**, *99*, 4215–4224.

[19] Hurum, D. C.; Agrios, A. G.; Gray, K. A.; Rajh, T.; Thurnauer, M. C. Explaining the enhanced photocatalytic activity of Degussa P25 mixed-phase TiO_2 using EPR. *J. Phys. Chem. B* **2003**, *107*, 4545–4549.

[20] Zhang, Z. Y.; Zuo, F.; Feng, P. Y. Hard template synthesis of crystalline mesoporous anatase TiO_2 for photocatalytic hydrogen evolution. *J. Mater. Chem.* **2010**, *20*, 2206–2212.

[21] Zhang, L. W.; Fu, H. B.; Zhu, Y. F. Efficient TiO_2 photocatalysts from surface hybridization of TiO_2 particles with graphite-like carbon. *Adv. Funct. Mater.* **2008**, *18*, 2180–2189.

[22] Yun, H. J.; Lee, H.; Joo, J. B.; Kim, W.; Yi, J. Influence of aspect ratio of TiO_2 nanorods on the photocatalytic decomposition of formic acid. *J. Phys. Chem. C* **2009**, *113*, 3050–3055.

[23] Ferrere, S.; Gregg, B. A. Photosensitization of TiO_2 by $[Fe^{II}(2,2'\text{-bipyridine-}4,4'\text{-dicarboxylic acid})_2(CN)_2]$: Band selective electron injection from ultra-short-lived excited states. *J. Am. Chem. Soc.* **1998**, *120*, 843–844.

[24] Adachi, M.; Murata, Y.; Takao, J.; Jiu, J. T.; Sakamoto, M.; Wang, F. M. Highly efficient dye-sensitized solar cells with a titania thin-film electrode composed of a network structure of single-crystal-like TiO_2 nanowires made by the "oriented attachment" mechanism. *J. Am. Chem. Soc.* **2004**, *126*, 14943–14949.

[25] Argazzi, R.; Bignozzi, C. A.; Yang, M.; Hasselmann, G. M.; Meyer, G. J. Solvatochromic dye sensitized nanocrystalline solar cells. *Nano Lett.* **2002**, *2*, 625–628.

[26] Granados-Oliveros, G.; Paez-Mozo, E. A.; Ortega, F. M.; Ferronato, C.; Chovelon, J. M. Degradation of atrazine using metalloporphyrins supported on TiO_2 under visible light irradiation. *Appl. Catal. B* **2009**, *89*, 448–454.

[27] Emeline, A. V.; Kuznetsov, V. N.; Rybchuk, V. K.; Serpone, N. Visible-light-active titania photocatalysts: The case of N-doped TiO_2s—properties and some fundamental issues. *Int. J. Photoenergy* **2008**, Article ID 258394.

[28] Anpo, M.; Takeuchi, M. The design and development of highly reactive titanium oxide photocatalysts operating under visible light irradiation. *J. Catal.* **2003**, *216*, 505–516.

[29] Choi, W. Y.; Termin, A.; Hoffmann, M. R. The role of metal-ion dopants in quantum-sized TiO_2—correlation between photoreactivity and charge-carrier recombination dynamics. *J. Phys. Chem.* **1994**, *98*, 13669–13679.

[30] Li, F. B.; Li, X. Z.; Hou, M. F. Photocatalytic degradation of 2-mercaptobenzothiazole in aqueous La^{3+}–TiO_2 suspension for odor control. *Appl. Catal. B* **2004**, *48*, 185–194.

[31] Sato, S. Photocatalytic activity of NO_x-doped TiO_2 in the visible light region. *Chem. Phys. Lett.* **1986**, *123*, 126–128.

[32] Asahi, R.; Morikawa, T.; Ohwaki, T.; Aoki, K.; Taga, Y. Visible-light photocatalysis in nitrogen-doped titanium oxides. *Science* **2001**, *293*, 269–271.

[33] Sakthivel, S.; Kisch, H. Daylight photocatalysis by carbon-modified titanium dioxide. *Angew. Chem. Int. Ed.* **2003**, *42*, 4908–4911.

[34] Khan, S. U. M.; Al-Shahry, M.; Ingler, W. B. Efficient photochemical water splitting by a chemically modified *n*-TiO_2. *Science* **2002**, *297*, 2243–2245.

[35] Chen, X.; Mao, S. S. Titanium dioxide nanomaterials: Synthesis, properties, modifications, and applications. *Chem. Rev.* **2007**, *107*, 2891–2959.

[36] Chen, D. H.; Huang, F. Z.; Cheng, Y. B.; Caruso, R. A. Mesoporous anatase TiO_2 beads with high surface areas and controllable pore sizes: A superior candidate for high-performance dye-sensitized solar cells. *Adv. Mater.* **2009**, *21*, 2206–2210.

[37] Kim, Y. J.; Lee, M. H.; Kim, H. J.; Lim, G.; Choi, Y. S.; Park, N. G.; Kim, K.; Lee, W. I. Formation of highly efficient dye-sensitized solar cells by hierarchical pore generation with nanoporous TiO_2 spheres. *Adv. Mater.* **2009**, *21*, 3668–3673.

[38] Bai, F.; Wang, D. S.; Huo, Z. Y.; Chen, W.; Liu, L. P.; Liang, X.; Chen, C.; Wang, X.; Peng, Q.; Li, Y. D. A versatile bottom-up assembly approach to colloidal spheres from nanocrystals. *Angew. Chem. Int. Ed.* **2007**, *46*, 6650–6653.

[39] Wang, D. S.; Xie, T.; Peng, Q.; Li, Y. D. Ag, Ag_2S, and Ag_2Se nanocrystals: Synthesis, assembly, and construction of mesoporous structures. *J. Am. Chem. Soc.* **2008**, *130*, 4016–4022.

[40] Lu, Z.; Ye, M.; Li, N.; Zhong, W.; Yin, Y. Self-assembled TiO_2 nanocrystal clusters for selective enrichment of intact phosphorylated proteins. *Angew. Chem. Int. Ed.* **2010**, *49*, 1862–1866.

[41] Lu, Z.; Duan, J.; He, L.; Hu, Y.; Yin, Y. Mesoporous TiO_2 nanocrystal clusters for selective enrichment of phosphopeptides. *Anal. Chem.* **2010**, *82*, 7249–7258.

[42] Lu, Z.; He, L.; Yin, Y. Superparamagnetic nanocrystal clusters for enrichment of low-abundance peptides and proteins. Chem. *Commun.* **2010**, *46*, 6174–6176.

[43] Trentler, T. J.; Denler, T. E.; Bertone, J. F.; Agrawal, A.; Colvin, V. L. Synthesis of TiO_2 nanocrystals by nonhydrolytic solution-based reactions. *J. Am. Chem. Soc.* **1999**, *121*, 1613–1614.

[44] Stober, W.; Fink, A.; Bohn, E. Controlled growth of monodisperse silica spheres in the micron size range. *J. Colloid Interface Sci.* **1968**, *26*, 62–69.

[45] Gribb, A. A.; Banfield, J. F. Particle size effects on transformation kinetics and phase stability in nanocrystalline TiO_2. *Am. Mineral.* **1997**, *82*, 717–728.

[46] Zhang, H. Z.; Banfield, J. F. Thermodynamic analysis of phase stability of nanocrystalline titania. *J. Mater. Chem.* **1998**, *8*, 2073–2076.

[47] Gao, Y. F.; Masuda, Y.; Peng, Z. F.; Yonezawa, T.; Koumoto, K. Room temperature deposition of a TiO_2 thin film from aqueous peroxotitanate solution. *J. Mater. Chem.* **2003**, *13*, 608–613.

[48] Tang, H.; Prasad, K.; Sanjines, R.; Schmid, P. E.; Levy, F. Electrical and optical-properties of TiO_2 anatase thin-films. *J. Appl. Phys.* **1994**, *75*, 2042–2047.

Photocatalysts

DOI: 10.1002/ange.201101969

A Highly Active Titanium Dioxide Based Visible-Light Photocatalyst with Nonmetal Doping and Plasmonic Metal Decoration**

*Qiao Zhang, Diana Q. Lima, Ilkeun Lee, Francisco Zaera, Miaofang Chi, and Yadong Yin**

Since the discovery of its photocatalytic activity under UV light, TiO_2 has been widely studied as a photocatalyst in applications such as water splitting and purification.[1] As pristine TiO_2 only absorbs UV light, much effort has been devoted to developing visible-light-active TiO_2 photocatalysts that can make use of both UV and visible radiation. Many strategies, including metal-ion[2] and nonmetal doping,[3] have been proposed to extend the absorption of TiO_2 to the visible spectrum, but, to date, new materials have typically suffered from low doping concentration and/or low stability against photocorrosion.[3d,4] Noble-metal nanoparticles such as Au and Ag have also been used to enhance the activity of photocatalysts in visible light because of their plasmonic properties.[5] In any case, an improved absorption of photons may not necessarily guarantee significantly better photocatalytic performance because the efficiency of a photocatalyst is also determined by charge separation and transport. As most excited charges may recombine and quench before reaching the surface, small grain size and high crystallinity would be desirable for enhancing charge-separation efficiency that would result in a reduced migration distance of charges and, consequently, in a lower recombination rate.[6] Additionally, metal decoration has also been shown to enhance charge separation in TiO_2 photocatalysts by serving as an electron reservoir.[7] It is therefore expected that a composite of small doped TiO_2 nanocrystals decorated with metal nanoparticles may be a powerful photocatalyst, as all the features discussed above are combined. However, the incompatibility between the synthesis, doping, and decoration procedures means that the production of such nanocomposites has remained a great challenge.

We report herein the design and synthesis, by combining simple sol–gel and calcination processes, of a highly efficient, stable, and cost-effective TiO_2-based photocatalyst with the desired properties mentioned above. The new catalyst has a sandwich structure that comprises a SiO_2 core, a layer of gold nanoparticles (AuNPs), and a doped TiO_2 nanocrystalline shell. The sol–gel process allows for the convenient incorporation of AuNPs into the catalyst with controlled loading and location. TiO_2 is doped with both N and C using an unconventional method that involves introducing 3-aminopropyl-triethoxysilane (APTES), which originally acts as a ligand for immobilization of AuNPs on the surface of the SiO_2 support, but upon subsequent decomposition at high temperature serves as a source of both N and C for doping. Compared to traditional Au/TiO_2 composites, in which AuNPs are loosely attached to the surface of TiO_2 such that they are unstable during calcination and subsequent photocatalysis, the sandwich structures with the AuNPs embedded inside a TiO_2 matrix protects the former from moving together and coagulating.[8] The encapsulation also increases the contact area between the AuNPs and the TiO_2 matrix, and therefore allows for more efficient electron transfer. A third advantage of our nanoarchitecture is that the precontact of Au with a TiO_2 surface can significantly increase the N loading by stabilizing the doped N inside the oxide, and the doped N in turn can enhance the adhesion of AuNPs on the oxide surface through an electron transfer process.[9] As discussed later, only a relatively small quantity (ca. 0.1 wt%) of AuNPs are required for optimal catalytic performance, thus making this catalyst feasible for large-scale practical applications. Herein we demonstrate the excellent performance of the new photocatalysts in degradation reactions of a number of organic compounds under UV, visible light, and direct sunlight.

The fabrication of the sandwich structures is depicted in Figure 1a. SiO_2 particles with a diameter of approximately 400 nm were first synthesized through the Stöber method,[10] then surface-modified with a monolayer of the coupling agent APTES by heating the mixture in isopropanol at 80°C. Citrate-stabilized AuNPs could then be adsorbed onto the silica surface by a strong chemical affinity towards primary amines, as confirmed by the color change of the original Au suspension from red to colorless after extraction by APTES-modified SiO_2 spheres. In the presence of hydroxypropyl cellulose (HPC), the Au/SiO_2 composite colloids were overcoated with a layer of amorphous TiO_2 by hydrolyzing tetrabutyl orthotitanate (TBOT) in ethanol solution.[6a,11]

[*] Q. Zhang, D. Q. Lima, Dr. I. Lee, Prof. F. Zaera, Prof. Y. Yin
Department of Chemistry, University of California
Riverside, CA 92521 (USA)
Fax: (+1) 951-827-4713
E-mail: yadong.yin@ucr.edu
Homepage: http://faculty.ucr.edu/~yadongy/
Dr. M. Chi
Materials Science Division, Oak Ridge National Laboratory
Oak Ridge, TN 37830 (USA)

[**] Financial support of this work was provided by the U.S. Department of Energy (DE-SC0002247). Y.Y. also thanks the Research Corporation for Science Advancement for the Cottrell Scholar Award, 3M for the Nontenured Faculty Grant, and DuPont for the Young Professor Grant. We thank the Central Facility for Advanced Microscopy and Microanalysis at UCR for access to TEM and SEM analysis. Part of the TEM work was performed at the SHaRE user facility at ORNL, which is supported by DOE-BES. The Brazilian National Council for Scientific and Technological Development (CNPq) (grant 202146/2008-1) supported the academic stay of D.Q.L. at University of California in Riverside to carry out part of her experimental work for her PhD thesis in chemistry (UFMG, Brazil).

Supporting information for this article is available on the WWW under http://dx.doi.org/10.1002/anie.201101969.

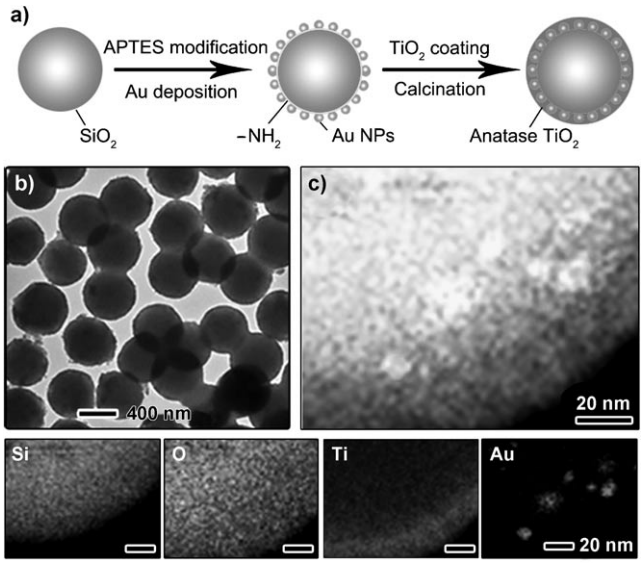

Figure 1. a) Schematic illustration of the fabrication process of the sandwich-structured $SiO_2/Au/TiO_2$ photocatalyst. b) Typical TEM image of the composite photocatalyst. c) Elemental mapping of a single particle with the distribution of individual elements shown in the bottom row.

The reddish composite was finally calcined at 500 °C for 2 h under ambient conditions to produce a blue powder consisting of uniform spheres with an average diameter of approximately 430 nm, as shown in the transmission electron microscopy (TEM) image in Figure 1 b. Energy dispersive X-ray (EDX) elemental mapping of a single sphere (Figure 1 c) clearly confirms the expected sandwich structure. Observation by TEM at higher magnification reveals that the outer TiO_2 shell is composed of small nanoparticle grains with sizes of 8–15 nm, which are optimal for anatase photocatalysts.[6a,12] Nitrogen adsorption–desorption isotherm measurements on this sample suggest an average BET surface area of approximately 45.1 $m^2 g^{-1}$, thus confirming the porous nature of the TiO_2 shell.

Figure 2 shows X-ray diffraction (XRD) data used to identify the crystallographic phases of the titania in the as-prepared sandwich-structured catalysts, along with two reference samples including commercial anatase TiO_2 powder and P25 aeroxide. As shown in Figure 2 a, the sandwich structures show all the characteristic diffraction peaks also found in commercial anatase TiO_2, with cell parameters $a = b = 3.78$ Å, $c = 9.51$ Å (JCPDS card no. 73-1764). The peak broadening of the sandwich structures suggests that the shells are composed of small nanocrystalline grains, as is consistent with our TEM observation. No characteristic peaks of crystallized gold can be found in our sample because of its very low concentration. As expected, P25 was found to be a mixture of anatase and rutile phases.[6a]

Diffuse reflectance UV/Vis spectroscopy was used to study the optical properties of the sandwich-structured photocatalyst and contrast those with the reference samples (Figure 2 b). While the commercial anatase sample strongly absorbs light only in the UV region, noticeable absorption in the visible region can be observed for all $SiO_2/APTES/TiO_2$ structures, even in the absence of AuNPs. This result confirms

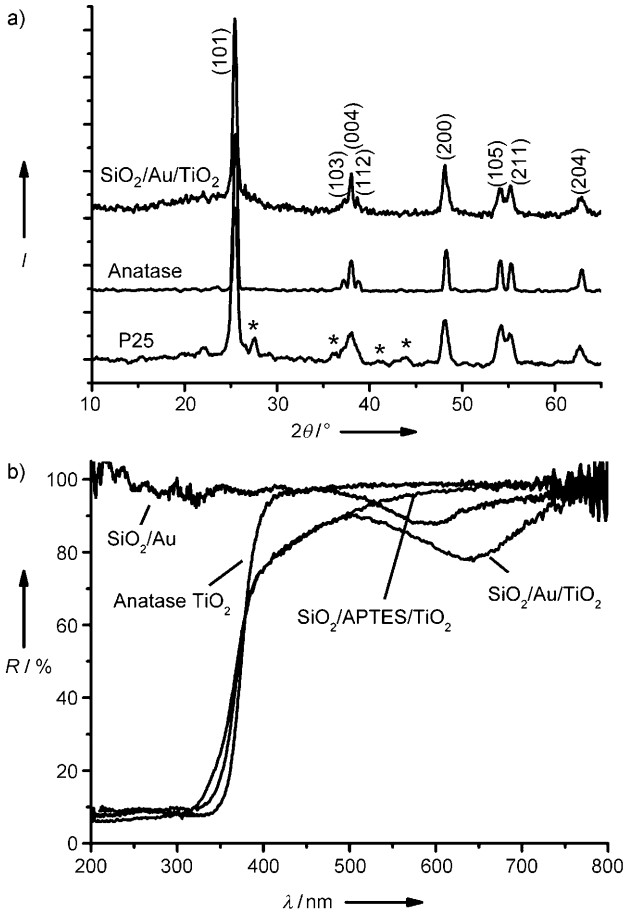

Figure 2. a) XRD patterns of the $SiO_2/Au/TiO_2$ photocatalyst, commercial anatase TiO_2 and P25 aeroxide. * denotes rutile phase TiO_2. b) UV/Vis diffuse reflectance spectra of the three TiO_2-based photocatalysts and a control sample of AuNP-decorated silica particles.

doping of TiO_2 with N and/or C as reported by Sato, and Giamello and co-workers.[13] Moreover, with AuNPs, another absorption band at around 650 nm appears, which can be mainly ascribed to the surface plasmon resonance of AuNPs. Compared to a reference sample consisting of AuNP-decorated SiO_2 spheres, which shows an absorption band at around 590 nm, the new absorption band in the $SiO_2/APTES/Au/TiO_2$ structure (simply denoted as $SiO_2/Au/TiO_2$ in later discussions) is red-shifted by approximately 60 nm, a difference that can be attributed to the high refractive index of the TiO_2 ($n = 2.488$ for pure anatase TiO_2) that surrounds the AuNPs.[5c] This result also suggests a good contact between AuNPs and TiO_2 grains.

X-ray photoelectron spectroscopy (XPS) was used to investigate the C and/or N doping in the TiO_2 shells. Without doping, for the simple TiO_2-coated SiO_2 sample, Ti exhibits a $2p_{3/2}$ peak at 458.5 eV, which corresponds to the binding energy of Ti^{4+} in TiO_2 (Figure 3 a).[14] Once APTES is introduced between the SiO_2 core and the TiO_2 shell, however, the Ti 2p peak shifts to a lower binding energy of 458.2 eV. This shift is indicative of the incorporation of N and/or C into the TiO_2 lattice.[15] The low loadings used and the TiO_2 overcoating result in relatively weak XPS signals for N and C, thus making it difficult to identify the exact nature of

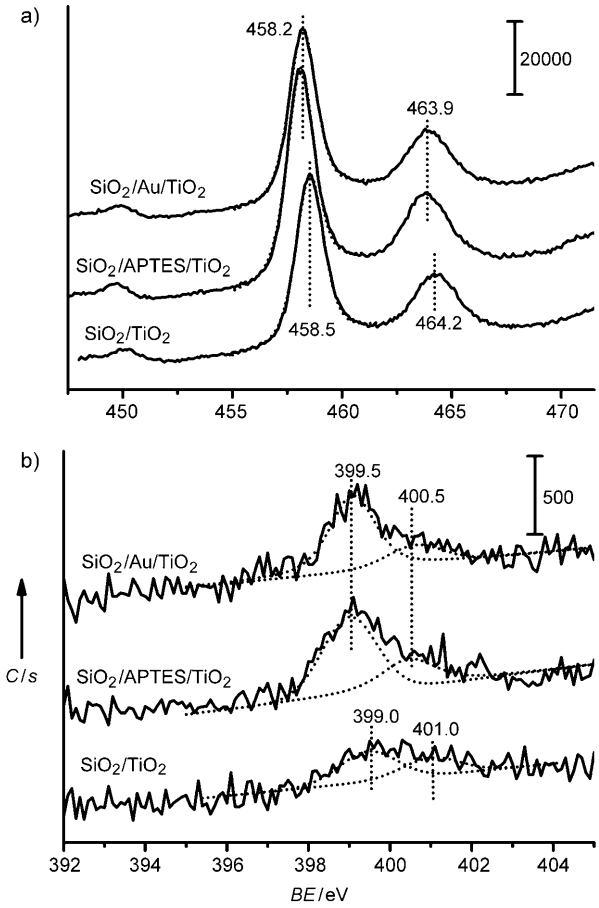

Figure 3. XPS measurements for the as-obtained $SiO_2/Au/TiO_2$ photocatalyst: a) Ti 2p, and b) N 1s. All the XPS data have been calibrated with the binding energy of Si–O from SiO_2 at 103.4 eV.

the doped species. As shown in Figure 3b, all the samples display a weak and broad N 1s XPS peak around 400.5–401.0 eV, which can be attributed to adsorbed N_2 molecules.[16] The N 1s XPS data of nitrogen-doped TiO_2 have recently been reported to exhibit a peak at 396 eV,[16–17] which arises from the substitutionally doped N^{3-} component of Ti–N, but we could not detect any signal at this position with our SiO_2/APTES/TiO_2 and SiO_2/Au/TiO_2 samples, probably because of the limited doping at the vicinity of SiO_2/TiO_2 interface. Instead, we observed a peak at 399.0 eV which may be produced by jointly bonded C–N in $TiO_{2-x-y}N_xC_y$ films.[18] The existence of additional C resulting from the decomposition of APTES has also been confirmed by the C 1s spectra (see the Supporting Information).[18–19]

The photocatalytic activity was evaluated by monitoring its characteristic absorption band at 553 nm to measure the degradation rate of rhodamine B (RhB) under light irradiation. Unlike many previous reports in which the incorporation of a metal into TiO_2 degrades catalytic performance in the UV region,[20] the sandwiched structures show performance comparable to P25 under UV irradiation, thus attesting to the overall positive impact of the nonmetal doping and gold decoration on the catalytic activity. Moreover, under visible light irradiation ($\lambda > 400$ nm), the $SiO_2/Au/TiO_2$ nanostructures display significantly higher efficiency than that of P25. As shown in Figure 4a, the sandwich-structured photocatalyst can decompose approximately 96% of RhB in 5 h, while P25 containing an equivalent amount of TiO_2 can convert only about 42% of RhB under identical conditions. Commercial anatase is essentially inactive.

To investigate the origin of the enhanced photocatalytic activity, we also compared the performance of the $SiO_2/Au/TiO_2$ photocatalyst to SiO_2/TiO_2 and SiO_2/APTES/TiO_2 composites synthesized under similar conditions by using silica cores of the same size and TiO_2 shells of the same thickness. Before catalysis, the TiO_2 in all samples was identified as pure anatase by XRD. As shown in Figure 4a, without the modification of APTES, the SiO_2/TiO_2 core–shell structures show very low activity under visible light irradiation. However, after C/N doping, the core–shell photocatalyst becomes active and shows 48% degradation of RhB in 5 h. This is already an improvement over the widely recognized P25 aeroxide photocatalyst, which shows considerable visible-light activity because of the presence of rutile phase.[21] Additional decoration of the SiO_2/TiO_2 interface with 0.1% of AuNPs further doubles the decomposition rate.

Chronoamperometry (CA) measurements were performed to characterize the photogenerated current density under a potential of 0.8 V and periodic illumination of visible light ($\lambda > 400$ nm). As indicated in Figure 4b, photogenerated currents were seen for all samples, but $SiO_2/Au/TiO_2$ showed a significantly higher value (ca. 0.80 $\mu A\,cm^{-2}$) than P25 (ca. 0.45 $\mu A\,cm^{-2}$) and SiO_2/APTES/TiO_2 (ca. 0.40 $\mu A\,cm^{-2}$). The shape of the CA curves is well maintained after many cycles of light illumination, thus implying very good photocatalytic stability.

It is clear that decoration of titania-based photocatalysts with AuNPs is an important factor to achieve the high catalytic efficiency. A systematic study was carried out to assess this effect by varying the loading of AuNPs from 0 to 0.5 wt% in six otherwise identical samples (Figure 4c). Interestingly, the visible-light activity of the samples peaks at 0.1 wt% loading of AuNPs. It is generally understood that AuNPs supported on TiO_2 have three probable functions in photocatalysis: 1) to help harvest the visible-light energy by their plasmonic properties,[5c] 2) to enhance charge separation by serving as an electron reservoir,[7,22] and 3) to act as a recombination center, which negatively affects catalytic activity.[23] When the loading of AuNPs is low, their primary function is to enhance the charge separation and hence promote the oxidation of organic molecules under visible light. However, excessive amounts of metal particles may also deteriorate the catalytic performance by increasing the occurrence of exciton recombination,[23] with the reaction rate gradually decreasing when the loading of AuNPs exceeds 0.1 wt%. The low loading (0.1 wt%) of the AuNPs required for achieving high catalytic performance also has practical significance in terms of cost: many prior reports on Au/TiO_2 composite photocatalysts require Au loading of approximately 1–5 wt%, which has prevented their large-scale application.[22b]

In addition to the effects on light harvesting and charge separation, the AuNPs may also contribute to the enhancement in nonmetal doping for TiO_2. Sanz and co-workers have

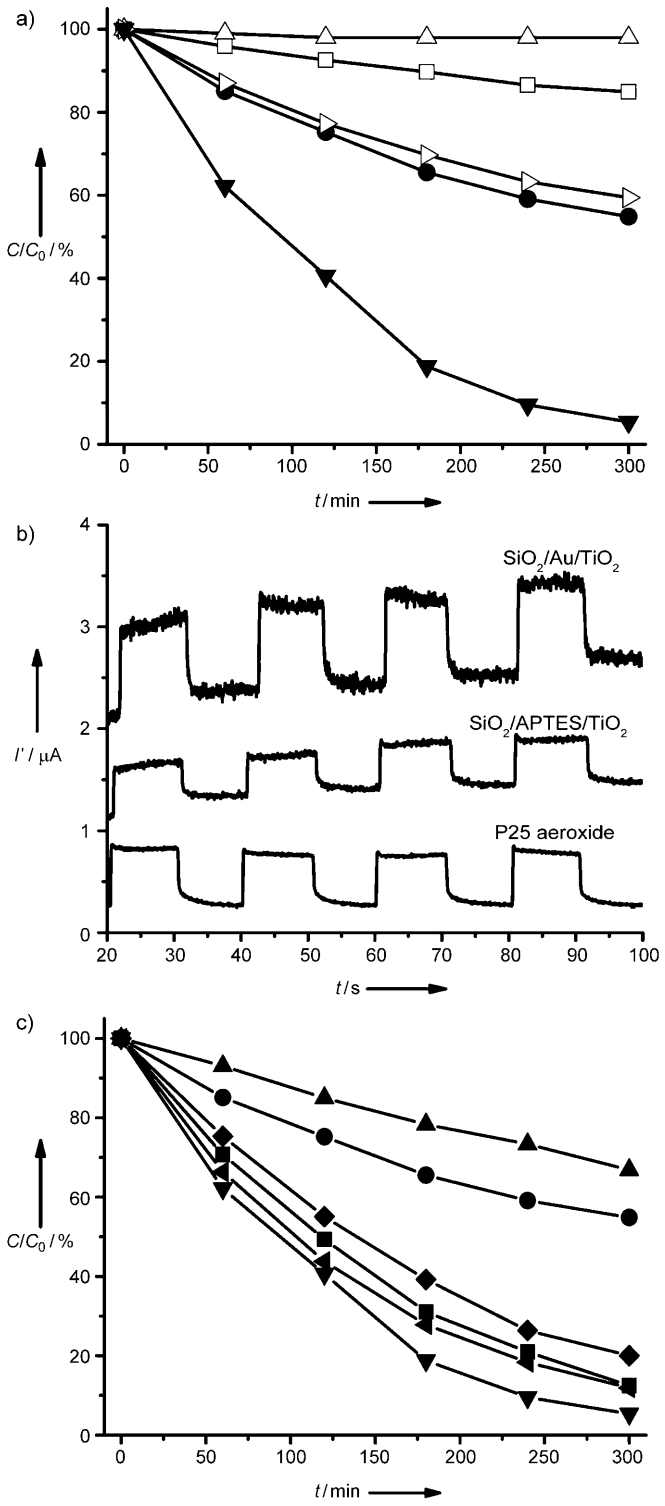

Figure 4. a) Photodegradation of RhB by using commercial anatase TiO_2 (△), SiO_2/TiO_2 (□), P25 aeroxide (▷), SiO_2/APTES/TiO_2 (●), and SiO_2/Au(0.1%)/TiO_2 (▼) as photocatalysts under visible-light illumination ($\lambda > 400$ nm). b) Chronoamperometry measurements of P25, SiO_2/APTES/TiO_2, and SiO_2/Au/TiO_2 under periodic illumination with visible light. c) Influence of AuNP loading (● 0.00, ◆ 0.05, ▼ 0.10, ◀ 0.20, ■ 0.30, ▲ 0.50% Au) on the catalytic activity of SiO_2/Au/TiO_2 sandwich structures studied by using the decomposition of RhB as the model system.

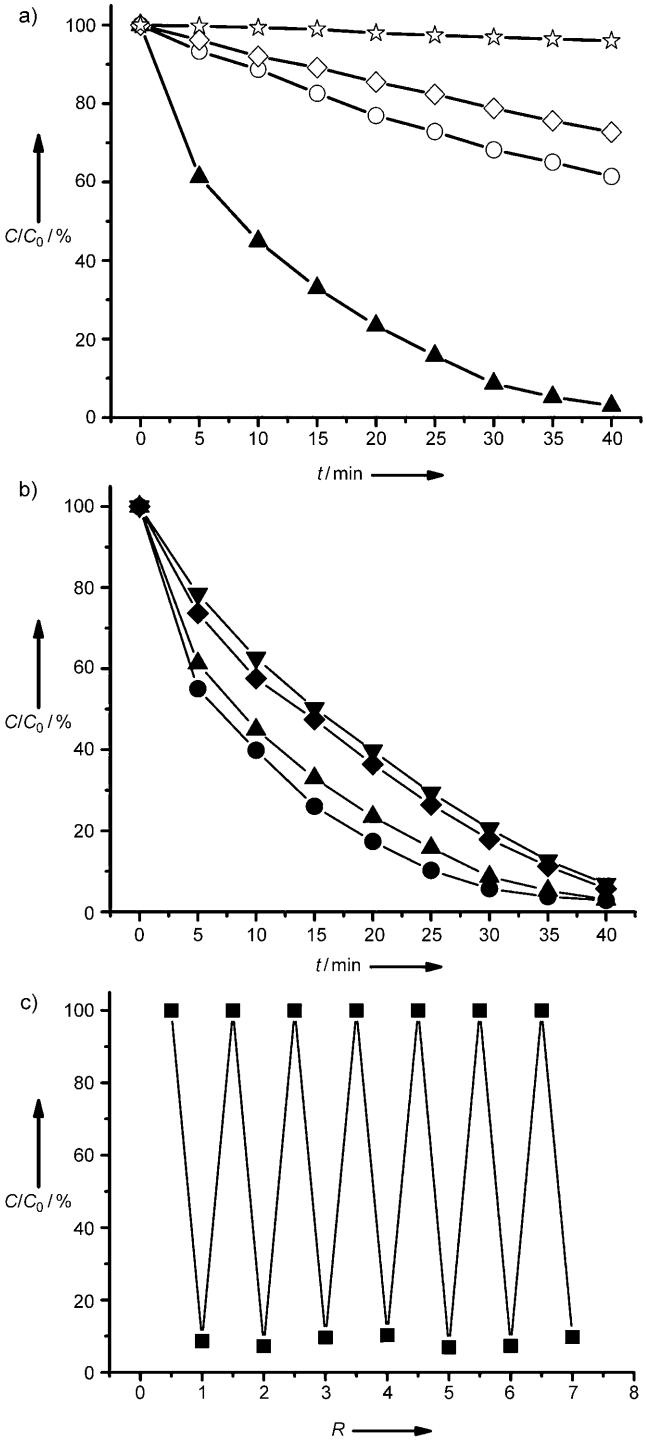

Figure 5. a) Photodegradation of RhB without catalyst (*) and with anatase TiO_2 (◇), P25 (○), and SiO_2/Au/TiO_2 (▲) as the photocatalysts under direct sunlight illumination. b) Photodegradation of RhB (▲), R6G (▼), methylene blue (●), and 2,4-dichlorophenol (◆) with SiO_2/Au/TiO_2 sandwich-structured catalyst under direct sunlight illumination. c) Seven cycles of the photodegradation of RhB with SiO_2/Au/TiO_2 photocatalyst under sunlight illumination. The duration of sunlight exposure in each cycle is 30 min.

demonstrated both theoretically and experimentally that Au preadsorption on TiO_2 surfaces can significantly stabilize implanted N, increase the reachable amount of N loading in the oxide, and enhance Au surface adhesion energy by electron transfer from the Au 6s orbitals to the partially occupied N 2p orbitals.[9] As the nonmetal doping process usually requires annealing at elevated temperatures, which may cause the AuNPs to sinter, the unique sandwich structure proposed in this work represents an ideal system to overcome sintering: AuNPs are unable to move within the TiO_2 matrix, and thus coagulation during calcination is prevented, high stability is ensured, and Au/TiO_2 surface contact is improved.

To explore the photocatalytic activity of our samples for real applications, the photodegradation of organic compounds was investigated under natural sunshine, which contains both UV, visible, and IR light. As shown in Figure 5a, sunlight can completely decompose RhB molecules within 40 min with the aid of sandwich-structured photocatalysts, while the conversion only reaches approximate values of 38% with P25 and 27% with the commercial anatase sample during the same period. We also tested the $SiO_2/Au/TiO_2$-catalyzed degradation of other organic molecules under sunlight, including rhodamine 6G (R6G), methylene blue (MB), and 2,4-dichlorophenol (2,4-DCP) at the same initial concentration. As shown in Figure 5b, all of those molecules can be decomposed almost completely ($>93\%$) within 40 min. As shown in Figure 5c, these photocatalysts are also mechanically robust and chemically stable: they can be recovered and reused to catalyze multiple cycles of degradation reactions under direct sunlight.

In summary, we have demonstrated a sandwich-structured $SiO_2/Au/TiO_2$ photocatalyst that shows high efficiency in catalyzing decomposition of organic compounds under illumination of UV, visible light, and natural sunlight. The structural design of the photocatalyst takes advantage of the synergetic interaction between adsorbed gold and implanted nitrogen, and produces stable nonmetal-doped anatase nanoparticles with precisely controlled AuNPs decoration. The excellent photocatalytic efficiency can be attributed to the interfacial nonmetal doping, which improves visible light activity, to the plasmonic metal decoration, which enhances light harvesting and charge separation, and to the small grain size of anatase nanocrystals, which reduces the exciton recombination rate.

Received: March 20, 2011
Revised: May 19, 2011
Published online: June 24, 2011

Keywords: doping · nanoparticles · photocatalysts · plasmonic metals · titanium dioxide

[1] a) A. Fujishima, K. Honda, *Nature* **1972**, *238*, 37–38; b) B. O'Regan, M. Gratzel, *Nature* **1991**, *353*, 737–740.
[2] W. Y. Choi, A. Termin, M. R. Hoffmann, *J. Phys. Chem.* **1994**, *98*, 13669–13679.
[3] a) R. Asahi, T. Morikawa, T. Ohwaki, K. Aoki, Y. Taga, *Science* **2001**, *293*, 269–271; b) S. Sakthivel, H. Kisch, *Angew. Chem.* **2003**, *115*, 5057–5060; *Angew. Chem. Int. Ed.* **2003**, *42*, 4908–4911; c) S. U. M. Khan, M. Al-Shahry, W. B. Ingler, *Science* **2002**, *297*, 2243–2245; d) A. Emeline, V. Kuznetsov, V. Rybchuk, N. Serpone, *Int. J. Photoenergy* **2008**, *2008*, 1–19; e) X. Chen, L. Liu, P. Y. Yu, S. S. Mao, *Science* **2011**, *331*, 746–750.
[4] a) J. Graciani, L. J. Alvarez, J. A. Rodriguez, J. F. Sanz, *J. Phys. Chem. C* **2008**, *112*, 2624–2631; b) M. Batzill, E. H. Morales, U. Diebold, *Phys. Rev. Lett.* **2006**, *96*, 026103; c) A. Nambu, J. Graciani, J. A. Rodriguez, Q. Wu, E. Fujita, J. F. Sanz, *J. Chem. Phys.* **2006**, *125*, 094706.
[5] a) A. Furube, L. Du, K. Hara, R. Katoh, M. Tachiya, *J. Am. Chem. Soc.* **2007**, *129*, 14852–14853; b) S. Naya, A. Inoue, H. Tada, *J. Am. Chem. Soc.* **2010**, *132*, 6292–6293; c) K. Awazu, M. Fujimaki, C. Rockstuhl, J. Tominaga, H. Murakami, Y. Ohki, N. Yoshida, T. Watanabe, *J. Am. Chem. Soc.* **2008**, *130*, 1676–1680.
[6] a) M. Ye, Q. Zhang, Y. Hu, J. Ge, Z. Lu, L. He, Z. Chen, Y. Yin, *Chem. Eur. J.* **2010**, *16*, 6243–6250; b) Q. Zhang, J.-B. Joo, Z. Lu, M. Dahl, D. Oliveira, M. Ye, Y. Yin, *Nano Res.* **2011**, *4*, 103–114.
[7] J. Li, H. C. Zeng, *Chem. Mater.* **2006**, *18*, 4270–4277.
[8] a) Q. Zhang, I. Lee, J. Ge, F. Zaera, Y. Yin, *Adv. Funct. Mater.* **2010**, *20*, 2201–2214; b) J. Ge, Q. Zhang, T. Zhang, Y. Yin, *Angew. Chem.* **2008**, *120*, 9056–9060; *Angew. Chem. Int. Ed.* **2008**, *47*, 8924–8928; c) I. Lee, Q. Zhang, J. Ge, Y. Yin, F. Zaera, *Nano Res.* **2011**, *4*, 115–123.
[9] J. Graciani, A. Nambu, J. Evans, J. A. Rodriguez, J. F. Sanz, *J. Am. Chem. Soc.* **2008**, *130*, 12056–12063.
[10] W. Stober, A. Fink, E. Bohn, *J. Colloid Interface Sci.* **1968**, *26*, 62–69.
[11] a) J. W. Lee, M. R. Othman, Y. Eom, T. G. Lee, W. S. Kim, J. Kim, *Microporous Mesoporous Mater.* **2008**, *116*, 561–568; b) M. Ye, S. Zorba, L. He, Y. Hu, R. T. Maxwell, C. Farah, Q. Zhang, Y. Yin, *J. Mater. Chem.* **2010**, *20*, 7965–7969.
[12] a) M. Anpo, T. Shima, S. Kodama, Y. Kubokawa, *J. Phys. Chem.* **1987**, *91*, 4305; b) S. Y. Chae, M. K. Park, S. K. Lee, T. Y. Kim, S. K. Kim, W. I. Lee, *Chem. Mater.* **2003**, *15*, 3326; c) C.-C. Wang, Z. Zhang, J. Y. Ying, *Nanostruct. Mater.* **1997**, *9*, 583.
[13] a) S. Sato, *Chem. Phys. Lett.* **1986**, *123*, 126–128; b) S. Livraghi, M. C. Paganini, E. Giamello, A. Selloni, C. Di Valentin, G. Pacchioni, *J. Am. Chem. Soc.* **2006**, *128*, 15666–15671.
[14] U. Diebold, T. Madey, *Surf. Sci. Spectra* **1996**, *4*, 227–231.
[15] J. Wang, D. N. Tafen, J. P. Lewis, Z. L. Hong, A. Manivannan, M. J. Zhi, M. Li, N. Q. Wu, *J. Am. Chem. Soc.* **2009**, *131*, 12290–12297.
[16] N. C. Saha, H. G. Tompkins, *J. Appl. Phys.* **1992**, *72*, 3072–3079.
[17] a) H. Irie, Y. Watanabe, K. Hashimoto, *J. Phys. Chem. B* **2003**, *107*, 5483–5486; b) T. Sano, N. Negishi, K. Koike, K. Takeuchi, S. Matsuzawa, *J. Mater. Chem.* **2004**, *14*, 380–384; c) O. Diwald, T. L. Thompson, T. Zubkov, E. G. Goralski, S. D. Walck, J. T. Yates, *J. Phys. Chem. B* **2004**, *108*, 6004–6008.
[18] J. Yang, H. Z. Bai, X. C. Tan, J. S. Lian, *Appl. Surf. Sci.* **2006**, *253*, 1988–1994.
[19] a) K. R. Wu, C. H. Hung, *Appl. Surf. Sci.* **2009**, *256*, 1595–1603; b) H. Kamisaka, T. Adachi, K. Yamashita, *J. Chem. Phys.* **2005**, *123*, 084704; c) G. Iucci, M. Dettin, C. Battocchio, R. Gambaretto, C. Di Bello, G. Polzonett, *Mater. Sci. Eng. C* **2007**, *27*, 1201–1206; d) W. J. Ren, Z. H. Ai, F. L. Jia, L. Z. Zhang, X. X. Fan, Z. G. Zou, *Appl. Catal. B* **2007**, *69*, 138–144; e) Q. Xiao, J. Zhang, C. Xiao, Z. C. Si, X. O. Tan, *Solar Energy* **2008**, *82*, 706–713.
[20] Z. Liu, W. Hou, P. Pavaskar, M. Aykol, S. B. Cronin, *Nano Lett.* **2011**, *11*, 1111–1116.
[21] D. C. Hurum, A. G. Agrios, K. A. Gray, T. Rajh, M. C. Thurnauer, *J. Phys. Chem. B* **2003**, *107*, 4545–4549.
[22] a) V. Subramanian, E. E. Wolf, P. V. Kamat, *J. Am. Chem. Soc.* **2004**, *126*, 4943–4950; b) A. Primo, A. Corma, H. Garcia, *Phys. Chem. Chem. Phys.* **2011**, *13*, 886–910.
[23] Y. M. Wu, H. B. Liti, J. L. Zhang, F. Chen, *J. Phys. Chem. C* **2009**, *113*, 14689–14695.

Angewandte Chemie
Eine Zeitschrift der Gesellschaft Deutscher Chemiker

Supporting Information

69451 Weinheim, Germany

A Highly Active Titanium Dioxide Based Visible-Light Photocatalyst with Nonmetal Doping and Plasmonic Metal Decoration**

*Qiao Zhang, Diana Q. Lima, Ilkeun Lee, Francisco Zaera, Miaofang Chi, and Yadong Yin**

ange_201101969_sm_miscellaneous_information.pdf

Supporting Information

Experimental

Chemicals. Ethanol (denatured), 2-propanol (99.9%), ammonium hydroxide aqueous solution (28%), commercial anatase TiO_2 powder and P25 aeroxide were obtained from Fisher Scientific. Tetrabutyl orthotitanate (TBOT, 99%) was purchased from Fluka. 3-Aminopropyl-triethoxysilane (APTES, 99%), rhodamine B (RhB, pure), and 2, 4-dichlorophenol (2, 4-DCP, 99%) were purchased from Acros Organics. Tetraethyl orthosilicate (TEOS, 98%), hydrogen tetrachloroaurate (III) trihydrate (99.9+%), sodium citrate tribasic dihydrate (99%), and hydroxypropyl cellulose (HPC, Mw = 80,000) were obtained from Sigma-Aldrich. Absolute ethyl alcohol (200 proof) was purchased from Gold Shield Chemical. All chemicals were directly used as received without further treatment.

Synthesis and modification of SiO_2 spheres: In a typical synthesis, 1 mL of TEOS was injected into a mixture of 4 mL of deionized H_2O, 1 mL of $NH_3 \bullet H_2O$ and 20 mL of isopropanol at room temperature under magnetic stirring. After reacting for 4 hours, the colloidal spheres were collected by centrifugation, re-dispersed in 8 mL of ethanol. After washing twice with ethanol by centrifugation and redispersion, the particles were transferred to a mixture of isopropanol (20 mL) and APTES (50 μL) and heated to 80 °C for 2 hours to functionalize the silica surface with $-NH_2$ groups. The surface modified particles were washed with ethanol and dispersed in deionized water (8 mL).

Synthesis of SiO_2/Au/TiO_2 In a separate reaction, Au nanoparticles were synthesized using the Turkevich method (Turkevich et al., *Discuss. Faraday Soc.* **1951**, *11*, 55). Briefly, a solution of hydrogen tetrachloroaurate trihydrate was prepared in water and heated to reflux with magnetic stirring, followed immediately by addition of 1 mL of 3 wt% freshly prepared trisodium citrate-water solution, which initiated the reduction of the hydrogen tetrachloroaurate trihydrate. The aurate-citrate solution was allowed to reflux for approximately 30 min. or until completion of the redox reaction as indicated by a change in the solution color from faint yellow to dark red. This method produces a stable, deep-red dispersion of gold particles with an average diameter of around 10 nm. The SiO_2/Au particles were prepared by mixing a

certain amount of the Au solution with modified SiO_2 spheres under sonication. After that, the particles were centrifuged, dispersed in H_2O and stirred with hydroxypropyl cellulose (HPC) overnight. The sample was then centrifuged and washed twice with ethanol. The outer layer of TiO_2 was prepared using a method developed by Lee et al (Lee, J. W. et al *Microporous and Mesoporous Materials* **2008,** 116, 561.). Typically, the above SiO_2/Au aqueous solution was mixed with 0.06 mL of distilled water, and 25 mL of absolute ethyl alcohol under vigorous magnetic stirring. An appropriate amount of tetrabutyl orthotitanate previously dissolved in 5 mL of ethanol was introduced drop by drop, followed by refluxing at 85 °C for 90 min. The final products were washed with ethanol several times, then dried in vacuum for 4 h and calcined in air at desired temperature.

Characterization. A Tecnai T12 transmission electron microscope (TEM) was used to characterize the morphology of the colloids in each step. Samples dispersed in water at an appropriate concentration were cast onto a carbon-coated copper grid, followed by evaporation under vacuum at room temperature. Elemental mapping was performed on a JEOL 2200FS equipped with a Bruker X-flash silicon drift detector (SDD) detector. The crystalline structures of the samples were evaluated by X–ray diffraction (XRD) analyses, carried out on a Bruker D8 Advance Diffractometer with Cu Kα radiation (λ = 1.5418 Å). A Philips ESEM XL30 scanning electron microscope (SEM) equipped with a field-emission gun operated at 10 kV was used to characterize the morphology of the as-obtained product. The XPS data were collected in an ultrahigh vacuum chamber equipped with an Al K_α ($h\nu$ = 1,486.6 eV) X-ray excitation source and a Leybold EA11 electron energy analyzer with multichannel detection. A constant band pass energy of 100.8 eV was used, corresponding to a spectral resolution of ≈2.0 eV. The porosity of the products was measured by the nitrogen adsorption–desorption isotherm and Barrett–Joyner–Halenda (BJH) methods on a Micromeritics ASAP 2020M accelerated surface area and porosimetry system. UV/Vis-NIR diffuse reflectance spectra were measured on a Shimadzu UV 3101PC double-beam, double-monochromator spectrophotometer. $BaSO_4$ powder was used as a reference (100 % reflectance). A probe-type Ocean Optics HR2000CG-UV-NIR spectrometer was used to

measure the UV-Vis absorption spectra of the solution to monitor the concentration of RhB and other organic dyes at different time intervals.

Photocatalytic activity measurement. Photocatalytic reactions for degradation of Rhodamine B (RhB) were carried out in a 100 mL beaker, containing 50 mL of reaction slurry. Agitation was provided by magnetic stirrer. The aqueous slurry, prepared with different kinds of catalysts and 1.0×10^{-5} M RhB was stirred in the dark for 30 min to ensure that the RhB was adsorbed to saturation on the catalysts. For the UV irradiation experiment, a 15 W UV lamp (254 nm, XX-15G, USA), 6 cm above the reaction slurry, was used as the UV radiation source. The average light intensity striking the surface of the reaction solution was about 1.55 $mWcm^{-2}$. The concentration of titania was about 200 mg/L for all the runs. For the visible light irradiation experiment, a 150 W tungsten lamp was used as the light source, and a cutoff filter was used to block the UV light (< 400 nm). The reaction flask was put in a cooling water system to keep the reaction at room temperature. The reaction was performed under constant magnetic stirring of 650 rpm. For the natural sunlight reaction, the reaction flasks were exposed to natural sunlight (estimated intensity: ~100-150 W/m^2) directly with constant magnetic stirring of 650 rpm.

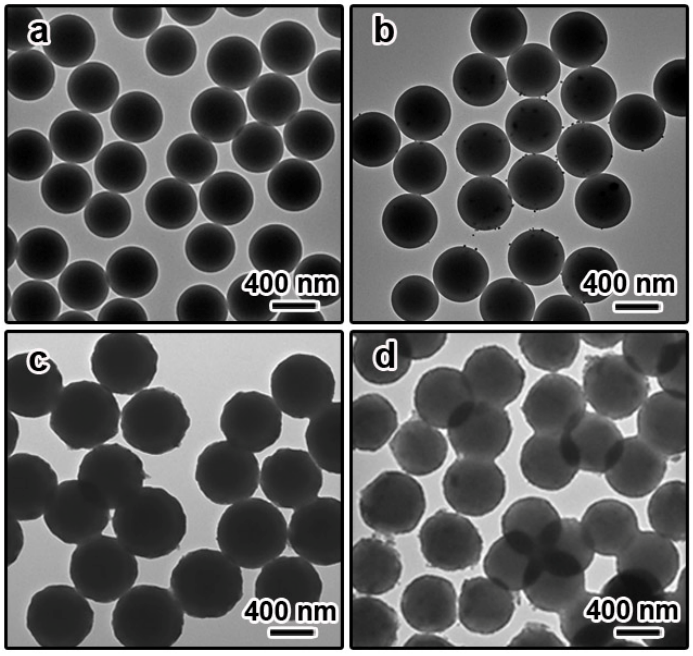

Figure S-1. TEM images showing the fabrication process of the sandwich-structured catalyst: (a) SiO_2 spheres; (b) SiO_2/Au; SiO_2/Au/TiO_2 before (c) and after (d) calcination.

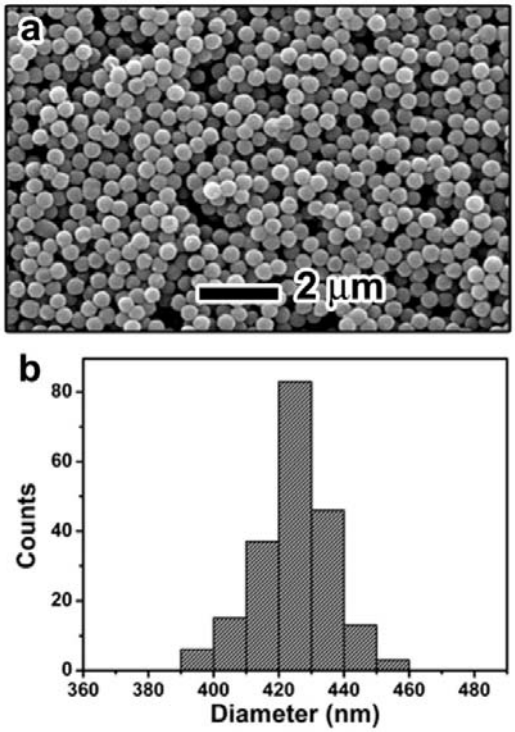

Figure S-2. SEM images (a) and size distribution (b) of the as-prepared sandwich-structured catalyst.

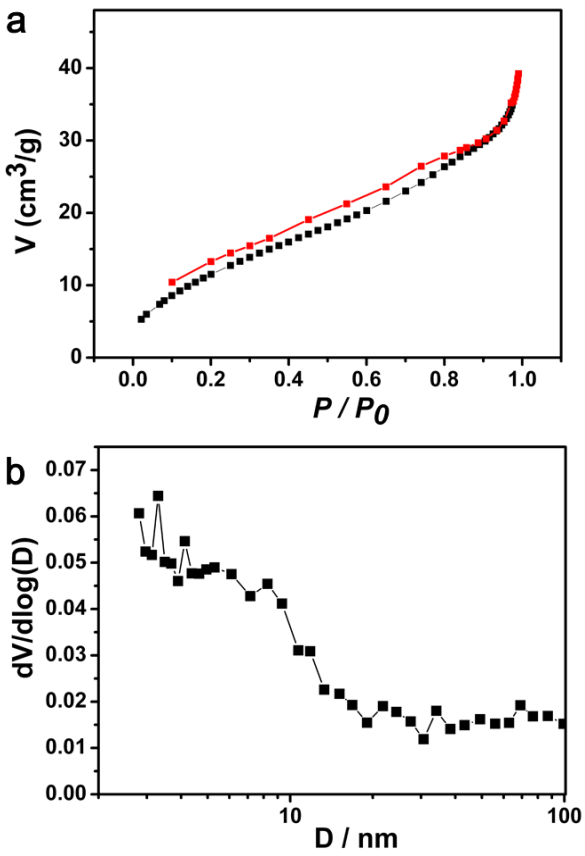

Figure S-3. (a) Nitrogen adsorption–desorption isotherm and (b) BJH pore-size distribution curve of the $SiO_2/Au/TiO_2$ sandwich-structured photocatalyst after calcination.

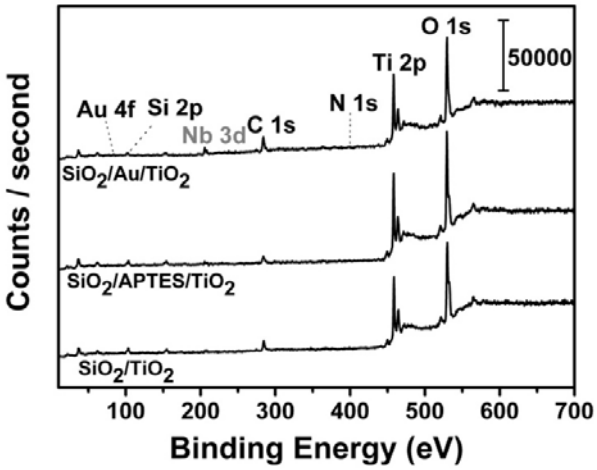

Figure S-4 XPS survey scan for $SiO_2/APTES/Au/TiO_2$ photocatalyst.

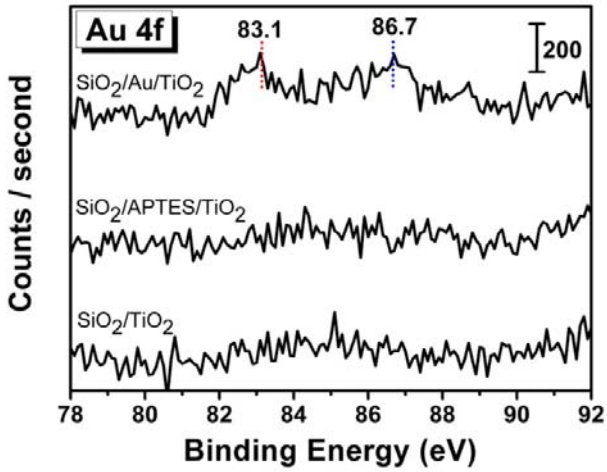

Figure S-5 XPS Au 4f spectra for $SiO_2/Au/TiO_2$, $SiO_2/APTES/TiO_2$, and SiO_2/TiO_2.

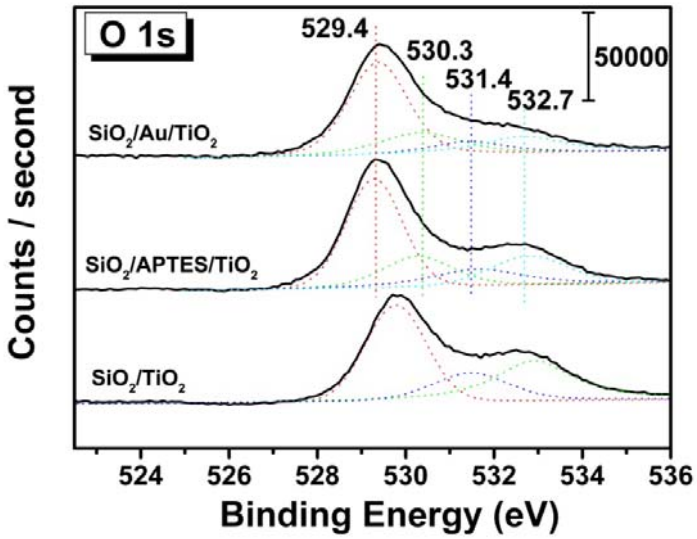

Figure S-6 XPS O 1s spectra for $SiO_2/Au/TiO_2$, $SiO_2/APTES/TiO_2$, and SiO_2/TiO_2.

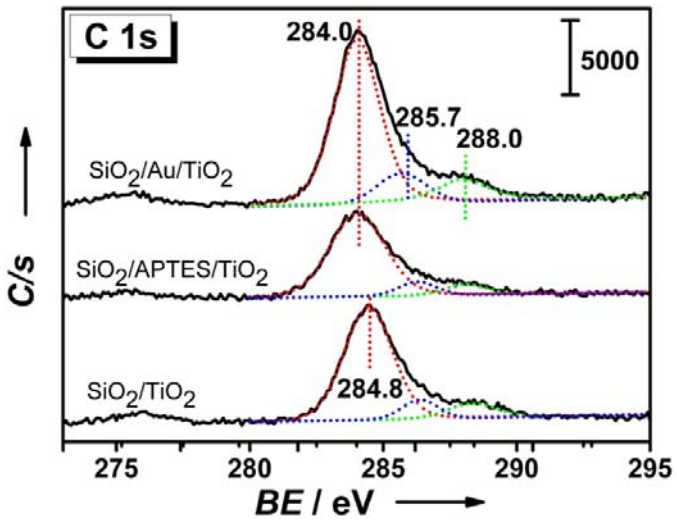

Figure S-7 XPS C 1s spectra for $SiO_2/Au/TiO_2$, $SiO_2/APTES/TiO_2$, and SiO_2/TiO_2.

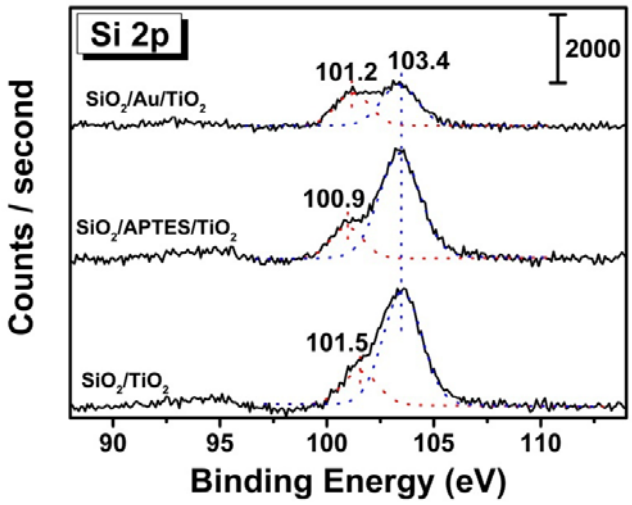

Figure S-8 XPS Si 2p spectra for $SiO_2/Au/TiO_2$, $SiO_2/APTES/TiO_2$, and SiO_2/TiO_2.

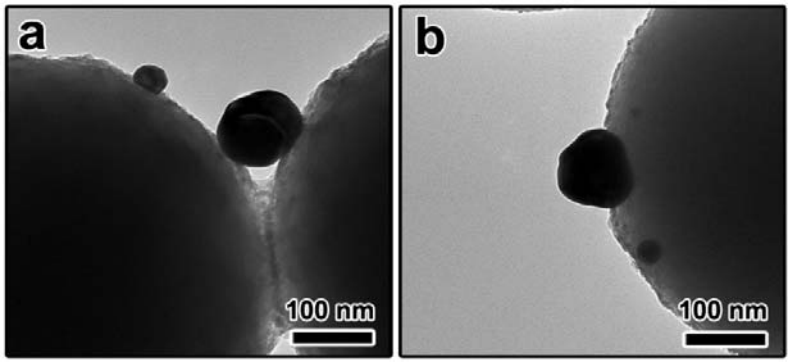

Figure S-9 TEM images showing that Au nanoparticles, if deposited on the outer surface of TiO_2, will severely coalesce under similar calcination conditions.

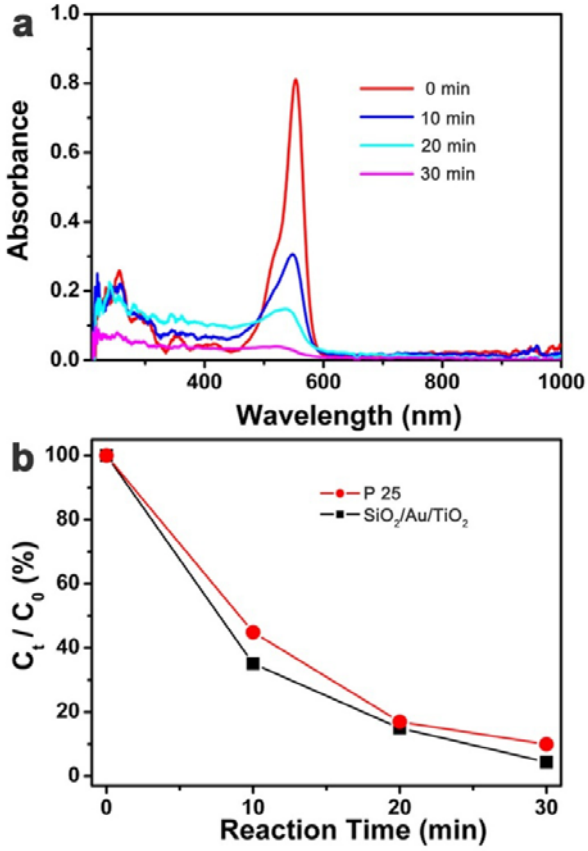

Figure S-10. Under 254 nm UV light irradiation: (a) representative UV absorption spectra of RhB during the conversion process by using $SiO_2/Au/TiO_2$ as the catalyst; (b) photocatalytic conversion of RhB by using P25 aeroxide (red) and $SiO_2/Au/TiO_2$ (black) as the photocatalyst, respectively.

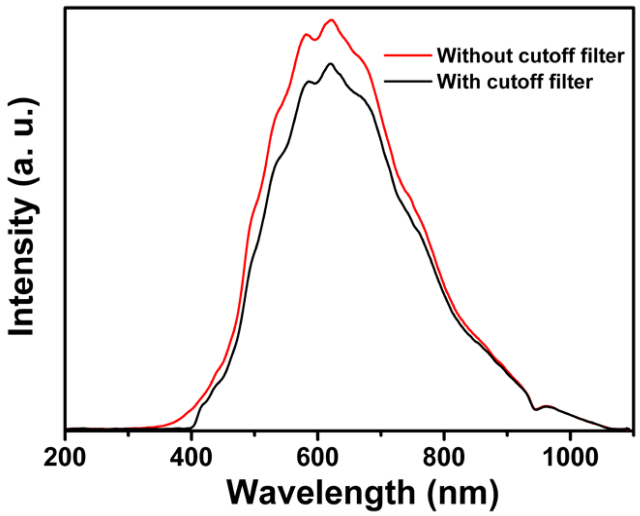

Figure S-11 Spectrum of visible light source before (red) and after (black) the use of 400 nm cutoff filter.

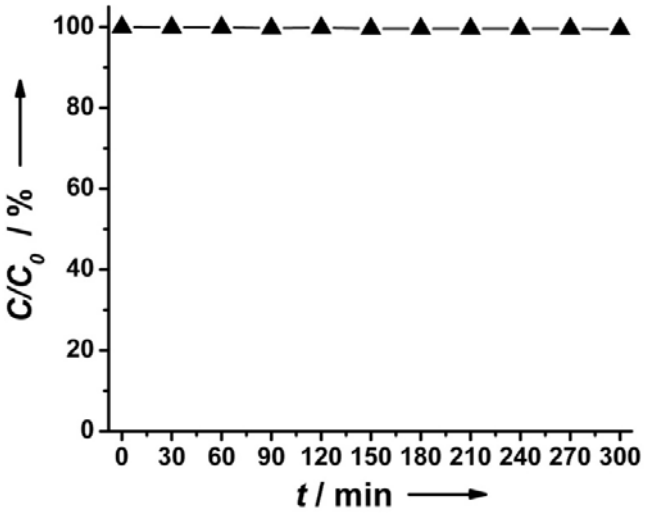

Figure S-12 The concentration change of RhB when mixed with SiO2/Au/TiO2 photocatalyst and kept at darkness. This control experiment rules out the effect of dye adsorption on the catalysts

Available online at www.sciencedirect.com
ScienceDirect
Applied Catalysis B: Environmental 83 (2008) 169–176
APPLIED CATALYSIS B: ENVIRONMENTAL
www.elsevier.com/locate/apcatb

Catalytic properties of goethite prepared in the presence of Nb on oxidation reactions in water: Computational and experimental studies

Luiz C.A. Oliveira [a,*], Teodorico C. Ramalho [a], Eugênio F. Souza [a], Maraísa Gonçalves [a], Diana Q.L. Oliveira [b], Márcio C. Pereira [b], José D. Fabris [b]

[a] *Departamento de Química, Universidade Federal de Lavras (UFLA), Caixa Postal 37, CEP 37200-000 Lavras, Minas Gerais, Brazil*
[b] *Departamento de Química, Universidade Federal de Minas Gerais (UFMG), Campus Pampulha, CEP 31270-901 Belo Horizonte, Minas Gerais, Brazil*

Received 9 March 2007; received in revised form 25 January 2008; accepted 30 January 2008
Available online 20 February 2008

Abstract

Nb-substituted goethites have been prepared and characterized by Mössbauer spectroscopy, XRD, FTIR and BET surface area measurements. The doublet formation in Mössbauer spectra and the decreasing of the crystallinity shown in XRD analyses indicated that the Fe domain size is small, which may be the result of either Fe^{3+} substitution for Nb^{5+} in the goethite structure or simply the formation of small particle-size goethite when Nb is present. FTIR analyses showed shifts and broadening of the bands as result of the incorporation of Nb^{5+} ions into the α-FeOOH structure. The insertion of Nb in the goethite structure caused a significant increase in the BET surface area of the material. The prepared materials were investigated for the H_2O_2 decomposition and the Fenton reaction in the oxidation of methylene blue dye. It was observed that the introduction of Nb during the synthesis of goethite produced a strong increase in the activity for the dye contaminant oxidation by H_2O_2. Theoretical quantum DFT calculations were carried out in order to understand the degradation mechanism for methylene blue with goethites.

Keywords: Goethite; Niobium; DFT; Fenton reaction

1. Introduction

Reactions involving hydrogen peroxide decomposition catalyzed by iron oxides, to generate radical *OH, have received special attention due to the advantages in relation to the classic homogeneous process involving iron soluble salts (Fenton reaction) [1]. These advantages are: (i) it is a heterogeneous system, facilitating all the operations in the treatment of the effluent; (ii) it operates in neutral pH, thus avoiding the need for acidification stages (pH 3) or further neutralization, thus preventing the generation of sludge; and (iii) the system can be recycled/regenerated by reducing surface Fe^{3+} species. Several recent studies have investigated different iron containing solids for the Fenton reaction, such as Fe_2O_3 and $Fe_2Si_4O_{10}(OH)_2$ [2,3], goethite [4–6], Fe(II) supported on zeolite, Al_2O_3 and SiO_2 [7,8] and Fe^0/Al_2O_3 [9]. It has been observed that depending on the conditions employed, these materials can promote the oxidation of different organic compounds, such as, aromatic and aliphatic acids, phenols, aromatic hydrocarbons, chloro compounds and textile dyes with hydrogen peroxide. However, many of these systems showed low activity or strong iron leaching due to low pH, which resulted in the classical homogeneous Fenton mechanism.

In the present work, the reactivity of the heterogeneous Fenton system over goethite was studied. Methylene blue dye was used as a probe contaminant. We carried out experiments to investigate the effect of niobium contents in goethite on the UV/vis and ESI-MS monitored degradation of dye in the presence of H_2O_2.

Targeting a better understanding of the role of niobium in the H_2O_2 decomposition, theoretical calculations were carried out at the Density Functional Theory (DFT) level.

2. Experimental

2.1. Goethite synthesis and characterization

All chemicals were high purity grade and were used as purchased. Goehite α-FeOOH was prepared from $FeCl_3{\cdot}6H_2O$,

* Corresponding author.
E-mail address: luizoliveira@ufla.br (L.C.A. Oliveira).

0926-3373/$ – see front matter © 2008 Elsevier B.V. All rights reserved.
doi:10.1016/j.apcatb.2008.01.038

NaOH and by co-precipitation followed by thermal treatment at 60 °C (72 h) [10]. The substituted goethites were prepared as described above with the addition of 4 (Nb4), 7 (Nb7) and 11% (Nb11) in mass of ammonium niobium oxalate (general formula $NH_4[NbO(C_2O_4)_2(H_2O)](H_2O)_n$ supplied by CBMM (Companhia Brasileira de Metalurgia e Mineração, Araxá-MG).

The surface area was determined by the BET method using N_2 adsorption/desorption in an Autosorb 1 Quantachrome instrument. Transmission Mössbauer spectroscopy experiments were carried out in a CMTE spectrometer model MA250 with a ^{57}Co/Rh source at room temperature using αFe as reference. The powder XRD data were obtained in a Rigaku model Geigerflex using Cu Kα radiation scanning from 2 to 75° at a scan rate of 4° min^{-1}. A scanning electron microscope (SEM) manufactured by JEOL Ltd., was used. SEM was coupled with EDS/INCA 350 (energy dispersive X-ray analyzer) manufactured by Oxford Instruments. DSC (RIGAKU MOD 8065 D1) analysis was operated in an air atmosphere with a heating rate of 10 °C min^{-1}.

2.2. Reactions

The hydrogen peroxide (Synth) decomposition study was carried out with 5 mL of 2.9 mol L^{-1} H_2O_2 and 10 mg of catalyst by measuring the formation of gaseous O_2 in a volumetric glass system. The oxidation of 50 mg L^{-1} methylene blue dye with H_2O_2 (0.3 mol L^{-1}) at pH 6.0 (natural pH of the H_2O_2 solution) was carried out with a total volume of 10 mL and 10 mg of the oxide catalyst. The reactions were monitored by UV–vis measurements (Shimadzu-UV-1601 PC). All the reactions were carried out under magnetic stirring in a recirculating temperature controlled bath kept at 25 ± 1 °C.

2.3. Studies by ESI-MS

In an attempt to identify the intermediate formation, the methylene blue decomposition was also monitored with the positive ion mode ESI-MS of an Agilent MS-ion trap mass spectrometer. The reaction samples were analyzed by introducing aliquots into the ESI source with a syringe pump at a flow rate of 5 mL min^{-1}. The spectra were obtained as an average of 50 scans of 0.2 s. Typical ESI conditions were as follows: heated capillary temperature of 1508 °C; sheath gas (N_2) at a flow rate of 20 U (4 L min^{-1}); spray voltage of 4 kV; capillary voltage of 25 V; tube lens offset voltage of 25 V.

2.4. Computational methods

The calculations were carried out with the package Gaussian98 [11]. All the transition states, intermediates and precursors involved were calculated. Each conformer was fully optimized by DFT [12]. Density Functional Theory (DFT) methods have been increasingly applied to the study of reaction mechanisms. This approach is interesting because it includes the effect of electronic correlations and allows for the calculation of larger systems [13,14]. Nowadays, that is a well-established technique applied to numerous cases [14–17]. The energy profile at selected DFT geometries along the reaction pathway has been computed at B3LYP level of theory using the 6-31+G (d,p) basis set. The DFT calculations were applied with the functional correlation of Lee, Yang and Parr (LYP), which includes both local and non-local terms [13,14], and Becke's 1988 function, which includes Slater exchange along with corrections involving the gradient of electronic density (B3LYP). For all the different calculation methods, the algorithms conjugate gradient and quasi-Newton-Raphson were used for the geometry optimization until a gradient of 10^{-9} atomic units was obtained. The final geometries were obtained with DFT using the density functional B3LYP using the basis set 6-311+G** [13,14]. This computational procedure has been employed previously on similar systems with success [15,16]. Furthermore, after each optimization the nature of each stationary point was established by calculating and diagonalizing the Hessian matrix (force constant matrix). The unique imaginary frequency associated with the transition vector (TV) [17], i.e., the eigenvector associated with the unique negative eigenvalue of the force constant matrix, has been characterized.

3. Results and discussion

3.1. Characterization

Elemental analysis by EDS confirmed that samples Nb4 and Nb11 contained 4 and 11% niobium, respectively. The powder XRD patterns of the pure goethite and Nb4 samples (not showed here) indicate the presence of a hexagonal crystalline phase (d = 0.497, 0.418, 0.336, 0.269, 0.244, 0.225 and 0.172 nm) relative to goethite. The broadening of the reflections of the Nb4 sample compared to reflections observed in the pure goethite sample indicates that niobium induces a decrease in particle size, but falls short of proving that isomorphic substitution of Fe^{3+} by Nb^{5+} has occurred because the ionic radius of both Fe^{3+} and Nb^{5+} is 64 pm and thus no change in lattice parameter can be observed. The increase in non-crystalline materials in the XRD patterns obtained for the Nb7 and Nb11 samples revealed that Nb induced a loss of crystallinity in the goethite which was proportional to the Nb content.

The Mössbauer parameters (Table 1) for the materials were consistent with a mixture of pure and substituted goethite particles. Pure, well crystallized goethite gives a magnetically ordered Mossbauer spectrum (sextet) at room temperature. As non-magnetic cations (e.g., Nb) substitute for Fe in the goethite structure, the magnetic domain size decreases and the magnetic order disappears, causing the sextet to collapse into a doublet. In agreement with XRD, the Mössbauer spectra for the Nb4, Nb7 and Nb11 samples therefore revealed that niobium substitution lead to a decrease in the crystallinity and/or particle size and crystalline perfection as evidenced by the appearance of the observed central doublets (Fig. 1). The quadrupole shift also decreased, indicating that the increased niobium content distorted the crystalline structure of the

Table 1
Fitted room temperature Mössbauer parameters for goethites (δ = isomer shift relative to αFe; ε = quadrupole shift, Δ = quadrupole splitting; B_{hf} = hyperfine field and RA = relative sub-spectral area)

Sample	δ (mm s^{-1})	ε, Δ (mm s^{-1})	B_{hf} (T)	RA (%)	Phase
Pure goethite	0.377(3)	−0.250(6)	36.5(1)	88.5(2)	Gt
	0.371(7)	0.69(3)		11.5(2)	$^{VI}Fe^{3+}$
Nb4	0.36(1)	−0.21(2)	35.98(1)	22.3(2)	Gt
	0.369(9)	0.70(3)		77.7(2)	$^{VI}Fe^{3+}$
Nb7	0.41(3)	−0.18	36.11(6)	7.8(2)	Gt
	0.354(2)	0.707(3)		92.2(2)	$^{VI}Fe^{3+}$
Nb11					
	0.346(2)	0.713(3)		100.0(5)	$^{VI}Fe^{3+}$

goethite due to the substitution of Fe by Nb. Moreover, the isomer shift of the doublets decreased with an increase of Nb content. This fact is evidence that isomorphic substitution of Fe by Nb is occurring in the goethite. Nb has a smaller electronegativity than Fe, which causes a decrease in the isomer shift. In Nb11 sample the magnetic domain size is so small that no magnetic order is observed. Some studies [18,19] asserted that the disappearance of the sextet in the Mössbauer spectra of goethite in favor of a doublet is evidence of oxygen vacancy sites in the goethite structure. Because the presence of niobium during the preparation of goethite produces a structure characterized by this same collapse of the sextet into a doublet, oxygen vacancy sites may be increasingly present in samples Nb7 and Nb11, which suggests the incorporation of Nb into the goethite structure. Morales et al. [20], Schwertmann et al. [21] and Krehula et al. [19,22] concluded that the main effect of doping with several cations, such as Ni, Cr, Mn, and Ga, was a reduced goethite crystallite size.

The FTIR spectrum of pure goethite (Fig. 2a) contains an intense band at 3150 cm^{-1}, due to bulk hydroxyl stretching, and important diagnostic O–H bending bands at about 890 (Fe–OH) and 793 (Fe–OH) cm^{-1}, which vibrate in and out of the plane, respectively [8], and at 635 cm^{-1} (Fe–O stretching). FTIR spectra of doped goethite showed similar features to the pure goethite, except the sample with high Niobium content (sample

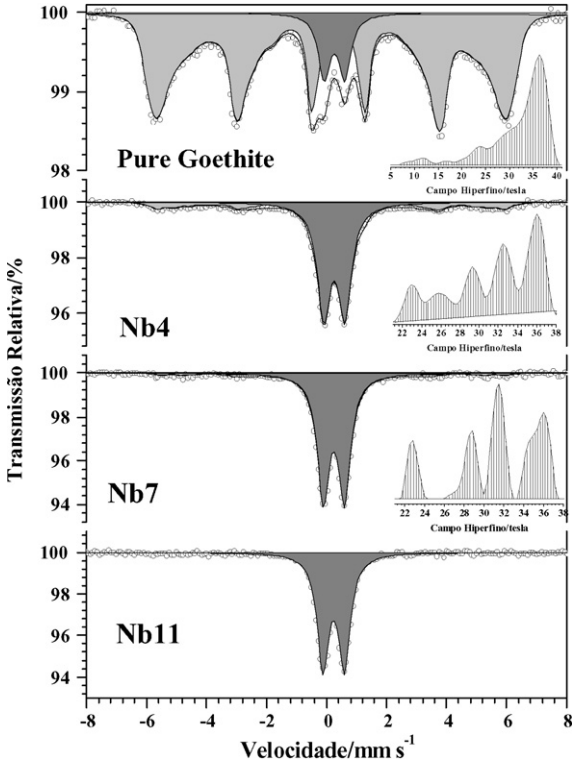

Fig. 1. Mössbauer spectra of the goethites at room temperature.

Nb11) exhibited noticeable spectral differences from pure goethite. The Fe–O stretching band was broadened and shifted to 609 cm^{-1} and the O–H bending band at 890 cm^{-1} shifted to 858 cm^{-1}, which is consistent with Nb being incorporated into the goethite structure [22]. Stiers and Schwertmann [23] also reported shifts in the O–H bending band at 888 cm^{-1} with increased substitution of Mn^{3+} or Al^{3+} for Fe^{3+} in goethite.

DSC analyses revealed that increasing the Nb content of the sample increased the temperature at which the phase transition of goethite to hematite occurred (Fig. 2b), shifting from approximately 218 °C for pure goethite in air to 251 °C and 271 °C for samples Nb7 and Nb11 in air, respectively. For synthetic and natural goethites the temperature of this

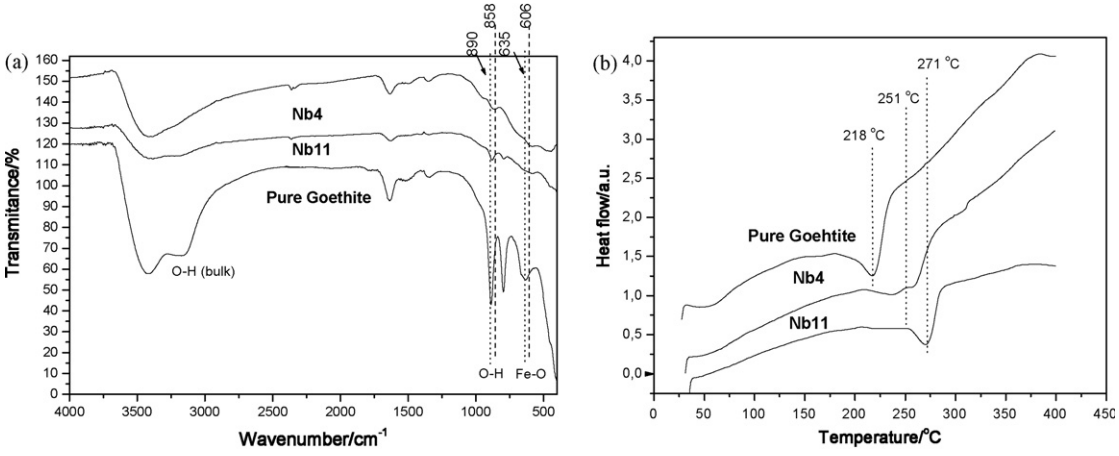

Fig. 2. FTIR (a) and DSC (b) analyses of the pure goethite, Nb4 and Nb11.

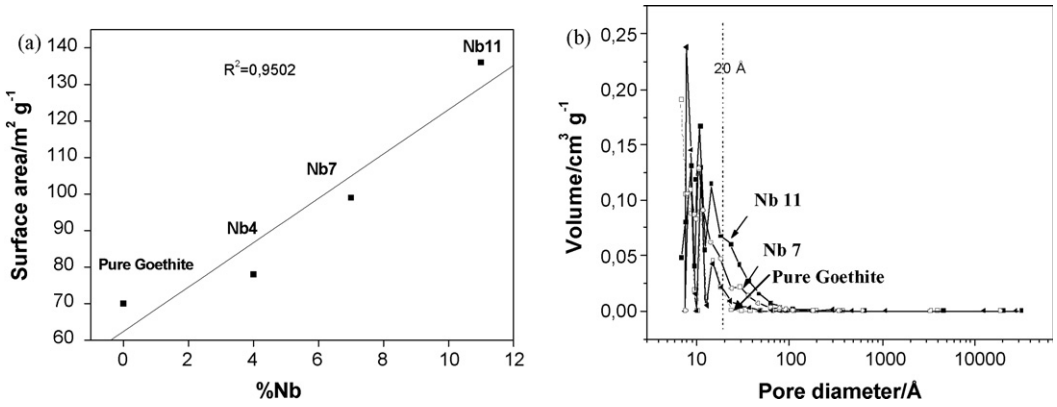

Fig. 3. Variation of specific surface area with Nb presence (a) BJH pore size distribution (b) of the goethites.

endothermic peak is well known to increase with increasing crystallite size [24–25]; but, as the XRD and Mössbauer data showed, increasing the Nb content actually decreases the crystallinity of the goethite [10]. This phenomenon was further confirmed by N_2 adsorption–desorption analysis, which found that the BET specific surface areas of pure goethite, Nb4, Nb7, and Nb11 (Fig. 3a) increased in the order 70, 78, 99, and 136 $m^2\ g^{-1}$, respectively. The crystallinity and crystallite size should vary inversely with these values, especially in the mesoporous region. The observed increase in BET surface area is likely also related to an increase in the pore diameter. The pore-size distributions were determined with the Barrett–Joyner–Halenda (BJH) pore size distribution for these samples (Fig. 3b) clearly showed that the presence of Nb gradually produced materials with greater pore diameters.

Scanning electron micrographs of the samples revealed that Nb substitution changes the morphology from a smooth surface in the pure goethite (Fig. 4a) to rough surface in samples Nb4 and Nb11 (Figs. 4c and e).

3.2. H_2O_2 decomposition

The catalytic activity of the goethites was studied using two reactions: (i) H_2O_2 decomposition to O_2 ($H_2O_2 \rightarrow H_2O + 1/2O_2$); and (ii) oxidation of the model contaminant methylene blue dye with H_2O_2 in aqueous medium. The decomposition of H_2O_2 in the presence of the different goethite samples approximately followed pseudo zero-order kinetics, as indicated by the nearly linear plots obtained between H_2O_2 concentration and time of reaction (Fig. 5a). Ferraz et al. [26] proposed that in the presence of other iron phases the decomposition mechanism involves radical formation, such as *OH or *OOH [25], but this apparently is not true in the present case, at least within the first 60 min, because the addition of phenol, a radical scavenger that would react with radical intermediates, had no inhibitory effect on the H_2O_2 decomposition rate in the presence of sample Nb11 (Fig. 5b). The same result was also observed when hydroquinone or ascorbic acid was added (Fig. 5b). Perhaps this is because of a competitive process involving the organic substrate and the active surface, such as proposed by Costa et al. [27]. In this scenario, oxygen vacancies $[]_{surf}$ at the oxide surface react with H_2O_2 to produce O_2 (Eq. (1) and (2)). This mechanism was first proposed, however, for oxides such as perovskite [27] and is believed to be uncommon in the iron oxides.

$$[] + H_2O_2 \rightarrow H_2O + [O_{ads}] \quad (1)$$

$$2[O_{ads}] \rightarrow O_2 \quad (2)$$

3.3. Methylene blue dye oxidation

The oxidation of methylene blue by H_2O_2 in the presence of goethite may be represented by Eq. (3):

$$\text{methyleneblue} \rightarrow \text{partiallyoxidizedintermediates} \rightarrow \rightarrow \rightarrow CO_2 + H_2O \quad (3)$$

and is monitored by UV–vis absorption at 663 nm. In the control experiment where goethite was absent, no significant discoloration was observed (Fig. 6) even after 120 min reaction. In the presence of pure goethite, a low activity of methylene blue dye oxidation was observed with only 15% color reduction after 120 min. On the other hand, in the presence of Nb-substituted goethite Nb11, catalytic discoloration of up to 85% was observed after 120 min.

3.4. Identification of intermediates via On-line ESI-MS monitoring

Reaction intermediates from oxidation of methylene blue dye in the presence of Nb11 were identified in real time using ESI-MS (Fig. 7). As expected, at zero reaction time (Fig. 7a), with the ESI-MS operating in the positive ion mode, the presence of only a single cation ($m/z = 284$) in aqueous solution was observed. However, after 60 min of reaction (Fig. 7b) a new and relatively intense signal with $m/z = 270$ was also clearly detected. After reaction time of 180 min (Fig. 7c) the signals with $m/z = 105, 129, 187, 227$, and 270 were detected. Based on the detection of these m/z signals a simple reaction scheme (Fig. 8) with intermediates **I–V.3** can be proposed for the oxidation of methylene blue dye by the Nb11 catalyst.

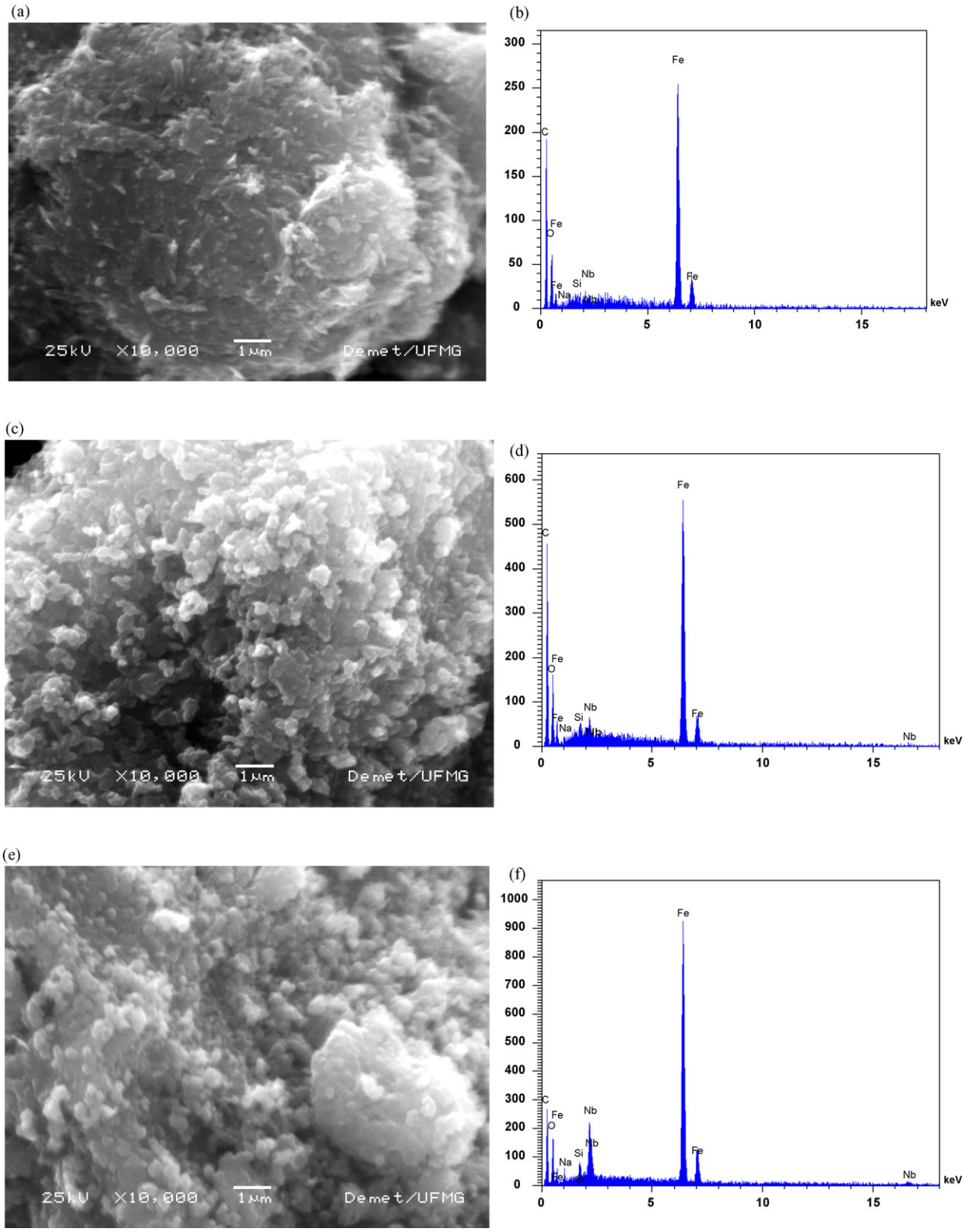

Fig. 4. SEM and EDS analyses of the goethites with niobium.

3.5. Theoretical results

According to the conventional mechanism for H_2O_2 decomposition in a Fenton reaction, the reaction may be initiated by an iron active site on the surface of the composite, at which the H_2O_2 produces a *OH; or, by a process that involves the peroxide itself which transfers an electron to an oxidizing site yielding a *OOH species [28]. According to the latter mechanism, the fragmentation pathway would be similar to the one described in a previous paper [25]; but, as shown in Fig. 7,

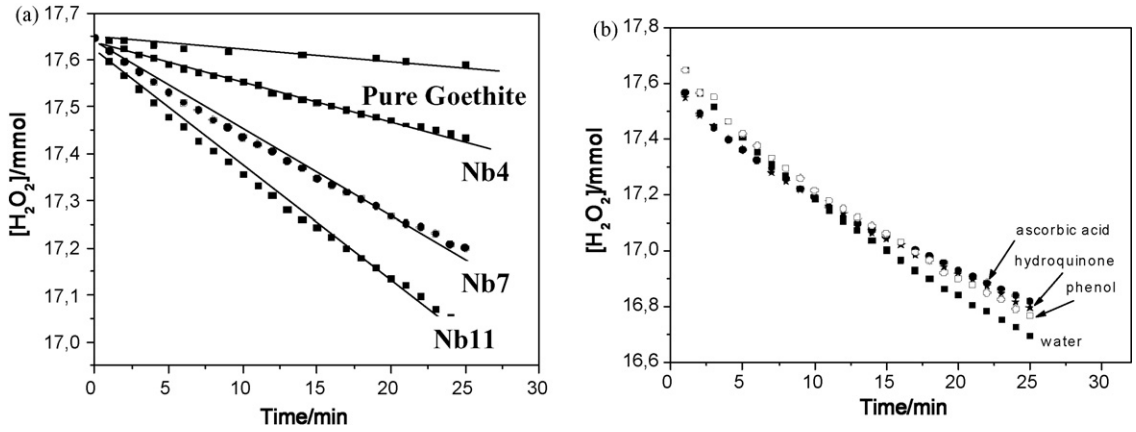

Fig. 5. The H_2O_2 decomposition in water (a) and with organic compounds (b) in the presence of the different goehites.

the fragmentation path for methylene blue dye observed in the present study was considerably different. Instead, previously uninvestigated degradation intermediates were observed. This strongly suggests a new reaction mechanism in which the reaction is initiated by neither of the conventional ways. The mechanism for the Nb-goethite catalyst could, therefore, involve oxygen vacancies at the goethite surface, which differs from the heterogeneous Fenton reaction described in the literature for iron phases [19].

In order to shed more light on this alternative reaction mechanism for Nb-substituted goethites, Gibbs free energy calculations were performed using the *Gaussian98* software to determine the stability of intermediates [11]. All discussions concerning the energy differences and the energy barriers refer to the Gibbs term, corrected for the zero point energy at 298.15 K. Results from the theoretical model agreed well with the experimental geometry for the methylene blue molecule [23]. After 60 min of reaction, the most intense fragment observed in mass spectra corresponded to $m/z = 270$ (Fig. 7), which is associated with the loss of a methyl group.

Further insight was obtained by performing *ab initio* calculations of thermodynamic stability (Table 2), which identified an energy barrier of 24 kcal mol^{-1} for the formation of intermediate product **II**. This energy is considerably lower than that involved in the hydroxylation of the aromatic ring [25]. As expected, the participation of the oxygen vacancies on the oxide surface in the oxidation reaction resulted in chemical species less reactive than the *OH radical in solution. The formation of **II** was followed by additional loss of a –N(CH3) group, resulting in intermediate product **III** ($m/z = 227$) with an energy barrier of +83.25 kcal mol^{-1} (Table 2, Fig. 8). The loss of the –NH(CH3) group can produce a neutral fragment (**IV**), $m/z = 198$, from **III** to **IV**, with an energy barrier of +58.67 kcal mol^{-1}. Due to its total charge, this fragment is undetected experimentally; however, we believe that **IV** could be a key intermediate for formation of an important fragment observed at $m/z = 187$ (Fig. 7). This fragment is associated with

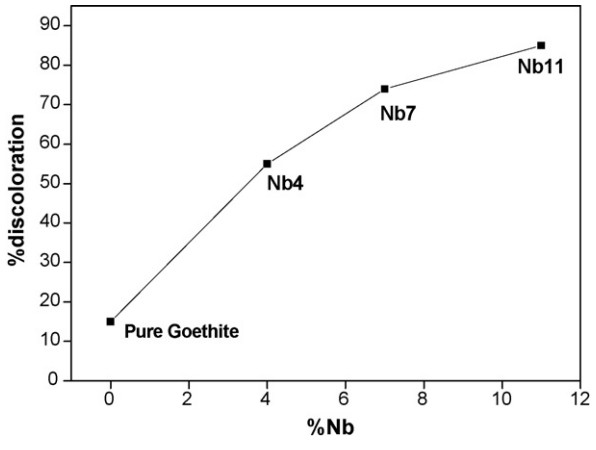

Fig. 6. Discoloration measurements using the dye methylene blue as probe molecule in the presence of goethites with niobium.

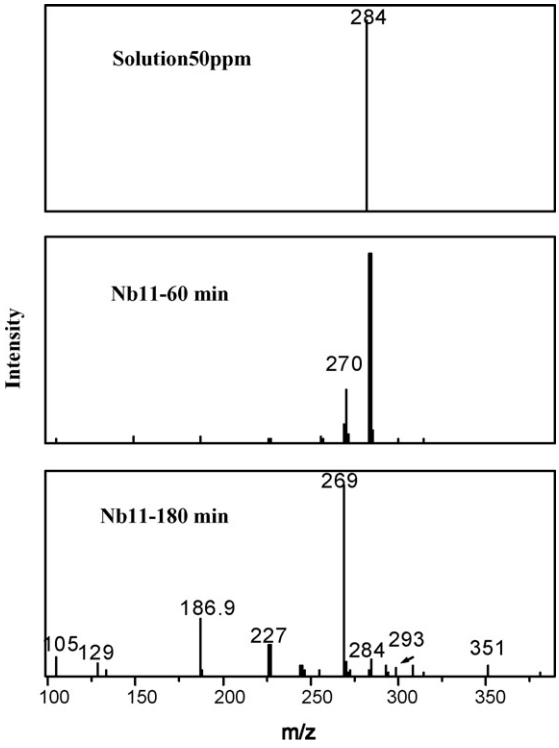

Fig. 7. ESI mass spectra in the positive ion mode for monitoring the oxidation of methylene blue dye in water by the goehites and H_2O_2 system at different reactions times.

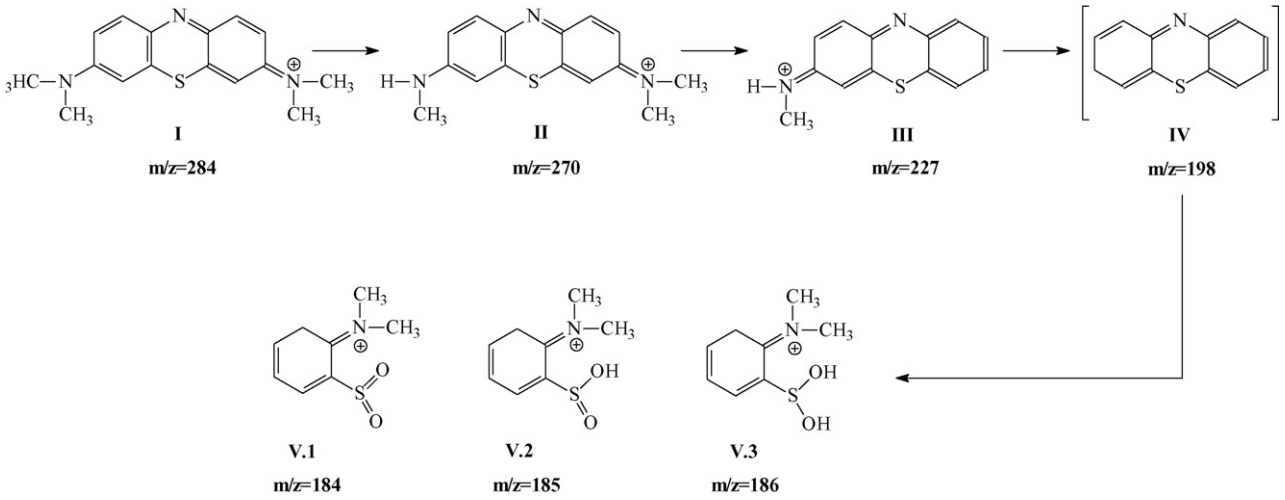

Fig. 8. Scheme with intermediates proposed for the oxidation of methylene blue dye ($m/z = 284$) by goethites and H_2O_2 system.

possible structures **V.1–3** (Fig. 8). According to data listed in Table 2, energy barriers of 1.29, 0.84, and 0.46 kcal mol^{-1} may be attributed to the intermediates **V.1**, **V.2** and **V.3**, respectively. This means that the intermediate **V.3** is more stable than other alternatives and that **IV** would be a key intermediate that points out the rapid and high probability of formation of **V.3**. Again, in this case no hydroxylation on the aromatic ring occurs, in contrast to a Fenton-like mechanism [25].

At the second step of the transformation (180 min of reaction), the magnitude of the signals $m/z = 105$, 129, and 351 are significant (Fig. 7). These signals have already been well characterized both experimentally and theoretically as a result of hydroxylation of aromatic ring through a Fenton-like mechanism, which was followed by formation of hydroquinone-like intermediates generated by *OH attack. This is an unstable, but key intermediate which points out the facility with which the chemical bonds of the aromatic ring rupture. This could then account for the formation of the signals $m/z = 105$ and 129. Thus, our results indicate that two competing mechanisms could occur: (i) reaction at the oxygen vacancy sites in Nb-substituted goethites, yielding the intense fragments $m/z = 270$, 227, and 187 (Fig. 7), which are associated with intermediates **II**, **III**, and **IV**, respectively (Fig. 8); and (ii) a Fenton mechanism resulting in fragments $m/z = 105$, 129, and 351. The fist step of the transformation (60 min of reaction) would occur preferentially via mechanism (i), whereas both mechanisms (i) and (ii) could occur simultaneously at the second step (180 min) of the transformation.

Table 2
Gibbs free energy of the reaction intermediates using B3LYP/6-311+G**

Intermediate	ΔG (kcal mol^{-1})
I	0.00
II	+24.59
III	+83.25
IV	+58.67
V.1	+1.29
V.2	+0.84
V.3	+0.46

As discussed above and as noted previously [25], the degradation of methylene blue via a Fenton-like mechanism exhibits an induction period at the beginning of the reaction, which suggests that some degradation intermediates play an important role in promoting the Fenton reaction. The presence of *OH in the reaction medium, nevertheless, probably invokes the oxidation of I, which in turn can generate, for instance, the stable species with $m/z = 105$, 129, and 351. In line with this observation, at the first moment of reaction the hydrogen peroxide decomposition could take place via mechanisms (i) generating the fragments $m/z = 270$, 227, and 187. These results are, therefore, evidence that the oxidation reaction of methylene blue in water with goethites likely occurs through both of the competitive mechanisms (i) and (ii), but further and more accurate theoretical calculations are needed to verify the vacancy sites mechanism (i).

Until now, no other theoretical study has investigated the degradation of methylene blue via a heterogeneously catalyzed Fenton reaction. One should keep in mind, however, that the mechanisms for hydrogen peroxide decomposition cannot be completely understood from these observations. Several electron transfer processes are thought to take place during that reaction.

4. Conclusion

The hypothesis that Nb substitution in goethite creates surface oxygen vacancies in the Nb-goethite is supported by Mössbauer spectra, by hydrogen peroxide decomposition behavior in the presence of radical scavengers, and by the catalytic oxidation of organic dye as shown by ESI-MS. Understanding the mechanisms for catalysis is relevant to the formulation of novel, efficient, and cost-effective processes for the remediation of organic contaminants in wastewaters. The theoretical results presented herein suggest that two competitive mechanisms could occur in Nb-substituted goethites; one involving surface oxygen vacancies in Nb-substituted goethite and the other following a Fenton-like process.

Acknowledgments

Work supported by CNPq and FAPEMIG (Brazil). Authors are indebted to prof. Dr. C. A. Taft (CBPF) for the computation facilities, Patricia-Patterson for SEM-EDS analyses, Profa. Irene Yoshida (UFMG) for DSC analyses and CAPQ (Ufla).

References

[1] R.C.C. Costa, M.F.F. Lelis, L.C.A. Oliveira, J.D. Fabris, J.D. Ardisson, R.R.V.A. Rios, C.N. Silva, R.M. Lago, J. Hazard. Mater. 129 (2006) 171.
[2] R.L. Valentine, H.C. Ann Wang, J. Environ. Eng. 124 (1998) 31–38.
[3] J. He, X. Tao, W. Ma, W. Jincai, Chem. Lett. (2002) 66–87.
[4] M. Lu, C. Chun, N. Jong, H.H. Huang, Chemosphere 46 (2002) 131–136.
[5] R. Andreozzi, A. D'Apuzzo, R. Marotta, Water Res. 36 (2002) 4691–4698.
[6] S.R. Kunel, B. Neppolian, H. Choi, J.W. Yang, Soil Sediment Contam. 12 (2003) 101–117.
[7] G. Ceti, P. Perathoner, T. Torre, M.G. Verduna, Catal. Today 55 (2000) 61–69.
[8] N. Al-Hayek, M. Dore, Water Res. 24 (1990) 973–982.
[9] R.J. Watts, M.D. Udell, S.H. Kong, Environ. Eng. Sci. 16 (1999) 93–103.
[10] R.M. Cornell, U. Schwertmann, The Iron Oxides, 2nd ed., Weinheim-VHC, New York, 2003.
[11] Gaussian 98, Revision A.9, M.J. Frisch, G.W. Trucks, H.B. Schlegel, G.E. Scuseria, M.A. Robb, J.R. Cheeseman, J.A. Montgomery Jr., T. Vreven, K.N. Kudin, J.C. Burant, J.M. Millam, S.S. Iyengar, J. Tomasi, V. Barone, B. Mennucci, M. Cossi, G. Scalmani, N. Rega, G.A. Petersson, H. Nakatsuji, M. Hada, M. Ehara, K. Toyota, R. Fukuda, J. Hasegawa, M. Ishida, T. Nakajima, Y. Honda, O. Kitao, H. Nakai, M. Klene, X. Li, J.E. Knox, H.P. Hratchian, J.B. Cross, V. Bakken, C. Adamo, J. Jaramillo, R. Gomperts, R.E. Stratmann, O. Yazyev, A.J. Austin, R. Cammi, C. Pomelli, J.W. Ochterski, P.Y. Ayala, K. Morokuma, G.A. Voth, P. Salvador, J.J. Dannenberg, V.G. Zakrzewski, S. Dapprich, A.D. Daniels, M.C. Strain, O. Farkas, D.K. Malick, A.D. Rabuck, K. Raghavachari, J.B. Foresman, J.V. Ortiz, Q. Cui, A.G. Baboul, S. Clifford, J. Cioslowski, B.B. Stefanov, G. Liu, A. Liashenko, P. Piskorz, I. Komaromi, R.L. Martin, D.J. Fox, T. Keith, M.A. Al- Laham, C.Y. Peng, A. Nanayakkara, M. Challacombe, P.M.W. Gill, B. Johnson, W. Chen, M.W.Wong, C. Gonzalez, J.A. Pople, Gaussian Inc., Wallingford CT, 1998.
[12] H.G. Li, G.K. Kim, C.K. Kim, S. Rhee, I. Lee, J. Am. Chem. Soc. 123 (2001) 2326.
[13] A.D. Becke, J. Chem. Phys. 98 (1993) 5648.
[14] S. El-Taher, R.H. Hilal, Int. J. Quantum Chem. 20 (2001) 242.
[15] T.C. Ramalho, C.A. Taft, J. Chem. Phys. 123 (2005) 54319–54326.
[16] T.C. Ramalho, R.R. da Silva, J.M. Santos, J.D. Figueroa-Villar, J. Phys. Chem. A 110 (2006) 1031–1040.
[17] J.W. McIver Jr., Acc. Chem. Res. 7 (1994) 72.
[18] S. Bocquet, R.J. Pollard, J.D. Cashion, Phys. Rev. B 46 (1992) 11657.
[19] C.A. dos Santos, A.M.C. Horbe, C.M.O. Barcellos, J.B.M. Cunha, Solid State Commun. 118 (2001) 449–452.
[20] A.L. Morales, C.A. Barrero, F. Jaramillo, C. Arroyave, J.M. Greneche, Hyp. Interact. 148 (2003) 135–144.
[21] U. Schwertmann, U. Gasser, H. Sticher, Geochim. Cosmochim. Acta 53 (1989) 1293–1297.
[22] S. Krehula, S. Music, S. Popovic, J. Alloys Compd. 403 (2005) 368–375.
[23] W. Stiers, U. Schwertmann, Geochim. Cosmochim. Acta 49 (1985) 1909–1911.
[24] L.C.A. Oliveira, J.D. Fabris, R.V.A. Rios, W.N. Mussel, R.M. Lago, Appl. Cat. A: Gen. 259 (2004) 253–259.
[25] L.C.A. Oliveira, J.D. Fabris, K. Sapag, M.C. Guerreiro, M. Gonçalves, M. Pereira, Appl. Cat. A: Gen. 316 (2007) 117–124.
[26] W. Ferraz, L.C.A. Oliveira, R. Dallago, L. Conceição, Catal Commun. 8 (2007) 131–134.
[27] R.C.C. Costa, F. Lelis, L.C.A. Oliveira, J.D. Fabris, J.D. Ardisson, R.R.A. Rios, C.N. Silva, R.M. Lago, Catal. Commun. 4 (2003) 525.
[28] F. Martínez, G. Calleja, J.A. Melero, R. Molina, Appl. Catal. B: Environ. 70 (2007) 452–460.

Hyperfine Interact
DOI 10.1007/s10751-009-0097-3

Niobian iron oxides as heterogeneous Fenton catalysts for environmental remediation

Diana Q. L. Oliveira · Luiz C. A. Oliveira · Enver Murad · José D. Fabris · Adilson C. Silva · Lucas Morais de Menezes

Abstract Heterogeneous Fenton or Fenton-like reagents consist of a mixture of an iron-containing solid matrix and a liquid medium with H_2O_2. The Fenton system is based on the reaction between Fe^{2+} and H_2O_2 to produce highly reactive intermediate hydroxyl radicals ($^{\bullet}OH$), which are able to oxidize organic contaminants, whereas the Fenton-like reaction is based on the reaction between Fe^{3+} and H_2O_2. These heterogeneous systems offer several advantages over their homogeneous counterparts, such as no sludge formation, operation at near-neutral pH and the possibility of recycling the iron promoter. Some doping transition cations in the iron oxide structure are believed to enhance the catalytic efficiency for the oxidation of organic substrates in water. In this work, goethites synthesized in presence of niobium served as precursors for the preparation of magnetites (niobian magnetites) via chemical reduction with hydrogen at 400°C. These materials were used as Fenton-like catalysts. Both groups of (Nb, Fe)-oxide samples were characterized by ^{57}Fe Mössbauer spectroscopy at 298 K. The results show that increasing niobium contents raise the catalytic potential for decomposition of methylene blue, which was, in this work, used as a model molecule for organic substrates in water.

Keywords Magnetite · Niobium · Fenton reaction

D. Q. L. Oliveira (✉) · E. Murad · J. D. Fabris · L. M. de Menezes
Department of Chemistry, Federal University of Minas Gerais, 31270-901 Belo Horizonte, Minas Gerais, Brazil
e-mail: dianaquintao@ufmg.br

L. C. A. Oliveira · A. C. Silva
Department of Chemistry, Federal University of Lavras, 37200-000 Lavras, Minas Gerais, Brazil

Published online: 26 September 2009

1 Introduction

Spinel iron oxides are of technological importance because of their structural, electronic, magnetic and catalytic properties [1]. Other metal cations can isomorphously replace iron in magnetite (Fe_3O_4), thereby changing selected physico-chemical properties of the material, depending on the nature and amount of the metal and on the structural site on which the metal is incorporated [1].

A novel and promising catalytic application of iron oxides is the chemical decomposition of organic contaminants in wastewaters, using H_2O_2 in a heterogeneous Fenton system [2–6]. In this heterogeneous Fenton system the iron oxide activates H_2O_2 to generate radicals, especially $^{\bullet}OH$, which can completely oxidize organics present in the aqueous medium [7]. Magnetite has been observed to be particularly active for the Fenton oxidation of organics by H_2O_2. This activity was assigned to the presence of Fe^{2+} species in the magnetite structure, which can activate H_2O_2 by a Haber–Weiss mechanism [8]. Recent work has shown that the activity of magnetite is strongly influenced by the presence of different metals in the spinel structure. Thus the introduction of cobalt and manganese in the magnetite structure remarkably increased the reactivity towards the Fenton chemistry, whereas nickel showed an inhibitory effect [9–11].

In this work, niobium associated with magnetite ("niobian magnetite") has been used to produce an active heterogeneous spinel system. Nb^{5+} shows interesting features for this system such as an ionic radius (64 pm in octahedral coordination) [12] that is comparable to that of high-spin octahedral Fe^{3+} (65 pm) and, based alone on size, might be structurally incorporated in magnetite, and a high reactivity towards H_2O_2 activation. To our knowledge, no systematic studies on iron-rich spinels prepared in a niobium-containing medium or their catalytic properties have been reported so far.

2 Experimental

2.1 Synthesis and characterization

The goethite samples were prepared by precipitation of $Fe(NO_3)_3{\cdot}6H_2O$ (1 mol L^{-1}) with potassium hydroxide (5 mol L^{-1}) and the addition of 2, 7 and 17 mol% niobium that is present in $NH_4[NbO(C_2O_4)_2(H_2O)](H_2O)_n$ supplied by CBMM (Araxá, MG, Brazil). The precipitates were washed with water until the pH became adjusted to 7; they were then transferred to a 2 L-beaker with distilled water and aged for 72 h at 60°C. The so produced goethites were finally reduced with hydrogen for 30 min at 400°C to produce magnetites.

The total iron was determined by $K_2Cr_2O_7$ titration and energy dispersive spectrometry (EDS) analyses were performed using a Jeol JXA-8900RL microscope. Mössbauer spectra were taken at room temperature (298 K) on a CMTE MA250 spectrometer with a constant acceleration drive and a $^{57}Co/Rh$ source at room temperature. The experimental data were fitted using Lorentzian functions with a least-squares procedure based on the NORMOS program, and calibration was effected and isomer shifts are given relative to α-Fe. Powder X-ray diffraction (XRD) was carried out on a Rigaku Geigerflex 3064 diffractometer equipped with

Table 1 Compositions of the niobian magnetites from chemical analyses and EDS data

Sample	Total Fe/%	Nb/%
(a) Pure Mt	70(3)	0
(b) Mt-Nb2	67(1)	2.1(2)
(c) Mt-Nb7	61(1)	7(1)
(d) Mt-Nb17	59(1)	17(2)

a Cu tube and a graphite diffracted-beam monochromator. To improve accuracy, additional scans of the samples were taken with Si as internal standard.

2.2 Reactions

The hydrogen peroxide decomposition was carried out by mixing 10 mL H_2O_2 2.9 mol L^{-1} and 10 mg catalyst and measuring the formed gaseous O_2 in a volumetric glass system. The oxidation of the methylene blue dye (50 mg L^{-1}) with H_2O_2 (0.3 mol L^{-1}) at pH 6.0 (the pH of the sole H_2O_2 solution) was carried out with a total volume of 10 mL and 10 mg of the oxide catalyst. The reactions were monitored by UV–vis measurements. All reactions were carried out under magnetic stirring in a recirculating controlled-temperature bath kept at 25 ± 1°C.

In an attempt to identify the intermediate products, the decomposition of methylene blue was also monitored with the positive ion mode ESI-MS in an Agilent MS-ion trap mass spectrometer (1100 Series). The reaction samples were analyzed by introducing aliquots into the ESI source with a syringe pump at a flow rate of 5 L min^{-1}. The spectra were obtained as an average of five scans of 0.2 s each. Typical ESI conditions were as follows: heated capillary temperature 325°C; sheath gas (N_2) at a flow rate of 20 units (ca. 4 L min^{-1}); spray voltage 4 kV; capillary voltage 25 V; tube lens offset voltage 25 V.

3 Results and discussion

3.1 Characterization of materials

Not unexpectedly, the chemical compositions of the niobian magnetites (Table 1) show a concurrent increase of niobium and decrease of iron.

Room-temperature Mössbauer spectra of the unsubstituted magnetite and the niobian series are shown in Fig. 1. While spectra of the pure magnetite and the samples prepared in presence of 2 and 7 mol% niobium show two characteristic sextets that can be assigned to Fe^{3+} on the A sites and Fe^{2+}/Fe^{3+} on the B sites of magnetite [13], the sample prepared in the presence of 17 mol% niobium shows only a minor indication of magnetite.

Analysis of the Mössbauer spectra (Table 2) shows the tetrahedral (A site) of the unsubstituted magnetite to have a hyperfine field (B_{hf}) of 49.0 T and the B (octahedral) site to have a hyperfine field of 45.8 T with isomer shifts (δ) relative to α-Fe of 0.28 and 0.67 mm s^{-1}, respectively. While these parameters resemble those of pure, stoichiometric magnetite [13], the area ratio of the B-site resonance to that of the A-site resonance (1.39) indicates the unsubstituted magnetite to have a composition given by $Fe_{2.94}O_4$, and thus to have undergone noticeable oxidation.

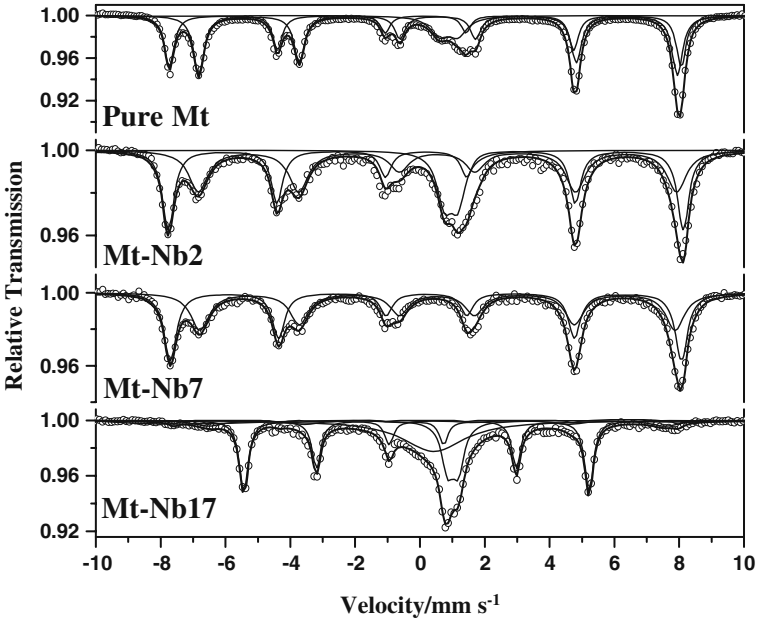

Fig. 1 Room-temperature Mössbauer spectra of the niobian magnetites

Table 2 Room-temperature (~298 K) Mössbauer parameters for pure magnetite and magnetites prepared in the presence of niobium

Sample	^{57}Fe site	δ/mm s^{-1}	2ε, Δ/mm s^{-1}	B_{hf}/T	Γ/mm s^{-1}	RA/%
Pure Mt	A	0.2831(8)	−0.010(1)	48.960(6)	0.349(2)	36.6(2)
	B	0.6680(7)	0.010(1)	45.786(5)	0.388(2)	50.8(2)
	Fe^{2+}	1.000(4)	0.571(7)	–	0.70[a]	12.6(1)
Mt-Nb2	A	0.295(2)	−0.013(3)	49.27(1)	0.433(5)	40.6(4)
	B	0.649(3)	0.012(6)	45.75(2)	0.72(1)	43.5(1)
	Fe^{2+}	1.076(3)	0.408(6)	–	0.55[a]	15.9(1)
Mt-Nb7	A	0.304(3)	−0.020(5)	48.90(2)	0.458(9)	50(1)
	B	0.642(5)	0.020(9)	45.46(4)	0.69(2)	50(1)
Mt-Nb17	A	0.30[a]	−0.02[a]	48.2(1)	0.42(6)	3.0(4)
	B	0.63[a]	0[a]	43.7(1)	0.71[a]	7.2(3)
	Fe^{2+}	1.124(3)	0.326(4)	–	0.42(1)	16.6(5)
	Fe^{0}	−0.0020(8)	0[a]	33.034(6)	0.323(3)	41.0(3)
	Doublet	0.59(2)	0[a]	–	2.29(4)	32.2(6)

δ isomer shift relative to α-Fe, 2ε quadrupole shift,Δ quadrupole splitting, B_{hf} magnetic hyperfine field, RA: relative sub-spectral area

[a]Parameter held fixed during fitting

The degree of oxidation rises with increasing niobium concentration during synthesis from the above value to $Fe_{2.92}O_4$ at 2% niobium in the synthesis solution and to $Fe_{2.91}O_4$ at 7% niobium. The line widths of the magnetites prepared in the presence of niobium, particularly those of the B sites, are furthermore significantly higher

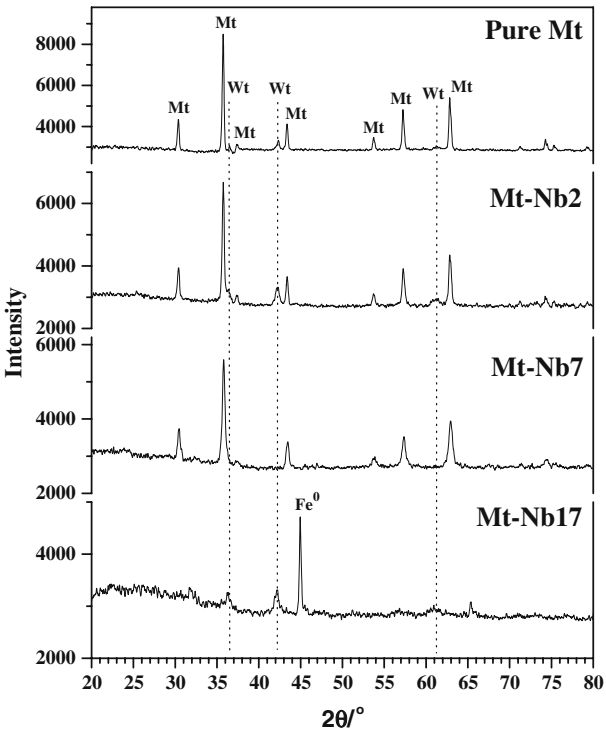

Fig. 2 X-ray diffraction diagrams of the niobian magnetites

than those of the pure magnetite. At a niobium concentration of 17%, magnetite formation is largely inhibited, but the Mössbauer spectrum indicates the presence of magnetically ordered metallic iron and paramagnetic Fe^{2+}. The magnetic hyperfine fields of the A site show no and the B-fields show little systematic variation as a function of the niobium concentration during synthesis. Because Nb^{5+} is a diamagnetic ion with a krypton configuration, this does not provide conclusive evidence for the concept that niobium has substituted iron in the magnetite structure. The lines of the magnetite components become broader as the concentration of niobium in the synthesis solution increases, indicating decreasing particle sizes. Mean coherence lengths calculated from broadening of the 311 diffraction line indicates a significant decrease from 62 to 45, 24 and 8 nm from the pure magnetite to the 2%, 7%, and 17% Nb samples, respectively.

Powder XRD (Fig. 2) also shows the samples to contain various proportions of magnetite (the sample prepared in the presence of 17% niobium again showing the lowest proportion of magnetite), and the samples prepared in the presence of 2% and 17% niobium show the presence of some wüstite ($Fe_{1-x}O$). Diffraction diagrams (not shown) were also taken under addition of Si as an internal standard for 2θ. The resulting patterns do not show a systematic variation of the position of the strongest magnetite peak (311) as a function of the niobium concentration, so that XRD also does not provide conclusive evidence for the incorporation of niobium in the magnetite structure.

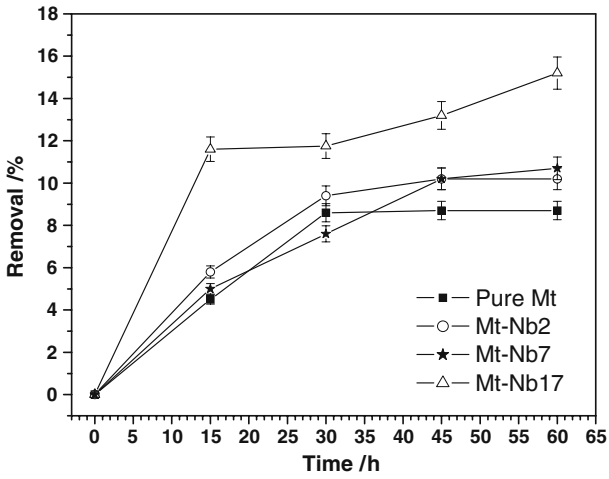

Fig. 3 Methylene blue discoloration in the presence of niobian magnetites

3.2 H_2O_2 decomposition and dye oxidation

The catalytic activity of the niobian magnetites was studied using two reactions: (1) the decomposition of H_2O_2 to O_2 ($H_2O_2 \rightarrow H_2O + 0.5\ O_2$) and (2) the oxidation of the model contaminant (methylene blue dye) with H_2O_2 in an aqueous medium. The reaction kinetics was investigated by UV/vis discoloration measurements to form non-colored intermediates. The discoloration of the solution of the dye is shown in Fig. 3.

The control experiment (only methylene blue and H_2O_2 but no catalyst) showed no significant discoloration even after a reaction time of 60 min. On the other hand, in the presence of the niobian magnetite catalyst and H_2O_2 as oxidant, discoloration can be observed. For the system niobian magnetite/H_2O_2, the discoloration is moderate in the presence of the pure magnetite and the magnetites prepared at low niobium contents. However, the sample prepared at high niobium content (Mt-Nb17) produces a catalytic discoloration of more than 15% after 60 min. This behavior can have several causes: sample mineralogy (e.g. the presence of metallic iron in the Mt-Nb17 sample), a catalytic enhancement due to the presence of Nb, and particle size changes. While some or all of these effects can act together to bring about the higher catalytic activity of the Mt-Nb17 sample, the drastic particle size reduction of magnetite in this sample indicates particle size to play a key role. Although H_2O_2 decomposition kinetics is a complex reaction, the linear behavior of the decomposition plots between 0 and 25 min suggests that the process can be approximated to pseudo-zero order kinetics [8].

Discoloration measured by UV–vis spectroscopy does not provide any information about reaction intermediates of the methylene blue oxidation. Such identification could be achieved by using mass spectroscopy with electrospray ionization. The identification of intermediates was studied obtaining spectra after 60 min of reaction in the presence of H_2O_2 (Fig. 4). The spectrum of methylene blue solution (without catalysts) indicated only one peak at $m/z = 284$ due to its cationic structure. After 1 h of reaction, intermediates were observed in the spectra, showing that the mineralization was not total. An intense peak at $m/z = 270$ suggested the beginning

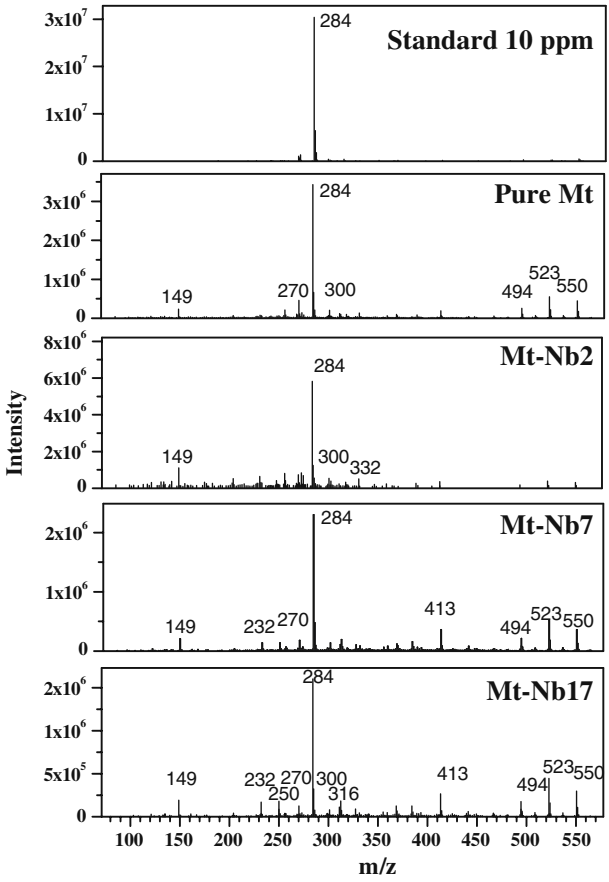

Fig. 4 Mass spectra of the reaction products of methylene blue oxidation with electrospray ionization as a function of the niobium concentration

of dye structure degradation. A signal at $m/z = 300$ and 316 is probably due to successive hydroxylation of the aromatic ring [14]. The peak at $m/z = 149$ is indicative of ring rupture and subsequent total mineralization [15].

4 Conclusions

The presence of niobium associated with magnetite has a significant effect on the crystallinity and catalytic activity of the oxide. In this study, the oxidation of organic compounds with H_2O_2 has been shown to probably take place via radicals, as suggested by ESI-MS data. An oxidation mechanism was indicated to occur by attack of the free radical *OH over the molecule, giving rise to hydroxylation products as principal by-products, although compounds resulting from ring cleavage are also detected. The presence of niobium increases the activity of the oxide for the H_2O_2 decomposition, and the surface niobian species seem to act directly in the catalytic properties of the niobian magnetites.

Acknowledgements Work supported by CAPES, CNPq and FAPEMIG (Brazil). The authors are indebted to the Brazilian Company of Metallurgy and Mining (CBMM) for providing the ammonium niobium oxalate salt from its industrial line. CNPq/Prosul (grant # 490132/2006-5) also supported the international mission by JDF to attend the Latin American Conference on the Applications of the Mössbauer Effect, LACAME 2008, in La Plata, Argentina.

References

1. Cornell, R.M., Schwertmann, U.: The Iron Oxides, 2nd edn. Wiley-VCH, Weinheim (2003)
2. Moura, F.C.C., Araújo, M.H., Costa, C.C., Fabris, J.D., Ardisson, J.D., Macedo, W.A.A., Lago, R.M.: Efficient use of Fe metal as an electron transfer agent in a heterogeneous Fenton system based on Fe/Fe_3O_4 composites. Chemosphere **60**, 1118–1123 (2005)
3. Lee, S., Oh, J., Park, Y.: Degradation of phenol with Fenton-like treatment by using heterogeneous catalyst (modified iron oxide) and hydrogen peroxide. Bull. Korean Chem. Soc. **27**, 489–494 (2006)
4. Baldrian, P., Merhautova, V., Gabriel, J., Nerud, F., Stopka, P., Hruby, M., Benes, M.J.: Decolorization of synthetic dyes by hydrogen peroxide with heterogeneous catalysis by mixed iron oxides. Appl. Catal. B **66**, 258–264 (2006)
5. Wu, R.C., Qu, J.H.: Removal of azo dye from water by magnetite adsorption–Fenton oxidation. Water Environ. Res. **76**, 2637–2642 (2004)
6. Lago, R.M., Moura, F.C.C., Ardisson, J.D., Macedo, W.A., Araujo, M.H., Silva, C.N.: Formation of highly reactive species at the interface Fe^0-iron oxides particles by mechanical alloying and thermal treatment: potential application in environmental remediation processes. Chem. Lett. **34**, 1172–1174 (2005)
7. Moura, F.C.C., Araujo, M.H., Dalmazio, I., Alves, T.M.A., Santos, L.S., Eberlin, M.N., Augusti, R., Lago, R.M.: Investigation of reaction mechanisms by electrospray ionization mass spectrometry: characterization of intermediates in the degradation of phenol by a novel iron/magnetite/hydrogen peroxide heterogeneous oxidation system. Rapid Commun. Mass Spectrom. **20**, 1859–1863 (2006)
8. Moura, F.C.C., Oliveira, G.C., Araujo, M.H., Ardisson, J.D., Macedo, W.A.A., Lago, R.M.: Highly reactive species formed by interface reaction between Fe^0-iron oxides particles: an efficient electron transfer system for environmental applications. Appl. Catal. A Gen. **307**, 195–204 (2006)
9. Costa, R.C.C., Lelis, M.F.F., Oliveira, L.C.A., Fabris, J.D., Ardisson, J.D., Rios, R.V.A., Silva, C.N., Lago, R.M.: Remarkable effect of Co and Mn on the activity of $Fe_{3-x}M_xO_4$ promoted oxidation of organic contaminants in aqueous medium with H_2O_2. Catal. Commun. **4**, 525–529 (2003)
10. Costa, R.C.C., Lelis, M.F.F., Oliveira, L.C.A., Fabris, J.D., Ardisson, J.D., Rios, R.V.A., Silva, C.N., Lago, R.M.: Novel active heterogeneous Fenton system based on $Fe_{3-x}M_xO_4$ (Fe, Co, Mn, Ni): the role of M^{2+} species on the reactivity towards H_2O_2 reactions. J. Hazard. Mater. **129**, 171–178 (2006)
11. Nejad, M.A., Jonsson, M.: Reactivity of hydrogen peroxide towards Fe_3O_4, Fe_2CoO_4 and Fe_2NiO_4. J. Nucl. Mater. **334**, 28–34 (2004)
12. Kaye, G.W., Laby, T.H.: Tables of Physical and Chemical Constants and some Mathematical Functions, p. 386. Longmans, Green and Co., London (1975)
13. Murad, E., Cashion, J.: Mössbauer Spectroscopy of Environmental Materials and their Industrial Utilization. Kluwer, Norwell (2004)
14. Oliveira, L.C.A., Ramalho, T.C., Gonçalves, M., Cereda, F., Carvalho, K.T., Nazzarro, M.S., Sapag, K.: Pure niobia as catalyst for the oxidation of organic contaminants: mechanism study via ESI-MS and theoretical calculations. Chem. Phys. Lett. **446**, 133–137 (2007)
15. Oliveira, L.C.A., Gonçalves, M., Guerreiro, M.C., Ramalho, T.C., Fabris, J.D., Pereira, M.C., Sapag, K.: A new catalyst material based on niobia/iron oxide composite on the oxidation of organic contaminants in water *via* heterogeneous Fenton mechanisms. Appl. Catal. A Gen. **316**, 117–124 (2007)

Applied Catalysis A: General 357 (2009) 79–84

Contents lists available at ScienceDirect

Applied Catalysis A: General

journal homepage: www.elsevier.com/locate/apcata

Nb-containing hematites $Fe_{2-x}Nb_xO_3$: The role of Nb^{5+} on the reactivity in presence of the H_2O_2 or ultraviolet light

Adilson C. Silva [a], Diana Q.L. Oliveira [a], Luiz C.A. Oliveira [a,*], Alexandre S. Anastácio [a], Teodorico C. Ramalho [a], João H. Lopes [b], Hudson W.P. Carvalho [c], Claudia E. Rodriguez Torres [d]

[a] Department of Chemistry, Federal University of Lavras, Lavras-MG 37200-000, Brazil
[b] Department of Chemistry, UNICAMP, Campinas-SP, Brazil
[c] Department of Physical-Chemistry, State University Júlio de Mesquita Filho, Araraquara-SP 14801-970, Brazil
[d] Department of Physical, National University of La Plata, La Plata - Bs.As 1900, Argentina

ARTICLE INFO

Article history:
Received 6 October 2008
Received in revised form 7 January 2009
Accepted 9 January 2009
Available online 16 January 2009

Keywords:
Hematite
Niobium
Organic oxidation
ESI-MS

ABSTRACT

A series of Nb-containing hematites, $Fe_{2-x}Nb_xO_3$ (%Nb = 0.00, 1.49, 5.00 and 9.24) was prepared using the conventional co-precipitation method. Mössbauer and temperature-programmed reduction (TPR) measurements suggested the formation of the crystalline phase with partial substitution of Fe^{3+} by Nb^{5+} in the structure. N_2 adsorption/desorption revealed that the presence of Nb has a remarkable effect on the textural properties of the material with an increase in the BET surface area. The reactivity of $Fe_{2-x}Nb_xO_3$ was investigated using the oxidation of the methylene blue dye used as a model pollutant. The obtained results showed that the presence of Nb seems not to act directly promoting the H_2O_2 decomposition, but improving the dye oxidation. The analysis using the ESI-MS technique showed partial oxidation observed through different intermediates before the mineralization. This suggests the use of Nb-doped hematite as an efficient catalyst in degradation reactions in the presence of H_2O_2 or ultraviolet light.

1. Introduction

Dye wastewater is characterized by large amounts of discharge, high concentration, and complex composition. Conventional dye wastewater treatment methods are gradually becoming inadequate to obtain higher environmental quality requirements. In recent years, various advanced oxidation processes such as, ozonation, wet air oxidation, supercritical water oxidation and photocatalytic oxidation have been proposed as substitutes for the conventional treatment techniques [1–4]. A novel and promising catalytic application for destruction of organic contaminants in wastewaters is the utilization of iron oxides and H_2O_2 in a heterogeneous Fenton system [5–10]. In this heterogeneous Fenton system the iron oxide activates H_2O_2 to generate radicals, especially $HO^{\bullet}$, which can completely oxidize organics present in the aqueous medium [11]. It has been observed that magnetite, Fe_3O_4, is especially active for oxidation of organics in the presence of H_2O_2. This activity was assigned to the presence of Fe^{2+} species in the magnetite structure, which can activate H_2O_2, by a Haber Weiss mechanism [12]. On the other hand, the activity of other iron oxide phases such as hematite, Fe_2O_3, can be improved by the presence of different metals in the structure. For example, the introduction of lanthanum or neodymium in the hematite structure remarkably increased the reactivity of the dehydrogenation reaction [13]. In heterogeneous catalysis, numerous applications involve Nb compounds as promoters and support for other metals mainly due to the increase of catalytic activity and stability of the catalyst. Recently, the photocatalytic properties of niobia compounds have been explored by many authors [14].

In this work, niobium was introduced in the hematite structure to produce for the first time an active heterogeneous system with H_2O_2 and also to improve the photocatalytic activity of the material. The reactions in the presence of H_2O_2 or ultraviolet light were carried out using the organic dye methylene blue as probe molecule. Niobium shows interesting features for this system such as: ionic ray compatible with the Fe structural and the high reactivity towards H_2O_2 activation [15,16]. Many studies in the literature with iron and niobium oxides can be found, however, no systematic investigation on Nb-doped hematite and no catalytic studies with this oxide in the presence of hydrogen peroxide or ultraviolet light have been carried out.

* Corresponding author. Tel.: +55 35 3829 1626; fax: +55 35 3829 1271.
E-mail address: luizoliveira@ufla.br (Luiz C.A. Oliveira).
URL: http://www.gqa.dqi.ufla.br

0926-860X/$ – see front matter © 2009 Elsevier B.V. All rights reserved.
doi:10.1016/j.apcata.2009.01.014

2. Experimental

2.1. Synthesis and characterization

The Nb-doped hematites were prepared from $Fe(NO_3)_3{\cdot}6H_2O$ (1.7 mol L^{-1}) and $NH_4NbO(C_2O_4)_2(H_2O)](H_2O)_n$ (CBMM-Companhia Brasileira de Metalurgia e Mineração, Araxá-MG) solutions (0.00, 0.61, 0.35 and 0.90 mol L^{-1}) by precipitation with sodium hydroxide (1.7 mol L^{-1}). The precipitates were washed with water until pH 7, dried at 100 °C for 12 h and thermally treated under O_2 atmosphere at 500 °C for 3 h to obtain the stable phase of hematite. The powder XRD data were obtained in a RIGAKU model GEIGERFLEX using Cu Kα radiation. Mössbauer spectra were obtained in a spectrometer CMTE model MA250 with a $^{57}Co/Rh$ source at room temperature.

The surface area was determined by the BET method using a 22-cycle N_2 adsorption/desorption in an Autosorb 1 Quantachrome instrument. Total organic carbon (TOC) measurements were carried out in TOC 500A Shimadzu.

Temperature-programmed reduction (TPR) experiments were performed in CHEMBET 3000 equipment with 20 mg_{sample} under 25 mL min^{-1} H_2 (5%)/N_2 with heating rate of 10 °C min^{-1}. EDS/INCA 350 (energy dispersive X-ray analyzer) is manufactured by Oxford Instruments. DSC (RIGAKU MOD 8065 D1) analysis was operated in an air atmosphere with a heating rate of 10 °C min^{-1}.

X-ray absorption spectroscopy (XAS) measurements were taken at room temperature in transmission mode at the Nb K-edge, using a Si (2 2 0) monochromator at the XAFS1 beamline of LNLS (Campinas, Brazil). EXAFS analysis was carried out using the IFFEFIT software package. Fitting was carried out using the FEFF7 phase and amplitudes. The ATOMS code was used as a tool to generate the input files for FEFF7 based on the Nb-substituting Fe in hematite crystallography data.

2.2. Reactions

The hydrogen peroxide (Synth) decomposition study was carried out with a 10 mL solution H_2O_2 of 2.9 mol L^{-1} with 10 mg catalyst by measuring the formation of gaseous O_2 in a volumetric glass system. The oxidation of the methylene blue dye (50 mg L^{-1}) with H_2O_2 (0.3 mol L^{-1}) at pH 6.0 (natural pH of the H_2O_2 solution) was carried out with a total volume of 10 mL and 10 mg of the oxide catalyst. The reactions were monitored by UV–vis measurements. All the reactions were carried out under magnetic stirring in a recirculating temperature controlled bath kept at 25 ± 1 °C.

The photocatalytic activity of hematite catalysts was tested in the degradation and mineralization of the dye solution at a constant temperature of 298 K, in a cylindrical batch photoreactor. A high-pressure mercury lamp (HPK 125 WPhilips) with a water-cooled filter served as a light source. The total reaction volume was 80 mL.

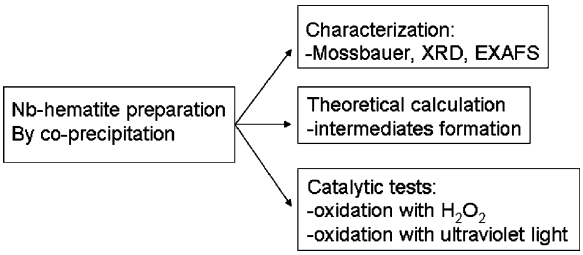

Fig. 1. Steps of the realized work.

In an attempt to identify the intermediate products, methylene blue decomposition was also monitored with the positive ion mode ESI-MS in an Agilent MS-ion trap mass spectrometer (1100 Series). The reaction samples were analyzed by introducing aliquots into the ESI source with a syringe pump at a flow rate of 15 L min^{-1}. The spectra were obtained as an average of 5 scans of 0.2 s. Typical ESI conditions were as follows: heated capillary temperature 325 °C; sheath gas (N_2) at a flow rate of 20 units (ca. 4 L min^{-1}); spray voltage 4 kV; capillary voltage 25 V; tube lens offset voltage 25 V. Fig. 1 shows a simple scheme of this work.

3. Results and discussion

3.1. Characterization of $Fe_{2-x}Nb_xO_3$

Elemental analysis by EDS confirmed the decreasing amount of iron by niobium incorporation by the hematites. The analyses showed the incorporation of 0.00, 1.49, 5.00 and 9.24% in the pure hematite (pure Hm), Hm-Nb2, Hm-Nb5 and Hm-Nb10, respectively. The EDS analyses for different hematites are displayed in Fig. 2. To confirm the Nb^{5+} incorporation in the structure other characterizations of the materials were done such as Mössbauer spectroscopy and EXAFS.

Room temperature Mössbauer analyses of the Fe_2O_3 and $Fe_{2-x}Nb_xO_3$ series showed typical spectra (Fig. 3). The fitted Mössbauer parameters are displayed in Table 1.

Mössbauer spectroscopy indicated that hematite was the main iron phase formed in the synthesis (Fig. 3a). A central doublet was present increasing its relative area according to the niobium content increased. Also, the hyperfine field value has decreased its value for lower Nb content. Even though the ionic radii of niobium

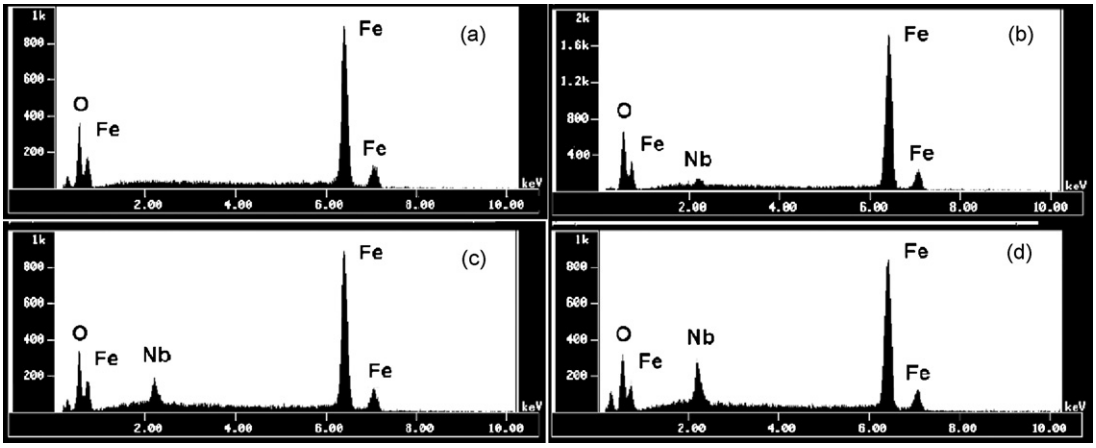

Fig. 2. EDS analyses for the hematites without niobium, pure Hm (a), Hm-Nb2 (b), Hm-Nb5 (c) and Hm-Nb10 (d).

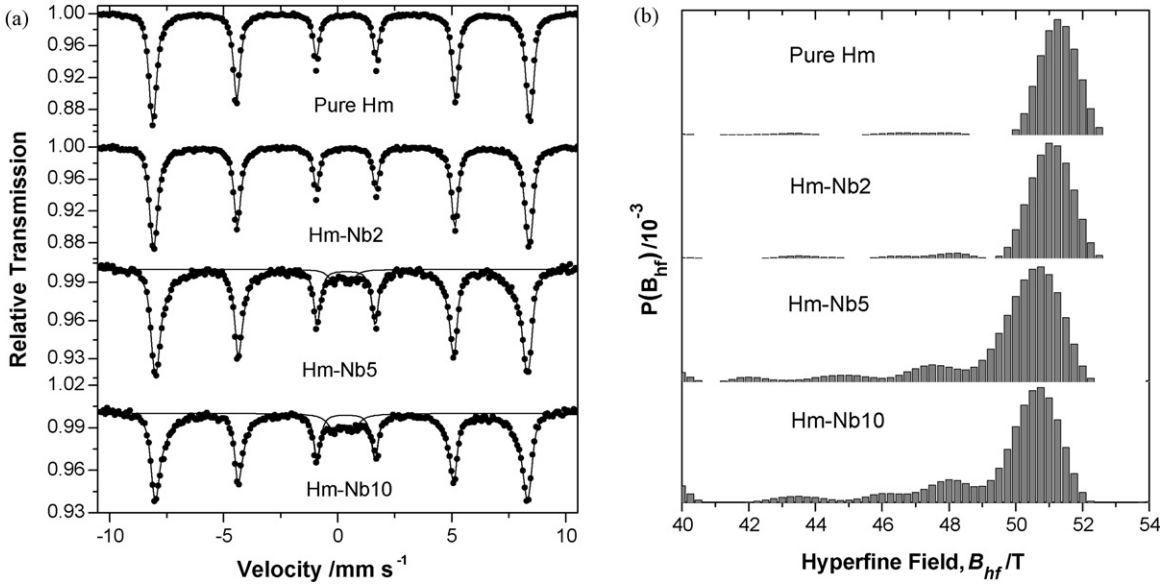

Fig. 3. Mössbauer spectrum of the $Fe_{2-x}Nb_xO_3$ series.

is very close to the Fe(III) ionic radius (69 pm for Nb^{5+} and 64 pm for Fe^{3+}), the charge balance introduce vacancies in the Nb-doped hematite structure ($5Fe^{3+}$ must be substituted for $3Nb^{5+}$). Such vacancies and the substitution of an ion with magnetic momentum for a non-magnetic, decrease the hyperfine field (Fig. 3b). Moreover, the appearance of the doublet and the increase in the width at higher Nb content can be attributed to superparamagnetic hematite with smaller particle size.

The specific surface area for the $Fe_{2-x}Nb_xO_3$ series was measured. A small surface area, i.e., 11 $m^2\,g^{-1}$ can be observed for Fe_2O_3. Upon Nb incorporation in the Fe_2O_3 structure a significant increase in the BET surface area is observed, presenting 17, 34 and 42 $m^2\,g^{-1}$ for Hm-Nb2, Hm-Nb5 and Hm-Nb10, respectively. This BET surface area increase is likely related to two factors: the decrease in particle size, as shown by XRD and Mössbauer analyses, and also by a decrease in the pore diameter.

TPR profile of the pure and doped hematites is shown in Fig. 4. It can be observed, for the pure hematite, a peak centered at 449 °C and a broad peak from 500 to 700 °C. In our previous work, XRD and Mössbauer analyses of the hematite with the reduction interrupted after the first peak at 500 °C showed the presence of magnetite mainly. Moreover, after reduction at 900 °C, only metallic Fe was detected by XRD, suggesting that the following reduction processes are taking place:

$$Fe_2O_3 + H_2 \rightarrow Fe_3O_4 + H_2O$$

$$Fe_3O_4 + H_2 \rightarrow Fe^0 + H_2O$$

Table 1
Mössbauer parameters of the Nb-doped hematites.

Sample	Site	δ (mm s^{-1})	Δ (mm s^{-1})	B_{hf} (T)	Γ (mm s^{-1})	AR (%)
Pure Hm	Hematite	0.37	−0.21	51.3	0.39	100
Hm-Nb2	Hematite	0.37	−0.21	51.1	0.42	100
Hm-Nb5	Hematite	0.37	−0.20	50.6	0.49	95
	Fe^{3+}(VI)	0.29	0.82	–	0.50[a]	5
Hm-Nb10	Hematite	0.35	−0.20	50.6	0.43	90
	Fe^{3+}(VI)	0.35	0.84	–	0.65[a]	10

[a] Fixed parameter in the fitting process. Fitted room temperature Mössbauer parameters for hematites (δ = isomer shift relative to αFe; ε = quadrupole shift, Δ = quadrupole splitting; B_{hf} = hyperfine field and RA = relative sub-spectral area).

It is interesting to observe that in the presence of niobium similar results were obtained (sample Hm-Nb10), but with strong displacement of the first peak to approximately 551 °C. It is indicative of the niobium in the structure of the hematite. The second peak is not affected suggesting that the Nb was expelled with the reduction process.

The magnitudes of the Fourier transforms of EXAFS spectra (denoted as FT) in the *k* range of 3.00–12.00 Å for samples Hm-Nb5 and Hm-Nb10 and for pure Nb_2O_5 (amorphous phase) are presented in Fig. 5. The first two peaks correspond to the octahedral *O* environment. These peaks are similar in both doped samples and also in Nb_2O_5. The next peak in Nb-doped samples is due to the first Fe atoms. In order to analyze the change in the structural parameters the FT was back transformed and fitted with: three layers for Nb-doped samples and two layers for Nb_2O_5. In Table 2 the obtained fitted parameters are reported. Table 2 displays the obtained fitted parameters. The obtained parameters for oxygen layers are equal, taking into account the experimental errors of the Nb_2O_5 but also in hematite the Fe–O distances are of same order. Therefore, taking into account these parameters, it is difficult to distinguish between Nb in Nb_2O_5 and Nb in hematite.

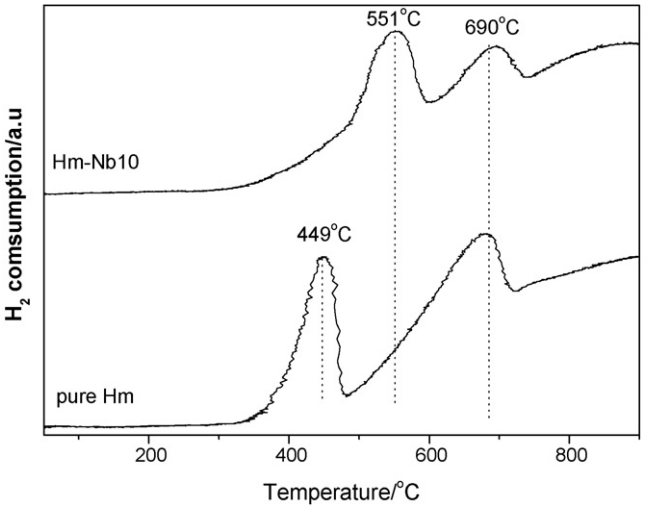

Fig. 4. Temperature-programmed reduction (TPR) profile.

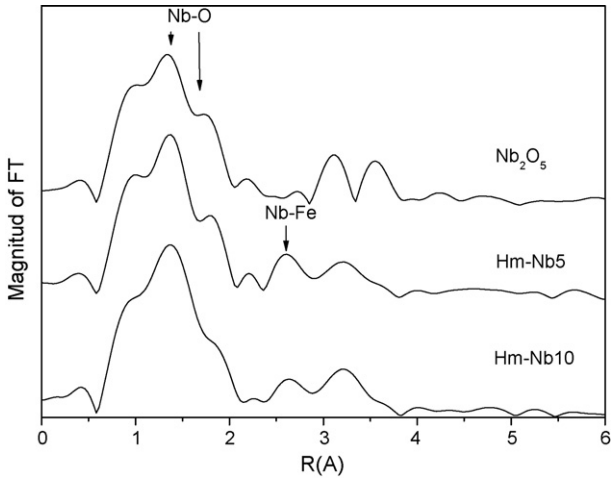

Fig. 5. EXAFS analyses of the hematites.

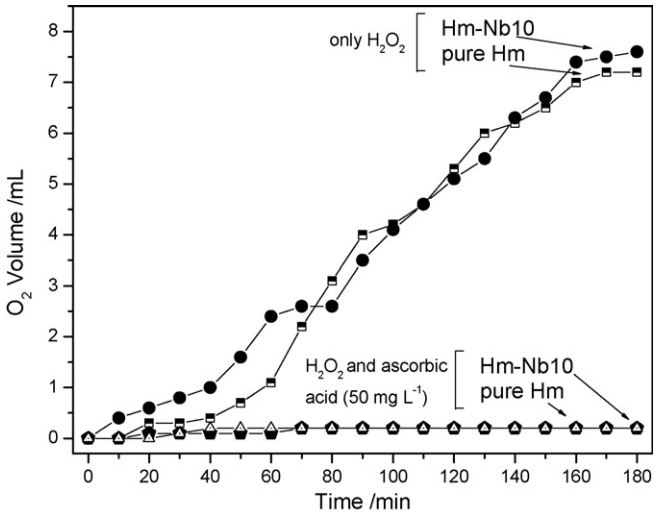

Fig. 6. The H_2O_2 decomposition in the presence of hematites.

Table 2
EXAFS parameters of the materials.

Sample	Atom type	*N*	*R* (A)	σ^2	E_0 (eV)
Nb_2O_5	O	3.0_2	1.869_9	0.004_1	7.9_8
	O	3.0_2	2.06_1	0.006_2	7.9_8
Hm-Nb5	O	3.0_2	1.869_9	0.004_1	7.9_8
	O	3.0_2	2.05_1	0.006_2	7.9_8
	Fe	0.9_3	3.04_2	0.003_5	7.9_8
Hm-Nb10	O	3.0_2	1.869_9	0.004_1	7.9_8
	O	3.0_2	2.04_1	0.006_2	7.9_8
	Fe	0.4_1	3.06_2	0.003_5	7.9_8
Pure Hm	O	3	1.92	–	–
	O	3	2.11	–	–
	Fe	1	2.86		
		3	2.95		
		3	3.34		

Subscripts numbers correspond to the error value.

The peak that appears around 2.7 Å in the FT of the doped samples was fitted with a layer of Fe. The distance results are similar to those expected for Nb-substituting Fe in hematite.

3.2. H_2O_2 decomposition and dye oxidation

The catalytic activity of the $Fe_{2-x}Nb_xO_3$ series was studied using two reactions: (i) the H_2O_2 decomposition to O_2 ($H_2O_2 \rightarrow H_2O + 0.5O_2$) and (ii) the oxidation of the model contaminant methylene blue dye with H_2O_2 in aqueous medium.

It has been observed that there was not significant discoloration of the methylene blue solution in contact with the H_2O_2 solution in absence of niobia. It can be also observed that all the decompositions are slower in the first 25 min of reaction (Fig. 6). Although, the H_2O_2 decomposition kinetics is a complex reaction, the linear behavior of the decomposition plots between 0 and 25 min suggests that the process approximates pseudo-zero order kinetics. After this time a strong increase can be observed in the activity for both materials (pure niobia (pure Hm) and that with the highest niobium content in the structure (Hm-Nb10)). These results suggest that a time to activate the catalyst, i.e., reduction of surface Fe^{3+} is necessary for the quick H_2O_2 decomposition. It can be observed also that the H_2O_2 decomposition is strongly inhibited by the presence of another organic compound (ascorbic acid). The reaction inhibition might be due to a competitive process involving the organic substrate and the active surface that could be related to (i) the adsorption of the organic compounds on the active sites of the composite and/or (ii) their reactions with intermediate species in the H_2O_2 decomposition reaction. Ascorbic acid is a radical scavenger and may be reacting with radical intermediates, such as *OH or *OOH, species that are presumably formed during the H_2O_2 decomposition cycle [16].

The reactions in the presence of H_2O_2 or ultraviolet light were carried out using the methylene blue dye as a probe molecule. The reaction kinetics to form non-colored intermediates were investigated by UV–vis discoloration measurements, the oxidation

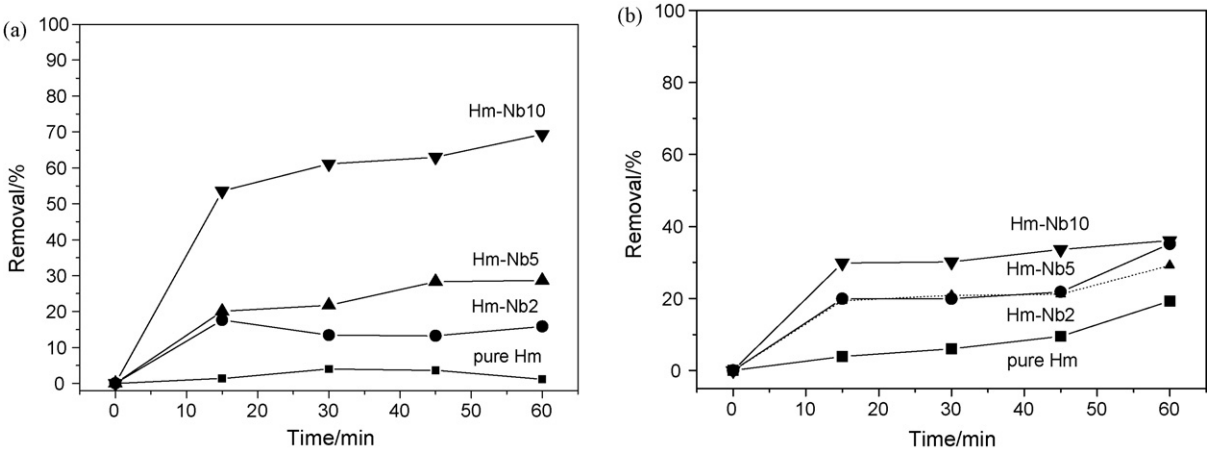

Fig. 7. Discoloration of methylene blue: (a) in the presence of H_2O_2 and (b) in the presence of ultraviolet light.

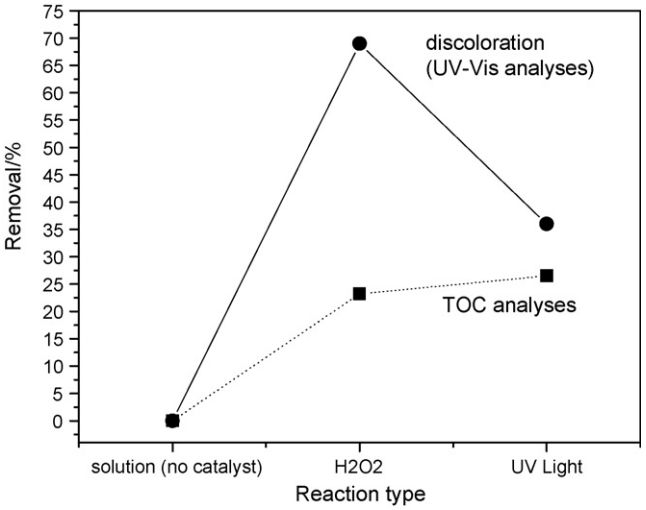

Fig. 8. TOC analyses compared with discoloration capacity.

efficiency was measured by TOC and the formation of intermediates was also investigated by ESI-MS. The discoloration of the dye solution is shown in Fig. 7a (in the presence of H_2O_2; no ultraviolet light) and Fig. 7b (under ultraviolet light; no H_2O_2).

It can be observed in the control experiment (only methylene blue and H_2O_2 or light but no $Fe_{2-x}Nb_xO_3$ catalyst) that there is no significant discoloration even after 60 min reaction. On the other hand, in the presence of the $Fe_{2-x}Nb_xO_3$ catalyst and H_2O_2 as oxidant agent a significant discoloration is observed (Fig. 7a). For the $Fe_{2-x}Nb_xO_3/H_2O_2$ system a low activity of color removal by the pure and low Nb content hematites was observed. However, in the sample with 10% Nb (Hm-Nb10) the catalytic discoloration of 70% was observed after 60 min.

Photocatalytic oxidation of methylene blue onto hematites was followed by UV–vis spectroscopy (Fig. 7b). Similar results were observed when the catalyst was doped with niobium. The sample with 10% Nb promoted the most discoloration capacity with approximately 40% removal after 60 min of reaction time. The results showed clearly that the removal in the presence of H_2O_2 is more efficient than ultraviolet light presence (photocatalysis).

Fig. 8 shows the TOC removal for the most active sample, Hm-Nb10, compared with discoloration capacity. It can be observed that although the presence of H_2O_2 showed high discoloration rates, it produced a similar TOC removal (approximately 25% of removal), suggesting that a chemical process (light or oxidant agent) might play a role in the removal process.

To investigate the possibility of homogeneous reactions produced by Fe and Nb species leached from the $Fe_{2-x}Nb_xO_3$ into the aqueous medium, atomic absorption analyses were carried out in the aqueous phases after all the reactions. The obtained concentrations of Fe and Nb were all below the detection limit of the atomic absorption equipment indicating that the reaction is not caused by homogeneous species in the solution. Moreover, the iron leaching was monitored by measuring the oxidation of quinoline solution in a batch experiment. The iron content in solution, observed in the leaching test presented a removal capacity of 3%, confirming that this reaction takes place mainly *via* a heterogeneous mechanism

Discoloration measured by UV–vis spectroscopy does not give any information about any reaction intermediates formed by the methylene blue oxidation reaction. Such identification could be achieved by using mass spectroscopy with electrospray ionization. Identification of intermediates was studied obtaining spectra after 60 min of reaction in the presence of H_2O_2 or ultraviolet light (Fig. 9). Spectrum of methylene blue solution (without catalysts) indicated only one peak at $m/z = 284$ due to its cationic structure. After 1 h of reaction the total mineralization was not achieved since reaction intermediates could be observed in the spectra. However, the peak at $m/z = 284$ had its intensity decreased more prominently in the reaction in the presence of ultraviolet light than hydrogen peroxide This is in agreement with the previous work confirming that the photoelectronic of hematite had been improved by doping with Nb [17]. Moreover, the spectrum indicated an intense peak at $m/z = 270$ suggesting the beginning of dye structure degradation under ultraviolet light. Also, signals at

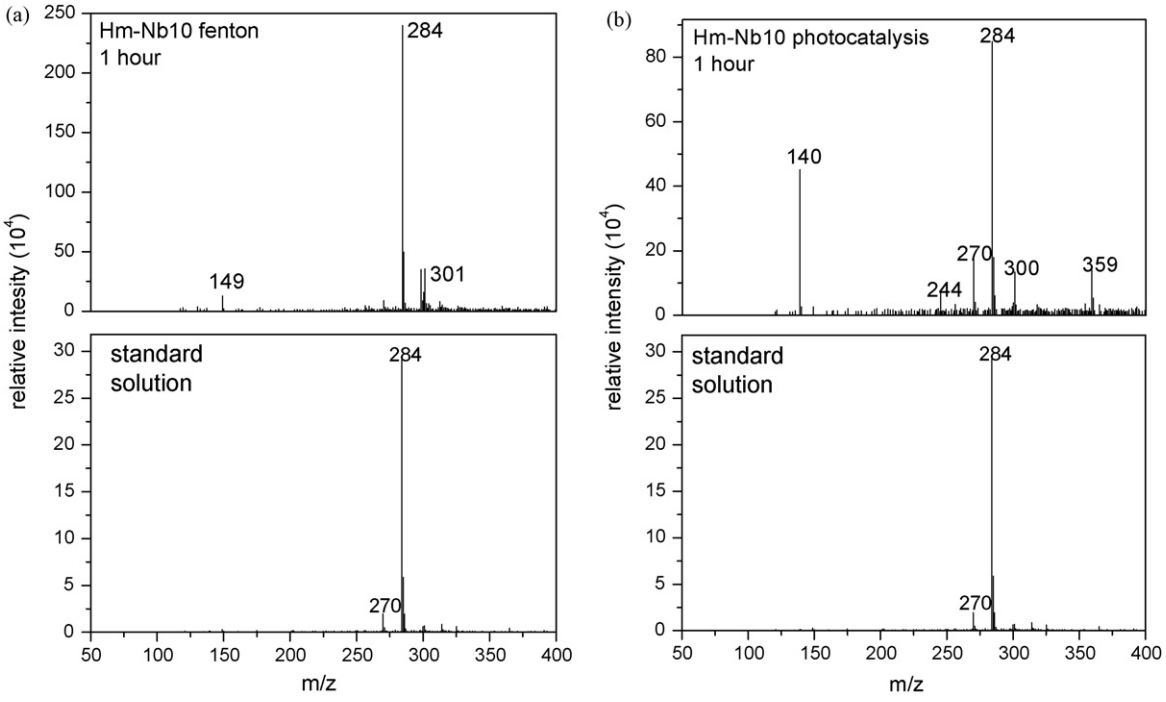

Fig. 9. ESI mass spectrum in the positive ion mode for monitoring the oxidation by the hematites in the presence of H_2O_2 (a) and ultraviolet light (b).

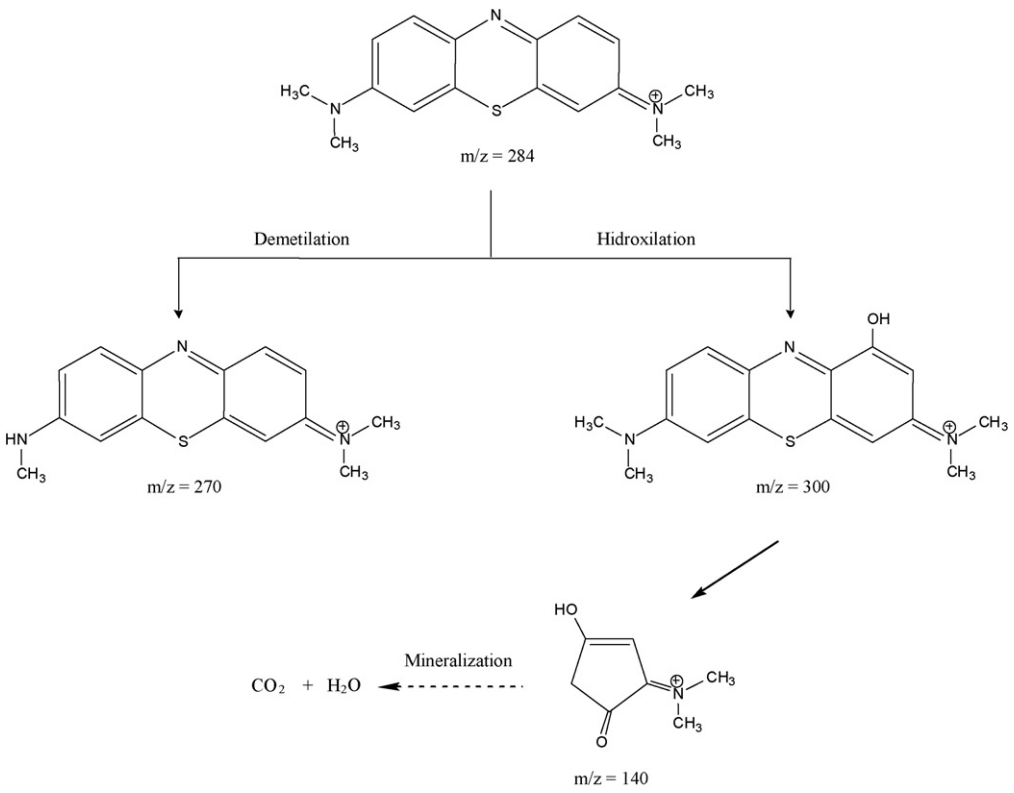

Fig. 10. Scheme with intermediates proposed for the oxidation of methylene blue dye.

m/z = 300 and 359 can be observed, probably due to successive hydroxylation of the aromatic ring, according to [16]. The peak at m/z = 140 is an indicative of ring rupture and subsequent total mineralization.

The possible intermediate structures are reported in Fig. 10. In order to get deeper insight about the m/z = 300 signal, the Gibbs free energy for the stability of some possible isomers with m/z = 300 at DFT level was calculated in our previous work [15,16]. From our data, one may note that the most stable fragment of the hydroxyl group is at C2 position. This could strongly suggest that the reaction with hematite catalysts is initiated by the activation of H_2O_2 or H_2O in the presence of ultraviolet light to produce an $^{*}OH$ radical.

4. Conclusions

Niobium can be gradually introduced in the hematite structure to form the $Fe_{2-x}Nb_xO_3$ oxides. The presence of Nb in the hematite structure has a remarkable effect on the crystallinity, surface area and catalytic activity of the oxide. Hematite with niobium is a good catalyst in the oxidation of a model molecule of organic contaminants.

In the present case, both reactions, i.e., hydrogen peroxide decomposition and oxidation of organic compounds with H_2O_2 are likely to take place *via* radicals, as suggested by the inhibitory effect observed during the H_2O_2 decomposition in the presence of ascorbic acid and ESI-MS studies. In this study, it was indicated that an oxidation mechanism may occur by the attack of the free $^{*}OH$ radical on the molecule giving rise to hydroxylation products as a principal byproduct but compounds resultant from the ring cleavage are also detected. The presence of niobium strongly increases the activity of the oxide for the H_2O_2 decomposition and the Nb surface species seem to act directly on the photocatalytic properties of the doped hematites.

Acknowledgements

The authors are grateful to CAPES, CNPq and FAPEMIG for financial support and also to the LNLS (Campinas, Brazil).

References

[1] F. Yi, S. Chen, C. Yuan, J. Hazard. Mater. 157 (2008) 79.
[2] Y. Liu, D. Sun, Appl. Catal. B: Environ. 72 (2007) 205.
[3] R.S. Yuan, R.B. Guan, W.Z. Shen, J.T. Zheng, J. Colloid Interf. Sci. 282 (2005) 87.
[4] N. Mohan, N. Balasubramanian, C. Ahmed Basha, J. Hazard. Mater. 147 (2007) 644.
[5] R.M. Lago, F.C.C. Moura, M.H. Araujo, R.C.C. Costa, J.D. Fabris, J.D. Ardison, W.A. Macedo, Chemosphere 60 (2005) 1118.
[6] S. Lee, J. Oh, Y. Park, Bull. Korean Chem. Soc. 27 (2006) 489.
[7] P. Baldrian, V. Merhautova, J. Gabriel, F. Nerud, P. Stopka, M. Hruby, M.J. Benes, Appl. Catal. B: Environ. 66 (2006) 258.
[8] R.C. Wu, J.H. Qu, Water Environ. Res. 76 (2004) 2637.
[9] F.C.C. Moura, M.H. Araújo, C.C. Costa, J.D. Fabris, J.D. Ardisson, W.A.A. Macedo, R.M. Lago, Chemosphere 60 (2005) 1118.
[10] R.M. Lago, F.C.C. Moura, J.D. Ardisson, W.A. Macedo, M.H. Araujo, C.N. Silva, Chem. Lett. 34 (2005) 23.
[11] R.M. Lago, F.C.C. Moura, R. Augusti, M.H. Araujo, I. Dalmazio, L.S. Santos, M.N. Eberlin, Rapid Commun. Mass Spectrom. 20 (2006) 1859.
[12] F.C.C. Moura, G.C. Oliveira, M.H. Araujo, J.D. Ardisson, W.A.A. Macedo, R.M. Lago, Appl. Catal. A: Gen. 307 (2006) 195.
[13] M.S. Ramos, M.S. Santos, L.P. Gomes, A. Albornoz, M.C. Rangel, Appl. Catal. A: Gen. 341 (2008) 12.
[14] A. Esteves, L.C.A. Oliveira, T.C. Ramalho, M. Gonçalves, A.S. Anastácio, H.W.P. Carvalho, Catal. Commun. 10 (2008) 330.
[15] L.C.A. Oliveira, T.C. Ramalho, M. Gonçalves, F. Cereda, K.T. Carvalho, M.S. Nazzarro, K. Sapag, Chem. Phys. Lett. 446 (2007) 133.
[16] L.C.A. Oliveira, M. Gonçalves, M.C. Guerreiro, T.C. Ramalho, J.D. Fabris, M.C. Pereira, K. Sapag, Appl. Catal. A: Gen. 316 (2007) 117.
[17] R.M. Cornell, U. Schwertmann, The Iron Oxides: Structure, Properties, Reactions Occurrences and Uses, second ed., Wiley-VCH, Weinheim, 2003.

Applied Catalysis A: General 368 (2009) 17–21

Contents lists available at ScienceDirect

Applied Catalysis A: General

journal homepage: www.elsevier.com/locate/apcata

Nb-doped hematites for decomposition of isopropanol: Evidence of surface reactivity by *in situ* CO adsorption

Luiz C.A. Oliveira [a,*], Francisco Zaera [a], Ilkeun Lee [a], Diana Q. Lima [a], Teodorico C. Ramalho [b], Adilson C. Silva [b], Emanuella M.B. Fonseca [b]

[a] Department of Chemistry, University of California, Riverside, CA 92521, USA
[b] Department of Chemistry, Universidade Federal de Lavras, Lavras, MG, 37200-000, Brazil

ARTICLE INFO

Article history:
Received 11 May 2009
Received in revised form 30 July 2009
Accepted 3 August 2009
Available online 8 August 2009

Keywords:
Hematite
Niobium
CO adsorption
Selective catalyst

ABSTRACT

A series of Nb-containing hematites, $Fe_{2-x}Nb_xO_3$ (%Nb = 0.00, 1.49, 5.00 and 9.24) were prepared using a conventional co-precipitation method. Room-temperature Mössbauer spectroscopy and powder X-ray diffraction measurements suggested the formation of a crystalline phase with partial substitution of Fe^{3+} by Nb^{5+}. The reactivity of these $Fe_{2-x}Nb_xO_3$ materials as catalysts was investigated using the decomposition of isopropanol as a model reaction. Theoretical calculations and CO adsorption monitored by *in situ* infrared absorption spectroscopy showed that the presence and the position of substituting niobium atoms in the structure of hematite modify its surface properties. The results from this study also show that the presence of Nb changes the catalytic properties toward a preferential formation of propene, presumably because of the addition of oxygen vacancies. All catalysts show high catalytic activity, and reach total isopropanol conversion above 375 °C. Moreover, the material with high Nb content reaches total conversion at lower temperatures, at approximately 290 °C with conversion to propene of 92%.

1. Introduction

Nano-iron oxides have been recently identified as novel and promising catalysts for industrial applications in selective oxidations [1,2]. Specifically, it has been reported that iron oxides such as magnetite, goethite, and hematite are especially active for oxidation reactions in aqueous medium [3–5]. Traditionally, this activity has been assigned to the formation of Fe^{2+} species in the magnetite structure, which can activate H_2O_2, by a Haber Weiss mechanism [6]. It has also been suggested that the activity of other iron oxide phases, mainly hematite (Fe_2O_3), can be improved by the incorporation of different metals in the structure to decrease the particle size to nanometric dimension and/or to modify the surface of the solid [3]. Along these lines, the introduction of lanthanum or neodymium in the hematite structure has been shown to remarkably increase its reactivity towards dehydrogenation reactions [7].

Another potential element to be used for modifying hematite is niobium. Nb compounds are often used either as promoters or as support for other metals. Also, the photocatalytic properties of niobia compounds have recently been explored by many authors [8–10]. Specific to the work reported here are previous reports showing that niobium increase the catalytic activity and stability of catalysts based on iron oxide. Indeed, niobium adds interesting features to this system such as ionic compatibility with the iron oxide structure and higher reactivity [8]. However, no systematic investigations on Nb-doped hematite, neither catalytic study with this system for selective oxidations, have been carried out to date.

In this work, the introduction of niobium into the structure of hematite was tested with the aim of producing a new active catalyst. The potential catalytic activity of the new materials was evaluated in gas phase by using isopropanol as the probe molecule. Isopropanol decomposition has been extensively employed as a test reaction for the investigation of oxide catalysts because not only activity but also selectivity can be assessed with respect to two important types of reaction, *i.e.* dehydration and dehydrogenation [11]. It was found here that Niobium can be gradually introduced in the hematite structure to form $Fe_{2-x}Nb_xO_3$ oxides, and that such incorporation leads to a remarkable effect on the catalytic activity and selectivity of the oxide, including an increase in selectivity toward the preferential formation of propene from decomposition of isopropanol.

2. Experimental details

2.1. Materials and characterization

The Nb substituted hematites were prepared from $Fe(NO_3)_3{\cdot}6H_2O$ (1.7 mol L^{-1}) and $NH_4NbO(C_2O_4)_2(H_2O)](H_2O)_n$

* Corresponding author. Tel.: +1 55 35 3829 1626; fax: +1 55 35 3829 1271.
E-mail address: luizoliveira@ufla.br (Luiz C.A. Oliveira).
URL: http://www.gqa.dqi.ufla.br

0926-860X/$ – see front matter © 2009 Elsevier B.V. All rights reserved.
doi:10.1016/j.apcata.2009.08.001

(CBMM-Companhia Brasileira de Metalurgia e Mineração, Araxá-MG) solutions (0.00, 0.61, 0.35 and 0.90 mol L^{-1}) by precipitation with sodium hydroxide (1.7 mol L^{-1}). The precipitates were washed with water until reaching a pH of 7, dried at 100 °C for 12 h, and thermally treated under O_2 atmosphere at 500 °C for 3 h to obtain the stable phase of hematite. Powder XRD data were obtained by using a RIGAKU spectrometer, model GEIGERFLEX, using CuK_α radiation. Mössbauer spectra were obtained at room temperature by using a CMTE spectrometer model MA250 with a ^{57}Co/Rh source.

2.2. CO adsorption by Fourier-transformed infrared (FT-IR) spectroscopy

For the CO adsorption tests, the catalyst powders were pressed into self-supporting 13 mm diameter discs weighing less than 20 mg. Those samples were placed inside a homemade quartz reactor [12,13] and treated under vacuum at 400 °C for 2 h, after which the temperature was set to either −100, −50, 25 or 50 °C to carry out the adsorption experiments. 10 Torr of CO was introduced in the cell for 20 min, after which it was evacuated for 20 min. Infrared spectra of the adsorbed CO were recorded with a resolution of 4 cm^{-1} using a Bruker Tensor 27 FT-IR spectrometer in transmittance mode and a DTGS detector [12]. The infrared spectra of the adsorbed CO were referenced to background traces recorded under similar conditions before CO adsorption.

2.3. Catalytic tests

The test reactions with isopropanol were carried out in a fixed-bed continuous-flow reactor system operated in a downflow mode. The samples (30 mg) were placed in a quartz tube and exposed to the isopropanol, which was fed by flowing nitrogen (30 mL min^{-1}) through a saturator containing the compound. The temperature in the saturator was kept at 0 °C to produce a pressure of 4 mmHg (or 0.57% of the organic compound in volume), while the temperature of the reactor bed was ramped to identify the transition temperature for the decomposition of isopropanol. The products were analyzed by an on-line chromatograph (Shimadzu GC 17A) equipped with a Carbowax (30 m × 0.32 mm × 0.25 μm) capillary column kept at 60 °C and a FID detector kept at 150 °C. The temperature of the injector was maintained at 100 °C.

2.4. Theoretical calculations

Theoretical calculations were carried out by using the Gaussian98 package using Molecular Mechanics and the ONIOM approach [14]. Each structure was fully optimized at a Molecular Mechanics (MM) level with a UFF force field. The influence of the Nb position on the ground-state potential energy surface (PES) was studied using single-point energy calculations with the Oniom approach at both UFF force field and pbe1pbe/SDD levels, with cluster geometries from the optimization procedure. The nature of the stationary point was established after each optimization. This same computational procedure has already been used successfully for similar systems [15].

3. Results and discussion

3.1. Characterization of the materials

The decreasing amount of iron upon niobium incorporation into the hematites was first established by EDS elemental analysis. Those analyses showed the incorporation of 0.00, 1.49, 5.00, and 9.24% Nb in the samples labelled pure hematite (pure Hm), Hm-Nb2, Hm-Nb5 and Hm-Nb10, respectively.

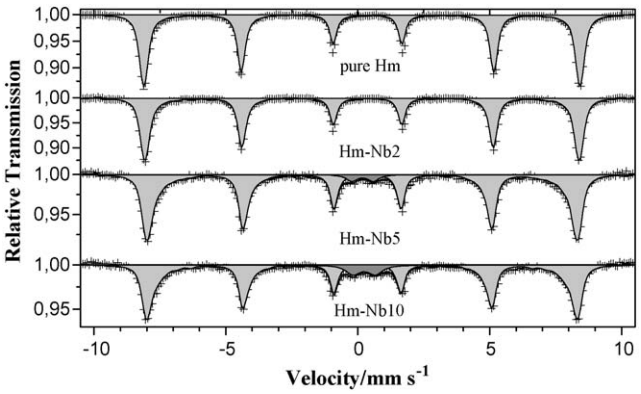

Fig. 1. Room-temperature Mössbauer spectra of the Nb-doped hematites.

XRD characterization experiments indicated the formation of hematite after the synthesis of the pure material (data not shown). It was also noticed that Nb^{5+} incorporation into the hematite structure leads to an important decrease in the average crystallite size of the materials, with the formation of nanomaterials. The particle sizes estimated by using the Scherrer equation [16] were 33, 25, 22, and 18 nm for the pure Hm, Hm-Nb2, Hm-Nb5 and Hm-Nb10 samples, respectively.

The room-temperature Mössbauer data obtained for the Fe_2O_3 and $Fe_{2-x}Nb_xO_3$ series also correspond to those of typical hematite (Fig. 1). Nevertheless, a central doublet can be seen in the last two traces, with a relative area that increases as the niobium content is increased. Moreover, the hyperfine field value decreases (51.3 and 50.6 tesla for the pure hematite and Hm-Nb10, respectively) with increasing Nb content. Even though the ionic radius of Nb(V) is quite close to that of Fe(III) (69 pm for Nb^{5+} versus 64 pm for Fe^{3+}) [10], the differences in charge between the two ions leads to the introduction of oxygen vacancies in the Nb-substituted hematite structure (five Fe^{3+} must be substituted for each three Nb^{5+}). Those vacancies, and the substitution of an ion with magnetic momentum for one that is non-magnetic, decreases the hyperfine field. Moreover, both the appearance of the doublet and the increase in the width of the peaks at higher Nb content can be attributed to superparamagnetic hematite with smaller particle size [10].

3.2. CO adsorption

In order to obtain information about the chemical behavior of the surface of the hematites, *in situ* infrared absorption spectroscopy studies were carried out to characterize the adsorption of CO (Figs. 2 and 3).

The spectra of CO adsorption on pure hematite presents a broad band centered at 2230 cm^{-1} that may be assigned to physically adsorbed CO coordination on Fe^{3+} cations (Fig. 2a) [13]. Interestingly, the sample doped with niobium ((Hm-Nb10)) yielded quite different CO adsorption spectra, with three main peaks at 2149, 2181 and 2198 cm^{-1} (Fig. 2b). The strong peaks at 2181 and 2198 cm^{-1} may be due the presence of Nb^{5+} Lewis-acid sites, as reported by Resini et al. [17]. CO adsorption on those sites may be fairly weak, given that all these the CO peaks disappear almost completely upon heating of the sample from −100 to 50 °C [18].

Fig. 3 shows a close up of IR spectra in the carbonate region for the pure and Nb-doped hematite (Hm-Nb10) recorded at different temperatures. It is interesting to observe that the signals assignable to carbonate species, the large peak around 1555–1575 cm^{-1}, are more intense in the pure hematite data, suggesting that the introduction of Nb^{5+} in the structure of hematite modify the surface as to inhibit any reaction of CO with the oxygen atoms

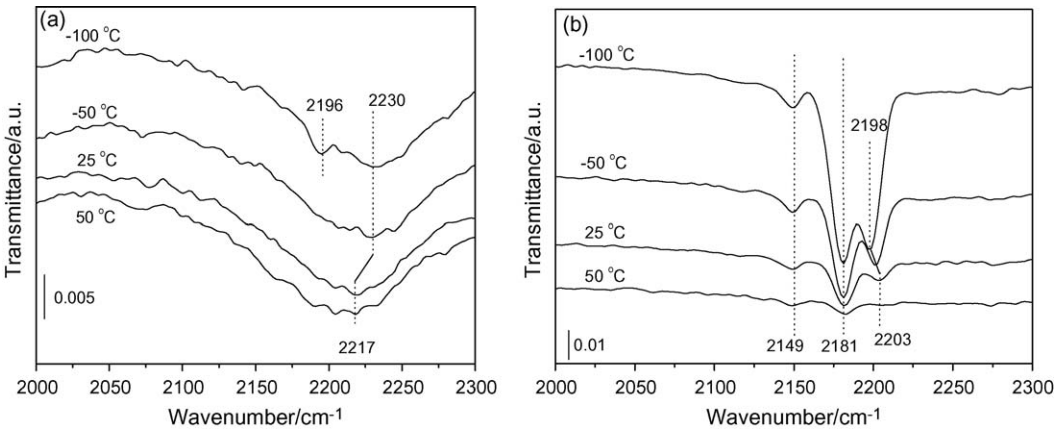

Fig. 2. FTIR spectra in the carbon-monoxide region from pure (a) and Nb-substituted hematite (b) catalysts after exposure to 10 Torr of CO and subsequent evacuation for 20 min.

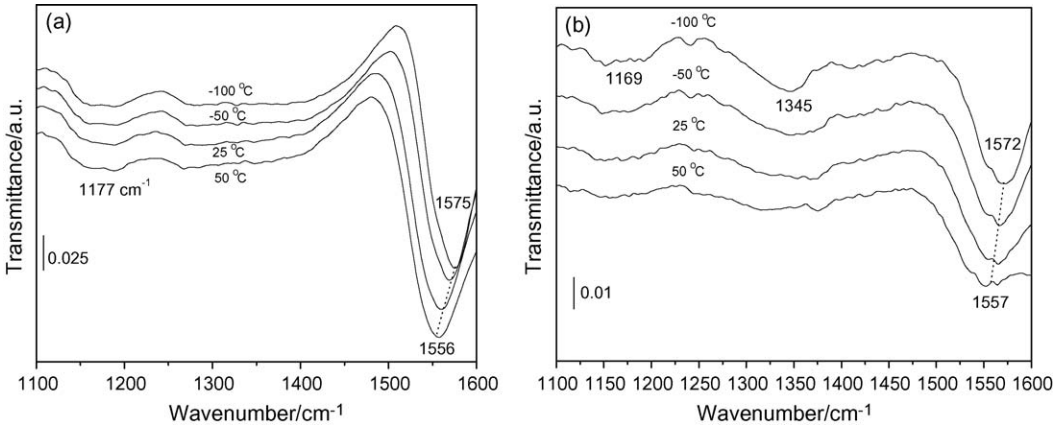

Fig. 3. FTIR spectra in the carbonate region from pure (a) and Nb-doped hematite (Hm-Nb10) (b) after addition of CO.

of the surface of the oxide. One viable interpretation for these changes is that the presence of Nb ions on the surface makes redox reactions between CO and the catalyst surface more difficult, either because of a higher stability of the lattice oxygen (due to the higher oxidation state of the substitution Nb ion) or a stronger CO-cation interaction (hence the new Lewis-acid sites identified in Fig. 2).

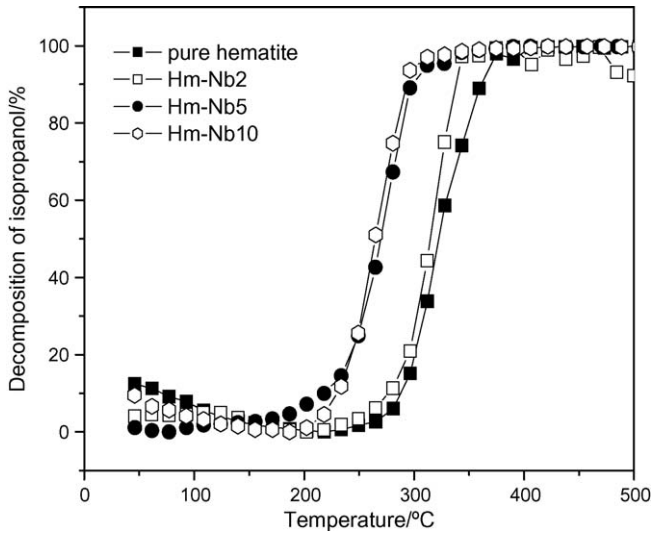

Fig. 4. Decomposition profiles for isopropanol on pure and Nb-doped hematites.

3.3. Catalytic tests: decomposition of isopropanol

Finally, the activity of the niobium-doped hematites as catalysts was tested by examining the thermal decomposition of isopropanol. Isopropanol is an ideal probe for selectivity in catalysis, because it can undergo both dehydrogenation and dehydration reactions according to the following equations [11]:

$$CH_3CH(OH)CH_3 \rightarrow CH_3COCH_3 + H_2 \quad (1)$$

$$CH_3CH(OH)CH_3 \rightarrow CH_3CH{=}CH_3 + H_2O \quad (2)$$

The reaction activity profiles versus reactor bed temperature obtained in our studies of isopropanol decomposition with the doped hematites are shown in Fig. 4. All catalysts show high catalytic activity, and reach total isopropanol conversion above 375 °C. However, the materials with high Nb content reach total conversion at lower temperatures, at approximately 290 °C. This

Table 1
Selectivity between dehydration to propene and dehydrogenation to acetone during the decomposition of isopropanol with Nb-doped hematites at 427 °C.

Catalyst	Conversion/%	
	Acetone	Propene
Pure Hm	78	22
Hm-Nb2	52	48
Hm-Nb5	43	57
Hm-Nb10	8	92

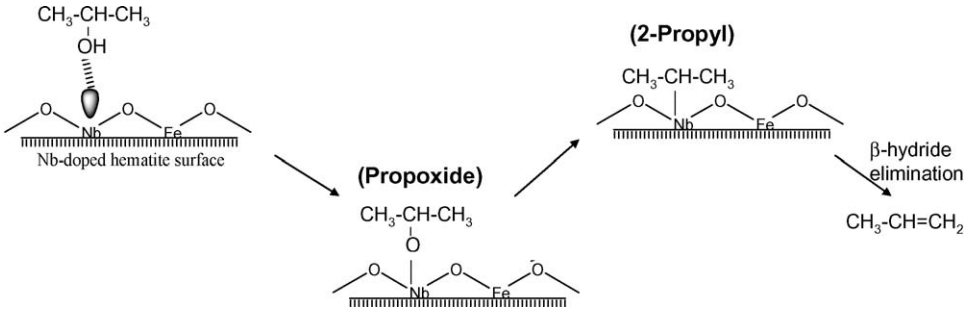

Fig. 5. Proposed mechanism for the decomposition of isopropanol on hematite surfaces.

highlights the role of the niobium in increasing the activity of the catalyst.

GC analysis of the reaction products indicates the production of expected organic products, acetone and propene, with all catalysts. However, while acetone was the main product with the pure hematite, much more propene was produced with the samples doped with niobium; such doping clearly enhances the selectivity toward the dehydration process (Table 1). The selectivity experiments were carried out at 427 °C, which corresponds to conditions of equal thermodynamic selectivity for dehydrogenation and dehydration [11] in order to assure that the selectivity seen here are driven by kinetic factors.

To explain the changes in selectivity seen above, it should be noted that a modification of the surface properties of the oxide by the isomorphic substitution of Fe^{3+} ions by Nb^{5+} can change the electrical properties of the material. This could lead to a change in reaction mechanism for the decomposition of isopropanol, as proposed in Fig. 5.

The proposed mechanism starts with the dehydrogenation of isopropanol, initially molecularly adsorbed via the coordination of the electron lone pairs of the oxygen atom with the surface metal, at the hydroxo hydrogen, and with the formation of a propoxide intermediate [19]. In pure hematite, that propoxide may undergo a direct beta-hydride elimination to produce acetone [20]. In this case the high production of acetone confirms a different mechanism, possibly due to difference in the intensity of the metal-oxygen bond generating fewer oxygen vacancies. Upon the addition of niobium to the lattice of the oxide, however, selectivity toward propene formation is promoted, presumably by the enhancement of a C–O bond-breaking step and the formation of a 2-propyl intermediate. Beta-H elimination from that species produces the olefin. It seems that the Nb addition creates more oxygen vacancies, as shown by Mössbauer data, and leads to an increase in adsorption energy for the alcohol. A stronger ion-oxygen interaction weakens the C–O bond, and facilitates its scission. It also appears that the pure hematite has more basic surface sites capable of promoting beta-H elimination steps directly from the propoxide intermediate.

3.4. Theoretical calculations

In order to shed more light on the reaction mechanism proposed above and to understand the role of Nb doping in determining the selectivity of isopropanol decomposition, some thermodynamic calculations were carried on the stability of Nb-doped hematites ($Fe_{2-x}Nb_xO_3$). In order to obtain the potential energy curves for the position change of the doping element, a Nb atom was placed in each of the four different Fe positions within the hematite structure, that is, in each of the four layers seen in that structure as taken from the American Mineralogist Crystal Structure Database and shown in Fig. 6 [21]. According to the results from those calculations, shown in Fig. 7, there is a stable state for Nb ions at the topmost layer of the material (layer A).

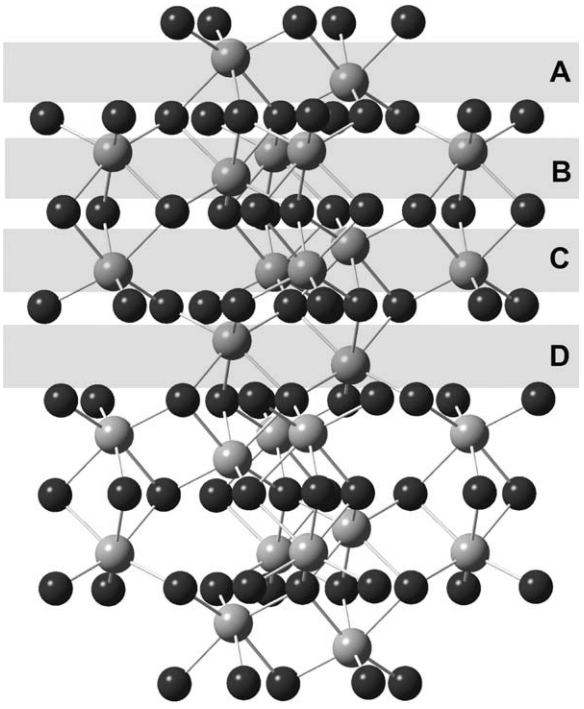

Fig. 6. Structure of pure hematite showing its four (A–D) layers. The gray and black balls correspond to iron and oxygen ions, respectively.

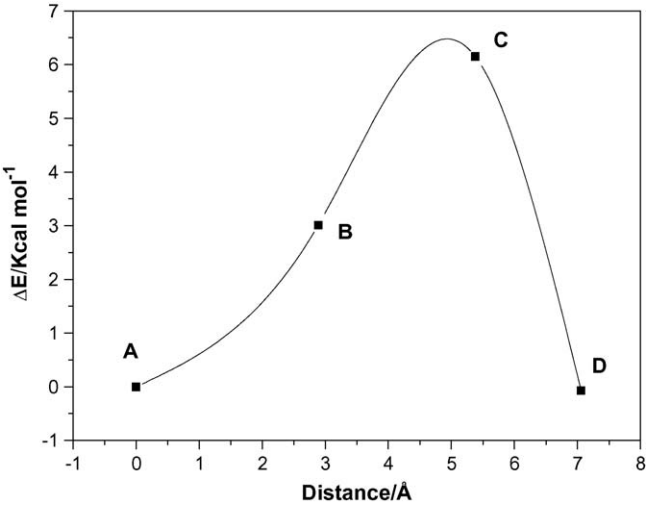

Fig. 7. Potential Energy Curve obtained for the hematite structure doped with Nb in the A–D positions.

Among other calculation methods, the choice of the Oniom approach (DFT/UFF) improved the results, so that they are completely satisfactory when they were compared to experimental data. The pbe1pbe/SDD method has been shown to be satisfactory on similar structures [22,23]. The smaller basis sets are unsatisfactory and the higher ones are too expensive. It must be remarked that density functional theory (DFT) with the pbe1pbe nonlocal exchange correlation functional has been applied as well to study these molecules and the previous theoretical calculations show similar studies on diffusion can support this hypothesis. Dunning and Hay [24] have used this kind of cluster model to study the adsorption. Vazquez et al. [25] and, Neaton et al. [26] have used DFT to examine charge transport across the interface between organic adsorbates and metal electrodes. DFT also performs in excellent agreement with experimental results for geometrical parameters for Au and Cu complexes [27]. Whereas the binding energies from DFT calculations are higher than MP2 results, both have the same tendency [27]. It is important to mention those results are also in good agreement with CASSCF/UFF values.

Interestingly, Fig. 7 shows energy barriers of 3.01 and 6.15 kcal mol^{-1} (referred to the energy of the ion in the A position) for the Nb ion to travel inside the channel defined by Fe position within layers B and C, at 3.5 and 5.5 Å from the top layer, respectively. This probably derives from the existence of high hindrance strength in this region, as supported by our X-ray diffraction measurements and structural data from theoretical calculations. In this scenario, Nb substitutions lead to the creation of oxygen vacancies at the hematite surface, which become available and get filled by the hydroxyl group from isopropanol. Since the number of oxygen vacancies is proportional to the number of Nb-doping atoms [10], selectivity toward the formation of propene is clearly increased with increasing Nb doping. Moreover, it is known that the dehydration of alcohols requires the simultaneous presence of acidic and basic centers in adequate proportions on the catalyst surface. The strength of the acid sites is crucial. A certain acidity level is required in order to have a high dehydration activity: if the acidity is too weak the dehydration activity decreases and if the acidity is too strong cracking may occur. The strength of the acid sites determines the reaction product distribution [28–30]. The selective formation of propene suggests that the niobium incorporation provides the appropriate acidity for that to occur, as a more selective catalyst.

4. Conclusions

Work has been carried out to identify the conditions that favor dehydration over dehydrogenation during the catalytic partial oxidation of alcohols on a new class of catalyst based on Nb-doped hematite. Niobium can be gradually introduced into the hematite structure to form $Fe_{2-x}Nb_xO_3$ oxides, a change that was shown to have a remarkable effect on the catalytic activity and selectivity of the oxide. It was shown that hematites, where Fe^{3+} ions are partially replaced by Nb^{5+}, are active and selective catalysts for the dehydration of isopropanol to propene. The changes seen in CO adsorption, as monitored by *in situ* infrared, support the presence of different surface groups on the catalysts after niobium introduction, and Mössbauer data points to the development of the oxygen vacancies possibly responsible for the change in chemistry reported.

Acknowledgment

The authors are grateful to the CNPq for the *postdoctoral* fellowship, CBMM (Brazil) for the niobium sample and also support from Department of Chemistry of the University of California at Riverside and US National Science Foundation.

References

[1] W. Ferraz, L.C.A. Oliveira, R. Dallago, L. Conceição, Catal. Commun. 8 (2007) 131.
[2] J. Ge, T. Huynh, Y. Hu, Y. Yin, Nano Lett. 8 (2008) 931.
[3] A.C. Silva, D.Q.L. Oliveira, L.C.A. Oliveira, T.C. Ramalho, Appl. Catal., A 357 (2009) 79–84.
[4] F. Magalhaes, M.C. Pereira, J.D. Fabris, R.M. Lago, L.C.A. Oliveira, Appl. Catal., A 332 (2007) 115–123.
[5] I.R. Guimaraes, L.C.A. Oliveira, T.C. Ramalho, M.C. Pereira, J.D. Fabris, J.D. Ardisson, Appl. Catal., A 347 (2008) 89–93.
[6] L.C.A. Oliveira, T.C. Ramalho, M. Gonçalves, F. Cereda, K.T.G. Carvalho, M.S. Nazzarro, K. Sapag, Chem. Phys. Lett. 446 (2007) 133.
[7] M.S. Ramos, M.S. Santos, L.P. Gomes, A. Albornoz, M.C. Rangel, Appl. Catal., A 341 (2008) 12.
[8] L.C.A. Oliveira, M. Gonçalves, M.C. Guerreiro, T.C. Ramalho, J.D. Fabris, M.C. Pereira, K. Sapag, Appl. Catal., A 316 (2007) 117.
[9] A. Esteves, L.C.A. Oliveira, T.C. Ramalho, M. Gonçalves, A.S. Anastácio, H.W.P. Carvalho, Catal. Commun. 10 (2008) 330.
[10] L.C.A. Oliveira, T.C. Ramalho, E.F. Souza, M. Gonçalves, D.Q.L. Oliveira, M.C. Pereira, J.D. Fabris, Appl. Catal., B 83 (2008) 169.
[11] D.K. Chakrabarty, B. Viswanathan, Heterogeneous Catalysis, New Age International Ltd., Publishers, New Delhi, 2008, pp. 185.
[12] F. Zaera, Int. Rev. Phys. Chem. 21 (2002) 433.
[13] H. Tiznado, S. Fuentes, F. Zaera, Langmuir 20 (2004) 10490.
[14] F. Maseras, K. Morokuma, J. Comput. Chem. 16 (1995) 1170.
[15] E.F.F. Da Cunha, R.B. de Alencastro, T.C. Ramalho, J. Theor. Comput. Chem. 3 (2004) 1.
[16] R.M. Cornell, U. Schwertmann, The Iron Oxides, Weinheim-VHC, New York, 2003, p. 63.
[17] C. Resini, T. Venkov, K. Hadjiivanov, S. Presto, P. Riani, R. Marazza, G. Ramis, G. Busca, Appl. Catal., A 353 (2009) 137.
[18] G. Pérez-Osorio, F. Castillón, A. Simakov, H. Tiznado, F. Zaera, S. Fuentes, Appl. Catal., B 69 (2007) 219.
[19] N.R. Gleason, F. Zaera, J. Catal. 169 (1997) 365.
[20] A.H. Ali, F. Zaera, J. Mol. Catal. A 177 (2002) 215–235.
[21] R.L. Blake, R.E. Hessevick, T. Zoltai, L.W. Finger, Am. Mineral 123 (1966) 51.
[22] Y. Liu, M. Li, Y. Suo, Surf. Sci. 600 (2006) 5117.
[23] T.C. Ramalho, A.P.L. Batista, C.A. Perez, A.L. Gobbi, J. Mater. Sci. 44 (2009) 1029–1034.
[24] T.H. Dunning Jr., J. Hay, in: H.F. Schaefer (Ed.), Modern Theoretical Chemistry, Plenum, New York USA, 1976.
[25] H. Vazquez, R. Oszwaldowski, P. Pou, J. Ortega, R. Perez, F. Flores, A. Kahn, Europhys. Lett. 65 (2004) 802–806.
[26] J.B. Neaton, M.S. Hybertsen, S.G. Louie, Phys. Rev. Lett. 97 (2006) 216405–216409.
[27] Y. Liu, Y. Liu, H. Wang, Y. Suo, Surf. Sci. 601 (2007) 1265–1272.
[28] J. Barbier, Appl. Catal. 23 (1986) 225–243.
[29] M. Ruwet, P. Berteau, B. Delmon, S. Ceckiewicz, Stud. Surf. Sci. Catal. 34 (1987) 245–258.
[30] H. Knozinger, in: B. Imelik, C. Naccache, G. Coudurier, Y. Ben Taarit, J.C. Vedrine (Eds.), Catalysis by Acids and Bases (Studies in Surface Science and Catalysis, vol. 20, Elsevier, Amsterdam, 1985, p. 111.

Applied Catalysis B: Environmental 107 (2011) 237–244

Contents lists available at ScienceDirect

Applied Catalysis B: Environmental

journal homepage: www.elsevier.com/locate/apcatb

Heterogeneous catalyst based on peroxo-niobium complexes immobilized over iron oxide for organic oxidation in water

Adilson C. Silva [a], Renata M. Cepera [a], Márcio C. Pereira [b], Diana Q. Lima [a], José D. Fabris [c], Luiz C.A. Oliveira [a,*]

[a] Department of Chemistry, ICEx, Federal University of Minas Gerais, 31270-901 Belo Horizonte, Minas Gerais, Brazil
[b] Institute of Science and Technology, Federal University of Jequitinhonha and Mucuri Valleys, 39803-371 Teófilo Otoni, Minas Gerais, Brazil
[c] Department of Chemistry, Federal University of Jequitinhonha and Mucuri Valleys, 39100-000 Diamantina, Minas Gerais, Brazil

ARTICLE INFO

Article history:
Received 11 April 2011
Received in revised form 5 July 2011
Accepted 12 July 2011
Available online 23 July 2011

Keywords:
Hematite
Maghemite
Peroxo-niobium
Hydrogen peroxide

ABSTRACT

Nb-doped iron oxides were used as heterogeneous catalyst to oxidize organic compounds in aqueous medium containing hydrogen peroxide. XRD data reveal that the composites contain hematite (α-Fe_2O_3), maghemite (γ-Fe_2O_3) and $FeNb_2O_6$. The H_2O_2 pretreatment of the solid catalyst promotes important surface and structural changes of the iron oxides mainly by peroxo-niobium complexes formation, which expressively enhances the catalytic properties of the composite. Transmission electron microscopy images show that the H_2O_2-treatment tends also to decrease the mean particle size of grains of the composite. Nb-doped iron oxides were found to impart an important role to the solid catalyst towards H_2O_2 reactions. The developed composites were confirmed to have remarkable catalytic activity on the oxidation of organic substrates and can be regenerated for several successive reaction cycles for degrading polluting organic in water.

1. Introduction

In heterogeneous catalysis, several applications involve niobium-bearing compounds as promoters or support for other metals, mainly due to their relatively high catalytic activity and chemical stability. During the last decades, peroxo and hydroperoxo complexes with different transition metals, including W, V, Mo, Ti and Nb, have drawn attention due to their outstanding catalytic activity in several processes, such as oxidation of alkenes, aliphatic and aromatic hydrocarbon compounds [1–9]. These complexes can be used either in stoichiometric or as catalysts in oxidation reactions involving H_2O_2, which is able to cyclically regenerate the active sites [10,11].

Catalysts based on niobium(V)-peroxo complexes for oxidation of organic and inorganic substrates and for epoxidation reactions have been reportedly documented [12–14]. However, these complexes were found to operate only an in homogeneous system, which makes the catalytic process more costly and difficult to execute, especially on a large scale [15,16]. As an alternative to the homogeneous systems, we have recently reported a novel heterogeneous catalyst based on niobium-peroxo complexes immobilized on niobia (Nb_2O_5) with high chemical activity for oxidation reactions of organic compounds [17–20]. However, the use of single niobium oxides as a catalyst for the oxidation of organic compounds in aqueous medium is scarcely reported. A study has been reported with niobium oxides as a catalyst for oxidation, but combined with an inorganic cation operating at high temperature [21]. In general, research has been focused on the study of the catalytic performance of Nb_2O_5-rich materials impregnated with metals [22]. Some known properties of niobium such as, more specifically, chemical activity in redox and catalytic systems, photosensitivity, acidity behavior constitute enough evidence to motivate understanding and an attempt to use niobium for catalytic purposes [23]. The Nb oxides are mainly used as acid catalysis due to its surface characteristics. In other recent research works of our group, we could report changes of Nb oxides with hydrogen peroxide, to enhance oxidation rates, as a chemical effect mediated by these materials [17–20]. Catalysts based on niobium(V)-peroxo complexes for oxidation of organic and inorganic substrates and for epoxidation reactions have also been reportedly documented elsewhere [12–14].

Herein, we report, for the first time, a highly reactive system designed to oxidize organic compounds based on Nb-peroxo complexes immobilized on iron oxides produced *in situ* by pretreatment of Nb-doped iron oxides composites with H_2O_2. The use of iron oxides as support for niobium is interesting for the following main raisons: (i) they are relatively stable in the solution pH range commonly used in oxidation reactions of organics in water; (ii) the

* Corresponding author. Tel.: +55 31 3409 6384; fax: +55 31 34095700.
E-mail address: luizoliveira@qui.ufmg.br (L.C.A. Oliveira).

0926-3373/$ – see front matter © 2011 Elsevier B.V. All rights reserved.
doi:10.1016/j.apcatb.2011.07.017

ionic radius of Nb^{5+} is comparable to that of Fe^{3+}, and this dimension similarity favors niobium to isomorphically replace iron in the iron oxides structure; (iii) iron oxides are efficient Fenton-like catalysts, (iv) relatively cheap and (v) of wide natural availability, as iron is one of the most abundant elements on the Earth crust.

2. Experimental methods

2.1. Materials preparation

Nb-doped iron oxides composites were prepared by first reacting $Fe(NO_3)_3{\cdot}6H_2O$ (1.7 M) with 0.88 M $NH_4[NbO(C_2O_4)_2(H_2O)](H_2O)_n$ (used as supplied by CBMM, which stands for Companhia Brasileira de Metalurgia e Mineração, Brazil), and precipitating with concentrated ammonium hydroxide (pH 9.5–10). The precipitates were washed with ammonium acetate solution (2.60 M), dried at 100 °C for 12 h and thermally treated under N_2 atmosphere at 400 °C for 2 h. The Nb-iron oxides composites were calcined at 500 °C for 1 h under O_2 atmosphere to obtain the material labeled Nb-NCBT (meaning before H_2O_2 treatment) and Nb-NCAT (after H_2O_2 treatment). The undoped iron oxides composites were synthesized in the same way of Nb-doped iron oxides composites, except that niobium salt was not added in the synthesis process. The doped materials were submitted to hydrogen peroxide treatment in order to generate active surface sites. This treatment was conducted adding 300 mg of catalyst, 4 mL of H_2O_2 (30% v/v) and 80 mL of distilled H_2O, leaving them in contact for 30 min. Soon afterwards the material was vacuum-filtered, washed with distilled H_2O and oven dried for 12 h at 100 °C.

2.2. Materials characterization

Mössbauer spectra of all samples were collected in a constant acceleration transmission mode with a ~20 mCi 57Co/Rh source. A spectrometer equipped with a transducer (CMTE model MA250) controlled by a linear function driving unit (CMTE model MR351) was used to obtain the spectra at 298 K. Data were stored in a 1024 channel-MCS memory unit, with the Doppler velocity ranging between about $\pm 10\ mm\ s^{-1}$, calibrated with a metallic iron (α-Fe) foil as absorber. The absorbers were prepared with a uniform thickness of ~10 mg Fe/cm^2, admixing sucrose to the samples. The experimental reflections were fitted to Lorentzian functions with the least-square fitting statistical procedure of the NORMOSTM-90 computer program. Saturation magnetization measurements were performed using a portable magnetometer with a fixed magnetic field of 0.3 T calibrated with Ni metal. The transmission electron microscopy (TEM) images of all samples were taken with a JEOL transmission electron microscope model JEM 2000EXII. Powder X-ray diffraction data (XRD) with synchrotron radiation (wavelength, λ = 1.23844 Å) of all samples were collected at the Brazilian National Laboratory of Synchrotron Light, in the Bragg-Brentano geometry beam, with parallel polarization correction, of a setup equipped with a graphite monochromator. XRD patterns corresponded to scans from 15 to 70° 2θ at a step width of 0.02°, 10 s per step. Silicon was used as an external standard. The Rietveld structural refinement was performed with FULLPROF 2010[24] program. The surface area of all samples was determined by the BET method, using N_2 adsorption/desorption in an Autosorb 1 Quantachrome instrument. Infrared spectra (FTIR) were obtained with a Digilab Excalibur, series FTS 3000 spectrometer and pressed samples as small discs using a spectroscopic grade KBr filling matrix.

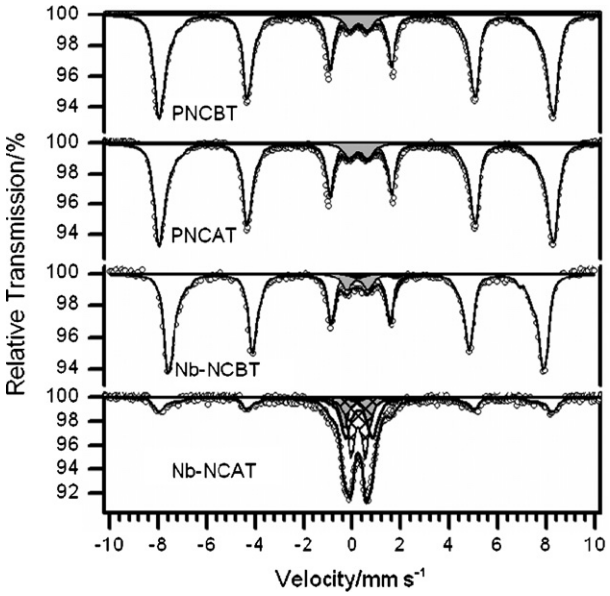

Fig. 1. ^{57}Fe Mössbauer spectra at 298 K for the pure iron oxides nanocomposites before (PNCBT) and after H_2O_2 treatment (PNCAT), Nb-doped iron oxides nanocomposites before (Nb-NCBT) and after H_2O_2 treatment (Nb-NCAT).

2.3. The catalytic chemical reaction

The oxidation of methylene blue (MB) dye (model molecule, $50\ mg\ L^{-1}$) with H_2O_2 (8 mM) at pH 6 (natural pH of MB solution) was carried out with a total volume of 10 mL, using 10 mg of composite. The methylene blue has interesting features as probe molecule for oxidation studies, including (i) its degradation can be monitored with simple spectrophotometric measurements, (ii) it is highly soluble in water and (iii) it models very satisfactorily the chemical behavior of most textile dyes, which are an important class of industrial water contaminant. All chemical reactions were performed under magnetic stirring in a recirculating temperature controlled bath kept at 25 ± 1 °C. The reactions were monitored with UV–vis spectroscopy (Shimadzu UV 1601 PC) at 665 nm.

2.4. Electron spray ionization (ESI)–mass spectrometry (MS)

To identify the intermediate chemical species of the methylene blue oxidation reaction an Agilent MS-ion trap mass spectrometer (1100 Series) was used in positive ion mode. The reaction samples were analyzed by introducing aliquots into the ESI source with a syringe pump at a flow rate of $15\ L\ min^{-1}$. Spectra were obtained as an average of 5 scans of 0.2 s. Typical ESI conditions were as follows: heated capillary temperature of 1508 °C; sheath gas (N_2) at a flow rate of 20 units (ca. $4\ L\ min^{-1}$); spray voltage of 4 kV; capillary voltage of 25 V; tube lens offset voltage 25 V.

3. Results and discussion

3.1. Composites characterization

^{57}Fe Mössbauer measurements were carried out to trace the physical and chemical changes on the pure and Nb-doped iron oxide nanocomposites, following the pretreatment of the material with H_2O_2. Mössbauer spectrum of pure iron oxide nanocomposites before treatment with H_2O_2 (PNCBT) (Fig. 1) shows a magnetic hyperfine field (B_{hf}) distribution with maximum probability value at 50.5 T (relative subspectral area for this spectral contribution, RA = 73%), which is a characteristic value assignable to hematite (α-Fe_2O_3). Components with lower hyperfine field val-

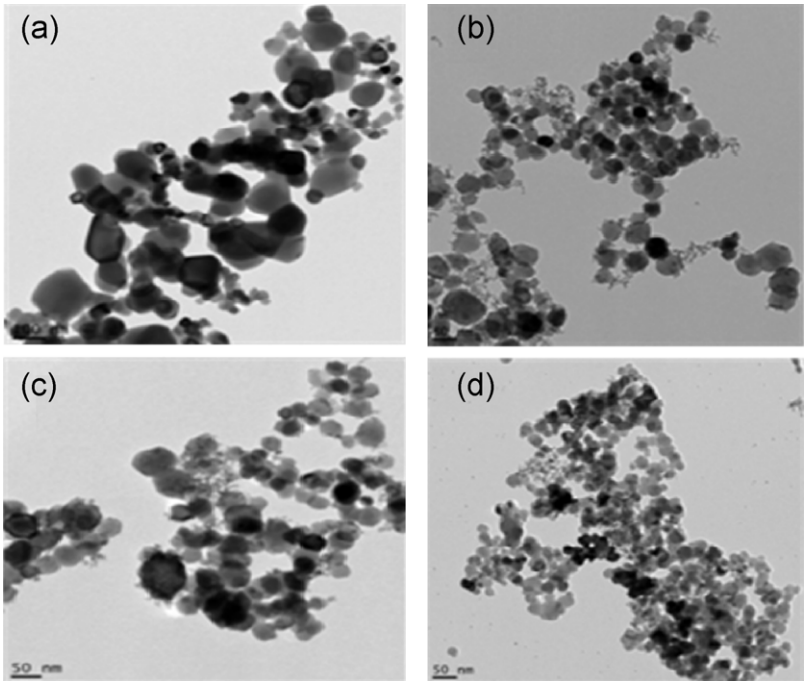

Fig. 2. TEM images for (a) PNCBT, (b) PNCAT, (c) Nb-NCBT and (d) Nb-NCAT.

ues, *viz* 45.8 T (RA = 3%) and 47.1 T (RA = 4%), for an averaged isomer shift relative to aFe (δ) of 0.35 mm s^{-1}, for the whole hyperfine distribution, are due to magnetically ordered high spin Fe^{3+}-bearing species other than hematite. The slightly lower value found for the specie corresponding to the dominant subspectral area, and hyperfine parameters assignable to hematite, may be an effect of (i) small particle-size distribution, (ii) defective structure to some variable extent, or (iii) any isomorphical replacement of iron by other non-magnetic cations in the atomic framework of the iron oxide. In addition to these magnetic contributions, an incipient doublet was observed with δ = 0.36 mm s^{-1} and quadrupole splitting, Δ = 0.76 mm s^{-1}, which can be assigned to superparamagnetic hematite (RA = 7%). The component with hyperfine field of 48.5 T and isomer shift of 0.33 mm s^{-1} corresponds to maghemite (γ-Fe_2O_3) (RA = 13%). Incidently, the value of saturation magnetization for this sample is σ = 5.1 J T^{-1} kg^{-1}, which is an additional datum confirming the occurrence of the ferrimagnetic iron oxide.

298 K-Mössbauer spectra for the nanocomposite sample after treatment with H_2O_2 (PNCAT) (Fig. 1) does not show any significant change relatively to the PNCBT sample. A slightly lower value of the hyperfine field was observed from 48.5 T (PNCAT) to 48.3 T (PNCBT) due to the decreasing particle sizes of maghemite, due to the chemical treatment. An increase of the relative subspectral area corresponding to maghemite, was observed to go from 13% (PNCBT) to 15% (PNCAT), which might be due to oxidation of any residual organic compounds formed during the synthesis process. Therefore, the saturation magnetization value slightly increased from 5.1 to 5.4 J T^{-1} kg^{-1}. Hematite was identified from their hyperfine fields of 50.5 T (RA = 74%) and 46.2 T (RA = 5%) and by a putative superparamagnetic component (RA = 7%), with corresponding δ = 0.37 mm s^{-1} and Δ = 0.77 mm s^{-1}.

298 K-Mössbauer spectrum for the sole Nb-doped iron oxide fraction of the nanocomposite before treatment with H_2O_2 (Nb-NCBT) is completely different from that of the PNCBT (Fig. 1). The Nb-NCBT spectrum is mainly constituted by maghemite (B_{hf} = 47.9 T, δ = 0.34 mm s^{-1} and RA = 53%). The large maghemite content is consistent with the high value of saturation magnetization (29 J T^{-1} kg^{-1}) of this sample. It is very well documented in the literature that the magnetic hyperfine field is very sensitive to the isomorphic substitution of iron with others cations [25]. In the present case, this can be confirmed by the lower value of the maghemite hyperfine field, from 48.5 T (sample PNCBT) to 47.9 T (Nb-NCBT). This immediately suggests that some Fe(III) was isomorphically replaced by Nb(V) in the maghemite structure. Other contributions corresponding to hyperfine fields of 44.2 (RA = 3%), 45.7 (RA = 14%) and 48.5 T (RA = 20%) and average isomer shift of 0.35 mm s^{-1} and quadrupole splitting of −0.19 mm s^{-1} and one Fe(III) doublet corresponding to superparamagnetic hematite (δ = 0.31 mm s^{-1}, Δ = 0.89 mm s^{-1} and RA = 7%) were also observed. An incipient Fe(II) doublet (δ = 1.10 mm s^{-1}, Δ = 1.55 mm s^{-1} and RA = 3%) was assigned to $FeNb_2O_6$ [26]. The maximum hyperfine field in the hyperfine field distribution profile that was initially observed for hematite was strongly diminished from 50.5 T (PNCBT) to 48.5 T (Nb-NCBT). This may suggest an important isomorphic replacement of Fe(III) by Nb(V) on the iron oxide structure. It was also observed that Nb(V) can stabilize the maghemite structure and retard the complete transformation of maghemite into hematite by heating at 500 °C, as it could be drawn from the high maghemite content in this sample.

The Mössbauer spectrum of Nb-doped iron oxide nanocomposites after treatment with H_2O_2 (Nb-NCAT) (Fig. 1) reveals that remarkable changes occurred within the hematite and maghemite structures. The intense sextet that appears in the Nb-NCBT sample is no longer observed in the Nb-NCAT. On the other hand, an intense doublet was observed in the Nb-NCAT spectrum, suggesting that the Nb-doped maghemite was more drastically affected by the treatment with H_2O_2. Mössbauer parameters indicate that this sample is constituted mainly by hematite, which is related to the hyperfine fields 45.5 (RA = 3%), 47.8 (RA = 3%), 50.0 (RA = 11%) and 51.2 T (RA = 7%), with an average isomer shift of 0.35 mm s^{-1} and quadrupole splitting of −0.21 mm s^{-1}. In addition to the hematite sextets, one Fe(III) doublet was identified corresponding to superparamagnetic hematite (RA = 37%) with δ = 0.39 mm s^{-1} and Δ = 1.11 mm s^{-1}. The high value of quadrupole splitting also suggests a distorted structure for hematite or related nanosized iron oxide, on treating the sample with H_2O_2. The increase in

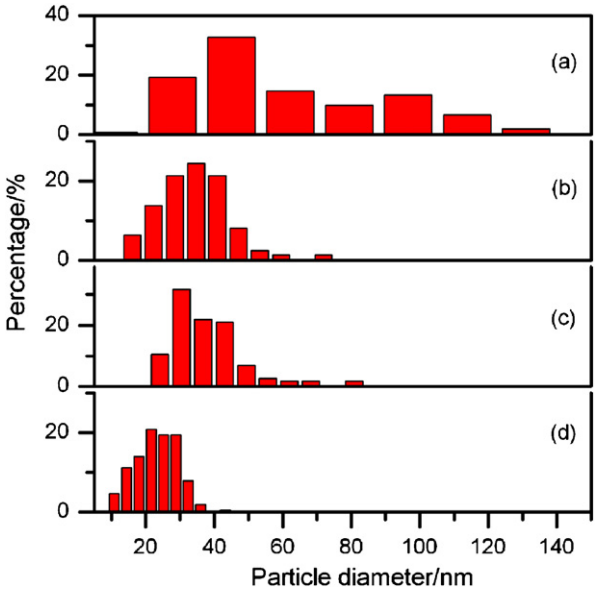

Fig. 3. Particle size distributions for (a) PNCBT, (b) PNCAT, (c) Nb-NCBT and (d) Nb-NCAT.

value of the hyperfine field indicates an increase of the mean particle size of hematite, as most of the hematite of this sample is thought to be produced from maghemite as direct precursor. An Fe(III) doublet on tetrahedral coordination ($\delta = 0.28\ mm\ s^{-1}$ and $\Delta = 1.00\ mm\ s^{-1}$, RA = 16%) and another doublet on octahedral coordination ($\delta = 0.36\ mm\ s^{-1}$ and $\Delta = 0.59\ mm\ s^{-1}$, RA = 20%) is assigned to superparamagnetic maghemite. The disappearing of the maghemite sextet observed in Nb-NCBT sample and the appearance of these maghemite doublets in Nb-NCAT is an indicative of a drastic structural disorder caused on the H_2O_2 treatment, which was chemically effective enough to suppress the magnetic ordering of iron atoms in the maghemite structure. The diminishing of the relative subspectral area from 53% (Nb-NCBT) to 36% (Nb-NCAT) suggests that maghemite was transformed to hematite. Because of the transformation of maghemite into hematite, the saturation magnetization decreased from 29 (Nb-NCBT) to $6\ J\ T^{-1}\ kg^{-1}$ (Nb-NCAT). $FeNb_2O_6$ still remains in the Nb-NCAT spectrum, as can be verified by the contribution of the Fe^{2+} doublet ($\delta = 1.04\ mm\ s^{-1}$ and $\Delta = 1.55\ mm\ s^{-1}$, RA = 3%).

Fig. 2 shows the TEM images for samples before and after H_2O_2 treatment. These images show the formation of irregular-shaped particle agglomerates. It is clearly observed from Fig. 2 that the particle size of the iron oxides in the composites may decreases after treatment with H_2O_2, according to XRD. PNCBT reveals a wide size distribution (20–140 nm) (Fig. 3a), whereas after H_2O_2 treatment (Fig. 3b) the distribution is narrower (10–80 nm). The presence of Nb on the synthesis process induces the formation of iron oxides with small particle size when compared with PNCBT, as can be verified in Fig. 3c. A strong decreasing of the particle size was observed after treatment of Nb-NCBT with H_2O_2 (Fig. 3b), indicating that the presence of niobium in the composite make it more reactive towards H_2O_2 reactions.

The vibration absorption bands (Fig. 4a) at $1612\ cm^{-1}$ in the samples before H_2O_2 treatment (PNCBT and Nb-NCBT samples) and $1626\ cm^{-1}$ in the samples after treatment (PNCAT and Nb-NCAT samples) and at $3400\ cm^{-1}$ are characteristic of adsorbed water molecules.

The band around $3630\ cm^{-1}$ that appears only in the PNCAT and Nb-NCAT samples correspond to surface OH groups of hematite and maghemite [24,25]. It suggests that H_2O_2 treatment can promote hydroxylation on the iron oxide surface, which can be interesting for use in a specific catalysis type. In order to provide better characterization of peroxo groups and M–O (M = metal) vibrations a fit of the FTIR spectra in the range of $1000–400\ cm^{-1}$ was performed. The obtained results are shown in Fig. 4b. Bands at 439, 531 and $601\ cm^{-1}$ in PNCBT spectrum were assigned to Fe–O vibration in hematite [25]. After H_2O_2 treatment (PNCAT sample) these bands were shifted to 413, 540 and $650\ cm^{-1}$, which is an indicative of hematite structure deformation. In addition the hematite bands, it was observed a small contribution of maghemite, characterized by the band at $690\ cm^{-1}$ in the PNCBT sample. After H_2O_2 treatment this band was shifted to $718\ cm^{-1}$, suggesting the maghemite structure deformation. The Nb-NCBT spectrum shows bands at 463, 579 and 696 which are characteristic of maghemite. After treatment, Nb-NCAT spectrum showed bands at 525 and $632\ cm^{-1}$, indicative of conversion of maghemite into hematite, as also verified by XRD. The shifted band at $739\ cm^{-1}$ suggests the strong distortion of maghemite structure promoted by H_2O_2 treatment. Actually, the generated defects following the isomorphous ionic substitution in an oxide structure can significantly modify their catalytic properties, as it can cause an increase of specific surface area and favor the transport of electrons, as the involved mechanism of redox reactions [19]. To analyze the NbO_2 and peroxo group vibrations it is usual to admit that the metal-peroxo grouping behaves as an equilateral triangle with local C_{2v} symmetry [27,28]. For these grouping, three active IR bands are expected. From these vibrations, the $\nu_1(A_1)$ mode has, essentially, the characteristics of an O–O stretching or an O–Nb–O deformation, whereas $\nu_2(A_1)$ is fundamentally a symmetric Nb–O stretch, partially coupled with O–O stretching. Finally, $\nu_3(B_1)$ originates basically in the antisymmetric Nb–O stretch. Bayot et al. (2005) [29] have described one band at $841–870\ cm^{-1}$ corresponding to ν(O–O). Spectrum of Nb-NCBT shows a band at $827\ cm^{-1}$, which is shifted to $858\ cm^{-1}$ and its relative intensity after H_2O_2 treatment is duplicated, indicative of ν(O–O). This band can be related with the formation of Nb-peroxo complexes immobilized on the iron oxide surface.

To better understand the origin of the changes in the chemical and physical properties of our iron oxide nanocomposites after H_2O_2 treatment and in order to determine if a similar change in structure is also occurring with our materials, a structural analysis was performed. The nanocomposites were analyzed by XRD in powder form. The subsequent Rietveld refinement of XRD data with Thompson-Cox-Hastings pseudo-Voigt * Axial divergence asymmetry peak fitting gave the structural parameters and the refinement reliability factors summarized in Table 1 along with the crystallite size as determined from the Scherrer equation. Fig. 5a shows the Rietveld refinement on XRD pattern of the samples.

The pattern of PCNBT shows diffraction peaks from hematite (91 wt.%) and maghemite (9 wt.%) and after H_2O_2 treatment (PCNAT) these proportions practically do not change (Fig. 5b). Otherwise, the hematite/maghemite proportion is strongly affected by presence of niobium in the composites. The pattern of Nb-NCBT mainly consists of hematite (32 wt.%) and maghemite (56 wt.%), whereas after treatment the sample Nb-NCAT is constituted by hematite (51 wt.%) and maghemite (38 wt.%), suggesting the conversion of maghemite into hematite. The high content of maghemite in the Nb-NCBT sample suggests that the Nb^{5+} ions can stabilize the maghemite structure. In addition these phases, diffraction peaks were observed corresponding to $FeNb_2O_6$ with 12 and 11 wt.% in Nb-NCBT and Nb-NCAT samples, respectively.

The crystallite size of maghemite after H_2O_2 treatment decreases drastically from 93 to 31 nm and from 90 to 13 nm (Table 1) for PNCAT and Nb-NCAT samples, respectively, which can be clearly observed in TEM images (Fig. 1). This explains the loss of magnetic ordering on maghemite structure observed in Nb-NCAT Mössbauer spectrum. On the other hand, the crystallite size of

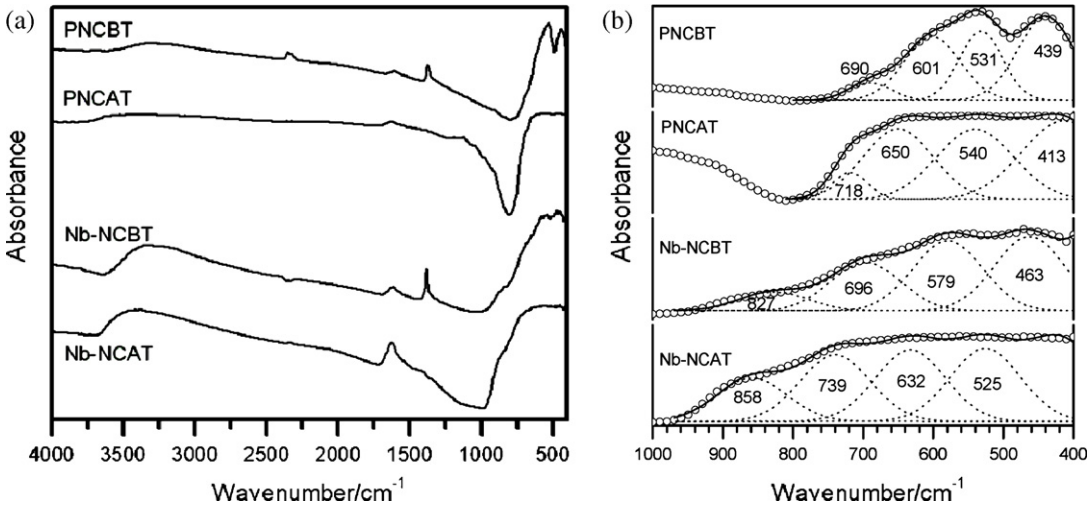

Fig. 4. (a) FT-IR spectra of pure and Nb-doped iron oxide nanocomposites before and after H_2O_2 treatment (b) Fitted expanded region of FTIR spectra of nanocomposites before and after H_2O_2 treatment.

Table 1
Crystallografic phase, chemical formula, lattice parameters, agreement factors for the refinements and average apparent size obtained from Rietveld refinement of the pure and Nb-doped iron oxides composites.

Sample	Phase	Chemical formula	Lattice parameters/A	Bragg *R*-factor	R_{f-} factor	Average apparent size li tn
PNCBT	Hematite	α-Fe_2O_3	a = 5.03715(5), c = 13.7666(3)	1.68	1.17	26(6)
	Maghemite	$[Fe^{3+}]\{F^{3+}_{1.67}\otimes_{0.33}\}O_4$	a = 8.3445(2)	2.94	2.27	93(8)
PNCAT	Hematite	$Fe^{3+}F^{3+}_{1.996}\otimes_{0.004}O_{2.994}$	a = 5.03174(4). c=l 3.7488(2)	2.46	1.78	20(4)
	Maghemite	$[Fe^{3+}]\{F^{3+}_{1.664}\otimes_{0.356}\}O_{3.966}$	a = 8.3369(2)	3.66	2.61	31(7)
Nb-NCBT	Hematite	$Fe^{3+}_{1.865}Nb^{5+}_{0.081}\otimes_{0.054}O_3$	a = 5.03168(8). c = 13.7658(4)	1.50	1.29	43(5)
	Maghemite	$[Fe^{3+}]\{F^{3+}_{1.512}Nb^{5+}_{0.093}\otimes_{0.395}\}O_4$	a = 8.3402(1)	2.08	1.64	90(1)
	Feme niobium oxide	$FeNb_2O_6$	a = 14.029(2), b = 5.6883(6), c = 5.0318(5)	3.16	1.38	23(9)
Nb-NCAT	Hematite	$Fe^{3+}_{1.835}Nb^{5+}_{0.067}\otimes_{0.395}\}O_{3.895}$	a = 5.02970(4). c = 13.7849(2)	2.57	2.53	52(9)
	Maghemite	$[Fe^{3+}]\{F^{3+}_{1.485}Nb^{5+}_{0.067}\otimes_{0.395}\}O_{3.895}$	a = 8.3245(7)	2.51	1.79	13(2)
	Ferric niobium oxide	$FeNb_2O_6$	a = 14.30(1), b = 5.099(5), c = 4.776(5)	3.S6	1.65	nd

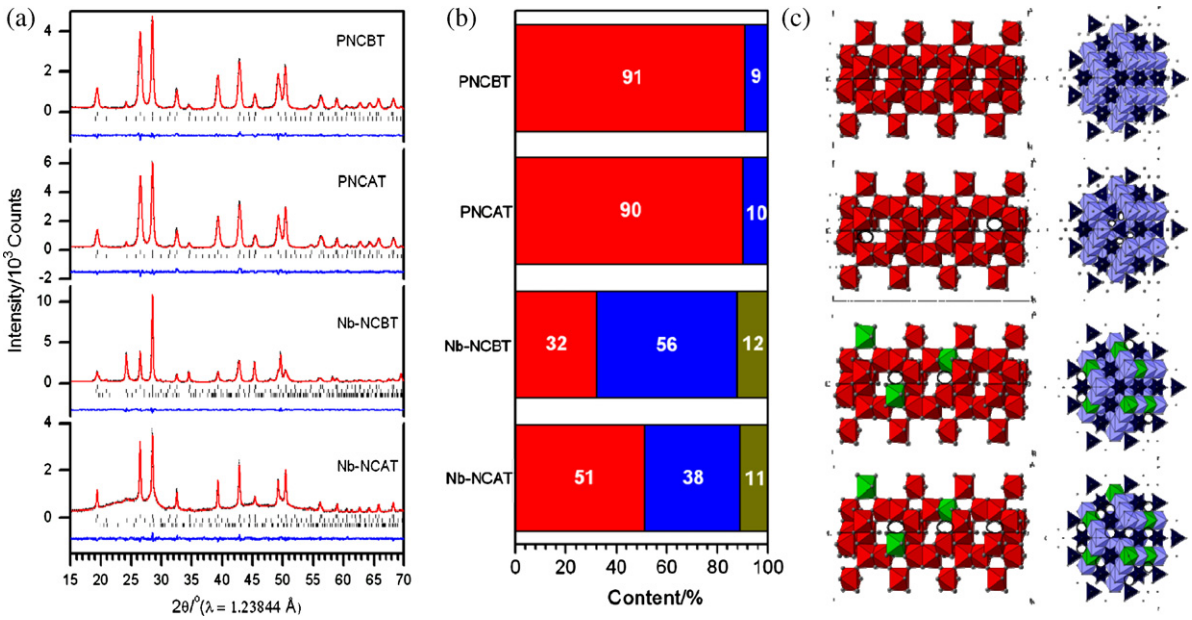

Fig. 5. (a) Rietveld refinement on XRD patterns of PNCBT, PNCAT, Nb-NCBT and Nb-NCAT samples. (b) The hematite (red), maghemite (blue) and $FeNb_2O_6$ (dark yellow) contents evaluated by Rietveld analyses. (c) Graphical representations of the crystal structure of hematite (red) and maghemite (blue). The polyhedrons and spheres on the edges represent the iron and oxygen atoms, respectively. Green polyhedrons represent niobium atoms. (For interpretation of the references to color in this figure legend, the reader is referred to the web version of the article.)

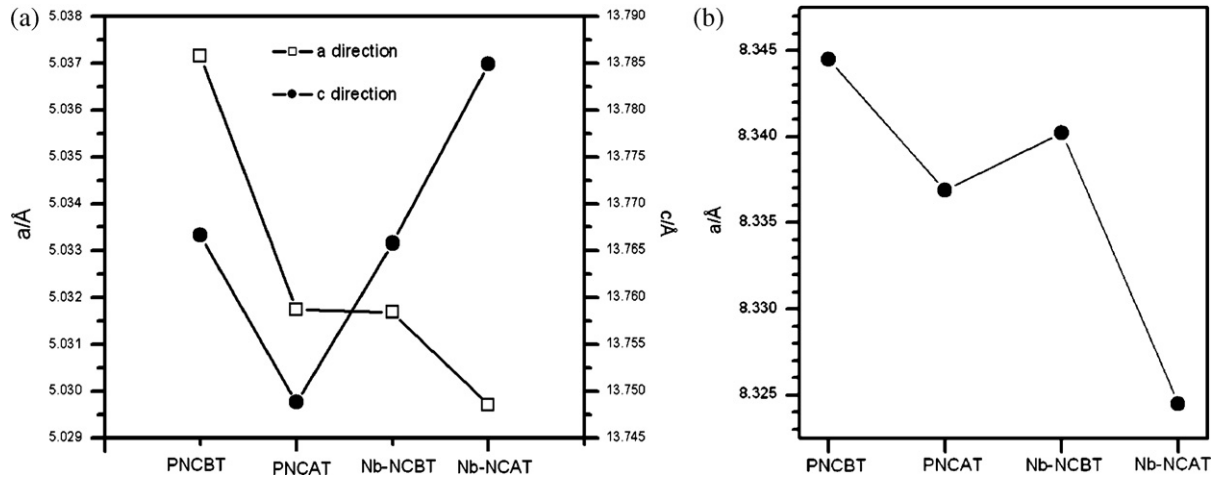

Fig. 6. (a) Lattice parameter of hematite in the different composites and (b) lattice parameter of maghemite.

hematite decreases slightly from 26 to 20 nm after H_2O_2 treatment in PNCAT and increases from 43 to 52 nm in Nb-NCAT. This suggests that H_2O_2 treatment induces the transformation of maghemite (large particle size) into hematite, leading to an increase of mean crystallite size on hematite. This is in agreement with the hematite sextet observed in Nb-NCAT Mössbauer spectrum.

The Rietveld refinement (Fig. 5a) yielded a profile residual factor, R_p, of approximately 4.5% for each sample, indicative of good quality refined models. With respect to the H_2O_2 treatment, the unit cell of hematite on PNCAT sample decreases in both "a" and "c" directions (Fig. 6a). This contraction of the unit cell is mainly due to cationic and anionic vacancies (Fig. 5c) produced by treatment of the nanocomposite with H_2O_2. On the other hand, the Nb-NCBT shows that the unit cell of hematite in "c" direction remains practically the same, whereas a slight decreasing in unit cell in the "a" direction from 5.03715 Å to 5.03168 Å could be observed. This suggests the isomorphic substitution of Fe by Nb in the hematite structure. The high spin Fe^{3+} ionic radii on octahedral coordination is 65 pm, while for Nb^{5+} it is practically the same, i.e. 64 pm. However, to keep the charge balance only $3Nb^{5+}$ are necessary for each $5Fe^{3+}$ and as result of this substitution two cationic vacancies arise in the hematite structure, which are the main responsible factors for contraction of its unit cell. After H_2O_2 treatment, the unit cell of hematite in Nb-NCAT is more drastically affected than the PNCAT sample (Fig. 5a), suggesting that Nb has a fundamental role towards H_2O_2 treatment. A decreasing in "a" direction was observed from 5.03168 Å to 5.02970 Å and a strong increase in "c" direction from 13.7658 Å to 13.7849 Å, indicative of strong distortion in the hematite structure. The unit cell of maghemite decreases from 8.3445 Å to 8.3369 Å (Fig. 6b) after H_2O_2 due to formation of cationic and anionic vacancies. The unit cell of Nb-doped maghemite decreases from 8.3445 to 8.3402 Å, confirming the isomorphic substitution of Fe^{3+} by Nb^{5+}. The H_2O_2 treatment promotes strong structural defects on Nb-doped maghemite as illustrated in Fig. 5c. The unit cell decreases from 8.3402 Å to 8.3245 Å. The chemical formula for each phase in the composite is showed in Table 1. The niobium content in the composites is completely in agreement with the niobium content (10 wt.%) determined by chemical analysis.

3.2. Catalytic tests

It has been observed (Fig. 7a) that there was no significant discoloration of the methylene blue dye solution in contact with the

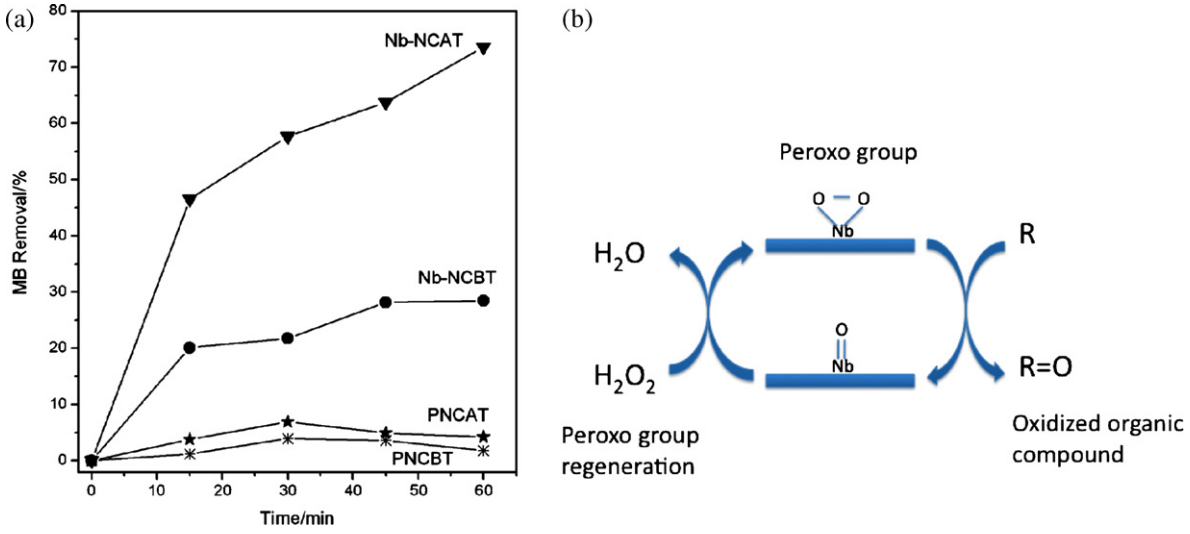

Fig. 7. (a) Removal of methylene blue dye (MB) monitored by UV–vis spectroscopy at 665 nm (10 mg of catalyst; [MB] = 50 mg L^{-1}; 8 mM of H_2O_2 (30% v/v)). (b) Sketch representation of the organic compound oxidation by the peroxo group.

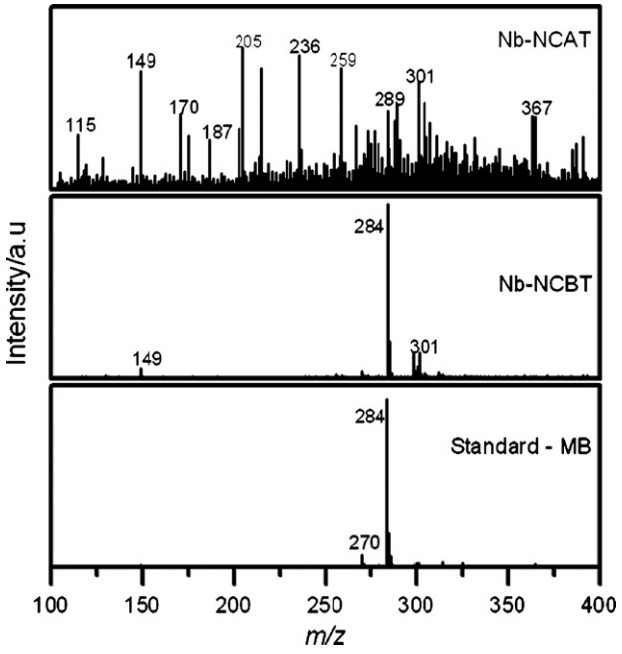

Fig. 8. ESI mass spectra in the positive ion mode for monitoring the oxidation of methylene blue dye.

H_2O_2 solution and undoped iron oxides (PNCBT and PNCAT). However, with the iron oxide modified by the presence of Nb (Nb-NCBT) a significant discoloration is observed after 60 min of reaction with approximately 30% discoloration. It is important to observe that the material without previous treatment with hydrogen peroxide needs some time prior to its use, to become more active. This "aging" time is needed to allow forming the peroxo group on the surface, as it could be reportedly found in our previous work on this catalytic system [18]. After the second modification, i.e. the previous treatment with hydrogen peroxide producing the catalyst Nb-NCAT, a strong discoloration of the solution was observed indicating that the treatment improves the catalytic activity on the dye oxidation. The oxidizer properties are generated after surface modification by the previous treatment with H_2O_2 of the iron oxide. This surface modification generates a strong oxidizer group called peroxo group on the iron oxide surface due to the presence of niobium [19]. The catalytic efficiency obtained in this work is comparable to others works where the authors used Cr-doped magnetite [30] or Cu-doped magnetite in the presence of hydrogen peroxide [31].

After six reaction cycles, the Nb-NCBT catalyst presented catalytic activity loss, but after H_2O_2 solution added into de system the catalytic activity was recovered suggesting that the oxidizing sites are regenerated by the addition of H_2O_2. These results suggest that the role of added H_2O_2 is for peroxo group regeneration on Nb-doped iron oxides composites [32]. Fig. 7b shows a schematic representation of the organic compound oxidation by the peroxo group and its regeneration.

The identification of reaction intermediates was performed on-line by the ESI-MS equipment during the oxidation of the methylene blue dye (Fig. 8). The sample without treatment with H_2O_2 (Nb-NCBT) produced few signals related to intermediate compounds according to discoloration study data. On the other hand, the previous treatment with H_2O_2 leads too much higher catalytic activity for the modified iron oxides composites. After 60 min of reaction strong signals corresponding to $m/z = 300$, 316 and 332 are detected, due to successive hydroxylation of the dye structure [33], as well as other signals related to the breakdown of the organic structure. In fact, the signals with values of m/z lower than 284 such as 115, 149 and 170 should correspond to intermediates formed by breaking the ring of organic dye, which would be consistent with other studies reported in the literature [33].

4. Conclusions

This work present a highly active iron oxides composite obtained by incorporation of niobium and treatment with H_2O_2. The innovative material produced presented a high activity for oxidation of organic dye in liquid phase. The analysis of the product with mass spectrometry showed that successive hydroxylations take place to produce several intermediate compounds. The characterization showed that the materials are constituted mainly by hematite, maghemite and $FeNb_2O_6$. The H_2O_2-treatment promotes surface and structural changes, which significantly enhance the catalytic properties of the composites. Moreover, it was shown that previous H_2O_2 treatment induces the decreasing of the particle size in the composites. Nb-doping of iron oxides and $FeNb_2O_6$ has an important role towards H_2O_2 reactions to produce Nb–O–O groups, which are the main reactive species in the system. The hydrogen peroxide decomposition and oxidation of organic compounds with H_2O_2 are likely to take place via radicals, as suggested by the ESI–MS studies. It was indicated that an oxidation mechanism should occur by the attack of the free $^{\bullet}OH$ radical on the molecule giving rise to hydroxylation products as a principal byproduct but compounds resultant from the ring cleavage are also detected. A scale-up of this system is in now progress intending to evaluate the real possibility of water purification in natural environment, by using the composite catalysts developed in this work.

5. Aknowledgements

This work was supported by the FAPEMIG, CNPq, CAPES, Department of Chemistry of the University of California at Riverside and US National Science Foundation, CBMM (Brazil) for the samples and National Laboratory of Synchrotron Light (Brazil).

References

[1] A. Maniatakou, C. Makedonas, C.A. Mitsopoulou, C. Raptopoulou, I. Rizopoulou, A. Terzis, A. Karaliota, Polyhedron 27 (2008) 3398–3408.
[2] M. Afsharpour, A.R. Mahjoub, M.M. Amini, Appl. Catal. A-Gen. 327 (2007) 205–210.
[3] H.I. Karunadasa, C.J. Chang, J.R. Long, Nature. 464 (2010) 1329–1333.
[4] D. Bayot, M. Devillers, Coord. Chem. Rev. 250 (2006) 2610–2626.
[5] K. Kamata, S. Kuzuya, K. Uehara, S. Yamaguchi, N. Mizuno, Inorg. Chem. 46 (2007) 3768–3774.
[6] A. Maniatakou, S. Karaliota, M. Mavri, C. Raptopoulou, A. Terzis, A. Karaliota, J. Inorg. Biochem. 103 (2009) 859–869.
[7] C.R. Waidmann, A.G. DiPasquale, J.M. Mayer, Inorg. Chem. 49 (2010) 2383–2391.
[8] Patent In, S. K., et al. Low temperature process for producing nano-sized titanium dioxide particles. US20060846231P, 2009.
[9] D.V. Deubel, J. Sundermeyer, G. Frenking, Inorg. Chem. 39 (2000) 2314–2320.
[10] D. Bayot, M. Degand, B. Tinant, M. Devilers, Inorg. Chim. Acta 359 (2006) 1390–1394.
[11] Patent Frank, M., et al. Molybdenum and tungsten peroxo complexes useful as oxidation catalysts. 05/842130, 1977.
[12] M.T.H. Tarafder, S.K. Tan, K.H. Su, G. Mariotto, Orient. J. Chem. 17 (2001) 83.
[13] L.C. Passoni, M.R.H. Siddiqui, A. Steiner, I.V. Kozhevnikov, J. Mol. Catal. A-Chem. 153 (2000) 103–108.
[14] D. Meunier, A. Piechaczyk, A. Mallmann, J.M. Basset, Angew. Chem. Int. Ed. 38 (1999) 35–38.
[15] D. Bayot, B. Tinant, M. Devillers, Catal. Today 78 (2003) 439–447.
[16] M. Kantcheva, H. Budunoğlu, O. Samarskaya, Catal. Commun. 9 (2008) 874–879.
[17] K.T.G. Carvalho, A.C. Silva, L.C.A. Oliveira, M. Gonçalves, Z.M. Magriotis, Quim. Nova 32 (2009) 1373–1377.
[18] T. Ramalho, L.C.A. Oliveira, K.T.G. Carvalho, E. Souza, E. da Cunha, M. Nazzaro, Mol. Phys. 107 (2009) 171–179.
[19] A. Esteves, L.C.A. Oliveira, T.C. Ramalho, M. Gonçalves, A.S. Anastacio, H.W.P. Carvalho, Catal. Commun. 10 (2008) 330–332.
[20] L.C.A. Oliveira, M. Gonçalves, D.Q.L. Oliveira, A.L.N. Guarieiro, M.C. Pereira, Quim. Nova 30 (2007) 925–929.
[21] K. Musialska, E. Finocchio, I. Sobczak, G. Busca, R. Wojcieszak, E. Gaigneaux, M. Ziolek, Appl. Catal. A-Gen. 384 (2010) 70.

[22] D.E. Keller, S.M.K. Airaksinen, A.O. Krause, B.M. Weckhuysen, D.C. Koningsberger, J. Am. Chem. Soc. 129 (2007) 3189–3197.
[23] Y. Rao, M. Trudeau, D. Antonelli, J. Am. Chem. Soc. 128 (2006) 13996.
[24] Fullprof_Suíte. Crystallographic tools for Rietveld, profile matching and integrated intensity refinements of X-ray and or neutron data 2010. [Online]. Available at: http://www.ill.eu/sites/fullprof/[Acessed Nov 7, 2010].
[25] R.M. Cornell, U. Schwertmann, The Iron Oxides–Structure, Properties, Reactions, Occurences and Uses, 2nd ed., Wiley-VCH, Weinheim, 2003.
[26] R. Garg, O.D. Rodrigues, E. Galvão da Silva, V.K. Garg, Hyperfine Interact. 67 (1991) 443–446.
[27] E.J. Baran, Monatsh. Chem. 108 (1977) 989–995.
[28] W.P.J. Griffith, Chem. Soc. 1005 (1964) 5248–5253.
[29] D. Bayot, M. Degand, M.J. Devillers, Solid State Chem. 178 (2005) 2635–2642.
[30] F. Magalhaes, M.C. Pereira, S.E.C. Botrel, J.D. Fabris, W.A. Macedo, R. Mendonça, R.M. Lago, L.C.A. Oliveira, Appl. Catal. A-Gen. 332 (2007) 115–123.
[31] I.R. Guimaraes, A. Giroto, L.C.A. Oliveira, M.C. Guerreiro, D.Q. Lima, J.D. Fabris, Appl. Catal. B-Environ. 91 (2009) 581–586.
[32] L.C.A. Oliveira, T.C. Ramalho, M. Gonçalves, D.Q.L. Oliveira, M.C. Pereira, J.D. Fabris, Appl. Catal. B-Environ. 83 (2008) 169–176.
[33] L.C.A. Oliveira, T.C. Ramalho, M. Gonçalves, F.C. Aguiar, K.T.G. Carvalho, M. Nazzarro, K. Sapag, Chem. Phys. Lett. 446 (2007) 133–137.

Journal of Magnetism and Magnetic Materials 322 (2010) 633–637

Contents lists available at ScienceDirect

Journal of Magnetism and Magnetic Materials

journal homepage: www.elsevier.com/locate/jmmm

Magnetic composites based on hybrid spheres of aluminum oxide and superparamagnetic nanoparticles of iron oxides

Tiago P. Braga [a], Igor F. Vasconcelos [b], José M. Sasaki [c], J.D. Fabris [d], Diana Q.L. de Oliveira [d], Antoninho Valentini [a,*]

[a] Langmuir – Laboratório de Adsorção e Catálise, Departamento de Química Analítica e Físico-Química, Universidade Federal do Ceará, CP 6021, CEP 60455-970 Campus do Pici, Fortaleza, Brazil
[b] Departamento de Engenharia Metalúrgica e de Materiais, Universidade Federal do Ceará, Fortaleza, Brazil
[c] Laboratório de Raios X, Departamento de Física, Universidade Federal do Ceará, Campus do Pici, Fortaleza, CE, Brazil
[d] Departamento de Química, Universidade Federal de Minas Gerais, Belo Horizonte, Brazil

ARTICLE INFO

Article history:
Received 15 July 2009
Received in revised form
8 October 2009
Available online 29 October 2009

Keywords:
Hybrid sphere
Nanoparticle
Iron oxide
Aluminum
Superparamagnetic

ABSTRACT

Materials containing hybrid spheres of aluminum oxide and superparamagnetic nanoparticles of iron oxides were obtained from a chemical precursor prepared by admixing chitosan and iron and aluminum hydroxides. The oxides were first characterized with scanning electron microscopy, X-ray diffraction, and Mössbauer spectroscopy. Scanning electron microscopy micrographs showed the size distribution of the resulting spheres to be highly homogeneous. The occurrence of nano-composites containing aluminum oxides and iron oxides was confirmed from powder X-ray diffraction patterns; except for the sample with no aluminum, the superparamagnetic relaxation due to iron oxide particles were observed from Mössbauer spectra obtained at 298 and 110 K; the onset six line-spectrum collected at 20 K indicates a magnetic ordering related to the blocking relaxation effect for significant portion of small spheres in the sample with a molar ratio Al:Fe of 2:1.

1. Introduction

Composite materials containing iron oxides are widely used in technologies of gas sensors [1], magnetic refrigeration [2], data storage in computer devices [3], adsorbents [4], and chemical catalysts [5]. Developing an efficient and sufficiently practical methodology to prepare such composites, as those based on magnetic iron oxides, has been a matter of many relatively recent research works, particularly those involving sol–gel method [6], electrochemical techniques [7], chemical vapor deposition [8], or pyrolysis [9].

Nanoscaled materials present unique physical and chemical features, comparatively to their bulk form, making them of particular interests from scientific and technological viewpoints. Nanoparticles with magnetic properties have potential applications in several more specific areas of either *in vivo* or *in vitro* biological researches on modern medical practices [10,11]. To gain practical uses, such small magnetic particles must have high saturation magnetization (M_S) and coercivity (H_C) [12]. Bulk metallic iron itself does present such a required high saturation but its coercivity is in practice rather low. On the other hand, the coercivity magnitude of metallic iron nanoparticles is significantly higher than the corresponding coarser, bulk material [13]. Superparamagnetic effects are somehow directly related to the exceptionally small size of magnetic nanoparticles, since particles with diameters below a given threshold values usually are recognized to exhibit these characteristics[14]. As a result of this, materials with superparamagnetic behavior have been extensively used in biomedical practices[15,16]. Previously reported results in the scientific literature have dealt with applications of nanoparticles of magnetic iron oxide to separate biochemical products or cells [17], to clinically treat cancer tumors [18].

The applicability and efficiency of a nanoparticulated material also depend upon particles uniformity both in size and in shape. Even though different shapes eventually represent, in some cases, particular advantages, spherical shape would be conceptually preferable, taking into their relatively higher surface area to volume ratio. The ability to control size and morphology of nanoparticles may determine the preparation of tailored materials destined to these specific applications [19].

In this work, we report results on the preparation of hybrid spheres, containing nanosized aluminum and iron oxide, obtained from a synthesis route starting on an organic substrate precursor. The synthesized material was characterized with scanning electron microscopy, X-ray diffraction, and Mössbauer spectroscopy.

2. Experimental procedures

Samples of hybrid spheres of aluminum oxide and iron oxide were obtained *via* a method employing chitosan, a polysaccharide

* Corresponding author.
E-mail address: valent@ufc.br (A. Valentini).

0304-8853/$ - see front matter © 2009 Elsevier B.V. All rights reserved.
doi:10.1016/j.jmmm.2009.10.028

derived from D-glucosamine, as an organic precursor, and aluminum and iron salts: 5.5 g of chitosan was dissolved in 300 mL of CH_3COOH solution (5% v/v); separately, 26.98 g of $Al(NO_3)_3 \cdot 9H_2O$ and 4.85 g of $Fe(NO_3)_3 \cdot 9H_2O$ were dissolved in 100 mL of water. The iron + aluminum aqueous solution was poured into the chitosan solution, under constant stirring. The resulting solution, from now on to be referred to as simply Fe–Al–chitosan solution, was drop wise pumped into a NH_4OH aqueous solution (30% v/v), under stirring, with a peristaltic pump. The gel spheres so formed were separated from the NH_4OH solution medium and dried at room temperature for 96 h. The dried samples were calcined in airflow, during 1 h at 500 °C, under a heating rate of 5 °C min^{-1}. During the polymeric precursor elimination process, the iron and/or aluminum oxide spheres were formed. The Fe–Al–chitosan solutions were prepared with a ratio of 2.5 ions (Fe and Al) to each monomer of chitosan. Samples with different Al to Fe molar ratios were prepared and labeled AlFe*X*, where *X* denotes the Al:Fe molar ratio. The sample labeled Al contained only aluminum oxide.

The morphology and mean diameter of spheres were examined with a Philips XL30 scanning electron microscope (SEM), operating with an accelerating voltage of 20 kV. The X-ray diffraction (XRD) analysis was performed in a Rigaku-DMAXB X-ray diffractometer using Bragg–Brentano geometry in the range of 10–80° with a rate of 0.5 °min^{-1}. CuKα radiation (λ=1.5405 Å) was used and the tube operated at 40 kV and 25 mA. The phase identification analysis was made by comparing obtained powder diffractograms with standard patterns from International Centre for Diffraction Data (ICDD). For the sample AlFe0, the experimental patterns were numerically fitted with the Rietveld algorithm [20] in a procedure to better identify and quantify crystallographic phases. Mean nanoparticles sizes, when applied, were estimated by using the Scherrer's equation [21]. Transmission Mössbauer spectra were recorded at room temperature, 110 K, and at 20 K, in constant acceleration mode setup, with a ^{57}Co (Rh) source. The Mössbauer data were fitted to discrete Lorentzian functions, using the least-square fitting routine of the NORMOS® software package. All isomer shift values (δ) are quoted relatively to αFe.

3. Results and discussion

Fig. 1 illustrates the hybrid spheres immediately after being separated from the aqueous solution of ammonia. The average diameter of spheres, determined at this stage, is 3.08 mm with standard deviation of 0.34; this mean value was determined considering a total of 350 spheres. Therefore, a reasonably uniformity of sizes throughout the entire sample mass is confirmed from the image (Fig. 1). After the drying process, the mean diameter of spheres is significantly reduced, as it can also be observed from SEM micrographs (Fig. 2), indicating that volumes of individual sphere are significantly influenced by water retained by particles during the chemical synthesis. After drying at room temperature, the mean diameters for samples $AlFe_6$ and $AlFe_0$ were found to be 1.42 and 1.69 mm, respectively. After calcination at 500°C under airflow, the mean diameters for samples $AlFe_6$ and $AlFe_0$ became 1.02 and 1.53 mm, respectively (Fig. 2a and c). The occurrence of some particles surface cracked (Fig. 2b and d) points to the need of improving further the mechanical resistance of the material. However, this is an issue being addressed in a future report, as corresponding data are still being more accurately collected.

The calcinated samples were also analyzed with X-ray diffraction; results are presented in Fig. 3. All patterns, except for sample AlFe0, present broad peaks, indicating that crystallites

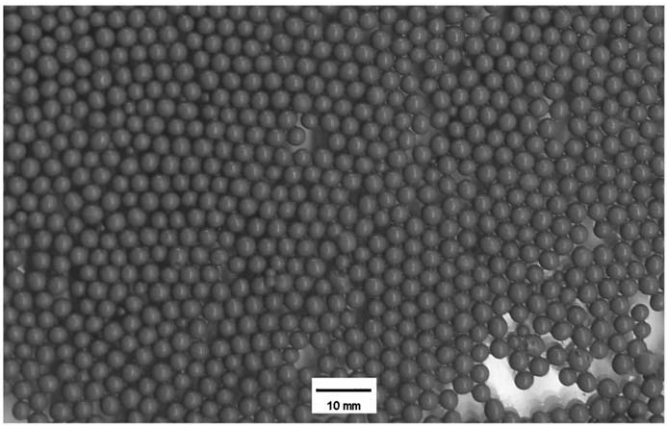

Fig. 1. Spheres immediately after the preparation process (AlFe6).

are rather small. Two crystalline phases of iron oxide were identified from the diffraction profile of sample AlFe0 (see Fig. 3b): αFe_2O_3 (hematite, JCPDS card # 87-1166) and γFe_2O_3 (maghemite, JCPDS card # 25-1402). Table 1 shows proportions of the main occurring phases.

The diffraction patterns for samples AlFe15, AlFe6, and Al (Fig. 3a) show the occurrence of Al_2O_3 (JCPDS card # 10-0425); figures for sample AlFe6 and AlFe2 reveal also the co-existence of iron oxide phases, namely αFe_2O_3 (hematite, JCPDS card # 87-1166) and γFe_2O_3 (maghemite, JCPDS card # 25-1402). Reflections associated with Al-bearing phases were not readily identified from the pattern for sample AlFe2, whereas Fe-bearing phases were not identified in the pattern for sample AlFe15. This is not unexpected as samples AlFe2 and AlFe15 have, respectively, the highest and lowest Fe:Al ratios of all samples containing simultaneously the two elements. These results suggest that the high aluminum ratio inhibits the formation of iron-containing compounds, such as hematite or magnetite, and are consistent with other reportedly results [22,23]. This influence may be explained in terms of the ionic radii of the elements as the radius of octahedral Al^{3+} (0.53 Å) is comparable to that of Fe^{3+} (0.67 Å). Similar ionic radii favor the insertion of isomorphic Al^{3+} into the structure of iron oxide, but this replacement tends to inhibit the hematite crystallization.

Any attempt to perform the Rietveld refinement of XRD data for samples Al, AlFe15, AlFe6, and AlFe2 did not yield reliable results as samples are poorly crystalline. The average crystallite diameter of the different phases as estimated with the Scherrer's formula [21] is shown in Table 1. The mean coherent lengths (MCL) for Al_2O_3 in samples Al, AlFe15, and AlFe6 were found to be, respectively, 2.0, 2.0, and 2.9 nm; for αFe_2O_3 in samples AlFe6 and AlFe2, 2.8 and 3.0 nm in diameter; for γFe_2O_3, 2.6 and 2.5 nm. MCL values for αFe_2O_3 and γFe_2O_3 in the more crystalline AlFe0 were found as being 9.9 and 9.0 nm. Data in Table 1 suggest that the increasing content of aluminum oxide tends to decrease in the diameter of iron oxide crystallites.

The local environment of iron atoms in the iron-containing samples was investigated by Mössbauer spectroscopy. Fig. 4 shows the fitted spectra; the corresponding hyperfine parameters are presented in Table 2. The room temperature spectra obtained for samples AlFe15, AlFe6, and AlFe2 (Fig. 4a) show similar features with a central doublet suggesting that iron is in a (super) paramagnetic state. The Mössbauer signal for sample AlFe15 corroborates the assumption that Fe-based phases are not identifiable by XRD due to low Fe:Al ratio and to the extremely small particle sizes.

XRD analysis confirms the existence of very fine-grained αFe_2O_3 and γFe_2O_3 (Table 1) in all samples, whereas the doublets

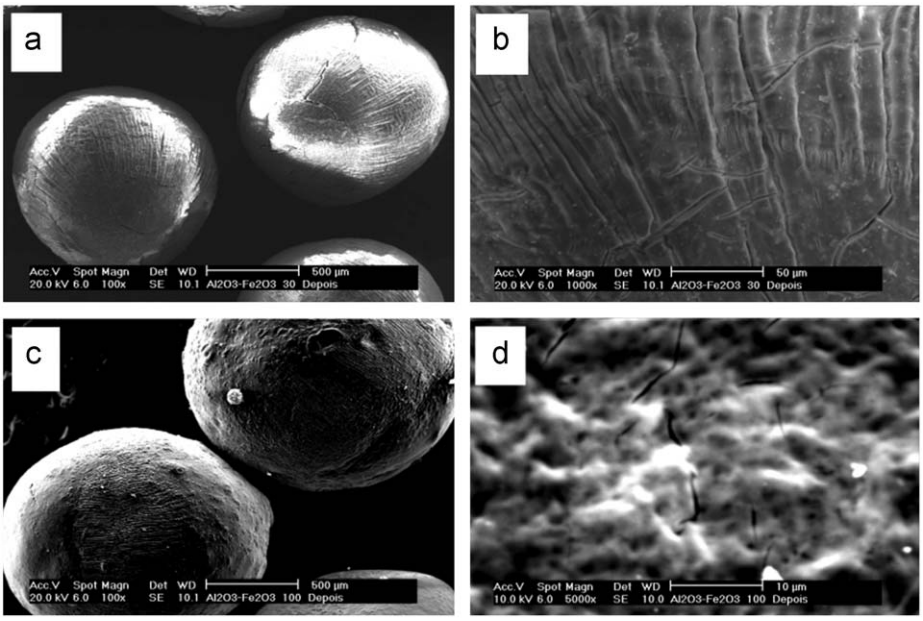

Fig. 2. SEM images of spheres: (a, b) AlFe6 sample after calcination, magnified by 100 and 1000 times, respectively. (c, d) AlFe0 sample after calcination, magnified by 100 and 5000 times, respectively.

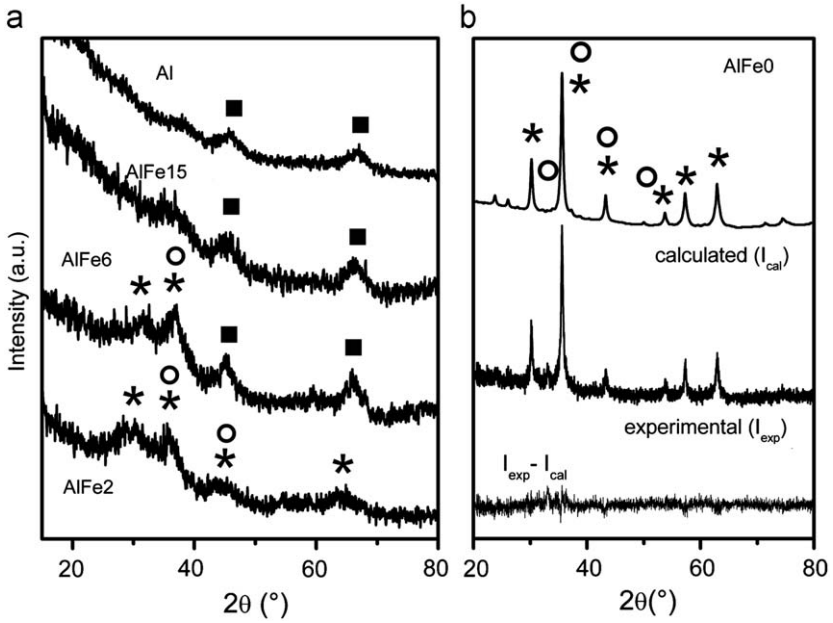

Fig. 3. X-ray powder diffraction of the spheres after calcination at 500°C: (a) Samples containing Al, and (b) AlFe0 sample. (■) Al_2O_3 phase, (○) αFe_2O_3 phase, (*) γFe_2O_3 phase, according to the standard diffractions.

Table 1
Relative mass percentage of the phases observed and grain size.

Sample	Mass of crystalline phase (%)			Grain size (nm)		
	Al_2O_3	αFe_2O_3	γFe_2O_3	Al_2O_3	αFe_2O_3	γFe_2O_3
Al	100.0	–	–	2.0	–	–
AlFe15	100.0	–	–	2.0	–	–
AlFe6	–	–	–	2.9	2.8	2.6
AlFe2	–	–	–	–	3.0	2.5
AlFe0	–	10.0	90.0	–	9.9	9.0

observed in the Mössbauer spectra confirm that the iron phases in samples AlFe15, AlFe6, and AlFe2 are in a superparamagnetic state. When particle sizes are smaller than a critical threshold, the superparamagnetic relaxation phenomenon occurs [24,25]. These observations are consistent with results recently published [26–28].

Mössbauer spectra (Fig. 4b) for sample AlFe2 taken at low temperatures confirm its superparamagnetic state. Corresponding hyperfine parameters are shown in Table 2. While at 110 K the sample still remains superparamagnetic, at 20 K a great deal of magnetic moments is blocked as it is evidenced by the appearance of a broad and asymmetric magnetic sextet. The remaining central doublet may suggest that moments are only partially blocked even at 20 K. The blocking temperature is a function of particle size. In this case, the mean diameters for aluminum-containing samples are in the range of 2.0 and ~3.0 nm (Table 1). The sample AlFe0, on the other hand, presents particles larger than those in

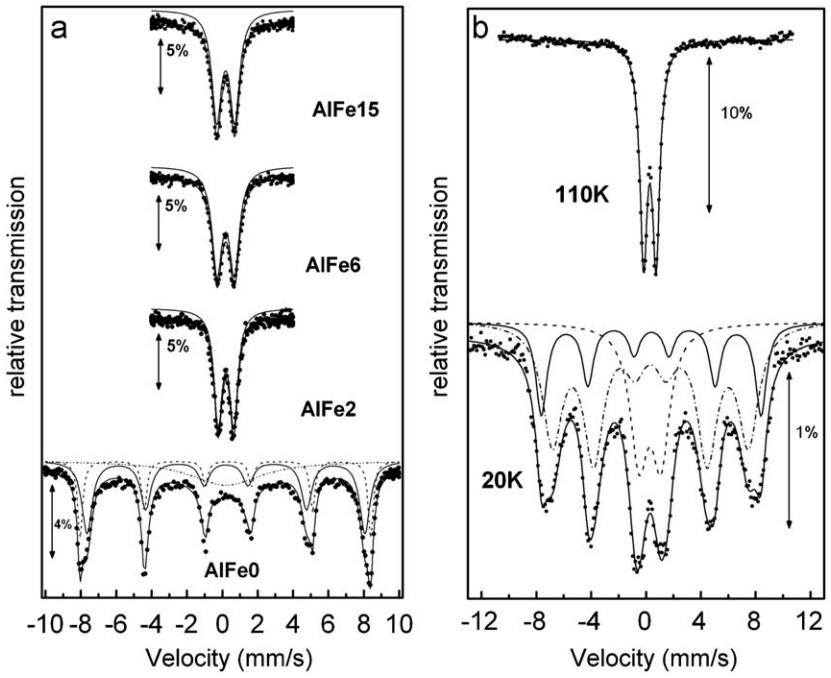

Fig. 4. 57Fe Mössbauer spectra for (a) the samples containing iron oxide, at room temperature, and (b) the sample AlFe2 at 110 and 20 K.

Table 2
^{57}Fe Mössbauer hyperfine parameters for samples containing iron.

Sample	Temperature (K)	δ (mm s^{-1}) ($\pm$0.05)	Δ or ε (mm s^{-1}) ($\pm$0.05)	B_{hf} (T) ($\pm$0.5)	*RA* (%) ($\pm$1)
AlFe15	300	0.30	1.02		100
AlFe6	300	0.30	0.98		100
AlFe2	300	0.32	0.91		100
AlFe0	300	0.37	−0.17	50.93	25
		0.32	~0	49.71	46
					28
AlFe2	110	0.39	0.91		100
AlFe2	20	0.39	1.59		22
		0.50	0.03	49.7	20
		0.43	0.01	44.3	58

δ: isomer shift relative do αFe; Δ: quadrupole splitting; ε: quadrupole shift; B_{hf}: hypefine field and *RA*: relative subspectral area.

the other samples and thus two six line-subspectra are observed in the corresponding Mössbauer spectrum at room temperature (Fig. 4a). One of them, with isomer shift relative to αFe δ=0.32 mm s^{-1}, quadrupole shift ε=−0.17 mm s^{-1}, and magnetic hyperfine field B_{hf}=50.93 T (Table 2) is assignable to hematite, while the other, with δ=0.32 mm s^{-1}, ε~0 mm s^{-1}, and B_{hf}=49.71 T, is due to maghemite, according to typical reported values for these iron oxides [29,30].

4. Conclusions

A simple method employing an organic precursor and metallic salts was used to prepare nanoparticles of aluminum oxide and of superparamagnetic iron oxides, and prepare composites with different iron:aluminum ratios, and relatively uniform spherical shapes and sizes. X-ray diffraction measurements confirmed the presence of fine-grained alumina, hematite, and maghemite all samples. Aluminum-bearing phases were not identified in the sample with the smallest aluminum:iron ratio, whereas iron oxides were not readily identified in the sample with the smallest iron:aluminum ratio. The doublet existence in the Mössbauer spectrum of the latter corroborates the assumption that Fe-based phases are not identifiable by XRD due for the smallest Fe:Al ratio due to extremely fined particle size. Room temperature Mössbauer spectra for the composites containing Fe and Al oxides presented (super)paramagnetic doublets rather than the expected sextets for bulk hematite or maghemite, suggesting that iron-bearing phases in these samples are actually in a superparamagnetic state, as sizes of particles are smaller than a critical threshold value. This assumption is confirmed by the Mössbauer measurement at 20 K, for which a great deal of blocked magnetic moments occurs, as evidenced by the appearance of magnetic sextets for magnetically ordered species. The sample with no aluminum in its composition contains particles with sizes above the critical value and thus two six-lined subspectra associated to hematite and maghemite are observed in its Mössbauer spectrum at room temperature.

Acknowledgments

This work was financially supported by CNPq/CT-PETRO, CNPq, and FAPEMIG (Brazil). CNPq also granted a scholarship to T.P. Braga. Authors are also particularly grateful to Dr. José Domingos Ardisson (Research Center for the Development of Nuclear Technology, of the Brazilian National Commission on Nuclear Energy, Belo Horizonte, Minas Gerais, Brazil) for the Mössbauer measurement at 20 K.

References

[1] L.N. Geng, S.H. Wu, Mater. Chem. Phys. 99 (2006) 15.
[2] R.D. McMichael, R.E. Watson, J. Magn. Magn. Mater. 111 (1992) 29.
[3] M.P. Pileni, J. Phys. Chem. B 105 (2001) 3358.
[4] J. Youngran, M. Fan, J.V. Leeuwen, J.F. Belczyk, J. Environ. Sci 19 (2007) 910.
[5] A.C. Oliveira, M.C. Rangel, Catal. Today 85 (2003) 49.
[6] G. Ennas, G. Spano, Chem. Mater. 10 (1998) 495.
[7] C. Pascal, J.C. Payer, Chem. Mater. 11 (1999) 141.
[8] H.R. Orthner, P. Roth, Mater. Chem. Phys. 78 (2002) 453.

[9] S. Veintemillas-Verdaguer, C.J. Serna, Mater. Lett. 35 (1998) 227.
[10] C.M. Niemeyer, Angew. Chem. Int. 40 (2001) 4128.
[11] M.W. Freeman, A. Arrot, H.H.L. Watson, J. Appl. Phys. 31 (1960) 404.
[12] M. Pardavi-Horvath, et al., IEEE Trans. Magn. 28 (1992) 3186.
[13] W.H. Meiklejohn, Rev. Mod. Phys. 25 (1953) 302.
[14] Q. Chen, et al., J. Magn. Magn. Mater. 194 (1999) 1.
[15] R.A. Whitehead et al. US Patent 4,695,392, 1987.
[16] M. Shinkai, J. Biosci. Bioeng. 94 (2002) 606.
[17] P. Tartaj, et al., J. Phys. D Appl. Phys 36 (2003) 182.
[18] B. Ben-Nissan, MRS Bull. (2004) 28.
[19] I. Safarik, et al., J. Appl. Bacteriol. 78 (1995) 575.
[20] H.M. Rietveld, J. Appl. Crystallogr 2 (1967) 65.
[21] L.V. Azaroff, in: Elements of X-ray Crystallography, McGraw-Hill Book Company, New York, 1968.
[22] M. Liu, H. Li, L. Xiao, W. Yu, Y. Lu, Z. Zhao, J. Magn. Magn. Mater. 294 (2005) 294.
[23] Y.B. Pithawalla, M.S. El Shall, S.C. Deevi, Intermetallics 8 (2000) 1225.
[24] M. Steen, J. Magn. Magn. Mater 39 (1983) 45.
[25] M. Steen, Polyteknisk Forlag, Denmark, 1981, 260 pp.
[26] Z. Huang, F. Tang, L. Zhang, Thin Solid Films 471 (2005) 105.
[27] Z. Huang, F. TangJ. Colloid Interface Sci. 275 (2004) 142.
[28] Y.G. Maa, et al., Mater. Chem. Phys. 65 (2000) 79.
[29] M. Gotic, G. Koscec, S. Music, J. Molec. Struct. 924 (2008) 347.
[30] I. Mitov, D. Paneva, B. Kunev, Thermochim. Acta 386 (2002) 179.

Hyperfine Interact
DOI 10.1007/s10751-011-0347-z

Structural characteristics of chalcopyrite from a Cu(Au) ore deposit in the Carajás Mineral Province, Brazil

Andreza Aparecida Ribeiro · Diana Quintão Lima · Hélio Anderson Duarte · Enver Murad · Márcio César Pereira · Marcos Tadeu de Freitas Suita · José Domingos Ardisson · José Domingos Fabris

Abstract Mössbauer spectra and X-ray diffraction data show a chalcopyrite from the Cristalino Cu(Au) deposit in the Carajás Mineral Province in northern Brazil to consist of a single, tetragonal phase. This is in stark contrast to a previously described chalcopyrite from the Camaquã copper mine in southern Brazil, obviously reflecting differences in mineral (and thus ore deposit) genesis.

Keywords Mössbauer spectroscopy · Chalcopyrite · Copper deposit · Rietveld analysis

1 Introduction

The Carajás Range in the central north of the State of Pará has been termed the main mineral province in Brazil [1]. A striking feature of the Carajás Mineral Province is

A. A. Ribeiro · D. Q. Lima · H. A. Duarte · E. Murad
Departamento de Química, ICEx, UFMG, Campus Pampulha, 31270-901 Belo Horizonte, Minas Gerais, Brazil

M. C. Pereira (✉)
Instituto de Ciência e Tecnologia, Universidade Federal dos Vales do Jequitinhonha e Mucuri, 39803-371 Teófilo Otoni, Minas Gerais, Brazil
e-mail: mcpqui@yahoo.com.br

M. T. de Freitas Suita
Departamento de Geologia, UFOP, 35400-000 Ouro Preto, Minas Gerais, Brazil

J. D. Ardisson
Centro de Desenvolvimento da Tecnologia Nuclear, 31270-901 Belo Horizonte, Minas Gerais, Brazil

J. D. Fabris
Universidade Federal dos Vales do Jequitinhonha e Mucuri, UFVJM, 39100-000 Diamantina, Minas Gerais, Brazil

Published online: 25 August 2011

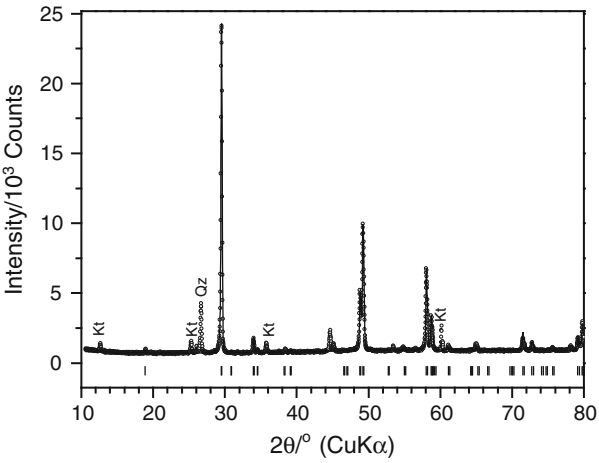

Fig. 1 XRD pattern of the chalcopyrite sample. *Qz* quartz, *Kt* kaolinite

the large number of Cu–Au mineralizations that are stratigraphically and tectonically related. Here we describe the properties of a chalcopyrite sample from the Cristalino Cu(Au) deposit, comparing its structural features with previously reported data for a sample from the Camaquã copper mine, a contrasting site in southern Brazil [2].

The Cristalino Cu(Au) deposit, located in the southeastern part of the Carajás Mineral Province, is a world class IOCG (iron oxide–copper–gold) type deposit with estimated resources greater than 500 Mt of ore averaging 1.0% Cu and 0.3 g/t Au [3]. Principal minerals constituting in this deposit are chalcopyrite, pyrite, native gold, bravoite, millerite and vaesite [3].

The main objective of the present study was to characterize a chalcopyrite from this deposit which had been used for isotope analysis [4] and compare its structural features with those of the previously mentioned chalcopyrite from southern Brazil.

2 Experimental

The studied sample was collected in the Carajás geo-province (2° 57′ 08″ S 5° 51′ 38″ W), State of Pará, Brazil. Chalcopyrite was manually separated under a binocular microscope.

A powder X-ray diffraction (XRD) pattern of this sample was obtained by slow scanning at 1/8° 2θ/min from 10° to 80° on a Rigaku Geigerflex 3064 diffractometer equipped with a Cu tube and a graphite-diffracted beam monochromator. Rietveld refinement was performed with FULLPROF 2010 [5] in order to estimate the structural parameters of the chalcopyrite. The average chemical composition was obtained by probing 13 points on seven polished sections of selected grains with a Jeol 733 scanning electron microscope equipped with an energy-dispersive X-ray spectrometer. A surface-scanning experiment was performed to assess the homogeneity of sample for Fe and Cu. Mössbauer spectra were obtained with the samples held at room temperature and at 80 K (liquid-N_2 bath cryostat) using a constant acceleration transmission spectrometer equipped with a ^{57}Co/Rh source of about 10 mCi. Data were stored in a 1024-channel MCS memory unit. The experimental

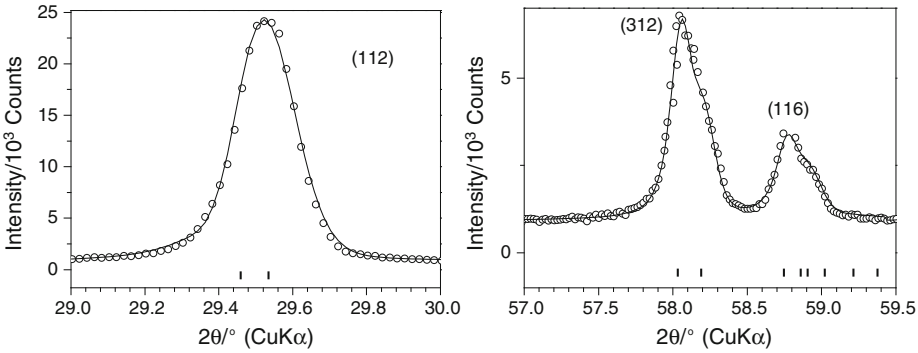

Fig. 2 XRD pattern of the chalcopyrite on an expanded 2θ-scale showing the Rietveld fits of the (*112*) reflection and (*312*) plus (*116*) reflections considering only the tetragonal chalcopyrite

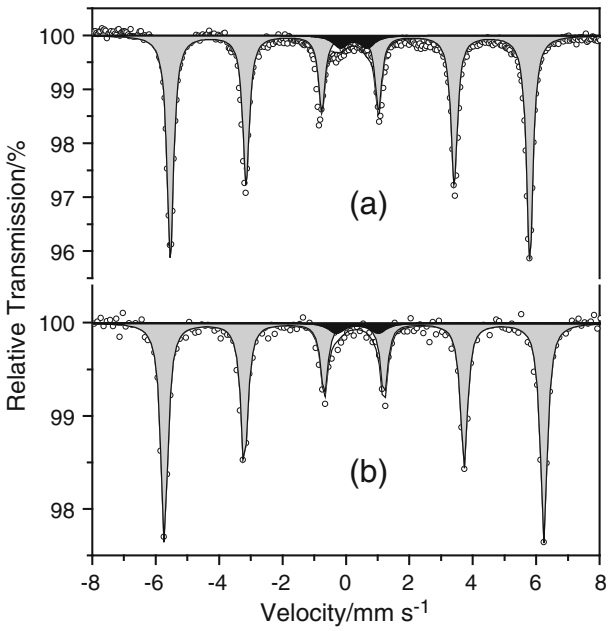

Fig. 3 Mössbauer spectra of the chalcopyrite sample **a** at room temperature and **b** at 80 K

data were fitted using Lorentzian functions with a least-squares fitting procedure based on the NORMOS program and isomer shifts are quoted relative to α-Fe.

3 Results and discussion

X-ray diffraction (XRD, Fig. 1) displays peaks at 2θ° (CuKα) of 29.46, 33.97, 48.83, 49.24, 58.04, 58.79, 71.54, 73.00, 79.15, 79.40, 79.77 and 80.00, which are characteristic of chalcopyrite. In addition to chalcopyrite, kaolinite and quartz could be identified by XRD. The XRD data were fitted using Rietveld analysis implying only one chalcopyrite with a tetragonal cell. The lattice parameter for the tetragonal

Table 1 Mössbauer parameters of the chalcopyrite sample at room temperature and 80 K

T(K)	δ/mm s^{-1}	2εQ, Δ/mm s^{-1}	B_{hf}/T	RA/%	Fe site
298	0.28 (1)	0.00 (2)	35.2 (1)	96 (1)	Chalcopyrite
	0.37 (1)	0.85 (1)	–	4 (1)	Fe^{3+} in kaolinite
80	0.37 (1)	0.00 (2)	37.1 (1)	95 (1)	Chalcopyrite
	0.47 (2)	1.33 (1)	–	5 (1)	Fe^{3+} in kaolinite

chalcopyrite were a = 5.27434(9) Å and c = 10.3885(2) Å. These lattice parameters are less than the values reported for stoichiometric chalcopyrite (a = 5.2855 Å and c = 10.4117 Å) [2], and possibly indicative of oxidation of Cu^{+} to Cu^{2+} and/or isomorphous substitution of Cu and Fe by other cations with smaller ionic radii. The kaolinite and quartz reflections were excluded from the Rietveld fitting using the exclusion zone. Figure 2 shows the good fitting of (112), (312) and (116) reflections, suggesting the existence of a unique phase, i.e. tetragonal chalcopyrite. The slight asymmetry is attributed to the different wavelengths of $K_{\alpha 1}$ and $K_{\alpha 2}$ radiation

Mössbauer data collected at 298 K consisted of a dominant sextet with hyperfine parameters that are typical for chalcopyrite (Fig. 3, Table 1). The sextet in Fig. 3 lacks the asymmetry characteristic for the chalcopyrite from Camaquã. A subordinate doublet in the spectrum can be ascribed to Fe^{3+} substituting for Al^{3+} in kaolinite.

4 Conclusions

The occurrence of a single crystalline phase in this chalcopyrite from the Cristalino deposit, Carajás Mineral Province in northern Brazil, presents an interesting differential characteristic compared to the chalcopyrite from the Camaquã copper mine [2]. For the chalcopyrite from Camaquã, the existence of two discrete modifications was attributed to an incomplete conversion of the high-temperature (cubic) variety to the low-temperature (tetragonal) variety, i.e. the cubic component was a remnant of an originally formed high-temperature phase. This is obviously not the case at the Cristalino deposit.

Acknowledgements CNPq, FAPEMIG and VALE (previously Companhia Vale do Rio Doce). CAPES (Brazil) grants the Visiting Professor PVNS fellowship to JDF at UFVJM. FAPEMIG also supported the travel of JDF to Lima, Peru, to attend LACAME 2010 (grant # PPM-00217/08) and the academic visit of EM to UFMG, Brazil (grant # BPV-00068/10). This work was also partially supported by the project named "Acqua Institute Mineral Resources, Water and Biodiversity", of the Brazilian National Program of Institutes of Science and Technology.

References

1. Rosière, C.A., Chemale, F. Jr.: Rev. Bras. Geociênc. **30**, 274 (2000)
2. Mussel, W.N., Murad, E., Fabris, J.D., Moreira W.S., Barbosa, J.B.S., Murta, C.C., Abrahão, W.P., de Mello, J.W.V., Garg, V.K.: Phys. Chem. Miner. **34**, 383 (2007)
3. Monteiro, L.V.S., Xavier, R.P., de Carvalho, E.R., Hitzman, M.W., Johnson, C.A., de Filho, C.R.S., Torresi, I.: Min. Dep. **43**, 129 (2008)
4. Ribeiro, A.A., Suita, M.T.F., Sial A.N., Fallick, A.E., Eli, F., Goulard, E.A.: Geochim. Bras. **23**, 159 (2009)
5. Fullprof_Suíte. Crystallographic tools for Rietveld, profile matching and integrated intensity refinements of X-ray and or neutron data 2010. http://www.ill.eu/sites/fullprof/ (2010). Accessed 7 Nov 2010